

https://dspace.org/

A study of the support effect of carbon dots-derived graphene-like sheets on the autoreduction of cobalt nanoparticles for Fischer–Tropsch synthesis

Mokoloko, Lerato Lydia

2022
https://hdl.handle.net/10539/37145

Downloaded from a DSpace repository. https://dspace.org/

A study of the support effect of carbon dots-derived graphene-like sheets on the autoreduction of cobalt nanoparticles for Fischer–Tropsch synthesis

By

Lerato Lydia Mokoloko
(MSc)
Student Number: 562061

A Thesis submitted for the faculty of Science at the University of Witwatersrand Johannesburg, in the fulfilment for the degree of

Doctor of Philosophy in Chemistry

Supervisor: Prof. Neil J. Coville
Co-Supervisor: Dr. Roy P. Forbes

Johannesburg, 18 October 2022

DECLARATION

I declare that this thesis is my own, unaided work under the supervision of Professor Neil J. Coville and Doctor Roy P. Forbes. It is being submitted for the degree of Doctor of Philosophy in the University of the Witwatersrand, Johannesburg. It has not been submitted before for any degree or examination in any other university.



(Signed) **Lerato Lydia Mokoloko**

On this 18th day of October 2022

SYNOPSIS

The aim of this study was to synthesize and characterize carbon dots (CDs) and to use them as a support material for cobalt (Co) based Fischer-Tropsch synthesis (FTS) reactions. The CDs were chosen for this study due to their small size (< 10 nm), easy surface functionalization and synthesis. The small size of the CDs was required for the study of inverse catalyst support effects. An inverse supported catalyst (in this case, the Co/CDs catalyst) refers to the dispersion of a support material that has a small size (d < 5 nm) onto the surface of a metal catalyst with a similar small size (d > 8 nm). The synthesis of this proposed catalyst was successful. FTS studies on the Co 'supported' CDs were attempted. Extremely poor FT activity was observed. Post analysis of the catalyst revealed that the CDs did not retain their quasi-spherical and small particle size morphology under the FTS reaction conditions (temperature 220 °C, 10 bar P; H_2:CO ratio = 2:1). Instead, upon exposure to a heat treatment, the CDs were transformed into layered structures with a unique resemblance to graphene-based nanosheets (GNSs). This transformation impacted on the use of these catalysts in the FTS reaction. However, this result indicated an unusual transformation of the CDs into another carbon shape. In light of the fascinating transformation phenomenon, annealing studies were then conducted to investigate the effect of annealing temperatures on the CDs structural changes.

The CDs (average d= ~ 2.5 nm) used in this study were obtained from the microwave-assisted carbonization of *L*-ascorbic acid and subjected to a heat treatment (i.e. annealing) at temperatures between 200 and 700 ℃ in a *horizontal* CVD apparatus under an inert nitrogen gas. It was observed that annealing transformed the CDs from 0-D qausi-spherical nanoparticles to 3-D multi-layered carbons (at 300-600 ℃) and finally 2-D layered materials (at 700 ℃). Furthermore, annealing at 700 ℃ yielded a 2-D single-layered material with comparable properties to traditionally reduced graphene oxide (rGO). A wide range of characterization techniques were used to gain an insight into the physicochemical properties of these novel CDs-derived allotropes as well as to rationalize their mechanism of formation. After evaluating the properties of these materials, it was clear that the surface oxygen functional groups, observed from XPS, ^{13}C NMR and other studies, were responsible for the CDs to rGO transformation. It was proposed that the CDs are assembled to form rGO (and other CDs-rGO derivatives) by either the Ostwald ripening (in which the carbons agglomerated via a gas phase) or a solid phase reaction (involving reaction of CD edges).

To further investigate the effect of annealing on the evolution of CDs to layered carbon structures, N-doped CDs (or NCDs) were also studied. The method used to make the pristine CDs was modified by incorporating urea as a nitrogen source to make the NCDs. Annealing the NCDs at temperatures between 200 and 700 ℃ also transformed the quasi-spherical NCDs (average d = ~ 4.1 nm) to multi-layered carbon sheets at temperature as low as 200 ℃. The CD transformation was also associated with the loss of surface functional groups, with % O and N contents of *ca.* 17 and 16 % (pristine NCDs) being reduced to *ca.* 8 and 7 % for NCDs annealed at 700 ℃. A similar mechanism for the formation of these N-doped layered carbon structures by annealing was also proposed here. For these samples, it was also observed that the N-bonds, especially the sp^3 type nitrogen bonds found on the edges of the NCDs, also took part in the coalescence of the NCDs to give the layered materials. XPS data suggested that in the process, these sp^3 type nitrogen bonds were transformed into sp^2 pyrrolic-N, pyridinic-N and Graphitic-N groups.

The annealed CDs products were used to support Co (called Co_3O_4/T250, Co_3O_4/T400 and Co_3O_4/T700 where T is the temperature at which the CDs were annealed) for use in FT studies. Studies were conducted to evaluate the effect Co hydrogen reduction temperatures verses autoreduction temperature, catalyst thermal stability and performance in the FTS reaction at 220 °C (10 bar P; H_2:CO ratio = 2:1). Upon investigation of the reduction behaviour of the Co/CDs derivative catalysts using *in situ* PXRD, it was found that these materials can successfully facilitate autoreduction of Co_3O_4 to Co face-centered-cubic (fcc) at temperatures > 400 ℃ by a reduction pathway similar to that observed using conventional H_2 reduction conditions. As expected, the reduction under H_2 took place at a lower activation temperature (> 250 ℃) than the autoreduction process. It was also noted that these novel carbon support derived from CDs gave reduced FTS performance compared to the unsupported Co, especially towards C_{5+} yields (< 30 % for all Co supported catalysts). These novel CDs-derived allotropes were found to have limited use as supports in Co-based FTS, due to Co agglomeration.

These NCDs-derived allotropes (annealed at 200 ℃, 400 ℃ and 700 ℃) were incorporated as active layers in the fabrication of chemoresistive sensing device detection of volatile organic compounds (VOCs). These layered showed enhanced chemical vapour sensing properties, especially for methanol and ethanol detection at room temperature. Therefore, although there are great limitations for applications of these CDs-derived layered allotropes in FTS reaction, these materials show a much better potential for applications in facile and cost effective VOC sensors. Further studies on this will be conducted.

DEDICATION

I dedicate this work to the people who supported me in this dream of mine: my mother, Lizzie Mokoloko, my grandmother, Pulane Nthapo, my siblings, Palesa Mokoloko and Kamohelo Nthapo. Thank you all for your immerse support, continuous prayers and your pure love.

To my late grandfather, James Rampai Nthapo (04 April 1953- 16 August 2022), whom I would have loved to celebrate my PhD graduation with.

Blessed is she who has believed that the Lord would fulfil His promises to her. **Luke 1:45**

ACKNOWLEDGEMENTS

Firstly, I would like to send my sincere gratitude to my supervisor **Prof Neil Coville** for the privilege to work with him in this research project. His insight, guidance and encouragement has profoundly inspired me. I am deeply moved by his patience, humility, and generosity towards me and all his students. This research project had a lot of twists and turns, so many unsuccessful experiments deterred us from the vision we initially had for the project. But from him I've learned that an unsuccessful experiment is just as important as a successful one, they both present an opportunity to advance our knowledge of materials and their properties, and it is where great scientific discoveries are made. I am grateful for the invaluable lessons I have learned from him, and his overall contribution to my scientific knowledge and skills.

I would like to express my appreciation to my co-supervisor **Dr Roy Forbes** for his helpful guidance especially in x-ray crystallographic analysis, as well as teaching me the skills necessary to interpret the data. I'm also grateful to him for acknowledging my hard work by giving me some incentive after every publication. That's very generous of you **Dr Forbes**.

I would like to greatly acknowledge the following people for their assistance in characterizations of the materials produced in this project:

Dr Rudolph Erasmus for the photoluminescence, ultraviolet-visible light spectroscopy as well as the Raman spectroscopy measurements, from the School of Physics, University of the Witwatersrand.

Dr Dean Barrett (School of Chemistry. University of the Witwatersrand, Johannesburg, South Africa and National Research Centre for Energy and Materials (CNPEM), **Dr Beatriz Moreno** and **Dr Graham King** (both from the Canadian Light Source Inc.) for PDF measurements performed at the Canadian Light Source. I'm truly thankful to **Dr Dean Barrett** for further helping us interpret the data.

Prof Alexandra Ziegler from the MMU (University of the Witwatersrand, Johannesburg, South Africa) for giving us the opportunity to use the microscope and x-ray diffraction facilities for characterization. I'd also like to acknowledge the staff members from the MMU unit: **Dr Manoko Maubane-Nkadimeng**, **Dr Zikhona Tetana**, **Dr Cebisa Linganiso** and **Ms Tutuzwa Xuma** for their assistance in operating and analysing our materials.

Ms Rhandzu Rhikhotso from the CSIR (Pretoria, South Africa) for the high magnification TEM analysis. As well as **Ms Petra Dinham** from the School of Chemical and Metallurgical Engineering (CHMT, University of the Witwatersrand, Johannesburg, South Africa) for the SEM analysis.

Dr Werner Jordaan (CSIR NMISA, Pretoria, South Africa) for XPS analysis.

Dr Memory Zimuwandeyi (School of Chemistry at University of the Witwatersrand, Johannesburg, South Africa) for NMR data collection, as well **Mr Mudzuli Maphupha** from the same institution for NMR data processing and some discussions.

Thank you all so much. Your expertise significantly shaped this project.

I wish to also thank **Dr Boitumelo Matsoso (University of Chemistry and Technology, Prague)** and **Dr Bridget Mutuma (Kirinyaga University in Kenya)** for their valuable discussions and mentorship. I'm looking forward to our collaborative work and publications in the future.

Thank you to the **CATMAT** research group members for their assistance.

I'd like to thank from the **DSI-NRF Centre of Excellence in Catalysis (c*change)**, the **NRF** grant holder funding as well as the **University of the Witwatersrand's postgraduate merit award** for their generous financial support.

I'm extremely grateful to my friends. These are the people who never helped me analyse or interpret my PXRD, XPS or TEM data (some don't even know what they are) but gave me enough encouragement to believe I could. They believed in me, supported me, inspired me and made sure I have a life outside the lab. **Ida Makhubela**, **Charity Tseka**, **Refilwe Moepya**, **Khanani Machumele**, **Jessica Thobejane**, **Zanele Machimane**, **Mudzuli Maphupha**, **Thapelo Mbhele**, **Lindelo Mguni**, **Phati Motake**, **Kananelo Lekau** and **Thapelo Ramathetse**, thank you all so much.

To my Joburg mom, **Dr Motlalepule Nathane**, for playing a role of a mother in my life over the past few years. I will forever cherish your love and words of encouragement.

I'm greatly indebted to my family for their prayers, patience, immersed support and many sacrifices.

I'm thankful for so many things in my life, but mostly God, because without Him, I would have nothing and no one else to be thankful for.

PUBLICATIONS, PRESENTATIONS, AWARDS AND WORKSHOPS

Publications from this study

The success of the project is shown through the publication of some of the significant findings in Open Access Journals, whilst other results are yet to be submitted for publication:

1. L. L. Mokoloko, B. J. Matsoso, R. P. Forbes, D. H. Barrett, B. D. Moreno, and N. J. Coville, "Evolution of large-area reduced graphene oxide nanosheets from carbon dots via thermal treatment," *Carbon Trends*, vol. 4, p. 100074, 2021, doi: 10.1016/j.cartre.2021.100074.
2. L. L. Mokoloko, R. P. Forbes, and N. J. Coville, "The simultaneous synthesis of carbon dots and carbon spheres with tuneable sizes using a vertical chemical vapour deposition method", *S Afr J Chem*, vol. 76, pp. 25–30, 2022, doi.org/10.17159/0379-4350/2022/v76a05.
3. L. L. Mokoloko, R. P. Forbes, and N. J. Coville, "The transformation of 0-D Carbon dots into 1-, 2- and 3-D carbon allotropes: A minireview," *Nanomaterials*, vol. 12, p. 2515, 2022, doi.org/10.3390/nano12152515.
4. L. L. Mokoloko, R. P. Forbes, and N. J. Coville, "Use of carbon dots-derived graphene-like sheets for the autoreduction of cobalt nanoparticles for Fischer–Tropsch synthesis: A limitation on the use of carbon supports" [To be submitted for publication].
5. L. L. Mokoloko, B. J. Matsoso, N. Antonatos, Z. Sofer, D. H. Barrett, B. D. Moreno, R. P. Forbes and N. J. Coville, "From 0D to 2D: N-doped carbon sheets for detection of alcohol-based chemical vapours," *RSC Adv.*, vol. 12 pp. 21440-21451, 2022, doi: 10.1039/d2ra03931a.

Publications from other studies

1. G. Hutchings, M. Bowker, R. Catlow, T. Nyathi, I. Abdullah, M. Claeys, N. Coville, A. Roldan, P. van Helden, N. Fischer, E. van Steen, L. Jewell, L. Mokoloko, D. Bahnemann, M. Neurock, F. Kapteijn, E. Iglesia, P. Gibson, K. Holt, K. Domen, and A. K. Gupta, "Novel photocatalysts: general discussion," *Faraday Discuss.*, vol. 197, pp. 533–546, 2017, doi: 10.1039/C7FD90013A.

Presentations

The results from the project were also disseminated at local and/or international conferences as well as symposia as listed below:

a) "Functionalized and non-functionalized carbon dots (Cdots) and their application as reducing and/or stabilizing agents for Fischer-Tropsch catalysts" (**Oral Presentation**), *Syngas meeting* hosted by the DSI centre of excellence in catalysis (*c*change*), Shangri-La Country Hotel (Limpopo), November 2018.

b) "Microwave-assisted synthesis of inverse Co_3O_4/Cdots: A potential catalyst for the Fischer-Tropsch reaction" (**Poster Presentation)**, *Catalysis Society of South Africa (CATSA)* Annual conference, Legend Golf & Safari Resort, Mookgopong (Limpopo), November 2018.

c) "The synthesis of carbon dots (Cdots) from a vertical chemical vapour deposition method for application in catalysis" (**Oral Presentation**), *10th annual Cross-Faculty Postgraduate Symposium*, Wits University, Johannesburg (Gauteng), September 2019.

d) "The synthesis of carbon dots (Cdots) from a vertical chemical vapour deposition method for application in the Fischer-Tropsch synthesis" (**Oral Presentation**), *Syngas meeting* hosted by the DST centre of excellence in catalysis (*c*change*), Krystal Beach Hotel, Gordon's Bay, Cape Town (Western Cape), October 2019.

e) "The synthesis of carbon dots (Cdots) from a vertical chemical vapour deposition method for application in catalysis" (**Poster Presentation**), *Catalysis Society of South Africa (CATSA)* Annual conference, Club Mykonos, Langebaan (Western Cape), November 2019.

f) "Novel amorphous graphene nanomaterials synthesis and application in synfuel production by means of cobalt-based Fischer-Tropsch reaction" (**Poster Presentation**), *11th annual Cross-Faculty Postgraduate Symposium*, Wits University, Johannesburg (Gauteng), October 2020.

g) "Evolution of large-area reduced graphene oxide nanosheets from carbon dots via thermal treatment" (**Flash Presentation**), *South African Chemical Institute's Young Chemists' Symposium* (SACI-YCS), Virtual event, July 2021.

h) "Use of carbon dots-derived graphene-like sheets for the autoreduction of cobalt nanoparticles for Fischer–Tropsch synthesis: A limitation on the use of carbon supports" (**Oral Presentation**), *Gauteng Catalysis Seminar*, Wits University, Johannesburg (Gauteng), July 2022.

Workshops

i. Attended the X-ray photoelectron spectroscopy (XPS) workshop hosted by the Department of Physics at the University of Johannesburg, South Africa (January 2018)
ii. Annual summer school and workshop in Calorimetry and Thermal Analysis held in Lyon, France (June 2018).
iii. Microscopy in material science workshop hosted by Microscopy Society of Southern Africa (MSSA), University of the Witwatersrand, South Africa (December 2018).
iv. SciTinyML: Scientific Use of Machine Learning on Low-Power Devices workshop hosted online by the International Centre for Theoretical Physics (ICTP), Trieste, Italy (October 2021).

Awards

A list of awards received during the PhD studies:

- 3rd place for best Oral presentation in the Faculty of Science, Wits Cross-Faculty Postgraduate Symposium (2019).
- University of the Witwatersrand's postgraduate merit award for outstanding academic merit (from 2019-2021).
- Golden Key International Honour Society member award for being part of the University of the Witwatersrand's top 15 % of academic achievers (2019).

TABLE OF CONTENT

DECLARATION ..... **ii**
SYNOPSIS ..... **iii**
DEDICATION ..... **v**
ACKNOWLEDGEMENTS ..... **vi**
PUBLICATIONS, PRESENTATIONS, AWARDS AND WORKSHOPS ..... **viii**
Publications from this study viii
Publications from other studies viii
Presentations ix
Workshops x
Awards x
TABLE OF CONTENT ..... **xi**
List of Figures xiv
List of Schemes xviii
List of Tables xviii
Appendix A: Chapter 4 Supplementary Information xix
Appendix B: Chapter 5 Supplementary Information xix
Appendix C: Chapter 6 Supplementary Information xx
Appendix D: Chapter 7 Supplementary Information xxi
GLOSSARY OF ACRONYMS ..... **xxii**
CHAPTER 1: INTRODUCTION **1**
1.1 Motivation 1
1.2 Aim and objectives 3
1.3 Overview of the thesis 5
1.4 References 7
CHAPTER 2: LITERATURE REVIEW **11**
2.1 Carbon dots literature review 11
The transformation of 0-D Carbon dots into 1-, 2- and 3-D carbon allotropes: A minireview 11
Abstract 11
2.1.1 Introduction 12
2.1.2 Synthesis and structure relationship of various CDs 15
2.1.3 Synthesis of larger carbon allotropes 16

2.1.4 Mechanism of formation of larger carbon materials from CDs 33
2.1.5 Application of the assembled CDs products 36
2.1.6 Conclusion and recommendations 37
2.1.7 References 40
2.2 Fischer-Tropsch synthesis reactions and catalyst support effects with carbon 57
2.2.1 Introduction 57
2.2.2 The Fischer-Tropsch synthesis (FTS) process 60
2.2.3 The FTS catalysts 62
2.2.4 Designing catalysts: Catalyst support effect 64
2.2.5 Conclusion 68
2.2.6 References 69
CHAPTER 3: ANALYSIS TECHNIQUES 79
3.1 Introduction 79
3.2 Characterization of carbon allotropes 80
3.2.1 Structural references 80
3.2.2 Basis of carbon allotropes interpretation 81
3.3 Characterization techniques 82
3.3.1 Techniques used to characterize the synthesized carbon allotropes 82
3.3.2 Characterization of Co_3O_4/rGO 87
3.4 References 89
CHAPTER 4: SYNTHESIS OF POORLY FUNCTIONALIZED CARBON DOTS 95
The simultaneous synthesis of carbon dots and carbon spheres with tuneable sizes using a vertical chemical vapour deposition method 95
Abstract 95
4.1 Introduction 96
4.2 Methods 97
4.2.1 Materials 97
4.2.2 Synthesis procedure 97
4.2.3 Characterization 100
4.3 Results and discussion 101
4.4 CDs and CSs growth mechanism 108
4.5 Conclusions 110
4.6 References 112
CHAPTER 5: REMOVAL OF CARBON DOTS SURFACE FUNCTIONAL GROUPS BY ANNEALING 118

Evolution of large-area reduced graphene oxide nanosheets from carbon dots via thermal treatment 118
Abstract 118
5.1 Introduction 119
5.2 Experimental section 120
5.2.1 Reagents 120
5.2.2 Sample synthesis 120
5.2.3 Sample characterization 122
5.3 Results and discussion 123
5.3.1 Morphology evaluation 123
5.3.2 Changes in the functional group content. 126
5.3.3 Structural changes 128
5.3.4 Optical properties. 134
5.3.5 Thermal properties 134
5.4 Mechanism of CD conversion 135
5.5 Conclusion 138
5.6 References 140
CHAPTER 6: APPLICATION OF THE CARBON DOTS-DERIVED GRAPHENE-LIKE SHEETS IN THE FISCHER-TROPSCH SYNTHESIS 150
Use of carbon dots-derived graphene-like sheets for the autoreduction of cobalt nanoparticles for Fischer–Tropsch synthesis: A limitation on the use of carbon supports 150
Abstract 150
6.1 Introduction 151
6.2 Experimental 154
6.2.1 Preparation 154
6.3 Results and discussion 157
6.3.1 Synthesis and characterization of Co_3O_4 157
6.3.2 Synthesis and characterization of Co/CD derived graphene 158
6.3.3 Fischer-Tropsch synthesis evaluation 168
6.4 Conclusion 169
6.5 References 170
CHAPTER 7: APPLICATION OF THE CARBON DOTS-DERIVED GRAPHENE-LIKE SHEETS IN VOLATILE ORGANIC COMPOUNDS SENSING 174
From 0D to 2D: N-doped carbon nanosheets for detection of alcohol-based chemical vapours 174
Abstract 174

7.1 Introduction 175
7.2 Experimental 177
7.2.1 Material synthesis and sensor preparation 177
7.2.2 Characterization 178
7.3 Results and Discussion 179
7.3.1 Temperature-dependent morphological evolution 179
7.3.2 Physicochemical properties 181
7.3.3 Composition analysis 184
7.3.4 Total scattering measurements (PDF) 187
7.3.5 Sensing properties 189
7.4 Conclusions 195
7.5 References 198
CHAPTER 8: CONCLUSION AND RECOMMENDATIONS 206
8.1 Synthesis of carbon dots (CDs) 206
8.2 Annealing of the CDs 207
8.3 Applications of CDs in the Fischer-Tropsch Synthesis reactions 209
8.4 Applications of CDs as volatile organic compound sensors 210
8.5 Future work 211
APPENDIX A: CHAPTER 4 SUPPLEMENTARY INFORMATION 212
APPENDIX B: CHAPTER 5 SUPPLEMENTARY INFORMATION 224
APPENDIX C: CHAPTER 6 SUPPLEMENTARY INFORMATION 235
APPENDIX D: CHAPTER 7 SUPPLEMENTARY INFORMATION 243

List of Figures

Figure 1. 1: a) cartoon representation and **b)** a TEM image of inverse Co/CDs (where the larger cubic particles are Co and the small quasi-spherical particles are the CDs). 2

Figure 1. 2: a) *in situ* PXRD pattern of Co_3O_4/CDs reduction under a H_2 atmosphere, with the broken line square highlighting the typical amorphous carbon PXRD region, and **b)** TEM image of the spent catalyst. 3

Figure 2. 1: The proposed representative structures of graphene quantum dot (GQD), carbon quantum dot (CQD), carbon nanodot (CND), and carbonized polymer dot (CPD). Adopted with permission from Wiley-VCH Verlag [12]. 13

Figure 2. 2: Illustrations of the shapes and TEM images of **(a,d)** hollow carbon dots (HCDs, adopted with permission from [85], Elsevier BV), **(b,e)** triangular carbon dots (triangular CDs, adopted with permission from [87], Springer Nature) and **(c,f)** single-crystal hexagonal graphene quantum dots (adopted with permission from [88], American Chemical Society)……..16

Figure 2. 3: Illustrations of the formation of 1-D carbons from 0-D CNTs: **(a,b)** CNTs (adapted with permission from [100], copyright 2012, American Chemical Society) and N-CNTs; **(c,d)** N-CNTs (reproduced with permission from [101], copyright 2021, Elsevier BV)……17

Figure 2. 4: Schematic representation of the synthesis procedure and TEM images of the resulting product formed during the conversion of 0-D CDs to 2-D graphene-like nanosheets using a **(a,b)** high-temperature (> 300 °C) treatment without a catalyst (reproduced with permission from [117], copyright 2021, Elsevier BV) and **(c,d)** lower-temperature (180 °C) treatment in the presence of a metal catalyst (reproduced with permission from [118], copyright 2017, Springer Nature)…….22

Figure 2. 5: (a) TEM and **(b)** HR-TEM of graphene-rich petal-like rutile TiO_2 from 0-D CDs and TiO_2 precursors (adopted with permission from [119], 2016 WILEY-VCH Verlag GmbH and Co. KGaA, Weinheim)…….23

Figure 2. 6: Schematic illustrations of the different synthesis methods used to convert 0-D CDs into 3-D **(a,b)** PCFs (reproduced with permission from [17], copyright 2015, Wiley-VCH), **(c,d)** N- and P-doped PCFs (reproduced with permission from [121], 2017 Elsevier Ltd.) and **(e)** N-PCFs (reproduced with permission from [122], copyright 2019, American Chemical Society)…….25

Figure 2. 7: Coal-derived CDs used as precursors for the template-assisted synthesis of **(a)** PCFs (adopted with permission from [91], 2017 Elsevier Ltd.), **(b,c)** N-PCFs (reproduced with permission from [123], 2022 Elsevier B.V.) and **(d–g)** ultra-microporous carbon (adopted with permission [124], 2018 WILEY-VCH Verlag GmbH and Co. KGaA, Weinheim), as well as the TEM images of the resulting products……27

Figure 2. 8: A schematic illustration of the template-assisted conversion of CDs into N- and S-doped **(a)** 1-D microrods, **(b)** 2-D carbon sheets and **(c)** 3-D PCFs (reproduced with permission from [127], 2021 Elsevier B.V)……30

Figure 2.9: The proposed FTS according to the **a)** CO insertion chain growth mechanism, and **b)** carbide mechanism [13]…….. 61

Figure 3. 1: Schematic representation of **a)** graphene as the starting material for **(b)** fullerene, **c)** SWCNTs and **d)** graphite (after Nasir *et al.*[17]). 80

Figure 4. 1: Illustration of the reactor used to make and collect the CDs (and CSs) from C_2H_2 using the vertical CVD method.....99

Figure 4. 2: TEM images and particle size distribution histograms of CDs produced at 1000 ^oC and different argon flow rates **a-b)** $CDs_{600/10/2}$, **c-d)** $CDs_{550/10/2}$, **e-f)** $CDs_{520/10/2}$.....103

Figure 4. 3: a) PXRD, **b)** PL, **c)** UV-Vis spectra, and **d)** TGA, data for $CDs_{600/10/2}$, $CDs_{550/10/2}$ and $CDs_{520/10/2}$, $CSs_{400/10/2}$ and $CSs_{350/10/2}$.....107

Figure 4. 4: CDs and CSs particle sizes as a function of Ar flow rate at 1000 °C. 109

Figure 4. 5: Possible mechanism to show growth of **a)** CDs and **b)** CSs from curved and planar PAHs. 109

Figure 5. 1: The TEM images of the a) pCDs, **b)** T250, **c)** T400 and **d)** T700 samples. 125

Figure 5. 2: a) FTIR spectra of samples pCDs, T200-T700 and **b)** ^{13}C NMR spectra (deconvoluted) of the T200, T400 and T700. 126

Figure 5. 3: Powder XRD patterns samples pCDs and T200-700. 129

Figure 5. 4: Raman spectra of samples T250-T700 samples. Inset: Spectra of pCDs and T200 samples.....131

Figure 5. 5: Zoomed region of PDFs of pCDs, T250, T400 and T700. 132

Figure 5. 6: DTG thermograms of pCDs and samples annealed at **a)** low and **b)** high temperatures. 135

Figure 5. 7: A schematic illustration showing a possible mechanism for the formation of rGO nanosheets from pCDs. 137

Figure 6. 1: a) TEM image and **b)** particle size distribution measured from TEM images of the Co_3O_4 nanoparticles. 158

Figure 6. 2: TEM images of samples after autoreduction. Before FTS **a)** T250, **b)** T400 and **c)** T700, **d)** Co_3O_4/T250, **e)** Co_3O_4/T400, **f)** Co_3O_4/T700 and after FTS. **g)** Co_3O_4/T250, **h)** Co_3O_4/T400, and **i)** Co_3O_4/T700.....159

Figure 6. 3: a) DTG curves of T250, T400 and T700 with and without Co_3O_4, and **b)** H_2-TPR profiles of Co_3O_4/250, Co_3O_4/T400 and Co_3O_4/T700 (inset: expanded regions below 500 °C). 161

Figure 6. 4: *In-situ* PXRD plot of **a)-b)** Co_3O_4/T250, and **c)-d)** Co_3O_4/T700 samples under H_2 (left) and N_2 (right) analysed at discrete temperatures 200 to 550 °C. The region in the dotted box shows the contribution of the carbon support to the PXRD pattern and the changes that occur as a result of an increase in temperature. 162

Figure 6. 5: The support effect on cobalt phase transformation at different temperatures under **a)** H_2 and **b)** N_2 atmosphere. 165

Figure 6. 6: A graphical illustration of possible Co oxide autoreduction mechanism when the released CO act as reducing agents.....167

Figure 7.1: (a) Low magnification TEM, **(b)** AFM images and **(c)** height profile of the NCDs700 sample. 181

Figure 7. 1: Raman spectra of **(a)** NCDs400 with inset showing that of NCDs200; and **(b)** NCDs700 samples, **(c)** ^{13}C NMR spectra for the variously annealed NCDs samples…….183

Figure 7.3: (a) XPS survey spectra for NCDs200 (red), NCDs400 (green), and NCDs700 (blue) samples, as well as **(b)** elemental composition of the as-synthesized samples……184

Figure 7.4: Peak fitted XPS curves for **(a)** C1s, **(b)** N1s, and **(c)** O1s of NCDs700 sample....185

Figure 7. 5: Zoomed region of the PDFs of pristine NCDs and annealed NCDs at 250, 400 and 700 ^oC…….187

Figure 7. 6: Inter and intralayer bond distances between carbon atoms in graphite. The values in brackets are given for nitrogen-doped graphene. These values correspond to the observed peaks in G(r)……...188

Figure 7. 7: Nyquist plots for the sensor devices after exposure to **(a)** 1200 ppm of MeOH and **(b)** 1100 ppm EtOH vapours, **(c)** representative equivalent Randle circuit…….190

Figure 7. 8: (a) Sensor response as a function of MeOH vapour concentrations for the NCDs700 sensor devices, **(b)** ionization of adsorbed O_2, and **(c)** detection mechanism of MeOH…….....193

Figure 7.9: Sensor response as a function of EtOH vapour concentrations for the **(a)** NCDs400 and **(b)** NCDs700 sensor devices; **(c)** detection mechanism of EtOH……194

List of Schemes

Scheme 2.1: Schematic depiction of the conversion of CDs to supra-CDs **(a)** in toluene (adopted with permission [128] from WILEY-VCH Verlag GmbH and Co. KGaA, Weinheim, 2015) and **(b)** in dimethylformamide (reproduced with permission from [130], Springer Nature, 2019), and **(c)** the covalent conjugation reaction of CDs (adopted with permission from [132], 2020 Elsevier BV)…….…...32

Scheme 7.1: Representation of evolution of N-configurations in NCDs with respect to annealing temperature……...……...…….……186

List of Tables

Table 2.1: A summary of methodologies followed for the transformation 0-D CDs into 1-, 2- and 3-D carbon allotropes. 28

Table 2.2: A summary of the established FTS plants around the world (reproduced from Gholami et al. [13]). 59

Table 2.3: The major products obtained from the FTS (reproduced from van Der Laan et al. [31]).....62

Table 2.4: Cartoon illustrations and data on the different catalyst models for Co-support catalysts (support - inorganic oxides and carbon allotropes). 66

Table 4.1: Parameters used for the syntheses of CDs and CSs at 25 sccm C_2H_2 and the resulting particle sizes derived from TEM images. 100

Table 5.1: The sheet sizes and % yields of T200-T700 samples. 121

Table 5.2: Chemical shift assignment and main peak estimated percentage abundance. 127

Table 6.1: Phase quantification and structural details of the Co_3O_4/T250, Co_3O_4/T400 and Co_3O_4/T700 catalysts obtained via Rietveld Refinement of the data collected *in-situ* PXRD experiments. 163

Table 6.2: The FTS performances of the prepared catalysts under different conditions 169

Table 7.1: Circuit parameters of the NCDs for detection of MeOH and EtOH.....191

Table 7.2: Comparative MeOH and EtOH detection for EIS-based devices.....19195

Appendix A: Chapter 4 Supplementary Information

Figure S4. 1: TEM image of products obtained in SCC#2 before purification 213

Figure S4. 2:a) TEM image with a **b)** particle size distribution histogram and a normal distribution curve of the $CSs_{600/10/1}$ 214

Figure S4. 3: a) TEM image with a **b)** particle size distribution histogram and a normal distribution curve of the $CSs_{550/10/1}$ 215

Figure S4. 4: a) TEM image with a **b)** particle size distribution histogram and a normal distribution curve of the $CSs_{520/10/1}$ 216

Figure S4. 5: HRTEM of **a)** $CDs_{600/10/2}$ showing their lattice fringes **b)** $CSs_{600/10/1}$ 217

Figure S4. 6: a) TEM image and **b)** particle size distribution histogram and a normal distribution curve of the $CDs_{600/9/2}$.....218

Figure S4. 7: a) TEM image and **b)** particle size distribution histogram and a normal distribution curve of the $CSs_{400/8/1}$ 219

Figure S4. 8: a) TEM image and **b)** particle size distribution histogram and a normal distribution curve of the $CSs_{400/8/2}$ 220

Figure S4. 9: a) Raman spectra and **b)** FTIR spectra of $CDs_{520/10/2}$, $CDs_{550/10/2}$ and $CDs_{600/10/2}$, $CSs_{400/10/2}$ and $CSs_{350/10/2}$ 221

Figure S4. 10: a) CDs_{600} and **b)** CDs from vitamin C in distilled water 222

Figure S4. 11: Derivative weight loss thermograms of the samples synthesized at 1000 °C 223

Appendix B: Chapter 5 Supplementary Information

Figure S5. 1: TEM image of pCDs by-product 225

Figure S5. 2: a) HRTEM and **b)** particle size distribution histogram and a normal distribution curve of the pCDs. 226

Figure S5. 3: a) TEM image and **b)** Particle size distribution histogram and a normal distribution curve of T200 sample. 226

Figure S5. 4: High resolution TEM images of the **a)** T250, **b)** T400 and **c)** T700 samples. 227

Figure S5. 5: TEM images of sample **a)** T300 **b)** T500, **c)** T600, **d)** *L*-ascorbic acid annealed at 700 °C and **e)** *L*-ascorbic acid and pristine CDs annealed at 700 °C. 227

Figure S5. 6: SEM images of **a)** T250 **b)** T400 and **c)** T700 samples. 228

Figure S5. 7: AFM images of **a)** T250 **b)** T400 and **c)** T700 samples. 229

Figure S5. 8: Expanded **a)** C1s and **b)** O1s survey XPS spectra of T200, T250, T400 and T700 229

Figure S5. 9: a) Defect density ratios and **b)** peak positions for samples T400-T700. 230

Figure S5. 10: PDFs of pCDs, T250, T400 and T700. 230

Figure S5. 11: PDF fitting of the Ni standard to determine fit variables as shown in **Table S4** below. 231

Figure S5. 12: PL spectra of pCDs and samples T200-T700. 231

Figure S5. 13: TGA profiles of pCDs and samples annealed at **a)** low and **b)** high temperatures. 232

Table S5. 1: (a-d) XPS C1s and O1s peak positions and percentage atomic abundance in samples T200, T250, T400 and T700. 232

Table S5. 2: Peak positions of the pristine CDs and samples T200-T700 233

Table S5. 3: Defect density ratios of the samples T400-T700 234

Table S5. 4: Fit variables determined from PDF fitting of the Ni standard 234

Appendix C: Chapter 6 Supplementary Information

Figure S6. 1: The Rietveld refinement results of the diffraction pattern of Co_3O_4/T700 at 550 ℃ 236

Figure S6. 2: a) PXRD pattern and **b)** H_2-TPR profile of the Co_3O_4 nanoparticles. 236

Figure S6. 3: HRTEM image of Co_3O_4/T250. 237

Figure S6. 4: BET isotherms of **a)** T250 **b)** T400, **c)** T700, **d)** Co_3O_4/T250 **e)** Co_3O_4/T400 and **f)** Co_3O_4/T700. 238

Figure S6. 5: DTG thermograms of T250, T400 and T700 with and without Co_3O_4 238

Figure S6. 6: In situ XRD plots of **a)-b)** Co_3O_4/T300, **c)-d)** Co_3O_4/T300, **e)-f)** Co_3O_4/T400 and **g)-h)** Co_3O_4/T700 analyse from 30 to 550 °C under H_2 (left) and N_2 (right). 239

Figure S6. 7: TEM image of the unsupported Co spent catalyst. 240

Table S6. 1: Surface area, porosity and approximate sheet size results of T250-T700 sample set before and after Co addition. 241

Table S6.2: Phase quantification and structural details of the of Co_3O_4/T300 and Co_3O_4/T400 catalysts obtained via Rietveld Refinement of the data collected in-situ PXRD experiments. 242

Appendix D: Chapter 7 Supplementary Information

Scheme S7. 1: Sensing device preparation and sensing set-up. 244

Figure S7. 1: Low magnification TEM micrographs of (a) pristine NCDs, (b) NCDs200, and (c) NCDs400 samples…….....244

Figure S7. 2: High resolution TEM micrographs of (a) pristine NCDs and (b) NCDs700 samples, with an inserted line profile. This does not show lines of similar heights or spacing between the lines indicating that theNCDs700 sample does not have graphitic character.…245

Figure S7. 3: AFM images of (a) NCDs200 and (b) NCDs400 samples as well as (c) their corresponding height profile. 246

Figure S7. 4: a) PXRD patterns, (b) DTG profile and (c) PL spectra of the N-doped samples after annealing from 200 °C to 700 °C……247

Figure S7. 5: Deconvoluted (a) C1s, (b) N1s, and **(c)** O1s spectra of NCDs200 sample.....248

Figure S7. 6: Deconvoluted **(a)** C1s, **(b)** N1s, and **(c)** O1s spectra of NCDs400 sample.. ..249

Figure S7. 7: (a) Carbon and **(b)** Nitrogen bonding state distributions for all samples.....249

Figure S7. 8: PDFs of pristine NCDs and annealed NCDs200, NCDs400 and NCDs700...250

Figure S7. 9: Sensor response as a function of MeOH vapour concentrations for the **(a)** NCDs200 and **(b)** NCDs400 sensor devices…….….250

Table S7. 1: Atomic compositions of the NCDs samples.....251

Table S7. 2: Sensing parameters of the NCDs devices for detection of MeOH and EtOH; sensitivity (*S*, ppm^{-1}) and LoD (ppm) 251

GLOSSARY OF ACRONYMS

C_2H_2 *Acetylene*
Al_2O_3 *Alumina*
Å *Angstrom*
~ *Approximately*
a.u *Arbitrary units*
AFM *Atomic force microscopy*
BJH *Barrett-Joyner-Halenda*
β-C_3N_4 CDs *Beta carbon nitride carbon dots*
BET *Brunauer, Emmett and Teller*
CB *Carbon black*
CO_2 *Carbon dioxide*
CDs *Carbon dots*
CPDs *Carbonized polymer dots*
CO *Carbon monoxide*
CNFs *Carbon nanofibers*
CNTs *Carbon nanotubes*
CQDs *Carbon quantum dots*
CSs *Carbon spheres*
^{13}C NMR *carbon 13 nuclear*
CVD *chemical vapor deposition*
ca. *circa (approximately)*
Co(fcc) *Cobalt face centered cubic*
Co(hcp) *Cobalt hexagonal closed packing*
C_3N QDs *Cyanoethynyl quantum dots*
°C *degree Celsius*
DTG *Derivative outputs of a thermogravimetric analyser*
D *Disorder-induced band*
d-spacing *Distance between planes of atoms*
EIS *Electrochemical impedance spectroscopy*
eV *Electron volts*
EtOH *Ethanol*
FTS *Fischer-Tropsch synthesis*
FT-IR *Fourier transform infrared spectroscopy*
FWHMs *Full width at half maximums*
GCE *Glassy carbon electrode*
g *Grams*
GO *Graphene oxide*
GQDs *Graphene quantum dots*
G *Graphitic band*
HCSs *Hollow carbon spheres*
H *Hour*
H_2 *Hydrogen gas*
I_D/I_G *Intensity ratio of D to G bands*
Q_{max} *Maximum total coherent scattering*
MSIs *Metal to support interactions*
MeOH *Methanol*
µm *Micrometer*
mL *Millileter*
Min *minutes*
MWCNTs *Multi walled carbon nanotubes*
viz. *Namely*
nm *nanometer*
NCDs *Nitrogen-doped carbon dots*
N-CNTs *Nitrogen-doped carbon nanotubes*
1-D *One dimensional*
PDF *Pair distribution function*
% *Percentage*
cm^{-1} *Per centimeter*
PL *Photoluminescence*
PVDF *Poly(vinylidene fluoride)*
PXRD *Powder X-ray diffraction*
Q_{broad} *Q-dependent broadening*
rGO *Reduced graphene oxide*
RS *resistance*
SEM *Scanning electron microscopy*
SiO_2 *Silica*
STA6000 *Simultaneous Thermal Analyzer 6000*
SWCNTs *Single-walled carbon nanotubes*
sccm *Standard cubic centimetres per minute*
Syngas *Synthesis gas*
TPR *Temperature-programmed reduction*
TiO_2 *Titania*
Q *The magnitude of the scattering vector*
G(r) *The real-space distribution of interatomic distances*
3-D *Three dimensional*
TEM *Transmission electron microscopy*
2-D *Two dimensional*
UV-vis *Ultra Violet-Visible*
VOCs *Volatile organic compounds*
XRD *X-ray diffraction*
XPS *X-ray photoelectron spectroscopy*
0-D *Zero dimensional*

CHAPTER 1: INTRODUCTION

The discovery of new nanomaterials presents new opportunities for the advancement of nanoscience as well as for nanotechnology applications [1], [2]. Carbon dots (or CDs), which were discovered in 2004, are such nanomaterials [2]. CDs are defined as quasi-spherical carbonaceous materials with nanoparticle sizes less than 10 nm [3], [4]. They have caught the attention of the scientific community not only because of their small sizes that generate quantum effects but also their inherent and tuneable fluorescence property - a property that is novel for carbon nanomaterials [3], [4]. Their various properties have made them nanomaterials of interest in fields such as biosensing, bioimaging, drug delivery, photocatalysis, electrocatalysis, solar cells and supercapacitors [5]–[9]. As a result, there has been an exponential increase in the number of publications on these topics since their discovery [10]. Another interesting fact about CDs is that their fluorescence properties are comparable with those observed for conventional metal-based quantum dots, except CDs show less toxicity than their inorganic equivalents [11]–[14]. Furthermore, they can be produced by various facile and cost-effective synthetic strategies [11]–[14]. Potential replacement of metal-based quantum dots with CDs in diverse applications has thus been investigated [11]–[14].

Although these nanomaterials show great potential for current and future nanotechnology research, the exploitation and exploration remain mainly limited to their photoluminescent properties. This begs the following question: are there other opportunities for CDs application outside the scope of their photoluminescence properties?

1.1 Motivation

To add to the library of novel CDs applications, herein we explore their potential use in the well-established heterogeneous catalysis area of Fischer-Tropsch synthesis (FTS). The FTS is a catalytic chemical reaction where synthesis gas (*syngas*) containing carbon monoxide (CO)/carbon dioxide (CO_2) and hydrogen (H_2) are converted to a range of fuels and other chemical feedstock [15].

The FTS conversion takes place on the surface of transition metal catalysts such as cobalt (Co), iron (Fe) and ruthenium (Ru). Co and Fe catalysts are used in industry while Co has some advantages including its high quality hydrocarbon production and better resistance to deactivation [16]–[18]. Typically, metal catalysts in the FTS reaction are dispersed on a support ma-

terial [19]. This increases the total area of the metal catalyst surface available for reactant conversion. Therefore, high syngas conversion is generally related to high metal catalyst dispersion [19], [20]. A variety of support materials have been used in FTS; this includes inorganic oxides such as silica (SiO_2), alumina (Al_2O_3), titania (TiO_2) and zeolites. Carbon nanomaterials such as graphene, carbon nanotubes (CNTs), carbon spheres (CSs) and hollow-carbon spheres (HCSs) have also been used as supports [21]–[23]. These support materials are known for having a high surface area, good chemical and thermal stability as well as providing good metal catalyst dispersion over their surfaces [19]. However, carbon nanomaterials have not been exploited as a support in industry.

In a previous study (MSc research project [23]), CDs were used for the synthesis of a uniquely designed catalyst known as an inverse support catalyst. In this catalyst, the CDs (the 'support') were dispersed on the surface of the Co metal catalysts (see **Figure 1.1**). The aim was to apply this catalyst in the FTS reaction. The interest in this type of catalyst model was inspired by previous studies on Co (and Fe) which were inversely supported on SiO_2 and Al_2O_3, and showed a high catalytic performance in FTS conversion compared to the use of conventional oxide supports mentioned earlier [24]–[28]. This type of catalyst also allowed for the study and tuning of the metal to support interactions (MSIs) [24]–[28]. To the best of our knowledge, the type of supported catalyst system studied in my MSc work was novel for carbon nanomaterials in FTS applications. This novelty was related to the fact that carbon nanomaterials used as supports are usually larger than the preferred catalyst nanoparticles (> 8 nm) [29], [30]; CDs (< 10 nm) and this type of arrangement presented an opportunity to study this catalyst type.

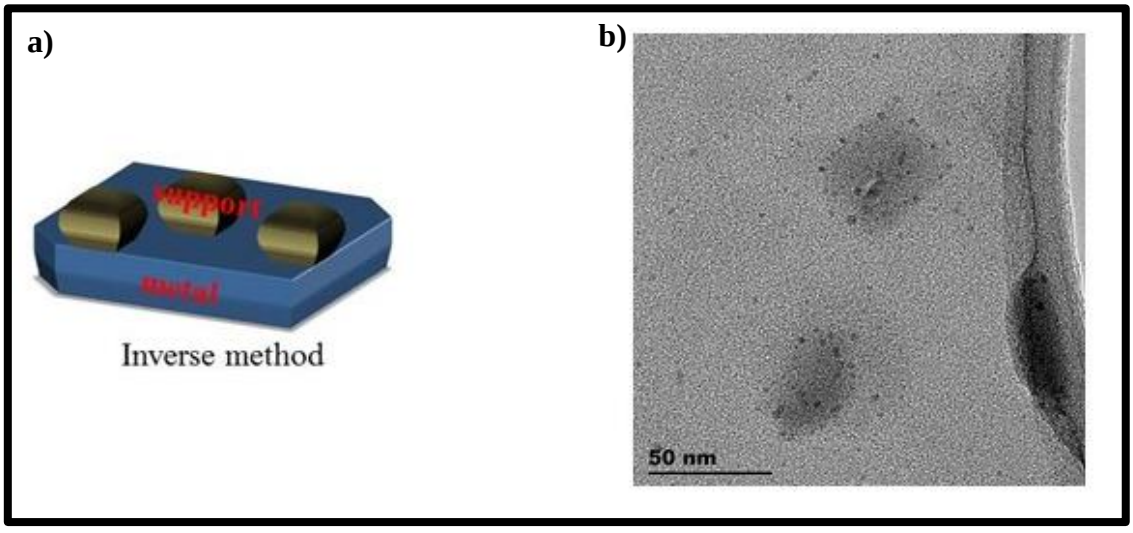

Figure 1. 1: a) cartoon representation and **b)** a TEM image of inverse Co/CDs (where the larger cubic particles are Co and the small quasi-spherical particles are the CDs).

A variety of interesting results were obtained from the MSc study [23], but of importance to this PhD research study was the thermal stability of the CDs under typical FTS reaction condition. The following discoveries were made:

1. The CDs appeared to undergo structural changes at temperatures above 200 °C. This was observed during pre-FTS catalysts testing by *in situ* PXRD (**Figure 1.2a)**), which showed changes in the shape of PXRD features at *ca.* 20 to 35 ° 2θ (Co Kα radiation), a region in the PXRD spectrum where the features of amorphous carbon nanomaterials are typically observed.
2. The TEM image of the spent catalyst (**Figure 1.2b)**), further supports the structural changes of the CDs into large-area, dimensional materials during the experiments (note that **Figure 1.1b)** was observed before heat treatment and **Figure 1.2b)** after heat treatment). Therefore, the inverse Co/CDs morphology was lost, which made it difficult to study the 'inverse' catalyst effect on the metal to support interactions (MSIs) and the catalysts performance as intended.
3. There seemed to be a correlation between structural changes and the removal of surface functional groups. This was investigated in details in the PhD study.

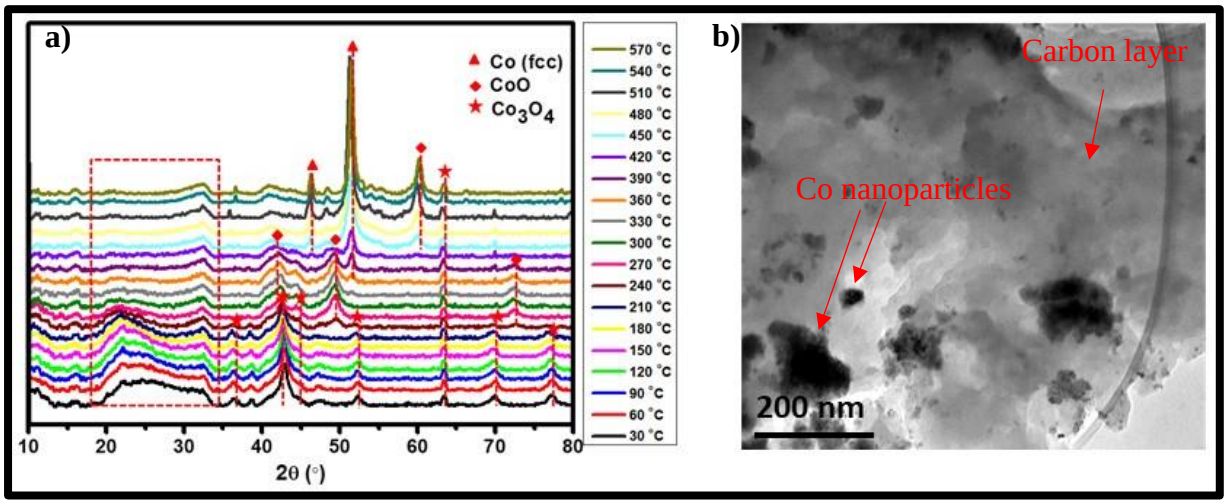

Figure 1. 2: a) *in situ* PXRD pattern of Co_3O_4/CDs reduction under a H_2 atmosphere, with the broken line square highlighting the typical amorphous carbon PXRD region, and **b)** TEM image of the spent catalyst.

1.2 Aim and objectives

The initial aim of this study was to advance the previous study from the MSc work by developing a facile method for the synthesis of non- or poorly-functionalized CDs for inverse

Co/CDs fabrication and application in the FTS. The shift to non- or poorly-functionalized CDs was motivated by the need to have CDs that are thermally stable and whose structures are not compromised under FTS testing, as it was observed in the earlier study.

The following approaches were employed for the synthesis of the non- or poorly-functionalized CDs:

1. A non-functionalized carbon source was used for the fabrication of the CDs.
2. The readily functionalized CDs were de-functionalized by annealing.

However, these approaches proved unsuccessful. The former approach produced the desired CDs (thermally stable and poorly functionalized), however, their yields were < 5 mg and could not be scaled up, even after many varied attempts (**Chapter 4**). This presented a challenge because the amount of support material needed to complete the FTS study was ~1 g. The latter method to make the CDs resulted in structural transformation of the CDs at temperatures as low as 250 °C, even under a nitrogen (N_2) atmosphere (**Chapter 5**). This meant that the structural transformation observed in earlier studies did not result from the H_2 atmosphere or the presence of the Co catalysts (as shown in *in situ* PXRD in **Figure 1.2a**) but could be attributed to the annealing temperature.

Although these results presented major setbacks to the initial aim of this research project, some interesting discoveries were made in the study. One key discovery was that the CDs self-assembled to form layered nanosheets that resembled the structure of one of carbon's 'wonder nanomaterials', *graphene*. Based on this discovery, several questions arose:

1. Could the annealing of the CDs be used as a new and facile synthesis pathway to make graphene-based sheets?
2. How do these novel sheets compare with the nanosheets produced from the conventional method?
3. Finally, are these sheets suitable for use as support materials for the Co-based FTS reaction?

These questions then led to the following aims and objectives for this study:

1. To investigate the temperature dependent structure of CDs and to gain insights into the physical and chemical properties of the resulting materials.

2. To undertake a comprehensive literature research on traditionally made graphene-based nanosheets and to compare and profile the products synthesized in this study with those in the literature.
3. To use these sheets to fabricate Co/carbon sheet catalysts and test them in the Co-based FTS reaction for the synthesis of synthetic fuels.

1.3 Overview of the thesis

Based on the results obtained throughout the project, the thesis content is thus structured as shown by the following detailed breakdown:

Chapter 1: Provides an overview of the scientific motivation, challenges, aims and objectives of this PhD work.

Chapter 2: The chapter is divided into two parts: the first part discusses the literature review on the transformation of carbon dots into other dimensional carbon allotropes. This work was published under the title: "*The transformation of 0-D Carbon dots into 1-, 2- and 3-D carbon allotropes: A minireview*", Nanomaterials, vol. 12, p. 2515, 2022.

The second half of this chapter describes the FTS process, and the use of carbon nanomaterials as supports in cobalt-based FTS.

Chapter 3: Provides an overview of how the physical and chemical properties of carbon nanomaterials are generally characterized, as well as a discussion of various characterization techniques used in this study.

Chapter 4: Reports the results of a novel synthesis of poorly functionalized CDs from the vertical chemical vapour deposition (CVD) method. This work has been published under the title: "*The simultaneous synthesis of carbon dots and carbon spheres with tuneable sizes using a vertical chemical vapour deposition method*", S Afr J Chem, vol. 76, pp. 25–30, 2022.

Chapter 5: Describes work that led to the shift in the initial motivation of this study. In this chapter, the fabrication and structural transformation of CDs to sheets (identified as reduced graphene oxide (or rGO)) under horizontal CVD-assisted annealing experiments are reported and discussed. This work has also been published under the title: "*Evolution of large-area reduced graphene oxide nanosheets from carbon dots via thermal treatment*," Carbon Trends, vol. 4, p. 100074, 2021.

Chapter 6: Reports on the synthesis of the novel catalysts consisting of the synthesis of Co_3O_4 nanoparticles as well as their dispersion on CDs-derived sheets (made in **Chapter 5)** for application in Co-based FTS. The detailed characterization procedures used to study the catalysts are also described. The findings in this chapter will also be submitted for publication under the title: "*Use of carbon dots-derived graphene-like sheets on the autoreduction of cobalt nanoparticles for Fischer–Tropsch synthesis: A limitation on the use of carbon supports.*"

Chapter 7: To further explore the potential use of these CDs-derived nanosheets, they were tested as active materials in the fabrication of the room temperature chemoresistive sensing devices. The results obtained were published under the title: "*From 0D to 2D: N-doped carbon sheets for detection of alcohol-based chemical vapours*," RSC Adv., vol. 12 pp. 21440-21451, 2022.

Chapter 8: The main conclusions resulting from this project are summarized in this chapter. Possible recommendations for future work related to this study are also included.

1.4 References

[1] S. Bayda, M. Adeel, T. Tuccinardi, M. Cordani, and F. Rizzolio, "The history of nanoscience and nanotechnology: From chemical-physical applications to nanomedicine," *Molecules*, vol. 25, no. 1, pp. 1–15, 2020, doi: 10.3390/molecules25010112.

[2] V. S. Sivasankarapillai, A. V. Kirthi, M. Akksadha, S. Indu, U. D. Dharshini, J. Pushpamalar and L. Karthik, "Recent advancements in the applications of carbon nanodots: Exploring the rising star of nanotechnology," *Nanoscale Adv.*, vol. 2, no. 5, pp. 1760–1773, 2020, doi: 10.1039/c9na00794f.

[3] A. Sciortino, A. Cannizzo, and F. Messina, "Carbon nanodots: A review—from the current understanding of the fundamental photophysics to the full control of the optical response," *J. Carbon Res.*, vol. 4, no. 4, p. 67, 2018, doi: 10.3390/c4040067.

[4] F. Yuan, T. Yuan, L. Sui, Z. Wang, Z. Xi, Y. Li, X. Li, L. Fan, A. Chen and M. Jin, "Engineering triangular carbon quantum dots with unprecedented narrow bandwidth emission for multicolored LEDs," *Nat. Commun.*, vol. 9, no. 1, pp. 1–11, 2018, doi: 10.1038/s41467-018-04635-5.

[5] M. Semeniuk, Z. Yi, V. Poursorkhabi, J. Tjong, S. Jaffer, Z.-H. Lu and M. Sain, "Future perspectives and review on organic carbon dots in electronic applications," *ACS Nano*, vol. 13, no. 6, pp. 6224–6255, 2019, doi: 10.1021/acsnano.9b00688.

[6] W. Su, H. Wu, H. Xu, Y. Zhang, Y. Li, X. Li and L. Fan, "Carbon dots: A booming material for biomedical applications," *Mater. Chem. Front.*, vol. 4, no. 3, pp. 821–836, 2020, doi: 10.1039/c9qm00658c.

[7] W. Liu, C. Li, Y. Ren, X. Sun, W. Pan, Y. Li, J. Wang and W. Wang, "Carbon dots: Surface engineering and applications," *J. Mater. Chem. B*, vol. 4, no. 35, pp. 5772–5788, 2016, doi: 10.1039/c6tb00976j.

[8] M. Tuerhong, Y. XU, and X.-B. YIN, "Review on carbon dots and their applications," *Chinese J. Anal. Chem.*, vol. 45, no. 1, pp. 139–150, 2017, doi: 10.1016/S1872-2040(16)60990-8.

[9] Z. Kang and S. T. Lee, "Carbon dots: Advances in nanocarbon applications," *Nanoscale*, vol. 11, no. 41, pp. 19214–19224, 2019, doi: 10.1039/c9nr05647e.

[10] J. Wang, H. S. Choi, and Y. X. J. Wáng, “Exponential growth of publications on carbon nanodots by Chinese authors,” *J. Thorac. Dis.*, vol. 7, no. 7, pp. E201–E205, 2015, doi: 10.3978/j.issn.2072-1439.2015.06.13.

[11] L. Cao, S.-T. Yang, X. Wang, P. G. Luo, J.-H. Liu, S. Sahu, Y. M. Liu and Y.-P. Sun, “Competitive performance of carbon ‘quantum’ dots in optical bioimaging,” *Theranostics*, vol. 2, no. 3, pp. 295–301, 2012, doi: 10.7150/thno.3912.

[12] P. G. Luo, S. Sahu, S.-T. Yang, S. K. Sonkar, J. Wang, H. Wang, G. E. LeCroy, L. Cao and Y.-P. Sun, “Carbon ‘quantum’ dots for optical bioimaging,” *J. Mater. Chem. B*, vol. 1, no. 16, pp. 2116–2127, 2013, doi: 10.1039/c3tb00018d.

[13] S. Y. Lim, W. Shen, and Z. Gao, “Carbon quantum dots and their applications.,” *Chem. Soc. Rev.*, vol. 44, no. 1, pp. 362–381, 2014, doi: 10.1039/c4cs00269e.

[14] H. Ding, L. W. Cheng, Y. Y. Ma, J. L. Kong, and H. M. Xiong, “Luminescent carbon quantum dots and their application in cell imaging,” *New J. Chem.*, vol. 37, no. 8, pp. 2515–2520, 2013, doi: 10.1039/c3nj00366c.

[15] S. Bahri, A. M. Venezia, and S. Upadhyayula, “Utilization of greenhouse gas carbon dioxide for cleaner Fischer-Tropsch diesel production,” *J. Clean. Prod.*, vol. 228, pp. 1013–1024, 2019, doi: 10.1016/j.jclepro.2019.04.310.

[16] W. T. Ralston, G. Melaet, T. Saephan, and G. A. Somorjai, “Evidence of structure sensitivity in the Fischer–Tropsch reaction on model cobalt nanoparticles by time-resolved chemical transient kinetics,” *Angew. Chemie - Int. Ed.*, vol. 56, no. 26, pp. 7415–7419, 2017, doi: 10.1002/anie.201701186.

[17] S. S. Ail, V. Benedetti, M. Baratieri, and S. Dasappa, “Fuel-rich combustion synthesized Co/Al_2O_3 catalysts for wax and liquid fuel production via Fischer-Tropsch reaction,” *Ind. Eng. Chem. Res.*, vol. 57, no. 11, pp. 3833–3843, 2018, doi: 10.1021/acs.iecr.7b04174.

[18] J. Huang, W. Qian, H. Zhang, and W. Ying, “In situ investigation on Co-phase evolution and its performance for Fischer-Tropsch synthesis over Nb-promoted cobalt catalysts,” *Catal. Sci. Technol.*, vol. 7, no. 23, pp. 5530–5539, 2017, doi: 10.1039/c7cy01325f.

[19] Z. Gholami, Z. Tišler, and V. Rubáš, “Recent advances in Fischer-Tropsch synthesis using cobalt-based catalysts: a review on supports, promoters, and reactors,” *Catal. Rev.*

- *Sci. Eng.*, vol. 63, no. 3, pp. 512-595, 2021, doi: 10.1080/01614940.2020.1762367.

[20] J. Hong, J. Du, B. Wang, Y. Zhang, C. Liu, H. Xiong, F. Sun, S. Chen, J. Li, "Plasma-assisted preparation of highly dispersed cobalt catalysts for enhanced Fischer-Tropsch synthesis performance," *ACS Catal.*, vol. 8, no. 7, pp. 6177–6185, 2018, doi: 10.1021/acscatal.8b00960.

[21] A. C. Ghogia, A. Nzihou, P. Serp, K. Soulantica, and D. Pham Minh, "Cobalt catalysts on carbon-based materials for Fischer-Tropsch synthesis: a review," *Appl. Catal. A Gen.*, vol. 609, no. July 2020, p. 117906, 2021, doi: 10.1016/j.apcata.2020.117906.

[22] N. J. Coville, S. D. Mhlanga, E. N. Nxumalo, and A. Shaikjee, "A review of shaped carbon nanomaterials," *S. Afr. J. Sci.*, vol. 107, no. 3/4, pp. 1–15, 2011, doi: 10.4102/sajs.v107i3/4.418.

[23] L. Mokoloko, "The effect of metal support interactions between a cobalt catalyst and carbon dots (Cdots) in cobalt fischer-tropsch catalysts," MSc dissertation, 2018, Available: http://wiredspace.wits.ac.za/handle/10539/26174.

[24] L. Macheli, A. Roy, E. Carleschi, B. P. Doyle, and E. van Steen, "Surface modification of Co_3O_4 nanocubes with TEOS for an improved performance in the Fischer-Tropsch synthesis," *Catal. Today*, vol. 343, pp. 176–182, 2020, doi: 10.1016/j.cattod.2018.10.018.

[26] L. Macheli, E. Carleschi, B. P. Doyle, G. Leteba, and E. van Steen, "Tuning catalytic performance in Fischer-Tropsch synthesis by metal-support interactions," *J. Catal.*, vol. 395, pp. 70–79, 2021, doi: 10.1016/j.jcat.2020.12.023.

[27] A. P. Petersen, M. Claeys, P. J. Kooyman, and E. van Steen, "Cobalt-based Fischer – Tropsch synthesis : A kinetic inverse model system," *Catalysts*, vol. 9, no. 10, pp. 794–807, 2019, doi.org/10.3390/catal9100794.

[28] R. P. Mogorosi, N. Fischer, M. Claeys, and E. Van Steen, "Strong-metal-support interaction by molecular design: Fe-silicate interactions in Fischer-Tropsch catalysts," *J. Catal.*, vol. 289, pp. 140–150, 2012, doi: 10.1016/j.jcat.2012.02.002.

[29] E. Iglesia, "Design, synthesis, and use of cobalt-based Fischer-Tropsch synthesis catalysts," *Appl. Catal. A Gen.*, vol. 161, no. 1–2, pp. 59–78, 1997, doi: 10.1016/S0926-860X(97)00186-5.

[30] J. Yang, V. Frøseth, D. Chen, and A. Holmen, “Particle size effect for cobalt Fischer-Tropsch catalysts based on in situ CO chemisorption,” *Surf. Sci.*, vol. 648, pp. 67–73, 2016, doi: 10.1016/j.susc.2015.10.029.

CHAPTER 2: LITERATURE REVIEW

2.1 Carbon dots literature review

The transformation of 0-D Carbon dots into 1-, 2- and 3-D carbon allotropes: A minireview

Abstract

Carbon dots (CDs) represent a relatively new type of carbon allotrope with a 0-D structure and with nanoparticle sizes < 10 nm. A large number of research articles have been published on the synthesis, characteristics, mechanisms and applications of this carbon allotrope. Many of these articles have also shown that CDs can be synthesized from "bottom-up" and "top-down" methods. The "top-down" methods are dominated by the breaking down of large carbon structures such as fullerene, graphene, carbon black and carbon nanotubes into the CDs. What is less known is that CDs also have the potential to be used as carbon substrates for the synthesis of larger carbon structures such as 1-D carbon nanotubes, 2-D graphene-based nanosheets and 3-D porous carbon frameworks. Herein, we present a review of the synthesis strategies used to convert the 0-D carbons into these higher-dimensional carbons. The methods involve the use of catalysts or thermal procedures to generate the larger structures. The surface functional groups on the CDs, typically containing nitrogen and oxygen, appear to be important in the process of creating the larger carbon structures that typically are formed via the generation of covalent bonds. The CD building blocks can also 'aggregate' to form so called supra-CDs. The mechanism for the formation of the structures made from CDs, the physical properties of the CDs and their applications (for example in energy devices and as reagents for use in medicinal fields) will also be discussed. We hope that this review will serve to provide valuable insights into this area of CD research and a novel viewpoint on the exploration of CDs.

KEYWORDS: carbon allotropes; carbon dots; carbon nanotubes; graphene-based nanosheets; porous carbon frameworks.

* author for correspondence: neil.coville@wits.ac.za

2.1.1 Introduction

Carbon is one of the most widely exploited elements that have been used in nanotechnology [1], [2]. This is no surprise, as carbon has many fascinating characteristics, including its most important ability to bond with itself, which has led to carbon being able to form 0-, 1-, 2- or 3-D naturally occurring and synthetically made allotropes. These carbon allotropes include graphite, diamond, graphene, fullerene, carbon nanotubes (CNTs), carbon nanofibers (CNFs), carbon black (CB), carbon nano-onions (CNOs), carbon spheres (CSs) and hollow carbon spheres (HCSs). Due to their remarkable chemical, mechanical, electrical and thermal properties, these allotropes have been used in drug delivery, electronics, composite materials, sensors, energy storage and conversion and field emission devices [1]–[4]. In addition, the various carbon allotropes can be derived from a range of highly abundant starting materials, including renewable sources and waste materials, using a wide variety of synthesis strategies. This makes the use of carbon even more important, especially towards green and sustainable nanoscience and nanotechnology applications [5]–[7].

Another relatively new carbon allotrope that has been made and studied is the carbon dot (CD). CDs are a group of carbon nanomaterials that are made of zero-dimensional (0-D) nanoparticles (<10 nm), and because of their small size they show intrinsic fluorescence properties [8]–[11]. These carbons include graphene quantum dots (GQDs), carbon quantum dots (CQDs), carbon nanodots (CNDs) and carbonized polymer dots (CPDs) [11]–[14]. The different CDs are shown in **Figure 2.1**. All of these CDs show excellent optical properties, water dispersibility, biocompatibility, resistance to photobleaching and low toxicity, and hence these materials have been used in bioimaging, catalysis, sensing and drug delivery [6], [15]. The increased attention given to CDs stems from their potential to replace traditional metal-based quantum dots (QDs), especially in the aforementioned applications [16]–[18]. This is because their competitive fluorescence properties are not associated with toxicity, environmental concerns and biohazard issues [19], [20].

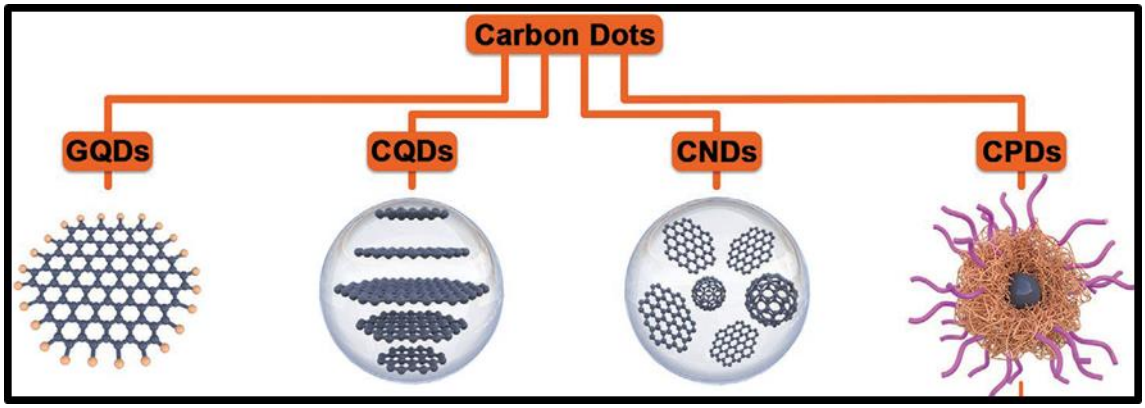

Figure 2. 1: The proposed representative structures of a graphene quantum dot (GQD), carbon quantum dot (CQD), carbon nanodot (CND) and carbonized polymer dot (CPD). Adopted with permission from Wiley-VCH Verlag [12].

The CDs were first reported in 2004 after they were serendipitously discovered during the purification of single-walled carbon nanotubes using gel electrophoresis [21], [22]. Then, in 2006, CDs were synthesized via the laser ablation of a targeted graphite powder and cement mixture surface [23]. Since then, CDs have been made via hydrothermal and solvothermal synthesis [24], electrochemical methods [25], [26] and microwave-assisted synthesis [27]. CDs can also be made using "top-down" methods using larger-sized carbon allotropes such as carbon nanotubes (CNTs), graphite, carbon nanofibers (CNFs), carbon black and candle soot [28], [29]. This is achieved by breaking down these larger carbon allotropes using strong oxidizing agents such as nitric acid or sulfuric acid [30]. They can also be made from carbon-containing molecules using a "bottom-up" method. These carbon sources range from carbohydrates such as sugar, sucrose and starch [31] to polymers (e.g., amino acids), biomass and municipal waste materials, such as fruits peels, hair and urine [32], [33].

Details on the synthesis methods [15], [19], [32], [34–38], yield [34–36], size [11], [39], physicochemical properties [29], [40–43] and applications [9], [14], [30], [32], [44–52] of the CDs have been extensively reported. Therefore, details on these topics may be found in other reports and will only be briefly mentioned in this review.

Of the two synthesis strategies, the "bottom-up" strategies are preferred because they show far better potential for the facile synthesis of CDs at low cost and large scale [5], [53]. However, it is important to note that the CDs produced via the "top-down" approach allow for better structural control and the use of easier purification methods compared to the "bottom-up" approaches [53]. Additionally, the CDs obtained from a "top-down" method obtain some of the

physical and chemical properties from the carbon allotropes from which they are derived. For example, graphene quantum dots (GQDs) derived from breaking down graphene oxide (GO) can inherit the crystallinity of the graphene oxide [54].

The conversion of one carbon allotrope to another via chemical or mechanical methods is not specific to the preparation of CDs from dimensional carbon allotropes. It is well-known that graphene nanolayers can be derived from graphite [55–58], and that graphite can be made from graphene [59]. Graphene can also be synthesized from fullerene [60–62]. Furthermore, fullerene can be exfoliated to form an atomic-scale 2-D polymeric network [63]. Reports have also indicated that graphene and graphene nanoribbons can be prepared by unravelling CNTs [64–70]. Further, CNTs can be grown on a CB substrate [71], [72]. Other examples include the transformation of CB to graphene-oxide-like nanosheets [73], [74] and HCSs [74]. Graphite can also be converted to diamonds, and vice versa [75–77]. Thus, the conversion of one allotrope to another is a well-known procedure for making high-quality carbon allotropes with size control [69], [72], [78], [79].

The ability to transform large carbon allotropes to smaller carbon entities suggests that the reverse should also be possible. Indeed, some recent studies have also shown that CDs can be used as carbon substrates in a "bottom-up" process to make CNTs, graphene-based nanosheets (GNSs) and porous carbon frameworks (PCFs). This route from CDs creates an interesting synthesis route to make novel 1-, 2- and 3-D carbon allotropes. Indeed, Chen et al. have summarized the early work on the synthesis of CDs and composites and reported on their unusual properties [80]. This conversion route from CDs could potentially be a simpler and more cost effective option than the alternate routes for the controlled synthesis of many carbon allotropes, since there is a huge library of CDs that have been made, many from renewable resources [6], [33]. Further, while some applications of these CD-derived carbon allotropes have been reported, very little detailed work has been done to exploit these materials [20], [81], [82]. In this review, we describe the methods that have been used to convert CDs to other allotropes and also provide details on the proposed mechanisms for the evolution of 0-D CDs to larger carbon allotropes (1-, 2- and 3-D carbon allotropes). A brief discussion of the applications of the final allotropes made from the CDs is given.

2.1.2 Synthesis and structure relationship of various CDs

Most CDs are typically made up of ordered or disordered graphitic flakes that constitute a carbon core, with the end carbon atoms terminated by hydrogen atoms or functional groups containing oxygen or nitrogen [6], [83]. The final structure and characteristics of the CDs are dependent on the type of synthesis approach employed in their fabrication. As previously mentioned, the CDs can be synthesized using either the "top-down" or the "bottom-up" synthesis approaches. The "top-down" synthesis approaches typically produce GQDs, which consist of a graphitic core encompassed by carbons containing oxygen-based functional groups. In contrast, "bottom-up" approaches, which involve the building up of small organic molecules and polymers via carbonization, are commonly used to make CQDs, CNDs and CPDs [14] (**Figure 2.1**). This approach results in the synthesis of an amorphous core of pure sp^3-type carbon or a core made with carbons with a range of sp^3/sp^2 carbon ratios, with the core terminated by carbon atoms with various functional groups. The CPDs are typically synthesized using polymers containing hydroxyl, carboxyl and amino groups, and possess an amorphous core terminated by polymer chains [84]. CQDs and CNDs on the other hand are typically built from carbohydrates and organic acids (e.g., ascorbic and citric acid). The CQDs and CNDs can be easily transformed into CPDs via the attachment of polymer moieties to their surfaces [5]. Biomass-derived precursors are also used in the "bottom-up" and "top-down" syntheses of different CD products [33].

Other forms of CDs include the hollow carbon dots that contain a functionalized amorphous shell formed from either a "top-down" or "bottom-up" approach [85], [86]. Highly graphitized and triangular CDs can also be obtained using a "bottom-up" synthesis approach [87]. Single-crystal hexagonal graphitic CDs with a controlled morphology can also be obtained via a "bottom-up" synthesis [88]. **Figure 2.2** shows these differently structured CDs. More recently, CDs have been made from carbon nitrides such as cyanoethynyl quantum dots and beta carbon nitride carbon dots [89,90]. Based on these discoveries, it is, therefore, safe to predict that many other derivatives of CDs will be discovered in the future.

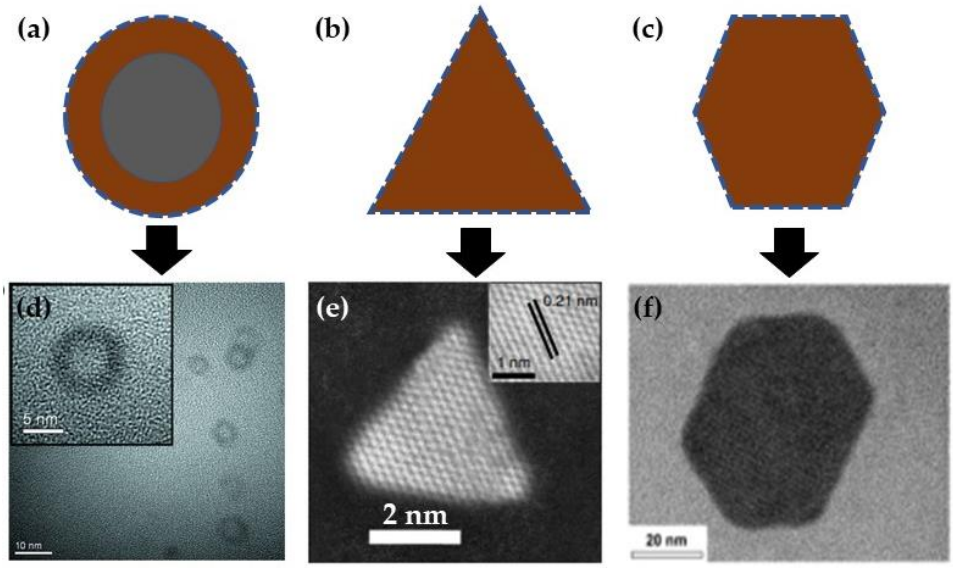

Figure 2. 2: Illustrations of the shapes and TEM images of **(a,d)** hollow carbon dots (HCDs, adopted with permission from [85], Elsevier BV), **(b,e)** triangular carbon dots (triangular CDs, adopted with permission from [87], Springer Nature) and **(c,f)** single-crystal hexagonal graphene quantum dots (adopted with permission from [88], American Chemical Society).

The unique structures of CDs capped with surface functional groups (oxygen- or nitrogen-based groups) allows for the easy modification of their physical, chemical, optical and electronic properties [8], [91]. These surface functional groups have also been shown to be important for the knitting together of CDs to form other carbon allotropes (see below).

2.1.3 Synthesis of larger carbon allotropes

Several different methods have been used to synthesize CNTs, graphene-based nanosheets (GNSs) and porous carbon frameworks (PCFs) from CD precursors. These routes, as well as the physicochemical properties of the resulting products with respect to their CDs precursors, are described below. Data on these processes are summarized in **Table 2.1**, and some examples of these routes are shown in **Figure 2.3**.

2.1.3.1 CDs used as precursors to make 1-D carbon allotropes

CNTs have been studied in detail since their synthesis and initial study by Iijima in 1991 [92]. CNTs are described as 1-D carbon allotropes made with predominantly sp^2-type carbon, rolled into a tubular structure, with typical diameters and lengths in the nano and micro or macro ranges, respectively [93], [94]. CNTs are known for their excellent mechanical, electrical and optical properties, and have been widely explored for use in energy storage, catalysis, sensors

and air filtration [95], [96]. The traditional synthesis methods used to make CNTs involve arc discharge, laser evaporation, catalytic pyrolysis and the flame method, and these methods have been described in detail elsewhere [96], [97]. While it is well known that CNTs can be cut down into CDs via chemical oxidation [98], [99], the ability of CNTs to be built up from CDs has been less studied.

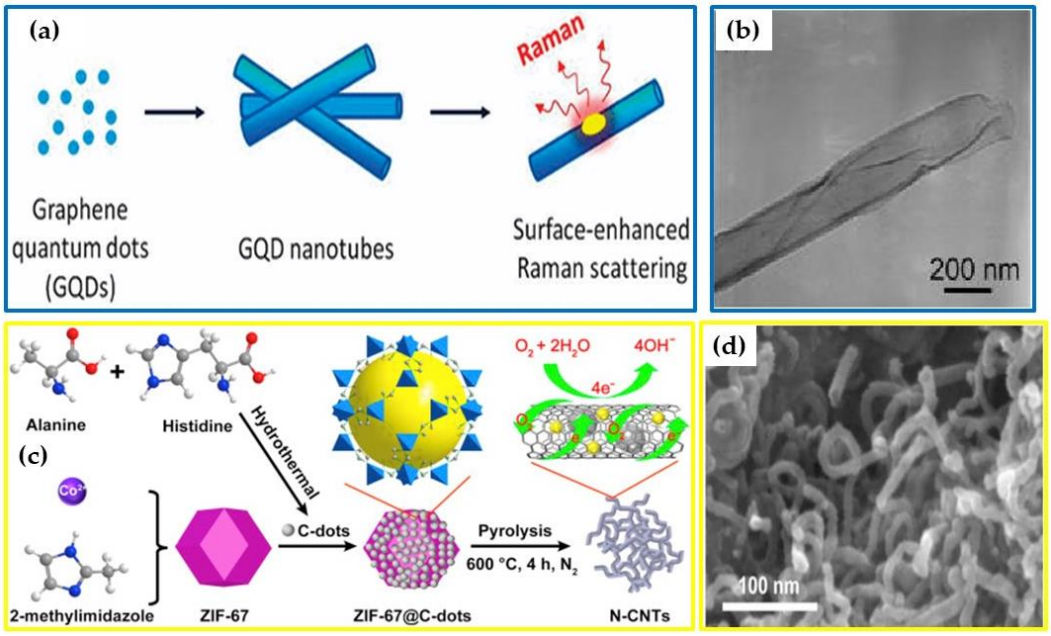

Figure 2. 3: Illustrations of the formation of 1-D carbons from 0-D CNTs: **(a,b)** CNTs (adapted with permission from [100], copyright 2012, American Chemical Society) and N-CNTs; **(c,d)** N-CNTs (reproduced with permission from [101], copyright 2021, Elsevier BV).

Cheng et al. showed that CDs can be transformed into CNTs via the electrophoresis deposition of CDs within a nanoporous anodic aluminum oxide template. The CDs were first synthesized via "top-down" electrochemical oxidation of graphene. The CDs were classified as graphene quantum dots (GQDs) and contained particles with an average size range of 3–5 nm [100]. The nanotubes obtained via the electrophoresis-aided transformation of the CDs were named graphene quantum dot nanotubes (GQD-NTs). A scheme summarizing the synthesis and TEM images of these GQD-NTs is shown in **Figure 2.3a), b)**. These GQD-NTs have similar features to those associated with traditional CNTs, such as having a hollow and tubular morphology. The average diameter range of these GQD-NTs was found to approximately 200–300 nm. The size and morphology of these GQD-NTs was highly dependent on the morphology of the AAO template. Interestingly, the formed GQD-NTs' structure still showed the individual CDs to be interconnected with an estimated gap of about 1 nm between the particles. The XPS studies

revealed the presence of hydroxyl and carboxyl functional groups on the GQDs and GQD-NTs' surfaces. They also revealed a decrease in the O/C ratio from 26.4 to 11.6 for the GQDs and GQD-NTs, respectively. This suggested that the GQD nanoparticles "merged" during the removal of the oxygen functional groups to form GQD-NTs on the AAO template.

Another study by Niu et al. showed that nitrogen-doped CNTs (N-CNTs) could be grown from a mixture of N-CDs and a metal–organic framework, ZIF-67 [101]. In this study, N-CDs were synthesized from a "bottom-up" hydrothermal reaction using alanine and histidine as precursors to give highly crystalline CDs with average particles sizes of approximately 10 nm. The ZIF-67 and N-CDs were mixed and reacted at 600 °C. The influence of the ZIF-67–N-CD ratios (30:1, 20:1 and 10:1) and reaction times (from 1 to 4 h) on the morphology of the product were investigated. The optimum reaction conditions for N-CNT formation were found to be a 20:1 (ZIF-67–N-CDs) ratio, pyrolyzed at 600 °C for 4 h (see reaction scheme in **Figure 2.3c**). Under these conditions, the N-CNTs that formed (**Figure 2.3d**) had an average diameter and length of about 15 nm and 300 nm, respectively. The N-CDs were responsible for reducing the cobalt ($Co^{2+/3+}$) ion in the ZIF-67 into metallic Co (Co^0). The N-CNTs were then grown on the Co catalyst surface during the carbonization of the organic residue of the ZIF-67 and the N-CDs under high temperature.

2.1.3.2 CDs used as precursors to make 2-D carbon allotropes

Graphene-based nanosheets (GNSs) are an interesting group of 2-D and 3-D carbon allotropes consisting of a single or a few layers of sp^2-type C atoms. These allotropes are known for their excellent mechanical properties, high surface area and versatile surface chemistry [102]–[104]. These attributes make them suitable for mechanical, optical, electrical and environmental applications, such as water purification [104]. GNSs can be made from pristine graphene, graphene oxide (GO) and reduced graphene oxide (rGO) starting materials. Pristine graphene consists of polycyclic aromatic rings forming a single layered nanosheet. In GO, the nanosheets are bonded to oxygen-based moieties, creating defects within the nanosheets. The C/O ratio is higher in rGO than in GO, and the structure has less defects [105]. GNSs are usually synthesized from "top-down" mechanical, chemical, thermal and electronic routes and via the solvent- or surfactant-based exfoliation of graphite. The "bottom-up" growth from molecular substrates has also been achieved, using the CVD method and via the graphitization of silicon carbide [106]–[112].

CDs with different morphologies and properties have been synthesized from graphene [100] and GO [39], [79]. Other studies have shown that both CDs and GO/rGO can be obtained simultaneously using the same synthesis method. For example, Dong et al. showed that GQDs and GO can be made via the "bottom-up" carbonization of citric acid at 200 °C for 30 min and 2 h, respectively [113]. Another study by Muthurasu et al. showed that GQDs and rGO can be obtained via the electrolysis of a graphite rod at a constant current density of 100 mA cm^{-2} for 3 h [114]. The resulting solution was divided into a supernatant and precipitate, where the supernatant contained GQDs and the precipitate contained the rGO. Different CDs have also been used as carbon substrates to make a variety of 2-D sheets with similar properties to those of GNSs.

Chen et al. showed that CQDs can self-assemble into layered carbon sheets when freeze-dried [115]. The CQDs with average particle sizes of approximately 7 nm were synthesized by decomposing fullerene (C60) in potassium hydroxide. The CQDs were then dispersed in water and the solution was freeze-dried to give layers of interconnected CQDs at the ice–crystal–water interface. The CQDs were interconnected via oxygen functional group interactions on the CQDs' surfaces. However, these layers rapidly dissociated into CQDs upon redispersion in water. To obtain the permanent layered carbon sheets, the CQDs were annealed at 600 and 800 °C for 30 min. At 800 °C the layered carbon sheets resembled a graphene morphology. However, there was no evidence of the hexagonal lattice fringes typical of graphene. The results from the XPS analysis showed an increase in the C/O ratio from 2.15 for CQDs to 3.14 for the annealed sample, with a significant decrease in the presence of the carbonyl functional groups, as confirmed by the FT-IR data. The study also showed that the layered carbon sheets contained a porous surface.

Hou et al. was able to obtain 2-D layered carbon nanosheets through the thermal treatment of CDs in the presence of metal ions [116]. In this study, CDs were obtained by mixing an acetaldehyde solution and NaOH at room temperature and pressure, and then allowing the mixture to stand for 3 days. The CDs had average particle sizes ranging between 3 and 5 nm. To obtain the 2-D carbon sheets, the CDs were combined with NaH_2PO_4, and then the mixture was thermally treated at temperatures between 400 and 900 °C. The transformation of the CDs to a 2-D carbon was observed to depend on both the temperature and the amount of NaH_2PO_4 used in generating the structure of the resulting sheets. The NaH_2PO_4 acted as a P-dopant and a source of Na^+, and the Na^+ metal ions catalyzed the transformation of CDs to nanosheets. The

Na^+ also controlled the sheet thickness. At 400 °C, the CDs transformed into carbon chunks, then finally at 900 °C they transformed into 2-D ultrathin sheets with lattice fringes of 0.42 nm. It was also observed that an increase in temperature increased the amount of P incorporated into the 2-D structures. On the other hand, without the NaH_2PO_4, the CDs only aggregated to form carbon chunks, and even at 900 °C no 2-D ultrafine nanosheets were observed. There was no significant difference in the C/O ratios of the samples, but the FT-IR spectra showed a significant decrease in the C=O bond intensity with increasing temperature. The authors proposed that the Na^+ ions catalyzed the decomposition of the C-O bonds, thereby increasing the amount of C species in the system. Under heat treatment, these C species then combined to form C-C bonds that assembled into the layered carbon nanosheets.

More recently, it was observed that the CDs formed 2-D graphene-like sheets without the need for a metal ion catalyst. In the study, the CDs were obtained via the microwave-assisted "bottom up" carbonization of *L*-ascorbic acid in water at 180 °C. These CDs were classified as CQDs and had average particle sizes ranging between 1 and 4 nm. These CQDs were then annealed at 200–700 °C for 10 min [117]. Carbon chunks similar to those observed by Hou et al. [116] were observed at 250 °C. These were further developed into multi-layered sheets at T ≥ 300 °C. Further heating to 700 °C gave thin layered graphene-like sheets that lacked lattice fringes. The thin layered graphene-like sheets were found to have similar properties to traditional rGO and they were, thus, referred to as rGO (**Figure 2.4a), b**). In the study, the temperature was shown to be the main contributing factor that induced the transformation of CDs to rGO. Solid-state NMR studies revealed that an increase in temperature resulted in deoxygenation of the CDs, as shown by an increase in the C/O ratio. An increase in C species led to the generation of C-C bonds and layered sheets.

In contrast, Bharathi et al. reported that a metal catalyst was needed for the formation of graphene sheets from GQDs [118]. In their study, the GQDs were synthesized via "bottom-up" hydrothermal synthesis using citric acid and urea in water at 180 °C for 3 h. The obtained CD average particle sizes were between 2 and 5 nm. The graphene sheets were obtained by adding varying amounts of zinc $ZnCl_2$ to the reaction mixture, while the reaction temperature was kept constant (**Figure 2.4c), d**). Upon the addition of 0.1 mol $ZnCl_2$ to the mixture, the GQDs' average size increased to ~10 nm. The addition of a larger amount of $ZnCl_2$ (0.3 mol) gave ~100 nm particles, while micro-sized graphene-like sheets were formed when 0.5–0.7 mol

$ZnCl_2$ was added. The XPS analysis of the formed sheet materials did not show changes in the C/O ratio.

In another study, Zhang et al. showed that CDs could be used as so-called "designer additives" in the synthesis of graphene-rich, petal-like rutile TiO_2 [119]. In this study, the CDs were synthesized from acetone mixed with NaOH. The solution was left to react for 5 days at room temperature [17]. The CDs synthesized using this method were classified as CQDs and contained average particle sizes ranging between 1.5 and 3 nm. The CQDs were then added together with the TiO_2 precursor (made from titanium(III) chloride) and CTAB (dissolved in n-pentanol and n-hexane) and reacted at 200 °C. The resulting product was further annealed at 800 °C for 2 h to give a graphene-rich, petal-like rutile TiO_2 (**Figure 2.5**). It was reported that these CQDs formed petal-like structures that acted as the TiO_2 template. The concentration of these CQDs affected the crystallite growth and resulting crystalline phases (rutile/anatase), as well as particle shapes of the TiO_2. The TEM studies revealed irregular TiO_2 products in the absence of CQDs. In the presence of the CQDs, the final annealed product indicated that the CQDs had been transformed into graphene layers that were wrapped around the TiO_2 particles. Other similar studies have shown that CDs can also be assembled on various other porous materials, including zeolites, carbonaceous porous materials, porous graphitic carbon nitride, mesoporous SiO_2 and metal–organic frameworks [80].

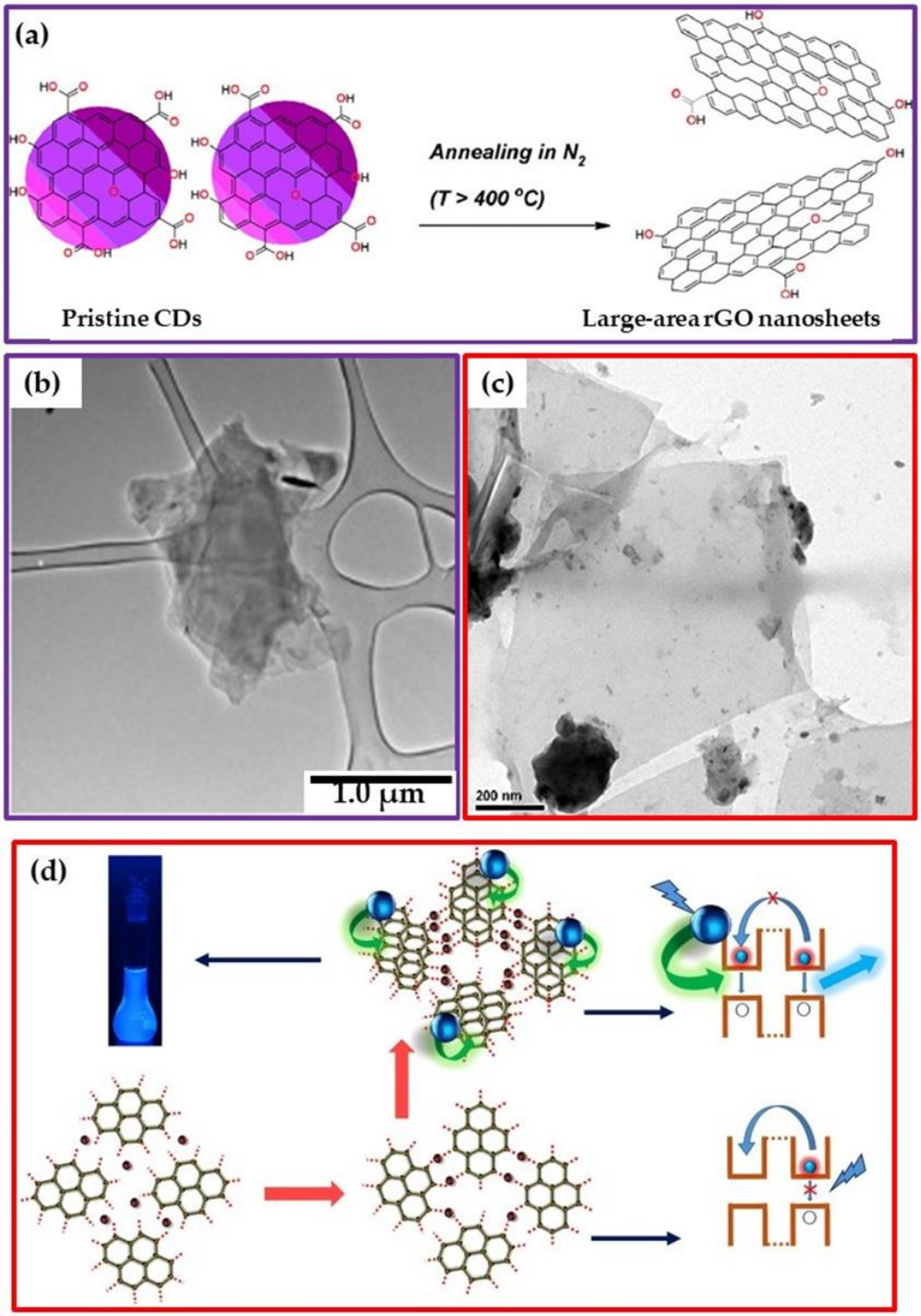

Figure 2. 4: Schematic representation of the synthesis procedure and TEM images of the resulting product formed during the conversion of 0-D CDs to 2-D graphene-like nanosheets using a **(a,b)** high-temperature (> 300 °C) treatment without a catalyst (reproduced with permission from [117], copyright 2021, Elsevier BV) and **(c,d)** lower-temperature (180 °C) treatment in the presence of a metal catalyst (reproduced with permission from [118], copyright 2017, Springer Nature).

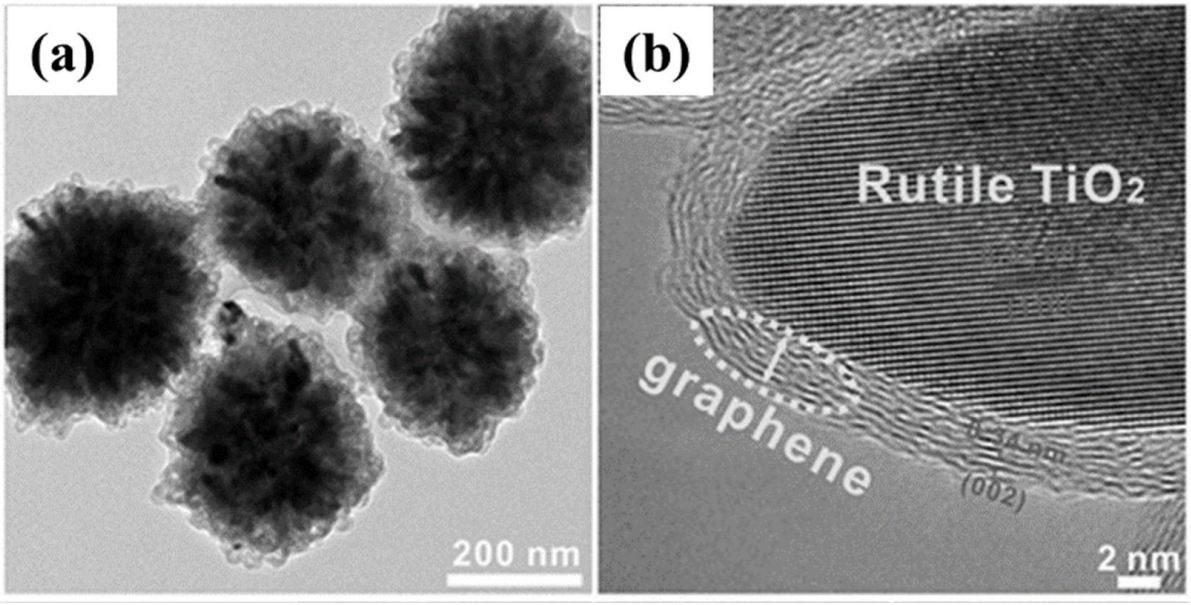

Figure 2. 5: (a) TEM and **(b)** HR-TEM of graphene-rich petal-like rutile TiO_2 from 0-D CDs and TiO_2 precursors (adopted with permission from [119], 2016 WILEY-VCH Verlag GmbH and Co. KGaA, Weinheim).

2.1.3.3 CDs used as precursors to make 3-D carbon allotropes

Porous carbon frameworks (PCFs) are an interesting group of materials known for their high surface area and tunable surface chemistry. These materials have been applied in fields such as catalysis, separation, gas storage and sensing. The traditional synthesis of these materials includes "bottom-up" synthesis strategies using organic or bio-molecules and graphene nanoribbons, while the "top-down" methods include the use of metal–organic frameworks or carbides [120]. The use of CDs as carbon precursors provides another alternative synthesis strategy to make these materials.

Hu et al. synthesized PCFs (**Figure 2.6a), b**) using CDs as precursors. The CDs were synthesized using a simple "bottom-up" approach that involved mixing acetone and NaOH (5 days at room temperature). The obtained CDs had average particle sizes ranging between 1.5 and 3 nm, and were classified as CQDs [17]. The XPS results showed that these CDs contained ~83% C and ~17% O, with C-OH, C=C, C-H and C=O as functional groups. The PCFs were obtained by calcining these CDs at 400, 600 and 800 °C under argon for 2 h at each temperature. During the transformation of the CDs to PCFs, the authors noted an increase in the C% from ~83% (for CDs) to ~94% for the calcined samples. Their results also showed that the materials showed a sharp increase in specific surface area with the increase in calcination temperature.

The mechanism of PCF formation from CDs was believed to involve a catalyst-assisted transformation.

Jiang et al. performed further modifications to Hu et al.'s method [17] to further alter the surface chemistry of the PCFs by doping them with nitrogen (N) and phosphorus (P) [121]. In this work, melamine and $C_3H_{12}NO_9P_3$ were used to form a supermolecular gel. The CQDs and supermolecular gel were then heat-treated at 800, 900 and 1000 °C under argon (Ar) for 1 h. The supermolecular gel acted as an N and P source and was also directly involved in the formation of the 3-D structure of the PCFs (**Figure 2.6c), d**). The authors also noted an increase in specific surface area with the increase in temperature, and noted that the doped PCFs were highly porous, with the pore volume increasing with the increase in treatment temperature, with a final pore volume of 0.542 $cm^3\ g^{-1}$ obtained at 900 °C. Interestingly, the authors also reported that annealing the CQDs without a supermolecular gel at 800 °C yielded 2-D graphene-like nanosheets.

In another study, nitrogen-doped CDs were used as precursors for the synthesis of fibrous 3-D PCFs. The CDs were produced via the microwave-assisted irradiation of citric acid and urea in DMF at 500 W and 160 °C [122]. After purification, the resulting solution was freeze-dried to obtain CDs with approximate average sizes ranging between 3 and 5 nm. To achieve the 3-D PCFs, the CDs were subjected to heat treatment at 800 °C under N_2 for 2 h (**Figure 2.6e**). The 3-D PCFs exhibited some graphitic characteristics, such as the lattice *d*-spacings of 0.12, 0.21, and 0.34 nm corresponding to the (002), (100) and (110) planes of a graphitic carbon, respectively. Additionally, the 3-D PCFs contained ~19 % nitrogen content, as confirmed by the XPS analysis. Interestingly, the XPS results also showed that the CDs contained predominantly pyrrolic-N, while the 3-D PCFs contained mainly pyridinic-N and graphitic-N. The data suggest that the transformation of the 0-D CDs to 3-D PCFs is also accompanied by the conversion of the pyrrolic-N to pyridinic-N and graphitic-N.

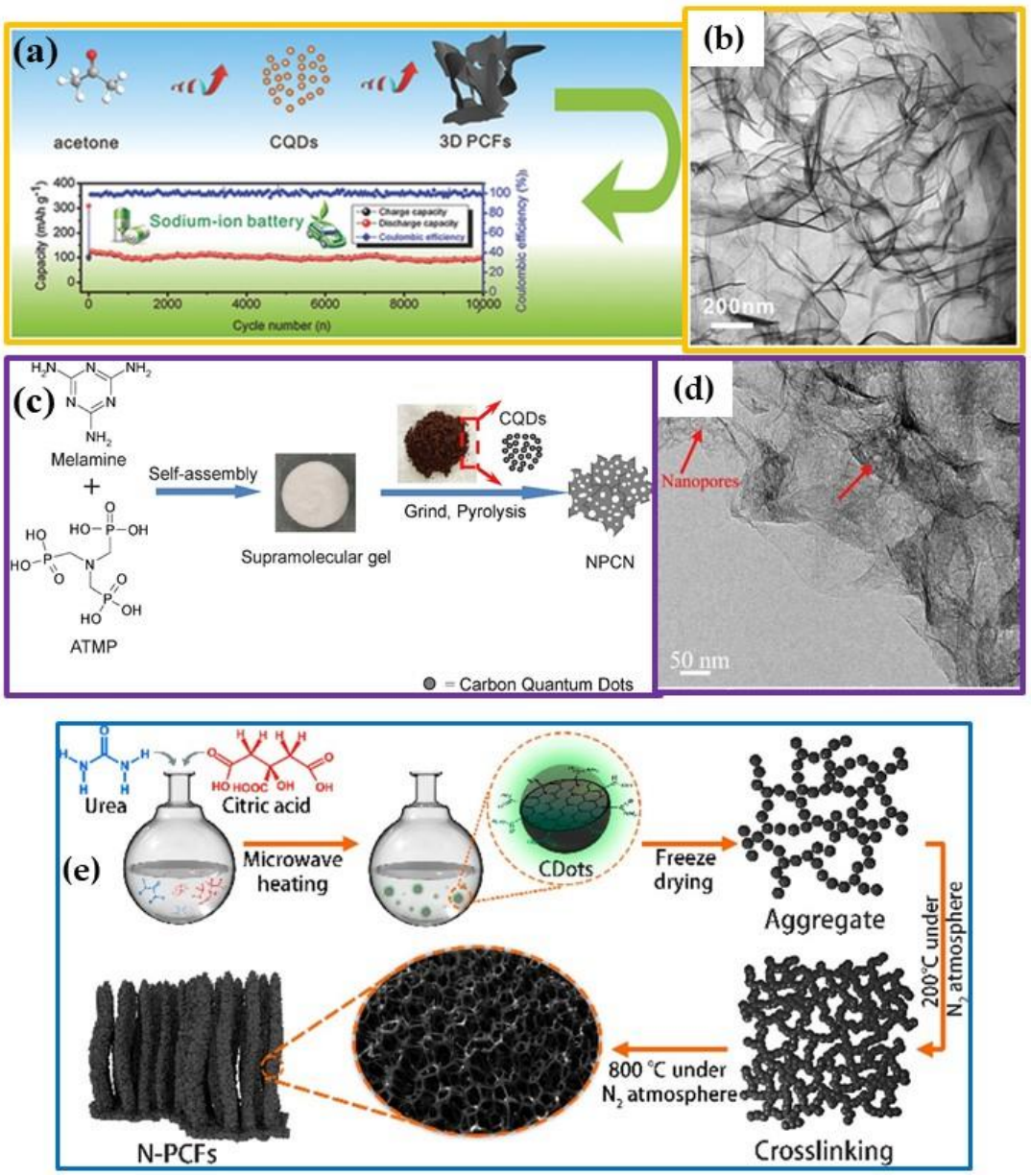

Figure 2. 6: Schematic illustrations of the different synthesis methods used to convert 0-D CDs into 3-D **(a,b)** PCFs (reproduced with permission from [17], copyright 2015, Wiley-VCH), **(c,d)** N- and P-doped PCFs (reproduced with permission from [121], 2017 Elsevier Ltd.) and **(e)** N-PCFs (reproduced with permission from [122], copyright 2019, American Chemical Society).

Zhang et al. devised a different template-assisted method for the synthesis of PCFs from CDs. To make their CDs, they used a "top-down" acid treatment (with HNO_3 and H_2SO_4) of bituminous coal [91]. The CDs were classified as GQDs and had average particle sizes in the 2–3 nm range. The transformation of GQDs to PCFs was done on a $Mg(OH)_2$ template (**Figure 2.7a**).

The amount of $Mg(OH)_2$ and the temperature (700–1000 °C) were varied to determine their effects on the resulting structure. The surface chemistry analysis revealed that these GQDs had abundant oxygen functional groups (~45%). As expected, increases in the annealing temperature and $Mg(OH)_2$ amount decreased the oxygen content to ~7%. The authors showed that the synthesis of GQDs to PCFs was induced by the $Mg(OH)_2$ template.

Recently, Lei et al. were able to prepare nitrogen-doped GQDs (~2–3 nm) by decomposing bituminous coal fine powder in HNO_3 and H_2SO_4. These GQDs were then mixed with the $Mg(OH)_2$ template and heat-treated at 800–1000 °C for 1 h under an Ar atmosphere (**Figure 2.7b,c**) [123]. The optimum results were obtained for a sample prepared at 900 °C. The resulting 3-D porous framework contained carbon (87.7%), nitrogen (4.1%) and oxygen (8.2%). As with the study by Zhang et al., increasing the temperature decreased the oxygen content. When GQDs were heated at 900 °C without the $Mg(OH)_2$ template, irregular block shapes were observed with a lower % carbon and nitrogen content but a higher oxygen content compared to the sample prepared with a $Mg(OH)_2$ template.

In another study, GQDs (made from coal, diameter of ~2.96 nm) and potassium hydroxide at different ratios (0, 0.5 and 1), gave ultra-microporous carbons (**Figure 2.7d–g**) [124]. At a 0.5 ratio, the HRTEM images showed that the GQDs were joined together to form layers, but the individual GQDs could still be observed (**Figure 2.7g**). Similar observations were noted in the formation of supra-CDs (see **Section 2.1.3.4**). When a reactant ratio of 1 was used, a 3-D structured carbon with pore sizes of approximately ~20 nm was formed. When the GQDs were heated alone, 2-D layered materials were formed. As expected, the XPS data showed that the O/C ratio decreased from 0.51 for the GQDs to 0.11 when the 0.5 ratio was used.

Strauss et al. produced a porous 3-D turbostratic graphene by irradiating N-doped CDs with an infrared laser [125]. The N-doped CDs were synthesized via "bottom-up" microwave-assisted irradiation of citric acid and urea in water, which produced nanoparticles with average sizes in the range of 1–5 nm [126]. To form the porous 3-D turbostratic graphene, the CNDs were first annealed at 300 °C to give CND aggregates (~50 nm). These CND aggregates were then laser-irradiated to form a porous 3-D turbostratic graphene. The laser irradiation induced decarboxylation of the CNDs and catalyzed the C-C bond formation between the CND moieties. Gases such as CO_2 were released during the laser irradiation, and this gave rise to the formation of the porous 3-D morphology of the graphene.

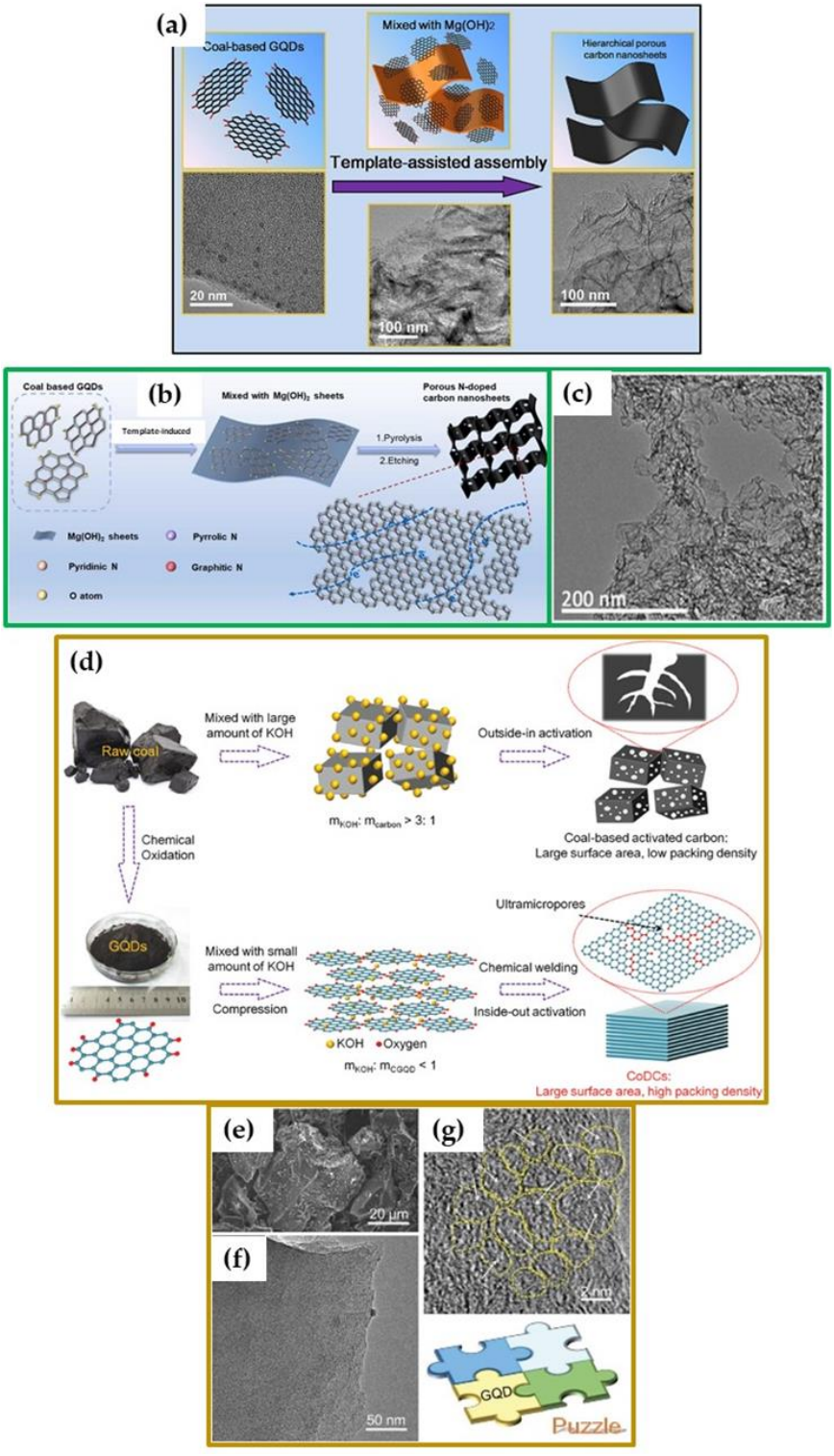

Figure 2. 7: Coal-derived CDs used as precursors for the template-assisted synthesis of **(a)** PCFs (adopted with permission from [91], 2017 Elsevier Ltd.), **(b,c)** N-PCFs (reproduced with permission from [123], 2022 Elsevier B.V.) and **(d–g)** ultra-microporous carbon (adopted with permission [124], 2018 WILEY-VCH Verlag GmbH and Co. KGaA, Weinheim), as well as the TEM images of the resulting products.

Table 2.1: A summary of the methodologies followed for the transformation of 0-D CDs into 1-, 2- and 3-D carbon allotropes.

No.	Carbon Dots			Assembly Process			
	Precursor(s)	Type	Average Size Range (nm)	Synthesis	Type of Carbon Allotrope	Dimensions (D)	Ref.
1	Graphene	GQDs	3–5	Assembled inside the anodic aluminum oxide via electrochemical deposition	GQD-NTs	1-D	[100]
2	Alanine and histidine	CQDs	~10	Pyrolyzed with ZIF-67 powder	N-CNTs	1-D	[101]
3	fullerene (C_{60})	CQDs	~7	Annealed under inert gas atmosphere	Layered sheets	2-D	[115]
4	acetaldehyde solution and NaOH	-	3–5	Mixed with NaH_2PO_4 and calcined under Ar gas atmosphere	carbon sheets	2-D	[116]
5	L-ascorbic acid	CQDs	1–4	Annealed under N_2 inert gas atmosphere	carbon sheets (rGO)	2-D	[117]
6	citric acid and urea	GQDs	2–5	Hydrothermal synthesis in the presence of ZnCl	graphene sheets	2-D	[118]
7	acetone and NaOH	CQDs	1.5–3	Reaction with TiO_2 precursors in an autoclave, then annealed under an Ar atmosphere	graphene	3-D	[119]
8	Acetone and NaOH	CQDs	1.5–3	Calcination under an Ar gas atmosphere	PCFs	3-D	[17]
9	Acetone and NaOH	CQDs	-	Pyrolyzed with melamine and $C_3H_{12}NO_9P_3$ under Ar atmosphere	N-, P-PCFs	3-D	[121]
10	Citric acid and urea	-	3–5	Freeze-dried and calcined under N_2 atmosphere	Fibrous N-doped PCFs	3-D	[122]
11	Bituminous coal	GQDs	2–3	carbonized on a $Mg(OH)_2$ template	Hierarchical PCFs	3-D	[91]
12	Bituminous coal	GQDs	2–3	carbonized on a $Mg(OH)_2$ template	N-doped PCFs	3-D	[123]

13	Bituminous coal	GQDs	~3	Carbonized with potassium hydroxide	Ultra-microporous carbons	2-/3-D	-
14	Citric acid and urea	CNDs	1–5	Thermolyzed in a tube furnace and laser irradiation with 40 W CO_2 laser	turbostratic graphene	3-D	[125]
15	Citric acid and aqueous ammonia	N-, S-CDs	~4	Pyrolyzed on Fe_2O_3, NaCl and SiO_2 spheres templates	microrods, carbon sheets and PCFs	1-/2-/3-D	[127]

GQDs: graphene quantum dots; GQD-NTs: graphene quantum dot nanotubes; CQDs: carbon quantum dots; N-CNTs: nitrogen nanotubes; 2-D: two dimensional; rGO: reduced graphene oxide; 3-D: three dimensional; PCFs: porous carbon frameworks; N-, P-PCFs: nitrogen- and phosphorus-doped porous carbon frameworks; CNDs: carbon nanodots.

Another interesting study was reported by Cheng et al., who were able to transform 0-D nitrogen-doped CDs into 1-, 2- and 3-D carbon structures using different metal templates [127]. In their study, citric acid and aqueous ammonia were used to synthesize nitrogen-doped CDs with an average particle size of 4 nm. These nitrogen-doped CDs were then mixed with thiourea and a template (Fe_2O_3 rods, NaCl and 3-D stacked SiO_2 spheres) to form nitrogen and sulfur co-doped structures (**Figure 2.8**). The mixtures were first freeze-dried, then heated at 300 °C and finally pyrolyzed at 900 °C for 4 h under a N_2 atmosphere. After the removal of the templates, it was observed that nitrogen and sulfur co-doped 1-D microrods (width ~100 nm), 2-D stacked carbon nanosheets and 3-D porous carbon frameworks (diameter of the 3-D stacked spheres = ~200 nm) had been made. Interestingly, the nitrogen and sulfur contents (XPS atomic abundance: N = 5.58 % and S = 1.64 %) were higher in the 2-D carbon structure when compared to the other structures, with pyrrolic-N being the dominant nitrogen configuration present. It was observed that the pyrolysis temperature played a significant role in the transformation of these nitrogen-doped CDs on differently structured templates, similar to the reports mentioned previously.

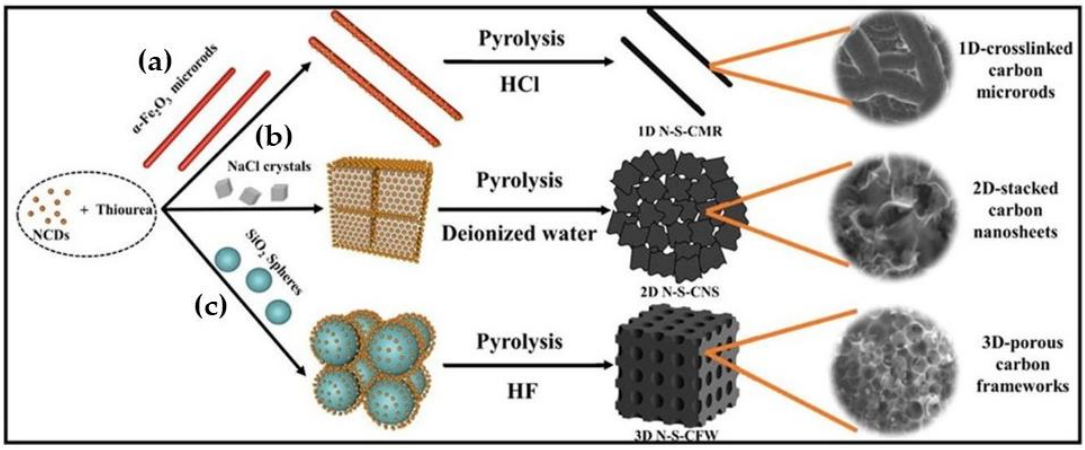

Figure 2. 8: A schematic illustration of the template-assisted conversion of CDs into N- and S-doped **(a)** 1-D microrods, **(b)** 2-D carbon sheets and **(c)** 3-D PCFs (reproduced with permission from [127], 2021 Elsevier B.V).

2.1.3.4 Other CDs assembly products

The other assembled structures produced from the CDs included the supra-CDs. Supra-CDs are typically non-permanent nanostructures of CDs formed by inter-particle interactions between CD nanoparticles via strong or weak bonding forces between surface functional groups.

The formation of supra-CDs has been used for the broadening of the PL absorption spectra of the CDs [128]–[130]. A variety of CDs have been used to produce these supra-CDs.

Lou et al. prepared CDs from a "bottom-up" synthesis method using citric acid and urea as the starting precursors. The modification of the CDs with 1-bromododecane gave partially functionalized CDs with average particle sizes ranging between 1 and 5 nm, with an amphipathic surface. In toluene, these partially functionalized CDs self-assembled through amphipathic interactions to give nanoclusters with sizes of 150–400 nm (see **Scheme 2.1a**), described as supra-CDs [128]. Li et al. showed that CDs made from citric acid and urea could self-assemble without attaching alkyl chains onto the CDs' surfaces. In their study, they also obtained CNDs with sizes ranging between 1 and 5 nm. When the CNDs were left under 60% humidity for 7 days, supra-CDs were formed. These supra-CDs were smaller when compared to the ones obtained by Lou et al., with sizes ranging between 5 and 25 nm [129]

Another study by Yang et al. showed that supra-CDs could be formed via the self-assembly of CDs obtained from melamine and dithiosalicylic acid in acetic acid. The CDs had average particle sizes ranging between 4 and 10 nm. When placed in dimethylformamide, these CDs interlinked with each other to form supra-CDs (see **Scheme 2.1b**) with sizes around 56 nm [130]. Hou et al. also showed that the CDs prepared via the "top-down" method could be used to make supra-CDs. In this study, CDs were synthesized by breaking down ultrafine coal pitch with formic acid and hydrogen peroxide. The obtained CDs were then dispersed in the surface microchannels of balsa wood. After drying at 60 °C, it was observed that the pore sizes of this wood decreased from 14.7 nm to about 1 nm, signifying that the CDs had self-assembled to form supra-CDs inside the pores of the wood [131]. It can also be assumed that the interconnected CQDs that were formed at the ice–crystal–water interface in a study by Chen et al. [115] (described in **Section 2.1.3.2**) were also another example of supra-CDs.

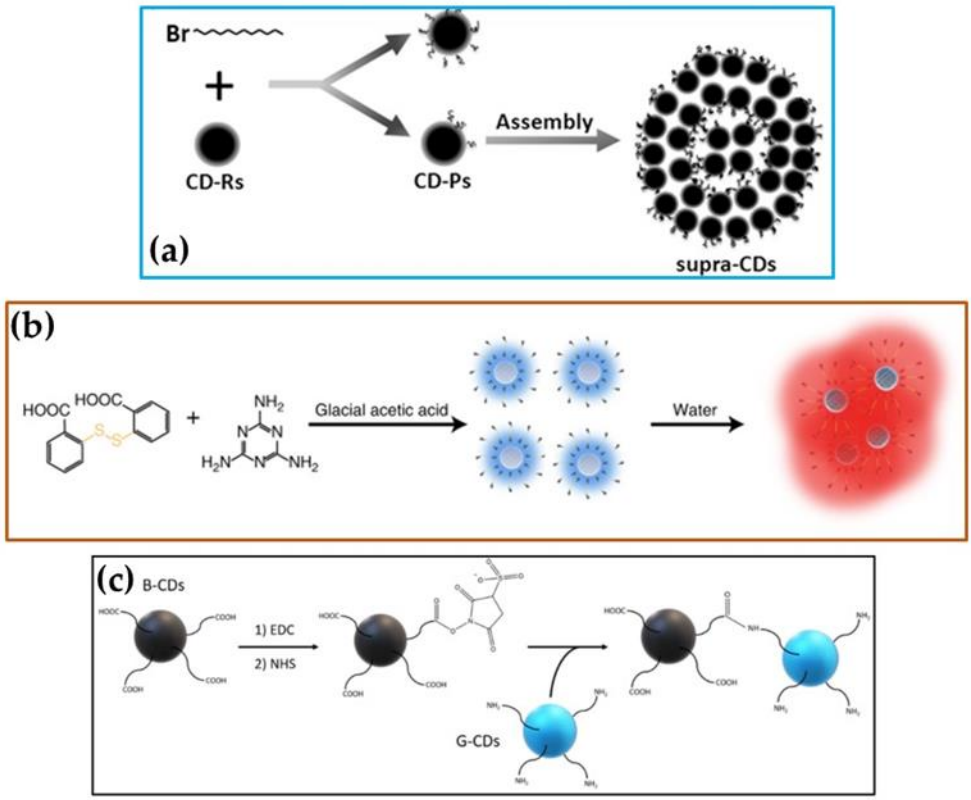

Scheme 2.1: Schematic depiction of the conversion of CDs to supra-CDs **(a)** in toluene (adopted with permission [128] from WILEY-VCH Verlag GmbH and Co. KGaA, Weinheim, 2015) and **(b)** in dimethylformamide (reproduced with permission from [130], Springer Nature, 2019), and **(c)** the covalent conjugation reaction of CDs (adopted with permission from [132], 2020 Elsevier BV).

The conjugation of differently functionalized CDs is another way of building dimensional carbon allotropes. In these reactions, chemical linkers are used to react with specific chemical groups on the CD surface to be conjugated, and these reactions form covalently coupled nanostructures [132,133]. For example, Zhou et al. performed an amidation reaction between "black CDs" (B-CDs) and "gel CDs" (G-CDs) [132]. The B-CDs were obtained via the "top-down" method involving breaking down carbon powder into H_2SO_4 and HNO_3, while the G-CDs were made in a "bottom-up" reaction, which involved reacting ethylenediaminetetraacetic acid with citric acid. The B-CDs were predominantly functionalized with -COOH groups, which were activated and stabilized using N-ethyl-N'-(3-(dimethylamino)propyl)carbodiimide/N-hydroxysuccinimide to form intermediates that were subsequently reacted with $-NH_2$ groups found on the surfaces of the G-CDs to form a conjugate (see **Scheme 2.1c**). The reactions were performed by first dispersing the CDs in phosphate-buffered saline solution (pH

7.4), then adding them together and allowing them to react overnight while stirring. Different B-CD-to-G-CD ratios were used in the reaction to produce different nanostructures. For example, when the B-CD-to-G-CD ratio was 5:3, the particles appeared to merge to form a figure-eight shape. When the ratios were changed to 5:100 and 5:300, nanofibers and some nanosheets were formed [132]. The conjugation reactions produced similar results to the heat-treated systems. However, in these reactions, higher-dimensional carbon structures were achieved by changing the ratio of the starting materials. In some instances, the CDs self-conjugated to form larger CD particles. For example, CDs (~2 nm) with predominantly –COOH and some $–NH_2$ were able to self-conjugate to form larger particle sizes (68 ± 30 nm). Conjugation reactions were also used to link the CDs with other species such as metal-based quantum dots [134] and drug molecules [135].

2.1.4 Mechanism of formation of larger carbon materials from CDs

From the discussion above, it is noted that the CD assembly process requires the alteration of surface functional groups, which leads to the transformation of the physical structure of the CDs.

2.1.4.1. Chemical Transformation

As mentioned in the introduction, CDs are terminated by functional groups, e.g., O- and N-based functional groups, depending on the type of synthesis procedure followed to make them. The CD assembly process appears to be highly dependent on the reduction or removal of surface functional groups, especially in a deoxygenation process. This reduction or removal leads to an increase in the C species, which then react to form C-C bonds and the larger carbon allotropes [17,117]. The XPS analysis results are usually used to confirm the functional group's removal or transformation. The evidence of this transformation is mostly shown by an increase in the C atomic %, accompanied by a decrease in the O atomic %. Additionally, there is also evidence that some of the O-based surface functional groups are transformed from one bonding configuration to another. For example, Strauss et al. noted that during the transformation of CNDs to porous 3-D turbostratic graphene, some of the C-O-H groups from the CNDs were transformed into C-O-C groups when the porous 3-D turbostratic graphene was formed [125].

In the case of the assembly of N-doped CDs to dimensional allotropes, some authors have shown that there are similar changes in the N-functional groups as with the O-functional groups. In most of the reported syntheses, the N-doped CDs are synthesized by using urea as a

nitrogen source. For example, Strauss et al. synthesized N-doped CDs using citric acid and urea and the authors reported that the N-H functional groups from the CDs were removed when the CDs were laser-irradiated [125]. In another example where N-doped CDs were also synthesized from citric acid and urea, Zhang et al. noted that the transformation of the N-doped CDs to PCFs (at 800 °C) led to a decrease in the N atomic %, as well as the conversion of N-pyrrolic functional groups in the CDs to graphitic- and pyridinic-N in the PCFs [122]. The transformation of N-pyrrolic functional groups in the CDs to graphitic- and pyridinic-N after the heat treatment was also observed in the transformation of N-doped CDs from *L*-ascorbic acid and urea to 2-D graphene-like sheets at temperatures ranging between 200 and 700 °C [136]. Interestingly, when the N-doped CDs from citric acid and urea were reacted in the presence of a Zn catalyst (different concentrations of the catalyst at 180 °C), the resulting 2-D sheets contained only graphitic-N [118].

Hou et al. synthesized N- and P-incorporated PCFs from CDs and noted a decrease in the O-based functional groups after heat treatment. The authors also noted an increase in the P atomic % with the increase in heat treatment from 400 to 900 °C [116]. However, it was not clear whether or not the P-configuration changed with the temperature or not. Investigations into how other heteroatoms are affected by the heat treatment or catalyst-induced transformation of the CDs are needed.

The functional groups are typically removed or transformed using a catalyst or thermal procedures by knitting together the sp^2/sp^3 carbon layers of the CDs to form the 1-, 2- and 3-D carbon allotropes. Thus, the study by Hou et al. showed that both the temperature and metal catalyst were needed for the transformation of CDs to larger carbon allotropes [17], [116]. However, other studies showed that only thermal procedures were needed to convert CDs and N-doped CDs to graphene nanosheets [117], [136], while Bharathi et al. formed layered sheets by varying only the catalyst concentration [118]. In contrast, the synthesis of supra-CD studies suggested that the CDs can assemble spontaneously [129] merely by adding them to a solvent [128], [130]; however, these are not permanent structures.

In the process of CD conjugation, the surface functional groups on the CDs undergo similar reactions to those of small organic molecules and form covalent bonds, which join together with CD particles to form different carbon structures [132], [133].

2.14.2. Physical Transformation

The resulting carbon morphology appears to be dependent on the template used to make the carbon material from the CDs. If a template is used, the CDs will assemble into the shape of the template. For example, the transformation of CDs to CNTs requires the use of a tubular-shaped template to achieve the hollow tube morphology [100], [101]. It is not yet clear what types of morphologies will result from the transformation of the CDs synthesized in the absence of a template. However, Jiang et al. showed that the CDs that were heat-treated at 800 °C in the presence of a supermolecular gel template yielded 3-D PCFs, while without this supermolecular gel template 2-D graphene-like nanosheets were obtained [121].

Also of note is the observation that the material that forms the CDs can influence the final structure. Thus, when CDs were produced using acetone as one of the precursors, excess acetone molecules were entrapped into the layered sheets. Their presence or removal during high-temperature annealing precluded the nanolayers from stacking on top of each other, as found in graphene and graphite [17], [121]. It will be interesting to establish whether the absence of surface heteroatoms (as in hydrophobic CDs) will still lead to the CDs' structural transformation in a solvent (as in supra-CDs), under high temperature and with a catalyst.

It is still not clear whether the CD identity (i.e., GQDs, CQDs, CNDs and CPDs) affects the structure of the final carbon allotrope that is formed. This arises since the classification of CDs is based on their synthesis, not on the products they form [14]. For example, only CDs obtained from the exfoliation of graphitic materials are called GQDs [137]. However, GQDs can also be obtained from non-graphitic natural starting materials such as durian [138], with crystallinity levels as high as those obtained from graphitic materials. Over the years, the better characterization and interpretation of the CDs properties has led to better-defined categories of CDs (GQDs, CQDs, CNDs and CPDs), with the classification not only being based on their synthesis but also their physicochemical properties as well [5], [14]. Even so, the current classification approach is still used inconsistently [5], [14]. Therefore, it is possible that some of the CDs used in earlier studies for the formation of larger carbon allotropes from CDs were misclassified. Further studies devoted to understanding the relationship between the identity of CDs and the type of carbon allotrope formed after their thermal- or catalyst-mediated transformation are needed. Our suggestion for this would be to take advantage of machine-learning-based techniques.

Recently, machine-learning-based techniques have been used to further our knowledge base and understanding of CDs. More importantly, machine learning has been used to gain a further understanding and build experimental models using data and algorithms to correlate the structure–property relationship of CDs [139]. Thus, machine-learning-based techniques have been used to develop strategies that allow the synthesis of CDs with targeted optical properties [140], [141], optimized quantum yields [142] and high selectivity in gas sensing [143]. Since machine learning is already shedding some light on the structure–property relationship, it is possible that this tool can potentially predict the identity of the CDs (i.e., GQDs, CQDs, CNDs and CPDs) and the type of dimensional carbon formed after heat treatment or catalysis reactions, and potentially can also help control the amount of dopant (e.g., N-, P-doping) in the final carbon structure.

2.1.5 Application of the assembled CDs products

A variety of literature reports have shown that carbon nanomaterials including CDs can be applied in clean and sustainable energy production. Similarly, studies have shown that the new 1-, 2- and 3-D carbon allotropes derived from CDs also show great potential for application in energy conversion and storage [14], [20]. Thus, these materials have been applied in electrode materials, separators and electrolytes for the fabrication of a new generation of batteries [14], [20]. For example, the N-CNTs derived from N-CDs proved to be useful in the study of metal-free electrocatalysts for oxygen reduction reactions (ORRs). Thus, N-CNTs derived from N-CDs showed high electrocatalytic performance, with a high positive potential of 0.80 V and peak current density of 1.21 mA/cm^{-2}. This high performance was attributed to the highly porous structure, high surface area and enhanced structural features obtained due to the use of N-CDs. This performance was shown to be better than the commercial Pt/C catalyst used under the same conditions [101]. Similarly, the 3-D P- and N-functionalized PCFs derived from CDs showed a high positive potential of 0.93 V and peak current density of 4.49 mA/cm^{-2} as compared to a commercial Pt/C [121].

The 2-D carbon allotropes derived from CDs have previously been used in supercapacitors. Chen et al. produced carbon layers that showed a high electrode density (1.23 g cm^{-3}), high volumetric capacitance (157.4 F cm^{-3}) and good rate capability (0.66 F cm^{-2}) behavior in 6 M KOH aqueous electrolytes. This high performance was also attributed to the highly porous nature of the carbon allotropes used in the fabrication of the supercapacitor electrodes [115].

The 3-D PCFs synthesized from CDs have a high surface area, appropriate pore sizes and allow the easy incorporation of different dopants to provide good storage sites for sodium or lithium ions in sodium or lithium ion batteries, with increased conductivity when used as high-density supercapacitor electrodes. The full scope of these results may be found in other reviews [20], [144]. Additionally, due to the properties mentioned, these materials have also been successfully used as catalysts for oxygen reduction reactions [123], [127].

The supra-CDs have not been extensively explored. However, they are known to cause significant modifications of the luminescence properties of the CDs and to subsequently expand the scope of the potential of the CDs in different applications, particularly in the medical fields. These materials have shown potential for use as fluorescence nanomaterials for biological applications [128], [129]. The supra-CDs can be used in near-infrared photothermal applications [129], [131]. Other future potential uses of these supra-CDs include their application in optical communications [128].

Conjugated CD structures have shown promising applications in nanomedicine and as drug nanocarriers. Conjugated CDs have been created to be able to deliver drugs through the blood–brain barrier to the central nervous system. For example, the B-CD and G-CD conjugates discussed earlier have properties that make them favorable as drug delivery nanostructures. These properties include their good aqueous stability and bone-targeting ability (B-CDs) and their rich –COOH and -NH_2 surface functional groups, which can assist during diffusion into the blood–brain barrier (G-CDs) [132]. These conjugated CDs can, thus, be used as drug carriers for central nervous system-related diseases [132], [133].

2.1.6 Conclusion and recommendations

The conversion of one carbon allotrope into another leads to materials with novel physicochemical properties that can be used for numerous applications. The transformation of CDs to 1-, 2-, and 3-D carbon allotropes as discussed here is no exception. Many reports have shown that these novel CD conversion processes represent facile synthesis strategies to make new and known dimensional carbon allotropes. Additionally, since CDs can be derived from a variety of cost-effective and recyclable carbons using simple synthesis strategies, these novel syntheses could potentially be a more cost-effective route for the synthesis of these larger carbon allotropes.

The assembly of CDs takes place via the interactions of the functional groups on the CD surface. The oxygen functional groups specifically are the ones driving this process. For the formation of supra-CDs, these interactions can be easily destroyed by redispersion, while in the 1-, 2- and 3-D carbon allotrope the functional groups are chemically removed or reduced, leading to a permanent merging of the CD nanoparticles into a larger carbon allotrope. The latter is achieved by using heat treatment or metal catalysts (e.g., Na^{+}, Zn^{2+}). It is important to further investigate the effect of each parameter separately and in detail. The studies on carbon nanomaterials have shown that they decompose at lower temperatures in the presence of metal catalysts. Therefore, it is possible that the 1-, 2- and 3-D carbon allotropes can be obtained at milder temperatures.

A current limitation to the formation of the larger structures using CDs relates to the size and surface chemistry associated with the CDs. The nanosized CDs are readily dispersible in solvents, and this makes their purification and collection using filtration techniques difficult. Further, the synthesized CDs have a range of sizes and 'molecular weights', and these factors will impact on their surface chemistry and use.

Thus far, not enough data have been generated to establish the CD identities (GQDs, CQDs, CNDs and CPDs) and their effect on the formation of the assembled carbon allotropes. Further studies on this topic still need to be conducted. Machine-learning-based techniques can potentially assist in this regard. The results, however, show that the carbon morphology is affected by using a template or by the nature of the starting materials. For example, CDs derived from acetone form 3-D carbon materials under thermal treatment because they contain excess acetone, which is removed under heat treatment, and this gasification alters the shape of the formed sheets from 2-D to 3-D. Without both gas and heat treatments, the resulting morphology is most likely to be a 2-D graphene-based sheet structure.

It is worth noting that there is an emergence in the literature of metal-free carbon composites involving CDs, such as CD–graphene and CD–CNT composites. These composites have shown that there is great synergy between the two carbon allotropes, which results in materials with improved properties for applications in energy materials and biological studies. The current studies have shown that these composites are, however, made by synthesizing the carbon allotropes separately and later mixing them to form a final composite product. This review shows that it is possible to adopt a one-step synthesis approach to make these composites. For

example, using methods such as the “bottom-up” carbonization of citric acid, researchers were able to produce 2-D allotropes that still contained some residual CDs within the layers, making their final products carbon composites. There is potential for other synthesis methods to be tuned in such a way that other carbon composites can be formed as well. It will also be worthwhile to conduct studies to compare the CD-derived allotropes and allotropes derived from conversional synthesis methods in terms of their physicochemical properties and performance in different applications.

These new carbons formed from CDs have already been exploited for use in capacitors and in nanomedicine. Further uses can be envisaged in these areas, as well as for uses in solar cell devices and as sensors due to their size and peculiar physical properties (e.g., fluorescence). It appears that the small differences in the new carbons-determined by their source have an impact on their properties. Thus, future studies could establish (i) the role of the type of CD (see **Figure 2.1**) on the final carbon product, (ii) the role of the functional groups in generating the new larger carbons, (iii) the advantages and disadvantages of these carbons made from CDs compared with equivalent carbons made using classical ‘top-down’ methods and (iv) whether they can be used in less traditional arenas such as in dielectrics and heat dissipation systems.

Author Contributions: Conceptualization, L.L.M. and N.J.C.; resources, N.J.C. and R.P.F.; data curation, L.L.M. and N.J.C.; writing-original draft preparation, L.L.M.; writing-review and editing, N.J.C., L.L.M. and R.P.F.; supervision, N.J.C. and R.P.F.; funding acquisition, N.J.C. All authors have read and agreed to the published version of the manuscript.

Funding: This research was funded by the University of the Witwatersrand (Funding; Wits Postgraduate Merit Award) and the DSI-NRF Centre of Excellence in Catalysis (*c**change), and The APC was funded by the DSI-NRF CENTRE OF EXCELLENCE IN CATALYSIS (*c**change).

Acknowledgments: We wish to thank the NRF, the University of the Witwatersrand and the DSI-NRF Centre of Excellence in Catalysis for their financial support.

Conflicts of Interest:

The authors declare no conflict of interest.

2.1.7 References

[1] S. K. Tiwari, V. Kumar, A. Huczko, R. Oraon, A. De Adhikari, and G. C. Nayak, "Magical allotropes of carbon: prospects and applications," *Crit. Rev. Solid State Mater. Sci.*, vol. 41, no. 4, pp. 257–317, 2016, doi: 10.1080/10408436.2015.1127206.

[2] P. S. Karthik, A. L. Himaja, and S. P. Singh, "Carbon-allotropes: Synthesis methods, applications and future perspectives," *Carbon Lett.*, vol. 15, no. 4, pp. 219–237, 2014, doi: 10.5714/CL.2014.15.4.219.

[3] S. Nasir, M. Z. Hussein, Z. Zainal, and N. A. Yusof, "Carbon-based nanomaterials/allotropes: A glimpse of their synthesis, properties and some applications," *Materials (Basel).*, vol. 11, no. 2, pp. 1–24, 2018, doi: 10.3390/ma11020295.

[4] N. J. Coville, S. D. Mhlanga, E. N. Nxumalo, and A. Shaikjee, "A review of shaped carbon nanomaterials," *S. Afr. J. Sci.*, vol. 107, no. 3/4, pp. 1–15, 2011, doi: 10.4102/sajs.v107i3/4.418.

[5] C. Xia, S. Zhu, T. Feng, M. Yang, and B. Yang, "Evolution and synthesis of carbon dots: From carbon dots to carbonized polymer dots," *Adv. Sci.*, vol. 6, no. 23, 2019, doi: 10.1002/advs.201901316.

[6] M. Kurian and A. Paul, "Recent trends in the use of green sources for carbon dot synthesis–A short review," *Carbon Trends*, vol. 3, p. 100032, 2021, doi: 10.1016/j.cartre.2021.100032.

[7] El-Shafey, A. M., "Carbon dots : Discovery , structure , fluorescent properties , and applications," *Green Process. Synth.*, vol. 10, pp. 134–156, 2021, doi.org/10.1515/gps-2021-0006.

[8] N. Tejwan, A. K. Saini, A. Sharma, T. A. Singh, N. Kumar, and J. Das, "Metal-doped and hybrid carbon dots: A comprehensive review on their synthesis and biomedical applications," *J. Control. Release*, vol. 330, pp. 132–150, 2021, doi: 10.1016/j.jconrel.2020.12.023.

[9] Z. Fan, S. Li, F. Yuan, and L. Fan, "Fluorescent graphene quantum dots for biosensing and bioimaging," *RSC Adv.*, vol. 5, no. 25, pp. 19773–19789, 2015, doi:

10.1039/c4ra17131d.

[10] Z. Wang, T. Hu, R. Liang, and M. Wei, "Application of zero-dimensional nanomaterials in biosensing," *Front. Chem.*, vol. 8, p. 320, 2020, doi: 10.3389/fchem.2020.00320.

[11] S. Sarkar, D. Banerjee, U. K. Ghorai, N. S. Das, and K. K. Chattopadhyay, "Size dependent photoluminescence property of hydrothermally synthesized crystalline carbon quantum dots," *J. Lumin.*, vol. 178, pp. 314–323, 2016, doi: 10.1016/j.jlumin.2016.05.033.

[12] L. Ai, R. Shi, J.Yang, K. Zhang, T. Zhang, and S. Lu, "Efficient combination of g-C_3N_4 and CDs for enhanced photocatalytic performance: A review of synthesis, strategies, and applications," *Small*, vol. 17, pp. 2007523, 2021, doi:10.1002/smll.202007523.

[13] L. Li and T. Dong, "Photoluminescence tuning in carbon dots: Surface passivation or/and functionalization, heteroatom doping," *J. Mater. Chem. C*, vol. 6, no. 30, pp. 7944–7970, 2018, doi: 10.1039/c7tc05878k.

[14] R. T. Guo, L. Li and B. W. Wang, "Functionalized carbon dots for advanced batteries," *Energy Storage Mater.*, vol. 37,pp. 8–39, 2021, doi: 10.1016/j.ensm.2021.01.020.

[15] M. Jorns and D. Pappas, "A review of fluorescent carbon dots , their synthesis , physical and chemical characteristics , and applications," *Nanomaterials*, vol. 11, no. 6, p. 1448, 2021, doi.org/10.3390/nano11061448.

[16] S. N. Baker and G. A. Baker, "Luminescent carbon nanodots: Emergent nanolights," *Angew. Chem., Int. Ed*, vol. 49, pp. 6726–6744, 2010, doi: 10.1002/anie.200906623.

[17] H. Hou, C. E. Banks, M. Jing, Y. Zhang, and X. Ji, "Carbon quantum dots and their derivative 3D porous carbon frameworks for sodium-ion batteries with ultralong cycle life," *Adv. Mater.*, vol. 27, no. 47, pp. 7861–7866, 2015, doi: 10.1002/adma.201503816.

[18] J. Gong, X. Lu, and X. An, "Carbon dots as fluorescent off–on nanosensors for ascorbic acid detection," *RSC Adv.*, vol. 5, no. 11, pp. 8533–8536, 2015, doi: 10.1039/C4RA13576H.

[19] X. Wang, Y. Feng, P. Dong, and J. Huang, "A mini review on carbon quantum dots: Preparation, properties, and electrocatalytic application," *Front. Chem.*, vol. 7, pp. 1–9, 2019, doi: 10.3389/fchem.2019.00671.

[20] C. Hu, M. Li, J. Qiu, and Y. P. Sun, "Design and fabrication of carbon dots for energy conversion and storage," *Chem. Soc. Rev.*, vol. 48, no. 8, pp. 2315–2337, 2019, doi: 10.1039/c8cs00750k.

[21] X. Xu, R. Ray, Y. L. Gu, H. J. Ploehn, L. Gearheart, K. Raker and W. A. Scrivens, "Electrophoretic analysis and purification of fluorescent single-walled carbon nanotube fragments," *J. Am. Chem. Soc.*, vol. 126, no. 40, pp. 12736–12737, 2004, doi.org/10.1021/ja040082h.

[22] Z. Peng, X. Han, S. Li, A. O. Al-Youbi, A. S. Bashammakh, M. S. El-Shahawi and R. M. Leblanc, "Carbon dots : Biomacromolecule interaction , bioimaging and nanomedicine," *Coord. Chem. Rev.*, vol. 343, pp. 256–277, 2017, doi.org/10.1016/j.ccr.2017.06.001.

[23] Y.-P. Sun, B. Zhou, Y. Lin, W. Wang, K. A. S. Fernando, P. Pathak, M. J. Meziani, B. A. Harruff, X. Wang, H. F. Wang, P. G. Luo, H. Yang, M. E. Kose, B. L. Chen, L. M. Veca and S.-Y. Xie, "Quantum-sized carbon dots for bright and colorful photoluminescence," *J. Am. Chem. Soc.*, vol. 128, no. 24, pp. 7756–7757, 2006, doi.org/10.1021/ja062677d.

[24] M. Xu, Z. Li, X. Zhu, N. Hu, H. Wei, Z. Yang and Y. Zhang, "Hydrothermal / solvothermal synthesis of graphene quantum dots and their biological applications," *Nano. Biomed. Eng.*, vol. 5, no. 2, pp. 65–71, 2013, doi: 10.5101/nbe.v4i3.p65-71.1.

[25] M. Zhang, L. Bai, W. Shang, W. Xie, H. Ma, Y. Fu, D. Fang, H. Sun, L. Fan, M. Han, C. Liu and S. Yang "Facile synthesis of water-soluble, highly fluorescent graphene quantum dots as a robust biological label for stem cells," *J. Mater. Chem.*, vol. 22, no. 15, pp. 7461–7467, 2012, doi: 10.1039/c2jm16835a.

[26] X. Tan, Y. Li, X. Li, S. Zhou, L. Fan, and S. Yang, "Electrochemical synthesis of small-sized red fluorescent graphene quantum dots as a bioimaging platform," *Chem. Commun.*, vol. 51, no. 13, pp. 2544–2546, 2015, doi: 10.1039/c4cc09332a.

[27] T. V. De Medeiros, J. Manioudakis, F. Noun, J. R. Macairan, F. Victoria, and R. Naccache, "Microwave-assisted synthesis of carbon dots and their applications," *J. Mater. Chem. C*, vol. 7, no. 24, pp. 7175–7195, 2019, doi: 10.1039/c9tc01640f.

[28] B. De and N. Karak, "Recent progress in carbon dot–metal based nanohybrids for

photochemical and electrochemical applications," *J. Mater. Chem. A*, vol. 5, no. 5, pp. 1826–1859, 2017, doi: 10.1039/C6TA10220D.

[29] S. Zhu, Y. Song, X. Zhao, J. Shao, J. Zhang, and B. Yang, "The photoluminescence mechanism in carbon dots (graphene quantum dots, carbon nanodots, and polymer dots): current state and future perspective," *Nano Res.*, vol. 8, no. 2, pp. 355–381, 2015, doi: 10.1007/s12274-014-0644-3.

[30] J. Zhou, H. Zhou, J. Tang, S. Deng, F. Yan, W. Li and M. Qu, "Carbon dots doped with heteroatoms for fluorescent bioimaging: a review," *Microchim. Acta*, vol. 184, no. 2, pp. 343–368, 2017, doi: 10.1007/s00604-016-2043-9.

[31] H. Peng and J. Travas-Sejdic, "Simple aqueous solution route to luminescent carbogenic dots from carbohydrates," *Chem. Mater.*, vol. 21, no. 23, pp. 5563–5565, 2009, doi: 10.1021/cm901593y.

[32] V. Sharma, P. Tiwari, and S. M. Mobin, "Sustainable carbon-dots: Recent advances in green carbon dots for sensing and bioimaging," *J. Mater. Chem. B*, vol. 5, no. 45, pp. 8904–8924, 2017, doi: 10.1039/c7tb02484c.

[33] W. Meng, X. Bai, B. Wang, Z. Liu, S. Lu, and B. Yang, "Biomass-derived carbon dots and their applications," *Energy Environ. Mater.*, vol. 2, no. 3, pp. 172–192, 2019, doi: 10.1002/eem2.12038.

[34] J. Zhang and S. H. Yu, "Carbon dots: large-scale synthesis, sensing and bioimaging," *Mater. Today*, vol. 19, no. 7, pp. 382–393, 2016, doi: 10.1016/j.mattod.2015.11.008.

[35] M. L. Liu, L. Yang, R. S. Li, B. Bin Chen, H. Liu, and C. Z. Huang, "Large-scale simultaneous synthesis of highly photoluminescent green amorphous carbon nanodots and yellow crystalline graphene quantum dots at room temperature," *Green Chem.*, vol. 19, no. 15, pp. 3611–3617, 2017, doi: 10.1039/c7gc01236e.

[36] B. Chen, F. Li, S. Li, W. Weng, H. Guo, T. Guo, X. Zhang, Y. Chen, T. Huang and X. Hong,"Large scale synthesis of photoluminescent carbon nanodots and their application for bioimaging," *Nanoscale*, vol. 5, no. 5, pp. 1967–1971, 2013, doi: 10.1039/c2nr32675b.

[37] H. Li, Z. Kang, Y. Liu, and S.-T. Lee, "Carbon nanodots: synthesis, properties and

applications," *J. Mater. Chem.*, vol. 22, no. 46, p. 24230, 2012, doi: 10.1039/c2jm34690g.

[38] Z. L. Wu, Z. X. Liu, and Y. H. Yuan, "Carbon dots: Materials, synthesis, properties and approaches to long-wavelength and multicolor emission," *J. Mater. Chem. B*, vol. 5, no. 21, pp. 3794–3809, 2017, doi: 10.1039/c7tb00363c.

[39] T. Fan, W. Zeng, W. Tang, C. Yuan, S. Tong, K. Cai, Y. Liu, W. Huang, Y. Min and A. J. Epstein, "Controllable size-selective method to prepare graphene quantum dots from graphene oxide," *Nanoscale Res. Lett.*, vol. 10, no. 1, p. 55, 2015, doi: 10.1186/s11671-015-0783-9.

[40] A. Sciortino, A.Cannizzo, and F. Messina, "Carbon nanodots: A review—from the current understanding of the fundamental photophysics to the full control of the optical response," *C J. Carbon Res.*, vol. 4, p. 67, 2018, doi:10.3390/c4040067.

[41] Z. H. Wen and X. B. Yin, "Excitation-independent carbon dots, from photoluminescence mechanism to single-color application," *RSC Adv.*, vol. 6, no. 33, pp. 27829–27835, 2016, doi: 10.1039/c5ra27172j.

[42] S. P. Jovanović, Z. M. Marković, Z. Syrgiannis, M. D. Dramićanin, F. Arcudi, V. La Parola, M. Budimir and B. M. Todorović Marković," Enhancing photoluminescence of graphene quantum dots by thermal annealing of the graphite precursor," *Mater. Res. Bull.*, vol. 93, pp. 183–193, 2017, doi: 10.1016/j.materresbull.2017.04.052.

[43] X. Miao, D. Qu, D. Yang, B. Nie, Y. Zhao, H. Fan and Z. Sun, "Synthesis of carbon dots with multiple color emission by controlled graphitization and surface functionalization," *Adv. Mater.*, vol. 30, no. 1, pp. 1–8, 2018, doi: 10.1002/adma.201704740.

[44] Z. Zhang, T. Zheng, X. Li, J. Xu, and H. Zeng, "Progress of carbon quantum dots in photocatalysis applications," *Part. Part. Syst. Charact.*, vol. 33, pp. 457–472, 2016, doi:10.1002/ppsc.201500243.

[45] W. Liu, C. Li, Y. Ren, X. Sun, W. Pan, Y. Li, J. Wang, and W. Wang, " Carbon dots: Surface engineering and applications," *J. Mater. Chem. B*, vol. 4, pp. 5772–5788, 2016, doi:10.1039/c6tb00976j.

[46] C. Ji, Y. Zhou, R. M. Leblanc, and Z. Peng, "Recent developments of carbon dots in biosensing: A review," ACS Sensors, vol. 5, no. 9, pp. 2724–2741, 2020, doi: 10.1021/acssensors.0c01556.

[47] W. Su, H. Wu, H. Xu, Y. Zhang, Y. Li, X. Li and L. Fan, "Carbon dots: A booming material for biomedical applications," Mater. Chem. Front., vol. 4, no. 3, pp. 821–836, 2020, doi: 10.1039/c9qm00658c.

[48] M. Semeniuk, Z. Yi, V. Poursorkhabi, J. Tjong, S. Jaffer, Z.-H. Lu and M. Sain, "Future perspectives and review on organic carbon dots in electronic applications," *ACS Nano*, vol. 13, no. 6, pp. 6224–6255, 2019, doi: 10.1021/acsnano.9b00688.

[49] U. A. Rani, L. Y. Ng, C. Y. Ng, and E. Mahmoudi, "A review of carbon quantum dots and their applications in wastewater treatment," *Adv. Colloid Interface Sci.*, vol. 278, p. 102124, 2020, doi: 10.1016/j.cis.2020.102124.

[50] Z. Kang and S. T. Lee, "Carbon dots: Advances in nanocarbon applications," *Nanoscale*, vol. 11, no. 41, pp. 19214–19224, 2019, doi: 10.1039/c9nr05647e.

[51] Y. Song, S. Zhu, and B. Yang, "Bioimaging based on fluorescent carbon dots," *RSC Adv.*, vol. 4, no. 52, pp. 27184–27200, 2014, doi: 10.1039/c3ra47994c.

[52] V. S. Sivasankarapillai, A. V. Kirthi, M. Akksadha, S. Indu, U. D. Dharshini, J. Pushpamalar and L. Karthik, "Recent advancements in the applications of carbon nanodots: Exploring the rising star of nanotechnology," *Nanoscale Adv.*, vol. 2, no. 5, pp. 1760–1773, 2020, doi: 10.1039/c9na00794f.

[53] F. Bruno, A. Sciortino, G. Buscarino, M. L. Soriano, Á. Ríos, M.Cannas, F. Gelardi, F. Messina and S. A. Agnello,"A comparative study of top-down and bottom-up carbon nanodots and their interaction with mercury ions," *Nanomaterials*, vol. 11, no. 5, 2021, doi: 10.3390/nano11051265.

[54] L. Minati and A. Del Piano, "Facile synthesis of water-soluble, highly-fluorescent graphene quantum dots from graphene oxide reduction for efficient cell labelling," *J. Carbon Res.*, vol. 5, no. 4, p. 77, 2019, doi.org/10.3390/c5040077.

[55] Y. Zhang and Y. Xu, "Simultaneous electrochemical dual-electrode exfoliation of graphite toward scalable production of high-quality graphene," *Adv. Funct. Mater.*, vol.

29, no. 37, pp. 1–14, 2019, doi: 10.1002/adfm.201902171.

[56] J. I. Paredes, S. Villar-Rodil, M. J. Fernández-Merino, L. Guardia, A. Martínez-Alonso, and J. M. D. Tascón, "Environmentally friendly approaches toward the mass production of processable graphene from graphite oxide," *J. Mater. Chem.*, vol. 21, no. 2, pp. 298–306, 2011, doi: 10.1039/c0jm01717e.

[57] K. H. Liao, A. Mittal, S. Bose, C. Leighton, K. A. Mkhoyan, and C. W. MacOsko, "Aqueous only route toward graphene from graphite oxide," *ACS Nano*, vol. 5, no. 2, pp. 1253–1258, 2011, doi: 10.1021/nn1028967.

[58] Y. Miyamoto, H. Zhang, and D. Tománek, "Photoexfoliation of graphene from graphite: An Abinitio study," *Phys. Rev. Lett.*, vol. 104, no. 20, pp. 19–22, 2010, doi: 10.1103/PhysRevLett.104.208302.

[59] B. Partoens and F. M. Peeters, "From graphene to graphite: Electronic structure around the K point," *Phys. Rev. B*, vol. 74, no. 7, pp. 1–11, 2006, doi: 10.1103/PhysRevB.74.075404.

[60] R. N. Tiwari, M. Ishihara, J. N. Tiwari, and M. Yoshimura, "Synthesis of graphene film from fullerene rods," *Chem. Commun.*, vol. 48, no. 24, pp. 3003–3005, 2012, doi: 10.1039/c2cc17512f.

[61] T.-S. Jun, N. H. Park, D. S. So, J. W. Lee, H. S. Lim, H. Ham and K.B. Shim, "Synthesis of graphene nano-sheet without catalysts and substrates using fullerene and spark plasma sintering process," *J. Korean Cryst. Growth Cryst. Technol.*, vol. 23, no. 1, pp. 27–30, 2013, doi: 10.6111/jkcgct.2013.23.1.027.

[62] Z. Wang, Y. Li, J. Liu, G. Tian, G. Liu, M. Wang, H. Ogata, W. Gong, A. K. Vipin and G. J. H. Melvin, "Microwave plasma-induced growth of vertical graphene from fullerene soot," *Carbon*, vol. 172, pp. 26–30, 2021, doi: 10.1016/j.carbon.2020.09.086.

[63] L. Hou, X. Cui, B. Guan, S. Wang, R. Li, Y. Liu, D. Zhu and J. Zheng, "Synthesis of a monolayer fullerene network," Nature, vol. 606, pp. 507–510, 2022, doi:10.1038/s41586-022-04771-5.

[64] N. L. Rangel, J. C. Sotelo, and J. M. Seminario, "Mechanism of carbon nanotubes unzipping into graphene ribbons," *J. Chem. Phys.*, vol. 131, no. 3, pp. 1–5, 2009, doi:

10.1063/1.3170926.

[65] P. Kumar, L. S. Panchakarla, and C. N. R. Rao, “Laser-induced unzipping of carbon nanotubes to yield graphene nanoribbons,” *Nanoscale*, vol. 3, no. 5, pp. 2127–2129, 2011, doi: 10.1039/c1nr10137d.

[66] S. Mohammadi, Z. Kolahdouz, S. Darbari, S. Mohajerzadeh, and N. Masoumi, “Graphene formation by unzipping carbon nanotubes using a sequential plasma assisted processing,” *Carbon*, vol. 52, pp. 451–463, 2013, doi: 10.1016/j.carbon.2012.09.056.

[67] E. Castillo-Martínez, J. Carretero-González, J. Sovich, and M. D. Lima, “High temperature structural transformations of few layer graphene nanoribbons obtained by unzipping carbon nanotubes,” *J. Mater. Chem. A*, vol. 2, no. 1, pp. 221–228, 2014, doi: 10.1039/c3ta13292g.

[68] C. S. Tiwary, B. Javvaji, C. Kumar, D. R. Mahapatra, S. Ozden, P. M. Ajayan and K. Chattopadhyay, “Chemical-free graphene by unzipping carbon nanotubes using cryo-milling,” *Carbon*, vol. 89, pp. 217–224, 2015, doi:10.1016/j.carbon.2015.03.036.

[69] D. V. Kosynkin, A. L. Higginbotham, A. Sinitskii, J. R. Lomeda, A. Dimiev, B. K. Price and J. M. Tour, “Longitudinal unzipping of carbon nanotubes to form graphene nanoribbons,” *Nature*, vol. 458, no. 7240, pp. 872–876, 2009, doi: 10.1038/nature07872.

[70] L. Jiao, L. Zhang, X. Wang, G. Diankov and H. Dai, “Narrow graphene nanoribbons from carbon nanotubes,” *Nature*, vol. 458, pp. 877–880, 2009, doi:10.1038/nature07919.

[71] Z. G. Chen, F. Li, W. C. Ren, H. Cong, C. Liu, G. Q. Lu and H. M. Cheng, “Double-walled carbon nanotubes synthesized using carbon black as the dot carbon source,” Nanotechnology, vol. 17, no. 13, pp. 3100–3104, 2006, doi: 10.1088/0957-4484/17/13/003.

[72] V. Asokan, D. N. Madsen, P. Kosinski, and V. Myrseth, “Transformation of carbon black into carbon nano-beads and nanotubes: the effect of catalysts,” *New Carbon Mater.*, vol. 30, no. 1, pp. 19–29, 2015, doi: 10.1016/S1872-5805(15)60172-X.

[73] M. Alfè, V. Gargiulo, R. Di Capua, F. Chiarella, J.-N. Rouzaud, A. Vergara and A. Ciajolo, “Wet chemical method for making graphene-like films from carbon black,” *ACS Appl. Mater. Interfaces*, vol. 4, no. 9, pp. 4491–4498, 2012, doi:

10.1021/am301197q.

[74] S. Khodabakhshi, P. F. Fulvio, and E. Andreoli, "Carbon black reborn: Structure and chemistry for renewable energy harnessing," *Carbon*, vol. 162, pp. 604–649, 2020, doi: 10.1016/j.carbon.2020.02.058.

[75] R. A. Khmelnitsky and A. A. Gippius, "Transformation of diamond to graphite under heat treatment at low pressure," *Phase Transitions*, vol. 87, no. 2, pp. 175–192, 2014, doi: 10.1080/01411594.2013.807429.

[76] B. L. V. Prasad, H. Sato, T. Enoki, Y. Hishiyama, Y. Kaburagi, A. M. Rao, P. C. Eklund, K. Oshida and M. Endo, "Heat-treatment effect on the nanosized graphite π-electron system during diamond to graphite conversion," *Phys. Rev. B*, vol. 62, no. 16, pp. 11209–11218, 2000, doi: 10.1103/PhysRevB.62.11209.

[77] M. Akaishi, T. Ohsawa, S. Yamaoka, and O. Fukunaga, "Synthesis of diamond from grahpite-carbonate systems under very high temperature and pressure," *Sci. Technol. New Diam.*, vol. 104, pp. 129–134, 1990, doi.org/10.1016/0022-0248(90)90159-I.

[78] R. P. B. Dos Santos, E. Perim, P. A. S. Autreto, G. Brunetto, and D. S. Galvão, "On the unzipping of multiwalled carbon nanotubes," *Nanotechnology*, vol. 23, no. 46, p. 465702, 2012, doi: 10.1088/0957-4484/23/46/465702.

[79] Y. Zhao, X. Wu, S. Sun, L. Ma, L. Zhang, and H. Lin, "A facile and high-efficient approach to yellow emissive graphene quantum dots from graphene oxide," *Carbon*, vol. 124, pp. 342–347, 2017, doi: 10.1016/j.carbon.2017.09.011.

[80] J. Chen, G. Xiao, G. Duan, Y. Wu, X. Zhao, and X. Gong, "Structural design of carbon dots/porous materials composites and their applications," *Chem. Eng. J.*, vol. 421, p. 127743, 2021, doi: 10.1016/j.cej.2020.127743.

[81] L. Yang, J. Shui, L. Du, Y. Shao, J. Liu, L. Dai and Z. Hu, "Carbon-based metal-free ORR electrocatalysts for fuel cells: Past, present, and future," *Adv. Mater.*, vol. 31, no. 13, pp. 1–20, 2019, doi: 10.1002/adma.201804799.

[82] V. C. Hoang, K. Dave, and V. G. Gomes, "Carbon quantum dot-based composites for energy storage and electrocatalysis: Mechanism, applications and future prospects," *Nano Energy*, vol. 66, p. 104093, 2019, doi: 10.1016/j.nanoen.2019.104093.

[83] Z. Li, L. Wang, Y. Li, Y. Feng, and W. Feng, “Frontiers in carbon dots: Design, properties and applications,” *Mater. Chem. Front.*, vol. 3, no. 12, pp. 2571–2601, 2019, doi: 10.1039/c9qm00415g.

[84] Y. Ru, L. Ai, T. Jia , X. Liu, S. Lu, Z. Tang and B. Yang, “Recent advances in chiral carbonized polymer dots: From synthesis and properties to applications,” *Nano Today*, vol. 34, p. 100953, 2020, doi: 10.1016/j.nantod.2020.100953.

[85] Q. Wang, X. Huang, Y. Long, X. Wang, H. Zhang, R. Zhu, L. Liang, P. Teng and H. Zheng “Hollow luminescent carbon dots for drug delivery,” *Carbon*, vol. 59, pp. 192–199, 2013, doi: 10.1016/j.carbon.2013.03.009.

[86] M. Tang, P. Teng, Y. Long, X. Wang, L. Liang, D. Shen, J. Wang, H. Zheng, “Hollow carbon dots labeled with FITC or TRITC for use in fluorescent cellular imaging,” *Microchim. Acta*, vol. 185, no. 4, 2018, doi: 10.1007/s00604-018-2761-2.

[87] F. Yuan, P. He, Z. Xi, X. Li, Y. Li, H. Zhong, L. Fan and S. Yang, “Highly efficient and stable white LEDs based on pure red narrow bandwidth emission triangular carbon quantum dots for wide-color gamut backlight displays,” *Nano Res.*, vol. 12, no. 7, pp. 1669–1674, 2019, doi: 10.1007/s12274-019-2420-x.

[88] S. H. Lee, D. Y. Kim, J. Lee, S. B. Lee, H. Han, Y. Y. Kim and O. O. Park, “Synthesis of single-crystalline hexagonal graphene quantum dots from solution chemistry,” *Nano Lett.*, vol. 19, no. 8, pp. 5437–5442, 2019, doi: 10.1021/acs.nanolett.9b01940.

[89] S. Yang, W. Li, C. Ye, G. Wang, H. Tian, C. Zhu, P. He, G. Ding, X. Xie, Y. Liu, Y. Lifshitz, S.-T. Lee, Z. Kang and M. Jiang,“ C_3N—A 2D crystalline, hole-free, tunable-narrow-bandgap semiconductor with ferromagnetic properties,” *Adv. Mater.*, vol. 29, no. 16, pp. 1–7, 2017, doi: 10.1002/adma.201605625.

[90] A. Sciortino, N. Mauro, G. Buscarino, L. Sciortino, R. Popescu, R. Schneider, G. Giammona, D. Gerthsen, M. Cannas and F. Messina, “β-C_3N_4 nanocrystals: Carbon dots with extraordinary morphological, structural, and optical homogeneity,” *Chem. Mater.*, vol. 30, no. 5, pp. 1695–1700, 2018, doi: 10.1021/acs.chemmater.7b05178.

[91] S. Zhang , J. Zhu, Y. Qing, C. Fan, L. Wang, Y. Huang, R. Sheng, Y. Guo, T. Wang, Y. Pan, Y. Lv, H. Song and D. Jia, “Construction of hierarchical porous carbon nanosheets from template-assisted assembly of coal-based graphene quantum dots for high

performance supercapacitor electrodes," *Mater. Today Energy*, vol. 6, pp. 36–45, 2017, doi: 10.1016/j.mtener.2017.08.003.

[92] K. Jurkiewicz, M. Pawlyta, and A. Burian, "Structure of carbon materials explored by local transmission electron microscopy and global powder diffraction probes," *J. Carbon Res.*, vol. 4, no. 4, p. 68, 2018, doi: 10.3390/c4040068.

[93] N. Gupta, S. M. Gupta, and S. K. Sharma, "Carbon nanotubes: synthesis, properties and engineering applications," *Carbon Lett.*, vol. 29, no. 5, pp. 419–447, 2019, doi: 10.1007/s42823-019-00068-2.

[94] X. Wang, A. Dong, Y. Hu, J. Qian, and S. Huang, "A review of recent work on using metal-organic frameworks to grow carbon nanotubes," *Chem. Commun.*, vol. 56, no. 74, pp. 10809–10823, 2020, doi: 10.1039/d0cc04015k.

[95] L. Sun, X. Wang, Y. Wang, and Q. Zhang, "Roles of carbon nanotubes in novel energy storage devices," *Carbon*, vol. 122, pp. 462–474, 2017, doi: 10.1016/j.carbon.2017.07.006.

[96] Q. Xu, W. Li, L. Ding, W. Yang, H. Xiao, and W. J. Ong, "Function-driven engineering of 1D carbon nanotubes and 0D carbon dots: Mechanism, properties and applications," *Nanoscale*, vol. 11, no. 4, pp. 1475–1504, 2019, doi: 10.1039/c8nr08738e.

[97] R. Shoukat and M. I. Khan, "Carbon nanotubes: a review on properties, synthesis methods and applications in micro and nanotechnology," *Microsyst. Technol.*, vol. 6, 2021, doi: 10.1007/s00542-021-05211-6.

[98] H. Q. Tao, K. Yang, Z. Ma, J. M. Wan, Y. J. Zhang, Z. H. Kang and Z. Liu, "In vivo NIR fluorescence imaging, biodistribution, and toxicology of photoluminescent carbon dots produced from carbon nanotubes and graphite," *Small*, vol. 8, no. 2, pp. 281–290, 2012, doi: 10.1002/smll.201101706.

[99] H. Wang, C. Liu, Z. Liu, J. Ren, and X. Qu, "Specific oxygenated groups enriched graphene quantum dots as highly efficient enzyme mimics," *Small*, vol. 14, no. 13, pp. 1–8, 2018, doi: 10.1002/smll.201703710.

[100] H. Cheng, Y. Zhao, Y. Fan, X. Xie, L. Qu, and G. Shi, "Graphene-quantum-dot assembled nanotubes: A new platform for efficient Raman enhancement," *ACS Nano*,

vol. 6, no. 3, pp. 2237–2244, 2012, doi: 10.1021/nn204289t.

[101] W. J. Niu, Y. P. Wang, J. Z. He, W. W. Liu, M. C. Liu, D. Shan, L. Lee and Y. L. Chueh, "Highly stable nitrogen-doped carbon nanotubes derived from carbon dots and metal-organic frameworks toward excellent efficient electrocatalyst for oxygen reduction reaction," *Nano Energy*, vol. 63, p. 103788, 2019, doi: 10.1016/j.nanoen.2019.05.074.

[102] O. Erol, I. Uyan, M. Hatip, C. Yilmaz, A. B. Tekinay, and M. O. Guler, "Recent advances in bioactive 1D and 2D carbon nanomaterials for biomedical applications," *Nanomed.: Nanotechnol. Biol. Med.*, vol. 14, no. 7, pp. 2433–2454, 2018, doi: 10.1016/j.nano.2017.03.021.

[103] N. Yousefi, X. Lu, M. Elimelech, and N. Tufenkji, "Environmental performance of graphene-based 3D macrostructures," *Nat. Nanotechnol.*, vol. 14, no. 2, pp. 107–119, 2019, doi: 10.1038/s41565-018-0325-6.

[104] K. Yang, J. Wang, X. Chen, Q. Zhao, A. Ghaffar, and B. Chen, "Application of graphene-based materials in water purification: From the nanoscale to specific devices," *Environ. Sci. Nano*, vol. 5, no. 6, pp. 1264–1297, 2018, doi: 10.1039/c8en00194d.

[105] M. Pumera, "Electrochemistry of graphene, graphene oxide and other graphenoids: Review," *Electrochem. commun.*, vol. 36, pp. 14–18, 2013, doi: 10.1016/j.elecom.2013.08.028.

[106] F. Liu, C. Wang, X. Sui, M. A. Riaz, M. Xu, L. Wei and Y. Chen," Synthesis of graphene materials by electrochemical exfoliation: Recent progress and future potential," *Carbon Energy*, vol. 1, no. 2, pp. 173–199, 2019, doi: 10.1002/cey2.14.

[107] U. Khan, A. O'Neill, M. Lotya, S. De, and J. N. Coleman, "High-concentration solvent exfoliation of graphene," *Small*, vol. 6, no. 7, pp. 864–871, 2010, doi: 10.1002/smll.200902066.

[108] V. B. Mohan, K. tak Lau, D. Hui, and D. Bhattacharyya, "Graphene-based materials and their composites: A review on production, applications and product limitations," *Compos. Part B Eng.*, vol. 142, pp. 200–220, 2018, doi: 10.1016/j.compositesb.2018.01.013.

[109] T. F. Emiru and D. W. Ayele, "Controlled synthesis, characterization and reduction of

graphene oxide: A convenient method for large scale production," *Egypt. J. Basic Appl. Sci.*, vol. 4, no. 1, pp. 74–79, 2017, doi: 10.1016/j.ejbas.2016.11.002.

[110] M. D. P. Lavin-Lopez, A. Romero, J. Garrido, L. Sanchez-Silva and J. L. Valverde, "Influence of different improved hummers method modifications on the characteristics of graphite oxide in order to make a more easily scalable method," *Ind. Eng. Chem. Res.*, vol. 55, no. 50, pp. 12836–12847, 2016, doi: 10.1021/acs.iecr.6b03533.

[111] R. Dagher, S. Matta, R. Parret, M. Paillet, B. Jouault, L. Nguyen, M. Portail, M. Zielinski, T. Chassagne, S. Tanaka, J. Brault, Y. Cordier and A. Michon, "High temperature annealing and CVD growth of few-layer graphene on bulk AlN and AlN templates," *Phys. Status Solidi Appl. Mater. Sci.*, vol. 214, no. 4, p. 1600436, 2017, doi: 10.1002/pssa.201600436.

[112] B. J. Matsoso, K. Ranganathan, B. K. Mutuma, T. Lerotholi, G. Jones, and N. J. Coville, "Time-dependent evolution of the nitrogen configurations in N-doped graphene films," *RSC Adv.*, vol. 6, no. 108, pp. 106914–106920, 2016, doi: 10.1039/c6ra24094a.

[113] Y. Dong, J. Shao, C. Chen, H. Li, R. Wang, Y. Chi, X. Lin and G. Chen," Blue luminescent graphene quantum dots and graphene oxide prepared by tuning the carbonization degree of citric acid," *Carbon*, vol. 50, no. 12, pp. 4738–4743, 2012, doi: 10.1016/j.carbon.2012.06.002.

[114] A. Muthurasu, P. Dhandapani, and V. Ganesh, "Facile and simultaneous synthesis of graphene quantum dots and reduced graphene oxide for bio-imaging and supercapacitor applications," *New J. Chem.*, vol. 40, no. 11, pp. 9111–9124, 2016, doi: 10.1039/c6nj00586a.

[115] G. Chen, S. Wu, L. Hui, Y. Zhao, J. Ye, Z. Tan, W. Zeng, Z. Tao, L. Yang and Y. Zhu, "Assembling carbon quantum dots to a layered carbon for high-density supercapacitor electrodes," *Sci. Rep.*, vol. 6, pp. 1–9, 2016, doi: 10.1038/srep19028.

[116] H. Hou, L. Shao, Y. Zhang, G. Zou, J. Chen, and X. Ji, "Large-area carbon nanosheets doped with phosphorus: A high-performance anode material for sodium-ion batteries," *Adv. Sci.*, vol. 4, no. 1, 2017, doi: 10.1002/advs.201600243.

[117] L. L. Mokoloko, B. J. Matsoso, R. P. Forbes, D. H. Barrett, B. D. Moreno, and N. J. Coville, "Evolution of large-area reduced graphene oxide nanosheets from carbon dots

via thermal treatment," *Carbon Trends*, vol. 4, p. 100074, 2021, doi: 10.1016/j.cartre.2021.100074.

[118] G. Bharathi, D. Nataraj, S. Premkumar, M. Sowmiya, K. Senthilkumar, T. D. Thangadurai, O. Y. Khyzhun, M. Gupta, D. Phase, N. Patra, S. N. Jha, and D. Bhattacharyya, "Graphene Quantum Dot Solid Sheets: Strong blue-light-emitting & photocurrent-producing band-gap-opened nanostructures," *Sci. Rep.*, vol. 7, no. 1, pp. 1–17, 2017, doi: 10.1038/s41598-017-10534-4.

[119] Y. Zhang, C. W. Foster, C. E. Banks, L. Shao, H. Hou, G. Zou, J. Chen, Z. Huang and X. Ji, "Graphene-rich wrapped petal-like rutile TiO_2 tuned by carbon dots for high-performance sodium storage," *Adv. Mater.*, vol. 28, no. 42, pp. 9391–9399, 2016, doi: 10.1002/adma.201601621.

[120] L. Borchardt, Q.-L. Zhu, M. E. Casco, R. Berger, X. Zhuang, S. Kaskel, X. Feng and Q. Xu, "Toward a molecular design of porous carbon materials," *Mater. Today*, vol. 20, no. 10, pp. 592–610, 2017, doi: 10.1016/j.mattod.2017.06.002.

[121] H. Jiang, Y. Wang, J. Hao, Y. Liu, W. Li, and J. Li, "N and P co-functionalized three-dimensional porous carbon networks as efficient metal-free electrocatalysts for oxygen reduction reaction," *Carbon*, vol. 122, pp. 64–73, 2017, doi: 10.1016/j.carbon.2017.06.043.

[122] X. Zhang, Z. Zhang, F. Hu, D. Li, D. Zhou, P. Jing, F. Du, S.Qu, "Carbon-dots-derived 3D highly nitrogen-doped porous carbon framework for high-performance lithium ion storage," *ACS Sustain. Chem. Eng.*, vol. 7, pp. 9848–9856, 2019, doi:10.1021/acssuschemeng.9b00407.

[123] J. Lei, K. Wang, B. Deng, Y.Li, S. Zhang, Y. Cao, "Enhanced oxygen reduction of porous N-doped carbon nanosheets with graphitic N and defects obtained from coal-based graphene quantum dots," *J. Alloy. Compd.*, vol. 914, p. 165359, 2022, doi:10.1016/j.jallcom.2022.165359.

[124] S. Zhang, J. Zhu, Y. Qing, L. Wang, J. Zhao, J. Li, W. Tian, D. Jia and Z. Fan, "Ultramicroporous carbons puzzled by graphene quantum dots: integrated high gravimetric, volumetric, and areal capacitances for supercapacitors, *Adv. Funct. Mater.*, vol. 28, p. 1805898, 2018, doi:10.1002/adfm.201805898.

[125] V. Strauss, K. Marsh, M. D. Kowal, M. El-Kady, and R. B. Kaner, "A simple route to porous graphene from carbon nanodots for supercapacitor applications," *Adv. Mater.*, vol. 30, no. 8, pp. 1–10, 2018, doi: 10.1002/adma.201704449.

[126] S. Qu, X. Wang, Q. Lu, X. Liu, and L. Wang, "A biocompatible fluorescent ink based on water-soluble luminescent carbon nanodots," *Angew. Chemie - Int. Ed.*, vol. 51, no. 49, pp. 12215–12218, 2012, doi: 10.1002/anie.201206791.

[127] R. Cheng, M. Jiang, K. Li, M. Guo, J. Zhang, J. Ren, P. Meng, R. Li and C. Fu, "Dimensional engineering of carbon dots derived sulfur and nitrogen co-doped carbon as efficient oxygen reduction reaction electrocatalysts for aluminum-air batteries," *Chem. Eng. J.*, vol. 425, p. 130603, 2021, doi:10.1016/j.cej.2021.130603.

[128] Q. Lou, S. N. Qu, P. T. Jing, W. Y. Ji, D. Li, J. S. Cao, H. Zhang, L. Liu, J. L. Zhao and D. Z. Shen, "Water-triggered luminescent 'nano-bombs' based on Supra-(carbon nanodots)," *Adv. Mater.*, vol. 27, no. 8, pp. 1389–1394, 2015, doi: 10.1002/adma.201403635.

[129] D. Li, D. Han, S. Qu, L. Liu, P. Jing, D. Zhou, W. Ji, X. Wang, T. Zhang and D. Shen," Supra-(carbon nanodots) with a strong visible to near-infrared absorption band and efficient photothermal conversion," *Light Sci. Appl.*, vol. 5, no. 7, pp. 1–8, 2016, doi: 10.1038/lsa.2016.120.

[130] H. Yang, Y. Liu, Z. Guo, B. Lei, J. Zhuang, X. Zhang, Z. Liu and C. Hu, "Hydrophobic carbon dots with blue dispersed emission and red aggregation-induced emission," *Nat. Commun.*, vol. 10, no. 1, pp. 1–11, 2019, doi: 10.1038/s41467-019-09830-6.

[131] Q. Hou, C. Xue, N. Li, H. Wang, Q. Chang, H. Liu, J. Yang and S. Hu, "Self-assembly carbon dots for powerful solar water evaporation," *Carbon*, vol. 149, pp. 556–563, 2019, doi: 10.1016/j.carbon.2019.04.083.

[132] Y. Zhou, K. J. Mintz, L. Cheng, J.Chen, B. C. Ferreira, S. D. Hettiarachchi, P. Y. Liyanage, E. S. Seven, N. Miloserdov, R. R. Pandey, B. Quiroga, P. L. Blackwelder, C. C. Chusuei, S. Li, Z. Peng and R. M. Leblanc,"Direct conjugation of distinct carbon dots as Lego-like building blocks for the assembly of versatile drug nanocarriers," *J. Colloid Interface Sci*., vol. 576, pp. 412–425, 2020, doi:10.1016/j.jcis.2020.05.005.

[133] Y. Zhou, J. Chen, N. Miloserdov, W. Zhang., K. Mintz, B. C. L. B Ferreira, M. Micic,

S. Li, Z. Peng and R. M. Leblanc, “Versatile drug nanocarrier assembly via conjugation of distinct carbon dots,” *Moroc. J. Chem.*, vol. 8, pp. 994–1007, 2020, doi:10.48317/IMIST.PRSM/morjchem-v8i4.22304.

[134] Y. Wang, C. Zhang, X. Chen, B. Yang, L. Yang, C. Jiang and Z. Zhang, “Ratiometric fluorescent paper sensor utilizing hybrid carbon dots–quantum dots for the visual determination of copper ions,” *Nanoscale,* vol. 8, pp. 5977–5984, 2016, doi:10.1039/c6nr00430j.

[135] S. Hettiarachchi, R. M. Graham, K. J. Mintz, Y. Zhou, S. Vanni, Z. Peng and R. M. Leblanc, “ Triple conjugated carbon dots as a nano-drug delivery model for glioblastoma brain tumors,” *Nanoscale*, vol. 11, pp. 6192–6205. 2019, doi:10.1039/c8nr08970a.

[136] L. L. Mokoloko, B. J. Matsoso, N. Antonatos, V. Mazánek, B. D. Moreno, R. P. Forbes, D. H. Barrett, Z. Sofer and N. J. Coville, “From 0D to 2D: N-doped carbon sheets for detection of alcohol-based chemical vapours,” *RSC Advances* (accepted).

[137] S. Shen, J. Wang, Z. Wu, Z. Du, Z. Tang J. and Yang, J. “Graphene quantum dots with high yield and high quality synthesized from low cost precursor of aphanitic graphite,” *Nanomaterials*, vol. 10, pp. 375, 2020, doi:10.3390/nano10020375.

[138] G. Wang, Q. Guo, D. Chen, Z. Liu, X. Zheng, A. Xu, S. Yang and G. Ding, “Facile and highly effective synthesis of controllable lattice sulfur-doped graphene quantum dots via hydrothermal treatment of durian,” *ACS Appl. Mater. Interfaces*, vol. 10, pp. 5750–5759, 2018, https://doi.org/10.1021/acsami.7b16002.

[139] H. Wu, H. Xu, Y. Shi, T. Yuan, T. Meng, Y. Zhang, W. Xie, X. Li, Y. Li and L. Fan, “Recent advance in carbon dots: from properties to applications,” *Chin. J. Chem*., vol. 39, pp. 1364–1388, 2020, doi:10.1002/cjoc.202000609.

[140] Q. Hong, X. Y. Wang, Y. T. Gao, J. Lv, B. B. Chen, D. W. Li and R. C. Qian, “Customized carbon dots with predictable optical properties synthesized at room temperature guided by machine learning,” *Chem. Mater*., vol. 34, pp. 998–1009, 2022, doi:10.1021/acs.chemmater.1c03220.

[141] X.-Y. Wang, B.-B. Chen, J. Zhang, Z.-R. Zhou, J. Lv, X.-P. Geng and R.-C.Qian, “Exploiting deep learning for predictable carbon dot design,” Chem. Commun., vol. 57, pp. 532–535, 2020, doi:10.1039/d0cc07882d.

[142] Y. Han, B. Tang, L. Wang, H. Bao, Y. Lu, C. Guan, L. Zhang, M. Le, Z. Liu and M. Wu, "Machine-learning-driven synthesis of carbon dots with enhanced quantum yields," *ACS Nano*, vol. 14, pp. 14761–14768, 2020, doi:10.1021/acsnano.0c01899.

[143] N. Shauloff, A. Morag, K. Yaniv, S. Singh, R. Malishev, O. Paz-Tal, L. Rokach and R. Jelinek, "Sniffing bacteria with a carbon-dot artificial nose," Nano-Micro Lett., vol. 13, p. 112, 2021doi:10.1007/s40820-021-00610-w.

[144] T. B. Song, Z,. H. Huang, X. Q. Niu, J. Liu, J. S. Wei, X. B. Chen, H. M. Xiong, "Applications of carbon dots in next-generation lithium-ion batteries," *ChemNanoMat*, vol. 6, pp. 1421–1436, 2020, doi:10.1002/cnma.202000355.

2.2 Fischer-Tropsch synthesis reactions and catalyst support effects with carbon

2.2.1 Introduction

Catalysis has played a dominant role in the development of many processes necessary for modern society, which includes the fields of energy generation and storage, environmental management, and general life sciences [1]. Furthermore, catalysis is used in over 90 % of all manufacturing processes worldwide, making it vital for the global economy [2]–[5]. Heterogeneous catalysis, in particular, is at the core of many industrial processes. This is because of its excellent ability to increase reaction kinetics, selectivity and yield at low process costs and lowered waste production [3], [4]. Over the past few years, research into high performance heterogeneous metal catalysts shifted from the use of macro- and microscale to designing catalysts in the nanoscale [6]. It has been shown that nanoscale (1-100 nm) metal catalysts present an increased surface area, multiple surface energies, opportunities for manipulation of the intrinsic properties and catalyst sites, and superior optimization of the catalyst performance for a more cost effective process relative to their bulk counterparts [5]–[7].

Heterogeneous metal catalysts are usually comprised of a metallic catalysts that are usually anchored or supported on the surface of a support material that serves to enhance the catalytically active metal's surface area while also improving their stability during various reactions [3]. Carbon allotropes have shown great potential when used as a catalyst support, and the carbon can even act as a catalyst in its own right [2], [8]. This is due to the surface area, surface chemistry and porosity of the carbon [2], [8]. The use of carbon allotropes particularly as a catalyst support is enhanced by their electron affinity which is influenced by their structure and high surface area. This promotes a high dispersion of the supported catalyst, and also of surface defects and this can enhance their capability for gas storage, adsorption and/or separation processes [2], [9]. Furthermore, carbon allotropes can be derived from highly abundant starting materials using a wide variety of synthesis strategies. This makes them cheap materials for use in catalysis applications [10]. For example, Fischer-Tropsch synthesis (FTS) is amongst the heterogeneous catalysis reactions where carbon allotropes have been studied as catalyst supports [10].

2.2.1.1 A short background history of Fischer-Tropsch synthesis (FTS)

The FTS is versatile method used for the conversion of carbon monoxide or carbon dioxide (CO/CO_2) and hydrogen (H_2) into fuels and fine chemicals [11]. The H_2/CO gas mixture is also

known as *syngas*. This process was named after Franz Fischer and Hans Tropsch, who in 1923, conducted several experiments where they reacted CO and H_2 (made from coal) over base-promoted iron chips at 100 – 150 atm pressure and temperatures ranging from 400 – 450 °C to produce synthol (a mixture of oxygenated aliphatic molecules) [12], [13]. This synthol was then converted to synthine (a mixture of hydrocarbons) and ultimately transportation fuel. The synthesized transportation fuel was used in a 1922 model NSU motorbike, and it was found that this FTS fuel showed comparable (and in some instances better) results when compared to conventional fossil fuel, and a "new" fuel production strategy was born [12].

From this point forward it became obvious that this technology would play a significant role in fuel production, especially in countries with a lack of, or limited access to, crude oil but with a high abundance of natural gas and/or coal reserves [14], [15]. Therefore, after great research effort, the FTS technology was quickly turned into an industrial scale process. This eventually led to the construction of industrial plants around the world utilizing coal-to-liquid (CTL) and gas-to-liquid (GTL) fuel conversion processes [13], [16]. The first FTS plant was the Ruhr-chemie (Germany) CTL plant that was built in 1927; thereafter, CTL plants were built in Japan in the 1940s [13], [16]–[18]. Other FTS plants, based on either CTL or GTL, were later built in South Africa, China, Malaysia and Qatar [16]–[18]. Currently, research in the economic viability of biomass-to-liquid (BTL) FTS, at industrial scale, has also commenced [19]–[21]. **Table 2.2** gives a summary of the commercial plants that have been built, their year of commercialization, their capacities, the *syngas* source, among others.

Table 2.1: A summary of the established FTS plants around the world (reproduced from Gholami et al. [13]).

Company/location	Feedstock	Reactor type	Catalyst type	Start-up date
Sasol/Sasolburg, South Africa	Coal (initially), natural gas (current)	HTFT circulating fluidized bed	Fused Fe/K	1955
		LTFT multitubular fixed-bed	Precipi-tated Fe/K	1955
		LTFT slurry phase	Precipi-tated Fe/K	1993
Sasol/Secunda, South Africa	Coal, natural gas	HTFT circulating fluid-ized bed	Fused Fe/K	1980
		HTFT SAS reactor	Fused Fe/K	1995
Shell/Bintulu, Malaysia	Natural gas	LTFT multitubular fixed-bed	Co/TiO_2, Co/SiO_2	1993
PetroSA/Mosselbay, South Africa	Natural gas	HTFT circulating fluidized bed	Fused Fe/K	1993
Sasol-QP (Oryx)/Ras Laffan, Qatar	Natural gas	LTFT slurry phase	Co/Al_2O_3	2006
Synfuels China, Taiyuan, Shanxi, China	Coal	HTFT slurry-bed	Fe	2006
NiQUAN GTL/Trinidad (Pointe-à-Pierre)	Natural gas	LTFT multitubular fixed bed (Compression two fixed-bed reactors with catalyst filled tubes)	Co	2008
Yitai CTL Plant/Inner Mongolia, China	Coal	MTFT slurry-bed	Fe	2009
Shenhua ICL/China	Coal	HTFT slurry-bed	Fe	2009
Shanxi Lu'an/Shanxi, China	Coal	HTFT fixed-bed	Fe, Co	2010
Shell (Pearl)/Ras Laffan, Qatar	Natural gas	LTFT multitubular fixed-bed	Co/TiO_2	2011
Sasol-Chevron/Escravos, Nigeria	Natural gas	LTFT slurry-bed	Co/Al_2O_3	2013

Synfuels China, Ningdong Energy, Ningxia, China	Coal	MTFT slurry-bed	Fe	2016

HTFT: High Temperature Fischer-Tropsch; LTFT: Low Temperature Fischer-Tropsch; MTFT: Medium Temperature Fischer-Tropsch; HTFT SAS: High Temperature Fischer-Tropsch Sasol advanced synthol

Over the past few decades, the accelerated interest in FTS was not only based on the limited access to crude oil reverses in some countries, but the depletion of crude oil reserves worldwide. Also of importance has been the environmental implications of crude oil use, especially its contribution to greenhouse gas (GHG) emission and climate change [21]. It has been reported that transportation fuel demands will rise by 60 % worldwide by 2035, due to factors such as population growth [19]. On the other hand, transportation fuel especially from crude oil produces large amounts of hazardous waste (> 30 %) that is a known contaminant of the air, water and soil [18]. This has increased the search for transportation fuel-based technologies that are carbon neutral and can be generated from renewable carbon resources and with reduced GHG emissions. The FTS technology is a mature process that has been successfully employed using coal and natural gas as a feedstock but it can also be retooled to become one of the essential technologies for the production of fuels from renewable resources, and can be produced with a reduction in GHG emission when compared to crude oil [22]–[24].

2.2.2 The Fischer-Tropsch synthesis (FTS) process

The FTS process starts with the conversion of coal, natural gas, or biomass to *syngas* (CO and H_2) via a gasification process [21], [25]. The produced *syngas* then undergoes a metal catalyst-mediated surface polymerization reaction to form hydrocarbons [13], [26]. The actual mechanism of this process is complicated and is still being debated [13], [27]. However, **Figure 2.9** shows a summary of the two mechanism (the CO insertion and the carbide mechanism) proposed for the chain initiation, growth and termination under the FTS [13]. Different hydrocarbons can be produced in the process with different chain lengths, as shown in **equation 2.2.1**. When *n* is between 5 and 11 (C_{5-11}), the product is petrol, when *n* is between 12 and 22 (C_{12-22}) the product is diesel, and the hydrocarbon of more than 23 carbon atoms (C_{23+}) the product is a wax [28], [29]. The resulting fuel products (and water) are then purified and separated by distillation [28], [29]. For the wax products (C_{23+}), the hydrocarbons are typically subjected to hydrocracking to form more petrol, diesel, among others [30].

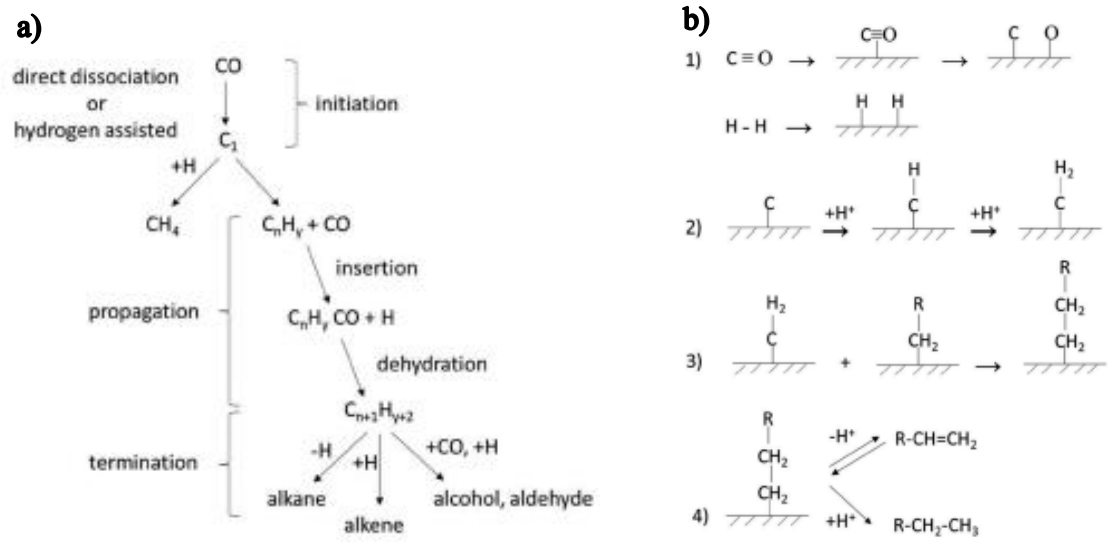

Figure 2. 9: The proposed FTS according to the **a)** CO insertion chain growth mechanism, and **b)** carbide mechanism [13].

The FTS reaction equation for fuel production: $nCO + (2n+1)H_2 \rightarrow C_nH_{2n+2} + nH_2O$..**eq. 2.2.1** [13]

The catalytic reaction takes place in different types of reactors. These include fixed bed reactors (suitable for low temperatures reactions, 200-240 °C), fluidized bed reactors (suitable for high temperature reactions, ~340 °C) and slurry phase reactors (also suitable for low temperatures reactions, 200 - 240 °C) [15].

It is important to note that **equation 2.2.1** does not show all of the products obtained from the FTS process. Olefins and alcohols are also made in the reaction, with the quantities that are produced being determined by the nature of the catalyst used and the reactor type/reactor conditions that are used [31]. In fact, one of the major disadvantages of the FTS is its poor selectivity. Since its first application, further synthesis strategies have been developed for the FTS process. This has been done in order to tune the selectivity of the process towards desired products (see **Table 2.3**). This has been achieved by using different metal catalysts from group 8-10 of the Periodic Table [27], [31], studying catalyst particle sizes [32]–[35], incorporating support materials like metal oxides and carbon supports [10], [27], [36], addition of promoters such as alkali metals [37] and nobel metals [38], using different reactor designs [12], [16], [27], and studying the reaction as a function of temperature and pressure [39].

Table 2.3 shows the valuable products that can be obtained from the FTS process. Interestingly, in March of 2020, at the start of the Covid-19 pandemic, the oil industry experienced a shocking fuel price drop of more than 100 % per barrel [40]. This impacted FTS fuel production negatively, but indirectly led to a surge in demand for other FTS products. For example, Sasol South Africa, an international leader in FTS technology, reported an approximately 400 % increase in the demand for alcohol-based products for use in the manufacture of sanitizer and disinfectant products [40]. Though these other valuable products can be synthesized from this technology, the utilization of the FTS process for transportation fuel remains its primary use.

Table 2.2: The major products obtained from the FTS (reproduced from van Der Laan et al. [31]).

Main reactions		
	1. Paraffins	$(2n+1)H_2 + nCO \rightarrow C_nH_{2n+2} + nH_2O$
	2. Olefins	$2nH_2 + nCO \rightarrow C_nH_{2n} + nH_2O$
	3. WGS reaction	$CO + H_2O \rightleftarrows CO_2 + H_2$
Side reactions		
	4. Alcohols	$2nH_2 + nCO \rightarrow C_nH_{2n+2}O + (n-1)H_2O$
	5. Catalyst oxidation/reduction	$a)\ M_xO_y + yH_2 \rightleftarrows yH_2O + xM$ $b)\ M_xO_y + yCO \rightleftarrows yCO_2 + xM$
	6. Bulk carbide formation	$yC + xM \rightleftarrows M_xC_y$
	7. Boudouard reaction	$2CO \rightarrow C + CO_2$

2.2.3 The FTS catalysts

The hydrogenation of CO to hydrocarbons via FTS can only take place in the presence of a metal catalyst [41]. As mentioned, metal catalysts from group 8-10 of the Periodic Table all have shown some activity towards the FTS reaction. However, ruthenium (Ru), cobalt (Co), iron (Fe) and nickel (Ni) are the four catalysts which have shown the greatest activity [38], [41]. Ru is the most active and selective FTS catalyst especially for the production of long chain hydrocarbon (C_{5+}). Additionally, Ru is also very stable under the FTS conditions, and the presence of water (the primary FTS by-product) does not decrease its activity, unlike other metal catalysts [15], [42]. However, Ru is a rare metal, and therefore very expensive when compared to other FTS metal catalysts [15], [42]. Although the use of Ru is not economically

feasible for industrial application, it is still used for academic research especially as a catalyst promoter [15]. Ni is highly selective towards methane (C_1) production, and therefore not a good catalyst for fuel production [43].

Fe is an active FTS metal catalyst used for long chain hydrocarbons (C_{5+}) production. Fe has high activity under high temperature (~340 °C) FTS synthesis conditions, it is relatively cheap compared to Co and Ru, but Fe is more susceptible to deactivation by water (FTS by-product) during the FTS reaction [15]. Co is the second most active metal catalyst (after Ru) for C_{5+} chain production, especially under low temperature (200 - 240 °C) FTS conditions. It is less prone to deactivation by water compared to Fe, and, although more expensive, it is the most preferred catalysts for FTS both in academic studies and industry because of its relatively high performance [44].

A few of the most important insights developed from what has been reported in the academic literature as it pertains to Co-based FTS catalyst are summarized below:

1. Co (like other catalysts) is introduced in its metal oxide form (Co_3O_4) and readily undergoes a two-step reduction process to form metallic Co (or Co^0), which is the active form of Co for the FTS reaction. The reduction process is an important step in controlling the activity of Co-based FTS reaction [37], [45].
2. The reduction process is usually accomplished by using pure hydrogen (99.9 %) at elevated temperatures (> 300 °C) [46], [47].
3. From these reduction steps, two crystallographic forms of metallic Co are produced, namely the hexagonal close packed (hcp) and/or the face centred cubic (fcc) phases. The Co(hcp) phase has proven to be the most desirable form of metallic Co due to its high activity in FTS compared to the Co(fcc) phase [48], [49]. For example, the Co(hcp) has a much lower CO dissociation barrier (101 kJ/mol) compared to the Co(fcc) phase (144 kJ/mol). The CO dissociation step is a rate determining step, and thus determines the overall hydrocarbon formation [49]. Therefore, the presence of Co(hcp) favours more C_{5+} formation.
4. Generally, FTS metal catalysts (including Co) are more cost-effective with lower loading and have a better efficiency when there is higher dispersion.
5. Co is thus, usually supported on high surface area support materials. The nature of the support affects the reduction temperatures, crystallographic phases, and overall performance of the catalyst [13].

6. Co nanoparticles with sizes < 8 nm are prone to deactivation via oxidation of the catalytically active metal during the FTS process, and in some cases, form strong bonds with the support materials, especially in alumina- and silica-based catalysts. This reduces the amount of Co_3O_4 that is converted to metallic Co. Hence, Co particles sizes > 8 nm but close to this value are preferred [50], [51].

It is clear that the support material influences the performance of the Co catalyst. Some of the support materials and their influence in the Co-based FTS are described here.

2.2.4 Designing catalysts: Catalyst support effect

Support materials are important for immobilizing and anchoring the active metal catalyst, improving its dispersion and durability, and aiding it in avoiding deactivation during FTS [52]. It has been reported that FTS catalyst dispersibility is directly proportional to the FTS reaction rate [51]. Metal to support interactions (MSI) are an important factor to consider when selecting a catalyst support as they directly influence the dispersibility, sintering, reducibility, and overall performance of the catalysts. MSIs are the physical and chemical interactions between the metal catalyst and the support [10], [53], [54]. The stronger the MSI, the more resistant the catalyst is to deactivation via sintering during FTS. However, high temperatures are required to overcome strong MSIs during the catalyst reduction process [10], [55]. Different materials such as inorganic/metal oxides and different carbon allotropes have been studied for use as support materials in the Co-based FTS processes.

2.2.4.1 Inorganic oxides as FTS supports

Inorganic oxide such as silica (SiO_2), alumina (Al_2O_3), titania (TiO_2) and zeolite Socony Mobil (ZSM) are the most used supports in both academic and industrial research studies [56]. These supports are known to form strong MSIs with Co metals. For example, SiO_2 forms strong MSIs, which helps keep the metal stable and increases their resistance to attrition during the FTS reaction [57]. However, due to the strong MSIs, high temperatures (> 500 °C) are required to reduce Co_3O_4 to Co^0 [37], [58]. Additionally, non-reducible composites such as dicobalt orthosilicates (Co_2SiO_4) are formed, and this reduces the amount of active catalytic species [37], [58]. Chemical promoters such as Ru have been incorporated during supported catalyst design to manipulate the MSIs and help improve the ease of reduction of metal oxides to active catalytic species [56].

Different supported catalysts designs (see **Table 2.4**) have also been studied so as to manipulate these strong MSIs. These include use of a conventional support where the metal nanoparticles are dispersed on the surface of a support, e.g. see references [37], [58]. Another approach is to use core-shell structures. The core-shell method can be used to disperse the metal catalysts nanoparticles on the inside of a hollow support [59]. Another approach is to use the inverse method where small amounts of the support are dispersed on top of the metal catalyst surface in such a way that the surface interaction between the metal and the oxide support is minimized but the metal catalyst dispersibility is not compromised [45], [55].

The inverse method has given an improved understanding of MSIs between Co and porous inorganic oxides. For example, a group from the University of Cape Town have reported on the role of MSIs between FTS catalysts and inorganic oxides using these inverse catalyst models. Different studies have been conducted on inverse Co/silica [60], [61], Co/alumina [45], [62], [63], Fe/silica [47] and Fe/titania [64] catalysts to better understand the effect of the supports' physicochemical properties on the reducibility and overall performance of a metal catalyst under FTS reaction conditions. For Co catalysts, it was reported that the reduction of the metal oxide (Co_3O_4) to the active metal catalyst takes place at high temperatures similar to the conventional support reduction. However, an increase in the activity of the catalysts, especially in CO conversion was noted with these catalysts. It was observed that the as the concentration of silica increased on the Co catalyst surface, the FTS reaction favoured the formation of long chain hydrocarbons (C_3-C_{10}) [60]. When alumina was used as a support, a high CO conversion was also observed, and this was attributed to the high degree of dispersibility of the Co catalysts by alumina as well as CO dissociation induced by the acidic alumina chemical sites. It was also noted that the selectivity to long chain hydrocarbons (C_{5+}) was also increased with an increase in alumina concentration on the Co surface [45]. In a nutshell, the selectivity and activity of Co supported on inorganic oxides via the inverse support model showed better catalyst performance compared to the conventional Co on support catalyst.

Table 2.3: Cartoon illustrations and data on the different catalyst models for Co-support catalysts (support - inorganic oxides and carbon allotropes).

Notation	Cartoon images of different support models	Type of support model	Description	Literature examples	
				Inorganic oxides	Carbon allotropes
1.		Conventional support	Small metal catalyst particles are dispersed on a large surface area support	[37], [58]	[65], [66]
2.		Core-shell support	Small metal catalyst particles are dispersed inside a support	[59], [67]	[68], [69]
3.	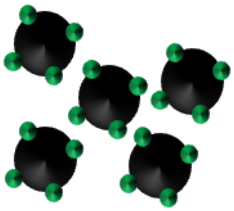	Inverse support	Small amounts of a support material are dispersed on the surface of a metal catalyst (forming "nano islands" around the metal)	[45], [60]–[62]	??

Co
Support

??: No known literature reports for the FTS catalysts yet

2.2.4.2 Carbon allotropes as FTS catalysts support

Carbon allotropes have been successfully used as catalysts supports in the FTS process because of their high surface area, chemical stability, and electron conductivity [10], [70]. Xiong *et al.*, wrote an informative review paper that described the different carbon supported catalysts in *syngas* conversion reactions, including the FTS. In their review, the properties of carbon nanotubes (CNTs), carbon nanofibers (CNFs), activated carbon (AC), carbon spheres (CSs), carbon black, ordered mesoporous carbon (OMCs), graphene, and diamond were evaluated [10]. Most

of the supported catalysts that were evaluated resembled the conventional support model, while some were of the core-shell type (e.g., Co/CNTs). It was reported that these carbon allotropes formed weak MSI with the metal catalysts. However, the overall performance of the catalyst supported on carbon was based on the morphology and chemical properties of the support. Since most carbon allotropes are inert in nature, the MSI can be improved by means of introducing oxygenic- and/or nitrogen-containing functional groups on the carbon support using an acid treatment or doping methods. These create defects in the carbon nanostructure and alter the electronic properties of carbon allotrope by introducing heteroatoms. These effects increase the dispersibility of the metal catalyst and decrease sintering during the reduction and the FTS process [10]. The improved interactions between the metal catalyst and the carbon support is also important for controlling the selectivity of the catalyst during the actual FTS [10]. For example, a Co metal catalyst supported on acid treated CNTs (i.e., oxygen-based surface functionalization of CNTs) showed improved selectivity towards liquid fuel (C_{5+} hydrocarbon) formation [69] compared to unfunctionalized CNTs [71].

For decades, carbon supports have been investigated as FTS supports using conventional catalysts supports and more recently the core-shell catalyst supports. However, to the best of our knowledge, there have not been any reports on carbon supported catalysts using the inverse catalyst approach. The reason for this is obvious - most carbon supports used in FTS are larger in size compared to the desired catalyst nanoparticle sizes ($\geq$ 8 nm). For example, the use of carbon allotropes such as carbon spheres (CSs) with d > 100 nm to create an inverse support will require very large sized Co nanoparticles (d in µm), and this would defeat the purpose of studying the inverse effect using such large metal particles. Therefore, to study the properties of carbon in an inverse catalyst model will require a carbon allotrope with particle size < 5 nm (since Co nanoparticles sizes of interest are $\geq$ 8 nm). This kind of inverse catalysts model requires use of the newest member of the carbon family known as carbon dots (CDs).

As mentioned in **Chapter 1** and **2.1**, the CDs are known for their small sizes (< 10 nm). CDs can be obtained, even functionalized, from their synthesis and do not require multiple synthesis steps to functionalize them as compared to the other carbon allotropes. For example, oxygen-functionalized CDs are obtained by using carbon precursors containing oxygen functional groups, such as ascorbic acid [73], [74], citric acid [75], [76] and sucrose [77]–[79], while nitrogen-functionalized CDs are derived from chitosan [80], [81], citric acid and urea [82], [83], ammonium citrate and triethylenetetramine [84]. These CDs are thus attractive for studying MSIs using the inverse Co support catalyst model.

Our early attempts in this study showed that the synthesized CDs are not thermally stable at temperatures > 200 °C, under inert (N_2) or reactive gases (hydrogen). It was found that the inverse catalyst approach could not be studied as the CDs structure was lost during heating. This was shown by *in-situ* PXRD studies contained in **Chapter 1** [85]. This implied that the CDs would also not be thermally stable under the FTS reaction conditions. Therefore, it became important to search for CDs with a high thermal stability or devise methods to improve the thermal stabilities of the CDs.

In this study, two different approaches were used to improve the thermal stability of CDs; 1) poorly functionalized CDs were synthesized via the vertical CVD method, and 2) the functionalized CDs were annealed to reduce the amount of surface functional groups. The former approach gave CDs with the desired thermal stability, but the yields were very low (< 5 w%), too low to use for FTS applications. The latter method led to the transformation of CDs to reduced graphene oxide (rGO) and CDs-rGO composites. These experimental results of both 1) and 2) are described in **Chapter 4** and **Chapter 5**, respectively. The transformation of CDs to rGO was unexpected and led to some changes in the thesis direction. The reaction provides a very interesting and novel graphene based nanosheets (GNSs) synthesis strategy. Therefore, the resultant rGO supports were evaluated for the Co-based FTS reactions. Co/rGO catalysts were synthesized and tested, adding to the literature of Co/rGO conventional supports for the FTS reactions. The FTS literature review based on graphene and the GNSs, as well as the results of Co/novel rGO obtained in this study are discussed in **Chapter 6**.

2.2.5 Conclusion

Support materials have a significant contribution, not only in reducing the amount and cost of the catalysts, but also in increasing the efficiency of the catalysts during FTS. It is important to study the properties of the support materials to gain insight so as to manipulate their surface chemistry such that they elevate the catalytic activity and selectivity of the catalyst. The inverse support model has added interesting perspectives to the MSI manipulation strategies. The idea of using CDs in inverse Co-based FTS reactions could advance the scope and understanding of the carbon to Co MSIs and close a significant gap in the literature, as emphasized by **Table 2.4**. The CDs used in this project indicated that their physical properties were not compatible with the FTS reaction conditions. Nonetheless, the products obtained during annealing of the functionalized CDs provided another avenue to study the FTS reaction. The conventional

Co/rGO catalysts based on the novel rGO sheets obtained in this project provided information on the carbon-Co interaction in FTS.

2.2.6 References

[1] C. Copéret, M. Chabanas, R. Petroff Saint-Arroman, and J. M. Basset, "Surface organometallic chemistry: Homogeneous and heterogeneous catalysis: Bridging the gap through surface organometallic chemistry," *Angew. Chemie - Int. Ed.*, vol. 42, no. 2, pp. 156–181, 2003, doi: 10.1002/anie.200390072.

[2] F. Rodriguez-Reinoso, "The role of carbon materials in heterogeneous catalysis," *Carbon*, vol. 36, no. 3, pp. 159–175, 1998, doi: 10.1109/ICL-GNSS.2013.6577279.

[3] J. C. Védrine, "Heterogeneous catalysis on metal oxides," *Catalysts*, vol. 7, no. 11, 2017, doi: 10.3390/catal7110341.

[4] X. Hu and A. C. K. Yip, "Heterogeneous catalysis: Enabling a sustainable future," *Front. Catal.*, vol. 1, pp. 1–3, 2021, doi: 10.3389/fctls.2021.667675.

[5] C. M. Friend and B. Xu, "Heterogeneous catalysis: A central science for a sustainable future," *Acc. Chem. Res.*, vol. 50, no. 3, pp. 517–521, 2017, doi: 10.1021/acs.accounts.6b00510.

[6] W. Liu, "Catalyst technology development from macro-, micro- down to nano-scale," *China Particuology*, vol. 3, no. 6, pp. 383–394, 2005, doi.org/10.1016/S1672-2515(07)60219-X.

[7] P. E. Strizhak, "Nanosize Effects in Heterogeneous Catalysis," *ChemInform*, vol. 44, no. 27, p. 2-21, 2013, doi: 10.1002/chin.201327226.

[8] N. J. Coville, S. D. Mhlanga, E. N. Nxumalo, and A. Shaikjee, "A review of shaped carbon nanomaterials," *S. Afr. J. Sci.*, vol. 107, no. 3/4, pp. 1–15, 2011, doi: 10.4102/sajs.v107i3/4.418.

[9] P. A. Berseth, A. G. Harter, R. Zidan, A. Blomqvist, C. M. Araujo, R. H. Scheicher, R. Ahuja and P. Jena, "Carbon nanomaterials as catalysts for hydrogen uptake and release in NaAIH 4," *Nano Lett.*, vol. 9, no. 4, pp. 1501–1505, 2009, doi: 10.1021/nl803498e.

[10] H. Xiong, L. L. Jewell, and N. J. Coville, "Shaped carbons as supports for the catalytic

conversion of syngas to clean fuels," *ACS Catal.*, vol. 5, no. 4, pp. 2640–2658, 2015, doi: 10.1021/acscatal.5b00090.

[11] S. Bahri, A. M. Venezia, and S. Upadhyayula, "Utilization of greenhouse gas carbon dioxide for cleaner Fischer-Tropsch diesel production," *J. Clean. Prod.*, vol. 228, pp. 1013–1024, 2019, doi: 10.1016/j.jclepro.2019.04.310.

[12] E. Makhura, J. Rakereng, O. Rapoo, and G. Danha, "Effect of the operation parameters on the Fischer Tropsch synthesis process using different reactors," *Procedia Manuf.*, vol. 35, pp. 349–355, 2019, doi: 10.1016/j.promfg.2019.05.051.

[13] Z. Gholami, Z. Tišler, and V. Rubáš, "Recent advances in Fischer-Tropsch synthesis using cobalt-based catalysts: a review on supports, promoters, and reactors," Catal. Rev. - Sci. Eng., vol. 63, no. 3, pp. 512-595, 2021, doi: 10.1080/01614940.2020.1762367.

[14] M. E. Dry, "High quality diesel via the Fischer – Tropsch process – a review," *J. Chem. Technol. Biotechnol.*, vol. 77, pp. 43–50, 2002, doi: 10.1002/jctb.527.

[15] H. Schulz, "Short history and present trends of Fischer – Tropsch synthesis," *Appl. Catal. A*, vol. 186, pp. 3–12, 1999, doi.org/10.1016/S0926-860X(99)00160-X.

[16] R. Guettel, U. Kunz, and T. Turek, "Reactors for Fischer-Tropsch synthesis," *Chem. Eng. Technol.*, vol. 31, no. 5, pp. 746–754, 2008, doi: 10.1002/ceat.200800023.

[17] R. G. dos Santos and A. C. Alencar, "Biomass-derived syngas production via gasification process and its catalytic conversion into fuels by Fischer Tropsch synthesis: A review," *Int. J. Hydrogen Energy*, vol. 45, no. 36, pp. 18114–18132, 2020, doi: 10.1016/j.ijhydene.2019.07.133.

[18] S. S. Ail and S. Dasappa, "Biomass to liquid transportation fuel via Fischer Tropsch synthesis – Technology review and current scenario," vol. 58, pp. 267–286, 2016, doi.org/10.1016/j.rser.2015.12.143.

[19] M. Kurian and A. Paul, "Recent trends in the use of green sources for carbon dot synthesis–A short review," *Carbon Trends*, vol. 3, p. 100032, 2021, doi: 10.1016/j.cartre.2021.100032.

[20] S. S. Ail and S. Dasappa, "Biomass to liquid transportation fuel via Fischer Tropsch synthesis - Technology review and current scenario," *Renew. Sustain. Energy Rev.*, vol.

58, pp. 267–286, 2016, doi: 10.1016/j.rser.2015.12.143.

[21] J. Hu, F. Yu, and Y. Lu, “Application of Fischer–Tropsch synthesis in biomass to liquid conversion,” *Catalysts*, vol. 2, no. 2, pp. 303–326, 2012, doi: 10.3390/catal2020303.

[22] S. Sorrell, J. Speirs, R. Bentley, A. Brandt, and R. Miller, “Global oil depletion: A review of the evidence,” *Energy Policy*, vol. 38, no. 9, pp. 5290–5295, 2010, doi: 10.1016/j.enpol.2010.04.046.

[23] O. P. R. van Vliet, A. P. C. Faaij, and W. C. Turkenburg, “Fischer – Tropsch diesel production in a well-to-wheel perspective : A carbon , energy flow and cost analysis,” *Energy Convers. Manag.*, vol. 50, no. 4, pp. 855–876, 2009, doi: 10.1016/j.enconman.2009.01.008.

[24] M. V. Kulikova, “The new Fischer-Tropsch process over ultrafine catalysts,” *Catal. Today*, vol. 348, pp. 89–94, 2020, doi: 10.1016/j.cattod.2019.09.036.

[25] M. E. Dry, “The Fischer – Tropsch process : 1950 – 2000,” *Catal. Today*, vol. 71, no. 3-4, pp. 227–241, 2002, doi.org/10.1016/S0920-5861(01)00453-9.

[26] A. B. Fontenelle and F. A. N. Fernandes, “Comprehensive polymerization model for Fischer-Tropsch synthesis,” *Chem. Eng. Technol.*, vol. 34, no. 6, pp. 963–971, 2011, doi: 10.1002/ceat.201000498.

[27] M. Martinelli, M. K. Gnanamani, S. LeViness, G. Jacobs, and W. D. Shafer, “An overview of Fischer-Tropsch Synthesis: XtL processes, catalysts and reactors,” *Appl. Catal. A Gen.*, vol. 608, p. 117740, 2020, doi: 10.1016/j.apcata.2020.117740.

[28] A. H. Sahir, Y. Zhang, E. C. D. Tan, and L. Tao, “Understanding the role of Fischer–Tropsch reaction kinetics in techno-economic analysis for co-conversion of natural gas and biomass to liquid transportation fuels,” *Biofuels, Bioprod. Biorefining*, vol. 13, no. 5, pp. 1306–1320, 2019, doi: 10.1002/bbb.2035.

[29] D. Leckel, “Diesel production from fischer - Tropsch: The past, the present, and new concepts,” *Energy and Fuels*, vol. 23, no. 5, pp. 2342–2358, 2009, doi: 10.1021/ef900064c.

[30] S. Tomasek, F. Lonyi, J. Valyon, A. Wollmann, and J. Hancsók, “Hydrocracking of Fischer-Tropsch paraffin mixtures over strong acid bifunctional catalysts to engine

fuels," *ACS Omega*, vol. 5, no. 41, pp. 26413–26420, 2020, doi: 10.1021/acsomega.0c02711.

[31] G. P. Van Der Laan and A. A. C. M. Beenackers, "Kinetics and selectivity of the Fischer-Tropsch Synthesis: A literature review," *Catal. Rev. - Sci. Eng.*, vol. 41, no. 3–4, pp. 255–318, 1999, doi: 10.1081/CR-100101170.

[32] G. Prieto, A. Martínez, P. Concepción, and R. Moreno-Tost, "Cobalt particle size effects in Fischer-Tropsch synthesis: structural and in situ spectroscopic characterisation on reverse micelle-synthesised Co/ITQ-2 model catalysts," *J. Catal.*, vol. 266, no. 1, pp. 129–144, 2009, doi: 10.1016/j.jcat.2009.06.001.

[33] J. M. G. Carballo, J. Yang, A. Holmen, S. Garcı´a-Rodrı´guez, S. Rojas, M. Ojeda and J. L. G. Fierro, "Catalytic effects of ruthenium particle size on the Fischer-Tropsch Synthesis," *J. Catal.*, vol. 284, no. 1, pp. 102–108, 2011, doi: 10.1016/j.jcat.2011.09.008.

[34] S. Rane, O. Borg, E. Rytter, and A. Holmen, "Relation between hydrocarbon selectivity and cobalt particle size for alumina supported cobalt Fischer-Tropsch catalysts," *Appl. Catal. A Gen.*, vol. 437–438, pp. 10–17, 2012, doi: 10.1016/j.apcata.2012.06.005.

[35] J. Yang, V. Frøseth, D. Chen, and A. Holmen, "Particle size effect for cobalt Fischer-Tropsch catalysts based on in situ CO chemisorption," *Surf. Sci.*, vol. 648, pp. 67–73, 2016, doi: 10.1016/j.susc.2015.10.029.

[36] J. A. Díaz, A. Romero, A. M. Garc´ıa-Minguill´an, A. GiroirFendler and J. L. Valverde, "Cobalt and iron supported on carbon nanofibers as catalysts for Fischer-Tropsch synthesis," *Fuel Process. Technol.*, vol. 128, pp. 417–424, 2014, doi: 10.1016/j.fuproc.2014.08.005.

[37] C. Qiu, Q. Meng, M. Panchal, C. Li, and B. Wu, "Enhanced Fischer-Tropsch activity in ammonium nitrate pretreated cobalt-silica catalyst," *Catal. Commun.*, vol. 147, no. July, p. 106149, 2020, doi: 10.1016/j.catcom.2020.106149.

[38] A. Y. Khodakov, W. Chu, and P. Fongarland, "Advances in the development of novel cobalt Fischer-Tropsch catalysts for synthesis of long-chain hydrocarbons and clean fuels," *Chem. Rev.*, vol. 107, no. 5, pp. 1692–1744, 2007, doi: 10.1021/cr050972v.

[39] K. Keyvanloo, M. J. Fisher, W. C. Hecker, R. J. Lancee, G. Jacobs, and C. H. Bartholomew, “Kinetics of deactivation by carbon of a cobalt Fischer-Tropsch catalyst: Effects of CO and H_2 partial pressures,” *J. Catal.*, vol. 327, pp. 33–47, 2015, doi: 10.1016/j.jcat.2015.01.022.

[40] M. P. Bailey, “SASOL , roquette join growing list of manufacturers adapting plants to produce hand sanitizer,” *Chemical Engineering essential for the CPI proffessionals*, pp. 1–6, Mar. 2020.

[41] H. Tian, X. Li, L. Zeng, and J. Gong, “Recent advances on the design of group VIII base-metal catalysts with encapsulated structures,” *ACS Catal.*, vol. 5, no. 8, pp. 4959–4977, 2015, doi: 10.1021/acscatal.5b01221.

[42] V. V. Ordomsky, A. Y. Khodakov, B. Legras, and C. Lancelot, “Fischer–Tropsch synthesis on a ruthenium catalyst in two-phase systems: an excellent opportunity for the control of reaction rate and selectivity,” *Catal. Sci. Technol.*, vol. 4, no. 9, p. 2896, 2014, doi: 10.1039/C4CY00803K.

[43] B. C. Enger and A. Holmen, “Nickel and Fischer-Tropsch synthesis,” *Catal. Rev. - Sci. Eng.*, vol. 54, no. 4, pp. 437–488, 2012, doi: 10.1080/01614940.2012.670088.

[44] M. Rahmati, B. Huang, M. K. Mortensen Jr., K. Keyvanloo, T. H. Fletcher, B. F. Woodfield, W. C. Hecker and M. D. Argyle, “Effect of different alumina supports on performance of cobalt Fischer-Tropsch catalysts,” *J. Catal.*, vol. 359, pp. 92–100, 2018, doi: 10.1016/j.jcat.2017.12.022.

[45] A. P. Petersen, M. Claeys, P. J. Kooyman, and E. van Steen, “Cobalt-based Fischer – Tropsch Synthesis : A kinetic inverse model system,” *Catalysts*, vol. 9, no. 10, pp. 794–807, 2019, https://www.mdpi.com/2073-4344/9/10/794.

[46] D. H. Chun, J. C. Park, S. Y. Hong, J. T. Lim, C. S. Kim, H. T. Lee, J. I. Yang, S. Hong and H. Jung, “Highly selective iron-based Fischer-Tropsch catalysts activated by CO_2-containing syngas,” *J. Catal.*, vol. 317, pp. 135–143, 2014, doi: 10.1016/j.jcat.2014.06.014.

[47] R. P. Mogorosi, N. Fischer, M. Claeys, and E. Van Steen, “Strong-metal-support interaction by molecular design: Fe-silicate interactions in Fischer-Tropsch catalysts,” *J. Catal.*, vol. 289, pp. 140–150, 2012, doi: 10.1016/j.jcat.2012.02.002.

[48] M. K. Gnanamani, G. Jacobs, W. D. Shafer, and B. H. Davis, “Fischer-Tropsch synthesis: Activity of metallic phases of cobalt supported on silica,” *Catal. Today*, vol. 215, pp. 13–17, 2013, doi: 10.1016/j.cattod.2013.03.004.

[49] S. Lyu, L. Wang, J. Zhang, C. Liu, J. Sun, B. Peng, Y. Wang, K. G. Rappé, Y. Zhang, J. Li and L. Nie, “Role of active phase in Fischer-Tropsch synthesis: Experimental evidence of CO activation over single-phase cobalt catalysts,” *ACS Catal.*, vol. 8, no. 9, pp. 7787–7798, 2018, doi: 10.1021/acscatal.8b00834.

[50] J. Yang, V. Frøseth, D. Chen, and A. Holmen, “Surface science particle size effect for cobalt Fischer – Tropsch catalysts based on in situ CO chemisorption,” *Surf. Sci.*, vol. 648, pp. 67–73, 2016, doi: 10.1016/j.susc.2015.10.029.

[51] E. Iglesia, “Design, synthesis, and use of cobalt-based Fischer-Tropsch synthesis catalysts,” *Appl. Catal. A Gen.*, vol. 161, no. 1–2, pp. 59–78, 1997, doi: 10.1016/S0926-860X(97)00186-5.

[52] S. J. Tauster, S. C. Fung, R. T. K. Baker, and J. A. Horsley, “Strong interactions in supported-metal catalysts,” *Science*, vol. 211, no. 4487, pp. 1121–1125, 1981.

[53] H. E. V. Dijk, “The Fischer-Tropsch synthesis : a mechanistic study using transient isotopic tracing,” Technische Universiteit Eindhoven, Eindhoven, 2001, DOI:

10.6100/IR542426.

[54] N. E. Tsakoumis, M. Rønning, Ø. Borg, E. Rytter, and A. Holmen, “Deactivation of cobalt based Fischer – Tropsch catalysts : A review,” *Catal. Today*, vol. 154, no. 3–4, pp. 162–182, 2010, doi: 10.1016/j.cattod.2010.02.077.

[55] L. Macheli, “Co_3O_4 -Nanocubes modified with TEOS as models to study support interactions in cobalt-based Fischer-Tropsch catalysts,” University of Cape Town, 2014.

[56] F. Bertella, C. W. Lopes, A. C. Foucher, G. Agostini, P. Concepcion, E. A. Stach and A. Martinez, “Insights into the Promotion with Ru of Co/TiO_2 Fischer-Tropsch Catalysts: An in Situ Spectroscopic Study,” *ACS Catal.*, vol. 10, no. 11, pp. 6042–6057, 2020, doi: 10.1021/acscatal.9b05359.

[57] H. J. Zhang, H. F. Ma, H. T. Zhang, W. Y. Ying, and D. Y. Fang, “Effect of incorporation manner of Zr promoter on precipitated ironbased catalysts for Fischer-

Tropsch synthesis," *J. Coal Sci. Eng.*, vol. 18, no. 2, pp. 182–187, 2012, doi: 10.1007/s12404-012-0213-x.

[58] M. Wolf, E. K. Gibson, E. J. Olivier, J. H. Neethling, C. R. A. Catlow, N. Fischer, M. Claeys, "In-depth characterisation of metal-support compounds in spent Co/SiO_2 Fischer-Tropsch model catalysts," *Catal. Today*, vol. 342, no. January 2019, pp. 71–78, 2020, doi: 10.1016/j.cattod.2019.01.065.

[59] J. L. Smarzaro, M. A. S. Baldanza, A. J. de Almeida, A. Caytuero, V. M. M. Salim, F. B. Passos and V. T. da Silva, "Effect of Silica Encapsulation on Cobalt-Based Catalysts for Fischer–Tropsch Synthesis under Different Reaction Conditions," *Ind. Eng. Chem. Res.*, 2021, doi: 10.1021/acs.iecr.1c01940.

[60] L. Macheli, A. Roy, E. Carleschi, B. P. Doyle, and E. van Steen, "Surface modification of Co_3O_4 nanocubes with TEOS for an improved performance in the Fischer-Tropsch synthesis," *Catal. Today*, vol. 343, no. October 2018, pp. 176–182, 2020, doi: 10.1016/j.cattod.2018.10.018.

[61] L. Macheli, E. Carleschi, B. P. Doyle, G. Leteba, and E. van Steen, "Tuning catalytic performance in Fischer-Tropsch synthesis by metal-support interactions," *J. Catal.*, vol. 395, pp. 70–79, 2021, doi: 10.1016/j.jcat.2020.12.023.

[62] A. P. Petersen, R. P. Forbes, S. Govender, P. J. Kooyman, and E. van Steen, "Effect of alumina modification on the reducibility of Co_3O_4 crystallites studied on inverse-model catalysts," *Catal. Letters*, vol. 148, no. 4, pp. 1215–1227, 2018, doi: 10.1007/s10562-018-2332-5.

[63] T. Van Heerden and E. Van Steen, "Metal – support interaction on cobalt based FT catalysts – a DFT study of model inverse catalysts," *Faraday Discuss.*, vol. 197, pp. 87–99, 2017, doi: 10.1039/C6FD00201C.

[64] R. P. Mogorosi, M. Claeys, and E. Van Steen, "Enhanced activity via surface modification of Fe-based fischer-tropsch catalyst precursor with titanium butoxide," *Top. Catal.*, vol. 57, no. 6–9, pp. 572–581, 2014, doi: 10.1007/s11244-013-0213-0.

[65] H. Xiong, M. Moyo, M. K. Rayner, L. L. Jewell, D. G. Billing, and N. J. Coville, "Autoreduction and catalytic performance of a cobalt Fischer-Tropsch synthesis catalyst supported on nitrogen-doped carbon spheres," *ChemCatChem*, vol. 2, no. 5, pp. 514–

518, 2010, doi: 10.1002/cctc.200900309.

[66] M. W. Dlamini, D. O. Kumi, T. N. Phaahlamohlaka, A. S. Lyadov, D. G. Billing, L. L. Jewell, N. J. Coville, "Carbon spheres prepared by hydrothermal dynthesis—A support for bimetallic iron cobalt Fischer–Tropsch catalysts," *ChemCatChem*, vol. 7, no. 18, pp. 3000–3011, 2015, doi: 10.1002/cctc.201500334.

[67] R. Xie, C. Wang, L. Xia, H. Wang, T. Zhao, and Y. Sun, "Controlled preparation of Co_3O_4@porous-SiO_2 nanocomposites for fischer-tropsch synthesis," *Catal. Letters*, vol. 144, no. 3, pp. 516–523, 2014, doi: 10.1007/s10562-013-1187-z.

[68] M. W. Dlamini, T. N. Phaahlamohlaka, D. O. Kumi, R. Forbes, L. L. Jewell, and N. J. Coville, "Post doped nitrogen-decorated hollow carbon spheres as a support for Co Fischer-Tropsch catalysts," *Catal. Today*, vol. 342, pp. 99–110, 2020, doi: 10.1016/j.cattod.2019.01.070.

[69] H. Xiong, M. A. M. Motchelaho, M. Moyo, L. L. Jewell, and N. J. Coville, "Cobalt catalysts supported on a micro-coil carbon in Fischer-Tropsch synthesis: A comparison with CNTs and CNFs," *Catal. Today*, vol. 214, pp. 50–60, 2013, doi: 10.1016/j.cattod.2012.10.018.

[70] S. Karimi, A. Tavasoli, Y. Mortazavi, and A. Karimi, "Cobalt supported on graphene - A promising novel Fischer-Tropsch synthesis catalyst," *Appl. Catal. A Gen.*, vol. 499, pp. 188–196, 2015, doi: 10.1016/j.apcata.2015.04.024.

[71] H. Xiong, M. A. M. Motchelaho, M. Moyo, L. L. Jewell, and N. J. Coville, "Correlating the preparation and performance of cobalt catalysts supported on carbon nanotubes and carbon spheres in the Fischer-Tropsch synthesis," *J. Catal.*, vol. 278, no. 1, pp. 26–40, 2011, doi: 10.1016/j.jcat.2010.11.010.

[72] M. Han, S. Zhu, S. Lu, Y. Song, T. Feng, S. Tao, J. Liu and B. Yang, "Recent progress on the photocatalysis of carbon dots: Classification, mechanism and applications," *Nano Today*, vol. 19, pp. 201–218, 2018, doi: 10.1016/j.nantod.2018.02.008.

[73] L. L. Mokoloko, B. J. Matsoso, R. P. Forbes, D. H. Barrett, B. D. Moreno, and N. J. Coville, "Evolution of large-area reduced graphene oxide nanosheets from carbon dots via thermal treatment," *Carbon Trends*, vol. 4, p. 100074, 2021, doi: 10.1016/j.cartre.2021.100074.

[74] A. Prasannan and T. Imae, “One-pot synthesis of fluorescent carbon dots from orange waste peels,” *Ind. Eng. Chem. Res.*, vol. 52, no. 44, 15673–15678, 2013, doi.org/10.1021/ie402421s.

[75] Y. Dong, J. Shao, C. Chen, H. Li, R. Wang, Y. Chi, X. Lin and G. Chen, “Blue luminescent graphene quantum dots and graphene oxide prepared by tuning the carbonization degree of citric acid,” *Carbon*, vol. 50, no. 12, pp. 4738–4743, 2012, doi: 10.1016/j.carbon.2012.06.002.

[76] R. Ludmerczki, S. Mura, C. M. Carbonaro, I. M. Mandity, M. Carraro, N. Senes, S. Garroni, G. Granozzi, L. Calvillo, S. Marras, L. Malfatti and P. Innocenzi, “Carbon dots from citric acid and its intermediates formed by thermal decomposition,” *Chem. - A Eur. J.*, vol. 25, no. 51, pp. 11963–11974, 2019, doi: 10.1002/chem.201902497.

[77] V. M. Naik, D. B. Gunjal, A. H. Gore, S. P. Pawar, S. T. Mahanwar, P. V. Anbhule and G. B. Kolekar, “Quick and low cost synthesis of sulphur doped carbon dots by simple acidic carbonization of sucrose for the detection of Fe^{3+} ions in highly acidic environment,” *Diam. Relat. Mater.*, vol. 88, pp. 262–268, 2018, doi: 10.1016/j.diamond.2018.07.018.

[78] B. Chen, F. Li, S. Li, W. Weng, H. Guo, T. Guo, X. Zhang, Y. Chen, T. Huang, X. Hong, S. You, Y. Lin, K. Zeng and S. Chen, “Large scale synthesis of photoluminescent carbon nanodots and their application for bioimaging,” *Nanoscale*, vol. 5, no. 5, p. 1967, 2013, doi: 10.1039/c2nr32675b.

[79] Y. Liu, “One-step microwave-assisted polyol synthesis of green luminescent carbon dots as optical nanoprobes,” *Carbon*, vol. 68, pp. 258–264, 2013, doi: 10.1016/j.carbon.2013.10.086.

[80] D. Xiao, D. Yuan, H. He, and J. Lu, “Microwave-assisted one-step green synthesis of amino-functionalized fluorescent carbon nitride dots from chitosan,” *Luminescence*, vol. 28, no. 4, pp. 612–615, 2013, doi: 10.1002/bio.2486.

[81] A. K. Keerthana and P. M. Ashraf, “Carbon nanodots synthesized from chitosan and its application as a corrosion inhibitor in boat-building carbon steel BIS2062,” *Appl. Nanosci.*, vol. 10, no. 4, pp. 1061–1071, 2020, doi: 10.1007/s13204-019-01177-0.

[82] W. Shang, M. Ye, T. Cai, L. Zhao, Y. Zhang and D. Liu and S. Liu, “Tuning of the

hydrophilicity and hydrophobicity of nitrogen doped carbon dots: A facile approach towards high efficient lubricant nanoadditives," *J. Mol. Liq.*, vol. 266, pp. 65–74, 2018, doi: 10.1016/j.molliq.2018.06.042.

[83] W. Kasprzyk, T. Świergosz, S. Bednarz, K. Walas, N. V. Bashmakova, and D. Bogdał, "Luminescence phenomena of carbon dots derived from citric acid and urea-a molecular insight," *Nanoscale*, vol. 10, no. 29, pp. 13889–13894, 2018, doi: 10.1039/c8nr03602k.

[84] W. Liu, R. Zhang, Y. kang, X. Y. Zhang, H. J. Wang, L. H. Li, H. P. Diao and W. L. Wei," Preparation of nitrogen-doped carbon dots with a high fluorescence quantum yield for the highly sensitive detection of Cu^{2+} ions, drawing anti-counterfeit patterns and imaging live cells," *New Carbon Mater.*, vol. 34, no. 4, pp. 390–402, 2019, doi: 10.1016/s1872-5805(19)30024-1.

[85] L. Mokoloko, "The effect of metal support interactions between a cobalt catalyst and carbon dots (Cdots) in cobalt fischer-tropsch catalysts," January, 2018, Available: http://wiredspace.wits.ac.za/handle/10539/26174.

CHAPTER 3: ANALYSIS TECHNIQUES

3.1 Introduction

A variety of characterization techniques were used to gain insights into the physical, chemical, and optical properties of the synthesized materials, and are discussed in this chapter. The synthesis, purification and optimization of poorly functionalized carbon dots (CDs) is elaborated in the manuscript titled: "*The simultaneous synthesis of carbon dots and carbon spheres with tuneable sizes using a vertical chemical vapour deposition method*", S Afr J Chem, vol. 76, pp. 25–30, 2022 [1], and forms part of **Chapter 4** of this thesis. The synthesis of functionalized CDs and their mechanism of evolution to rGO sheets is described in the manuscript titled: "*Evolution of large-area reduced graphene oxide nanosheets from carbon dots via thermal treatment*", Carbon Trends, vol. 4,100074, 2021 [2], which may be found in **Chapter 5**. The synthesis of nitrogen doped carbon dots (NCDs) is detailed in **Chapter 7**, which was also published under the title: "*From 0D to 2D: N-doped carbon sheets for detection of alcohol-based chemical vapours*", RSC Adv., vol. 12, 21440-21451, 2022 [3]. The synthesis of cobalt oxide (Co_3O_4) and the Co_3O_4/rGO are described in **Chapter 6**. Therefore, the various synthesis strategies will be omitted from this section to avoid repetition.

It is important to note that the CDs were synthesized using the "bottom-up" synthesis approach instead of the "top-down" approach because it is cost effective and produces higher yields of product compared to the "top-down" approach [4], [5]. For the synthesis of poorly functionalized CDs, acetylene (C_2H_2) was chosen as a carbon source because it is one of the most commonly used carbon sources for the synthesis of a wide variety of carbon allotropes via the chemical vapour deposition method (CVD) [6]. Additionally, carbon allotropes such as carbon spheres (CSs), carbon nanotubes (CNTs) and carbon nanofibers (CNFs), that have been synthesized via CVD assisted reaction using C_2H_2 as a carbon source, have been shown to be thermally stable under the Fischer-Tropsch synthesis (FTS) reactions [7], [8]. *L*-ascorbic acid was used in the synthesis of functionalized CDs because it is a cheap and renewable carbon source [9]. The Co_3O_4 nanoparticles were synthesized using the so called "benzyl alcohol route". Traditionally, Co_3O_4 nanoparticles are synthesized using methods such as the sol-gel and the reverse micelle method. The "benzyl alcohol route" has some benefits over these methods, and includes offering a more facile synthesis route, better particle size control, highly dispersed nanoparticles, better yields and no need for surfactants [10]–[13].

3.2 Characterization of carbon allotropes

3.2.1 Structural references

The characterization of many carbon allotropes is usually done by comparing data collected to that of the properties of graphene and graphite. Graphene is viewed as the foundation to the structures of many carbon allotropes [14], [15]. Graphene is a sheet-like carbon allotrope consisting of sp^2 type carbon ordered in two-dimension (2-D) [14]–[16] and graphite contains multiple planar layers (≥10 layers) of graphene "stacked" on top of each other to form a three-dimensional (3-D) structure[15]–[17]. Graphene can be "wrapped" to form a zero-dimensional (0-D) fullerene (buckyball consisting of hexagonal and pentagonal faces) type carbon allotrope [15], [17]. Carbon nano-onions (CNOs) are multiple graphene layers are "wrapped" around each other to form concentric fullerene shells [18]. Graphene can be "rolled" to form one-dimensional (1-D) single walled carbon nanotubes (SWCNTs) [15]–[17], and consequently, concentric walls of SWCNTs form the multi-walled carbon nanotubes (MWCNTs) [15], [19]. Carbon dots (CDs), specifically graphene quantum dots (GQDs), can be regarded as "pieces" of graphene, and these can be obtained from breaking down graphene, graphite and CNTs into smaller nanosheets [20]–[22]. **Figure 3.1** summarizes some these graphene transformations.

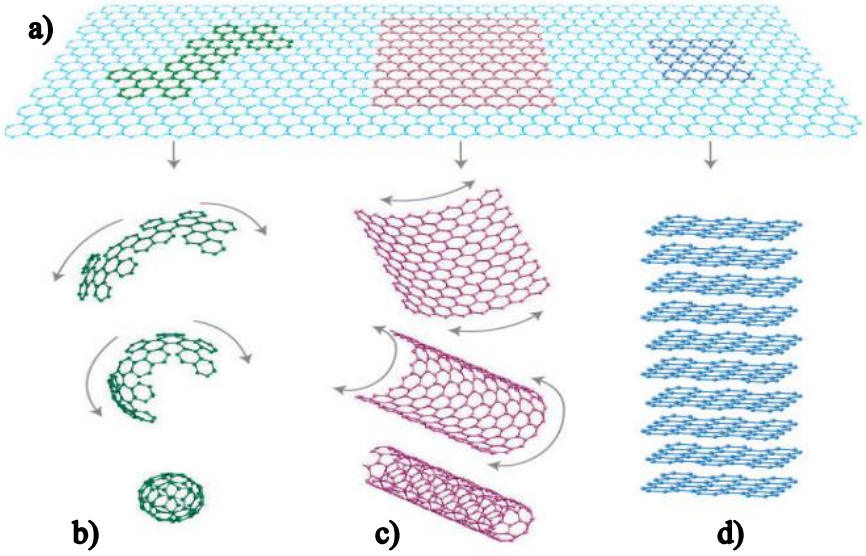

Figure 3. 1: Schematic representation of **a)** graphene as the starting material for **(b)** fullerene, **c)** SWCNTs and **d)** graphite (after Nasir et al.[17]).

3.2.2 Basis of carbon allotropes interpretation

Highly ordered (or crystalline) carbon allotropes are often classified as "graphitic" materials. The degree of graphitization depends on the sp^2/sp^3 C ratios within a carbon structure. These sp^2/sp^3 C ratios also affects the geometric arrangements of carbon allotropes. The lower the ratio, the less ordered (or less graphitic) the carbon allotrope. For example, CNTs are less graphitic compared to graphene sheets. This is because during CNTs synthesis, the sp^2 aromatic C of graphene are "forced" into a cylindrical shape. The edge C that gets knitted into a cylindrical shape do not only form aromatic (or hexagonal) rings, but pentagons and heptagons are formed too. These generate defects within the CNTs structure and therefore give rise to the sp^3 C character [23]. This decrease in the sp^2/sp^3 ratio of CNTs can be observed in the Raman spectrum of CNTs compared to graphene [24]. More on Raman analysis will be explained later. Another way of producing the same carbon allotrope with different properties is by incorporating functional groups on the carbon surface. For example, surface functionalized CNTs give rise to defects and more sp^3 C type within the structure compared to the pristine (or non-functionalized) CNTs [25], [26]. Conversely, the sp^2 C type character of many carbon allotropes can be increased by thermal treatment [27]. Carbon materials belonging to the same allotrope can different properties depending on their sp^2/sp^3 C ratios. For example, graphene quantum dots (GQDs) and carbon quantum dots (CQDs) are both fall under the carbon dots (CDs) group, however, GQDs are made predominantly of sp^2 C of graphene and CQDs contain a mixture of sp^2/sp^3 [28].

It has been proven that the surface defects on different carbon allotropes are highly important for metal catalysts dispersion, and consequently increasing the catalysts' performance under the FTS reactions [26], [29]–[31]. Additionally, the heteroatoms that are integrated into the carbon structure becomes the anchoring sites for metal catalysts and can influence the electronic properties of the catalysts via the metal to support interactions (MSIs) [31], [32]. MSIs are explained further in **Chapter 2.2**. The MSI phenomena was studied by comparing the effect oxygen functional groups (found on the surface of the CDs-derived carbon), on the Co_3O_4/CDs-derived carbons catalytic performance as discussed later in **Chapter 6**.

In this work, carbon dots (CDs), carbon spheres (CSs, "by-products" in the CVD synthesis of CDs in **Chapter 4**), nitrogen-doped CDs (NCDs), reduced graphene oxide (rGO) and its intermediates, cobalt oxide (Co_3O_4) and the Co_3O_4/rGO were analysed. The chemical and physical properties of the carbon allotropes obtained in this work were analysed using the traditional

comparison of graphene and/or graphite structure as explained previously. Each characteristic technique used as well as information of interest obtained from it are explained in **3.3**.

3.3 Characterization techniques

3.3.1 Techniques used to characterize the synthesized carbon allotropes

3.3.1.1 Transmission electron microscopy (TEM):

TEM technique gives information such as morphology (shape and size), crystal structure and phases as well as elemental composition of different materials. TEM is one of the common techniques used to distinguish between different carbon allotropes especially through their morphologies [33], [34]. Here, TEM images of the carbon allotropes were determined using a FEI G2 TECNAI Spirit T12, operated at 120 kV. The images obtained here were used to evaluate particle size distribution and plot the size histogram with curve fitted to the data applying a Gaussian model from the **ImageJ** software [35].

High Resolution transmission electron microscopy (HRTEM) analysis was used to detect/determine the lattice spacings (or *d*-spacings) of the synthesized carbon allotropes. This aided classify the prepared CDs as there are three types of CDs known. Typically, graphene quantum dots (GQDs) have a lattice *d*-spacing of *ca.* 0.24 nm, corresponding to the (100) lattice plane of graphite, and carbon quantum dots (CQDs) have a lattice spacing of *ca.* 0.34 nm, which is associated with the (002) planes of graphite [36]. Determining these lattice spacings also helped in gaining some information regarding the structural differences between the CDs and CSs (explained further in **Chapter 4**). For these analyses, a JEOL JEM 2100 high resolution TEM fitted with a LaB6 gun and operated at 200 kV was used. After imaging, the lattice fringes were obtained using fast Fourier-Transform (FFT) of a single CD. This produced the line profile. The average distance between the lines of similar heights were then divided by the number of spacing between them to get the *d*-spacing. This value was compared with the known lattice *d*-spacings of graphene and graphite to determine the chemical and physical nature of the CDs produced in this work.

Before imaging, the samples were dispersed in different solvent and sonicated for 2 hrs at room temperature. Toluene was used as a solvent for CDs and CSs in **Chapter 4**, water was used to disperse the functionalized CDs and NCDs in **Chapter 5** and **7**, respectively. Ethanol was used to disperse the CDs derivatives in **Chapter 5**, **Chapter 7** and the Co_3O_4/rGO in **Chapter 6**.

Then the dispersed sample was drop casted on a carbon-coated copper grid. The copper grid was allowed to air dry for several hours before analysis.

3.3.1.2 Scanning electron microscopy (SEM):

SEM was used to study the morphology of the samples, especially their external surfaces. SEM images were collected using a ZEISS SIGMA 03–39 FESEM operating at 20 kV. Similar to sample preparation for TEM, the samples were dispersed in different solvents. The dispersed samples were then drop casted on a carbon tape and allowed to air dry for several hours. Thereafter, the samples were coated with two layers of gold and palladium (Au/Pd) before analysis. Coating was done to inhibit charging from carbon allotropes, and thereby improving imaging during analysis.

3.3.1.3 Atomic force microscopy (AFM):

AFM was used to study the 3-D topography of the samples. A Veeco Di-3100 operating in a tapping mode was employed. The samples were first dispersed in a solvent then drop casted on Indium Tin Oxide (ITO) coated glass and the solvent was allowed to evaporate. Once dry, data was collected on each sample.

3.3.1.4 Powder x-ray diffraction (PXRD):

Powder X-ray diffraction is used to study the crystallographic features of the samples. Unlike HR-TEM, PXRD is a bulk characterization technique that produces gives a structural information that is obtained from a much larger sample volume. As a result thereof, the data is more representative of the bulk sample when compared to the data obtained from HR-TEM [34].

As described earlier, carbon allotropes can be ordered, semi-crystalline (possess short-range order/turbostratic carbon) or can be disordered (or amorphous). Graphene and graphite are the most ordered carbon allotropes. Natural graphite contains an ABAB type of stacking order, with weak van der Waals forces between the graphene layers. The PXRD of this graphite exhibit multiple peaks, with the main peak at *ca.* 26 ° under copper (Cu) radiation corresponding to the (002) miller plane [37]. For semi-crystalline (possess short-range order/turbostratic carbon) or disordered (or amorphous) carbon allotropes, the graphite layers are less ordered, curved, and defective [37]. This then leads to an increase in the full width at half maximum (FWHM) as well as a decrease in the diffraction angles of the (002) plane. The extent of these changes in data are more pronounce with decreasing crystallinity [34], [37]. Changes in the shapes of the peaks is observed across the entire 2θ range. Although many carbon allotropes

have poor diffraction patterns, some useful information regarding their structure may still be obtained [34].

For PXRD analysis, a Bruker D2 Phaser X-ray diffractometer equipped with a $CuK_{\alpha 1/2}$ radiation ($\lambda_{K\alpha}$= 1.5406 Å) source and a Lynxeye detector. Samples were scanned over the 2θ range from 10 - 90 ° 2θ using a 0.026 ° step size. The powdered samples were analysed without any further manipulation.

3.3.1.5 Pair distribution function (PDF):

PDF is a synchrotron-based technique that can be used to provide information on the structure of semi-crystalline (possess short-range order/turbostratic carbon) or disordered (or amorphous) carbon allotropes. Unlike PXRD, PDF measures all X-ray scattering resulting from a sample (also called total scattering). In the PDF technique, scattering provides information about the interatomic distances within a given sample [38]. This makes it possible to determine the local structure of poorly crystalline materials [38], [39], like the carbon allotropes produced in this work. The PDF technique was used to gain insights on the evolution of CDs to rGO sheets in **Chapter 5** as well as the NCDs-derivatives in **Chapter 7**. PDF data was collected on the Brockhouse high energy wiggler beamline at the Canadian Light Source using a wavelength of λ = 0.2081 Å and a PerkinElmer XRD1621 area detector placed 160 mm after the sample. The data was processed using GSAS-II [40]. The Q_{max} used to produce the PDF of the measured samples was 23.4 $Å^{-1}$. The instrumental resolution parameters Qdamp and Qbroad, as defined in PDFgui software, were determined by fitting a Ni powder standard measurement. Further data analysis was done using xPDFsuite [41].

3.3.1.6 Raman spectroscopy:

Raman spectroscopy measures the inelastic scattering resulting from the vibrational modes induced when samples interact with light, also called the Stroke Raman shifts. Carbon allotropes are characterized based on the Stroke Raman shifts of diamond and graphite reference. The Raman spectrum of diamond (sp^3 C type) consists of a sharp peak around *ca.* 1300 cm^{-1}, this peak is called the D peak, and graphite (sp^2 C type) spectrum consists of a peak at *ca.* 1600 cm^{-1}, called the G peak [42]. There are also some minor peaks which appears at *ca.* ~2700 cm^{-1} *ca.* 2900 cm^{-1} corresponding to the 2D and D+G overtones, respectively [43]–[45]. The 2D band (or second order D band, at *ca.* 2700 cm^{-1}) shape is used to determine the number of graphene layers within a material, and the D+G bands (at *ca.* ~2900 cm^{-1}) overtones are also an indication

of the presence of disorders within the samples. Semi-crystalline (possess short-range order/turbostratic carbon) or disordered (or amorphous) carbon allotropes contain both the G and D bands. The ratio of these two bands (based on their peak area) are used to determine whether the allotrope was graphitic (more ordered) or amorphous (less ordered). Raman spectroscopy data were collected using a Horiba LabRAM HR micro-Raman spectrometer (frequency double Lexel SHG argon ion laser). Silica was used as a substrate. Raman measurements were done with a 514.5 nm (green) laser. The samples were analysed by packing a small amount on a silica substrate. The samples were analysed without any further manipulation.

3.3.1.7 Photoluminescence (PL) spectroscopy:

PL spectroscopy is used to determine the emission peaks resulting from the energy level transition of valence electron of the samples. The technique gives information regarding the light intensity that materials can emit for a certain wavelength. PL is one of the routinely used characterizations of various CDs. In fact, it was the PL properties of CDs that made them stand out during their discovery. These PL properties are amongst the properties that made them extremely fascinating for different applications. The shape and size of the CDs PL peaks are often used to differentiate between the CD types and sizes [46]. The PL properties for CDs were not important for application in this thesis; however, the studies were conducted because it is the standard technique for CDs characterization. The PL studies were conducted concurrently with the Raman spectroscopy analysis (described above), and the measurements were done with a 244 nm excitation wavelength.

3.3.1.8 Ultraviolet to visible light (UV-vis) spectroscopy:

Uv-vis spectroscopy is used to determine the absorption peaks resulting from the energy level transition of valence electron of the samples. The transition takes place between the σ bonding electrons, π bonding electrons and non-bonding (n) electrons, i.e., $\sigma \rightarrow \sigma^*$, $n \rightarrow \sigma^*$, $\pi \rightarrow \pi^*$ and $n \rightarrow \pi^*$ (* symbolizes the excited state). This transition gives insight on the type of chemical bonding that exists in a sample. Just as with PL spectroscopy, UV-vis analyses are also very important and routinely used analysis for CDs. Here, the UV-vis measurements were carried out on a Agilent Technologies Cary (100) Series UV-Vis spectrophotometer, using a tungsten halogen light source. The samples were excited at 350 nm and the measurements were taken between 200 and 800 nm. Before the measurements, the samples in **Chapter 4** were dispersed toluene.

3.3.1.9 Fourier transform infrared spectroscopy (FT-IR) spectroscopy:

FT-IR spectroscopy was used to measure the infrared absorption or transmission of the samples based on their molecular vibrations which takes place when the molecules in a sample interact with infrared light. As such, chemical bonds information that exists in the synthesized carbon allotropes were abstracted. For these measurements, a Brucker TENSOR 27 FT-IR spectrometer, scanning between 4000 and 600 cm^{-1}, for 128 scans. The resulting vibrational modes such as the stretch and bending vibrations were identified and characterized. The powdered samples were taken for FT-IR analysis without any further modification.

3.3.1.10 Solid state carbon-13 nuclear magnetic resonance (^{13}C NMR) spectroscopy:

^{13}C NMR spectroscopy is used to characterize the structure of samples based on the functional groups content based on the observed chemical shifts under applied magnetic resonance [39]. For these samples, the interest was on the C hybridization (sp^2/sp^3 C) found in the skeleton. This then gave insights on the possible structure of the carbon allotropes during the transformation of CDs to graphene-like allotropes discussed in **Chapter 5** and **Chapter 7**. The different functional groups found in the samples were deduced from the obtained chemical shift values. For these measurements, a Bruker-500 MHz NMR spectrometer operating at a spinning frequency of 62.5 kHz (4.0 µs, 115 W) was used.

3.3.1.11 X-ray photoelectron spectroscopy (XPS):

XPS analysis was used to determine the elemental composition as well as the chemical states of the samples. Chemical information of each sample was characterized based on the binding energies peaks resulting from the photoelectronic emission of the elements within the samples when irradiated with X-rays. The binding energy peak heights are directly proportional to the amount of a specific element found in a sample. Here, XPS measurements were conducted employing a Physical Electronics Quantum 2000 using a monochromatic AlKα excitation source operating at 1486.7 eV.

3.3.1.12 Thermogravimetric analysis (TGA):

TGA was used to determine the thermal stability of the samples as a function of temperature while also under oxidizing atmosphere. The temperature of decomposition and the corresponding (approximate) mass loss (%) were determined. A PerkinElmer STA6000 analyser was used, and decomposition as a function of temperature were measured from 35 up to 900 °C at a heating rate of 10 °C/min, using air at 10 sscm and N_2 at 20 sccm flow rate as the purge gas.

3.3.1.13 Brunauer–Emmett–Teller (BET) surface analysis:

The specific surface area, pore diameter and pore volume were determined using the BET method. In these studies, nitrogen gas (N_2) at specific pressure was absorbed into the surface of the samples under cooling conditions until the surface was saturated, then once the surface was saturated, the samples were then heated up to remove the absorbed N_2. This then gives the absorption/desorption isotherms. In this study, the surface area results were obtained from adsorption data measured from the relative pressure range P/P_0=0.05–0.30 (P= pressure, P_0= partial pressure). Additionally, total pore volumes were calculated at P/P_0= 0.995. Finally, the N_2 isotherm desorption data were used to calculate the Barrett-Joyner-Halenda (BJH) pore size distributions.

3.3.2 Characterization of Co_3O_4/rGO

Co_3O_4 and Co_3O_4/rGO were also characterized by TEM, PXRD, FT-IR, TGA and BET. In addition, the following characterization techniques were also conducted:

3.3.2.1 In-situ powder X-ray diffraction (PXRD):

In-situ PXRD was used to determine the temperature required to reduce supported Co_3O_4 to CoO and Co^0. This was performed under different H_2 and N_2 atmosphere. Reduction under N_2 conditions was employed to evaluate whether the synthesized carbon allotropes can reduce Co_3O_4 to its active catalytic form Co^0 under inert atmosphere (i.e., the autoreduction effect). These studies provide some insights regarding the temperature at which the Co^0 metal catalyst is produced, as well as the type of Co^0 formed, i.e., Co hexagonal close-packed (or Co(hcp)) and Co face-centred cubic (or Co(fcc)). In these studies, the *in-situ* PXRD data was also used to investigate the effect of the support material on the reduction behaviour of the Co_3O_4 due to suspected MSI. This was performed on a Bruker D8 Advance diffractometer and the samples were heat treated in an Anton Paar XRK 900 reaction furnace. The measurements were carried out using CuKα X-ray radiation (1.5406 Å) operated at 40 kV and 40 mA. The data was collected from 10 to 80 ° 2θ using a 0.028 2θ step size for a total of 1 h per scan. The measurements were collected at 30 °C; and then from 200 – 550 °C every 25 °C. The data was collected under hydrogen (H_2) atmosphere flowing at 50 sccm and 1-2 bar pressure. For autoreduction studies, N_2 gas at flow rate of 50 sccm and 1-2 bar pressure was used to create an inert atmosphere.

3.3.2.2 Temperature-programmed reduction (TPR):

The TPR measurements, just like the *in-situ* PXRD, was used to study the thermal reduction of Co_3O_4 to Co^0 under H_2 environment. However, TPR does not provide information regarding the phase change. The reduction of Co_3O_4 as a result of temperature at constant H_2 was obtained from the Micromeritics AutoChem II instrument. Prior to the measurement, *ca.* 100 mg of the samples were heated at 150 °C for 30 min under helium (He, flow rate 50 sccm) atmosphere to degas the samples. The TGA analysis of the samples show that the samples are thermally stable at temperatures < 200 °C, hence the samples were degassed at 150 °C. There TPR measurement were then recorded for temperatures between 50 and 800 °C at a 10 °C/min heating rate under 5% H_2 (balanced with Ar gas) gas flowing at 50 sccm.

3.4 References

[1] L. L. Mokoloko, R. P. Forbes and N.J. Coville, "The simultaneous synthesis of carbon dots and carbon spheres with tunable sizes using a vertical chemical vapour deposition method," S Afr J Chem, vol. 76, pp. 25–30, 2022, doi.org/10.17159/0379-4350/2022/v76a05.

[2] L. L. Mokoloko, B. J. Matsoso, R. P. Forbes, D. H. Barrett, B. D. Moreno, and N. J. Coville, "Evolution of large-area reduced graphene oxide nanosheets from carbon dots via thermal treatment," *Carbon Trends*, vol. 4, p. 100074, 2021, doi: 10.1016/j.cartre.2021.100074.

[3] L. L. Mokoloko, B. J. Matsoso, N. Antonatos, Z. Sofer, D. H. Barrett, B. D. Moreno, R. P. Forbes and N. J. Coville, "From 0D to 2D: N-doped carbon sheets for detection of alcohol-based chemical vapours," *RSC Adv.*, vol. 12 pp. 21440-21451, 2022, doi: 10.1039/D2RA03931A.

[4] C. Xia, S. Zhu, T. Feng, M. Yang, and B. Yang, "Evolution and synthesis of carbon dots: From carbon dots to carbonized polymer dots," *Adv. Sci.*, vol. 6, no. 23, 2019, doi: 10.1002/advs.201901316.

[5] F. Bruno, A. Sciortino, G. Buscarino, M. L. Soriano, Á. Ríos, M. Cannas, F. Gelardi, F. Messina and S. Agnello, "A comparative study of top-down and bottom-up carbon nanodots and their interaction with mercury ions," *Nanomaterials*, vol. 11, no. 5, 2021, doi: 10.3390/nano11051265.

[6] X. Qi, C. Qin, W. Zhong, C. Au, X. Ye, and Y. Du, "Large-scale synthesis of carbon nanomaterials by catalytic chemical vapor deposition: A review of the effects of synthesis parameters and magnetic properties," *Materials (Basel).*, vol. 3, no. 8, pp. 4142–4174, 2010, doi: 10.3390/ma3084142.

[7] H. Xiong, M. A. M. Motchelaho, M. Moyo, L. L. Jewell, and N. J. Coville, "Correlating the preparation and performance of cobalt catalysts supported on carbon nanotubes and carbon spheres in the Fischer-Tropsch synthesis," *J. Catal.*, vol. 278, no. 1, pp. 26–40, 2011, doi: 10.1016/j.jcat.2010.11.010.

[8] H. Xiong, M. A. M. Motchelaho, M. Moyo, L. L. Jewell, and N. J. Coville, "Cobalt

catalysts supported on a micro-coil carbon in Fischer-Tropsch synthesis: A comparison with CNTs and CNFs," *Catal. Today*, vol. 214, pp. 50–60, 2013, doi: 10.1016/j.cattod.2012.10.018.

[9] A. Prasannan and T. Imae, "One-pot synthesis of fluorescent carbon dots from orange waste peels," *Ind. Eng. Chem. Res.*, vol. 52, no. 44, 15673–15678, 2013, doi.org/10.1021/ie402421s.

[10] N. Pinna, "The 'benzyl alcohol route': an elegant approach towards organic–inorganic hybrid nanomaterials," *J. Mater. Chem.*, vol. 17, no. 27, pp. 2769–2774, 2007, doi: 10.1039/B702854G.

[11] M. Hu, J. Xu, J. Gao, S. Yang, J. S. P. Wong, and R. K. Y. Li, "Benzyl alcohol-based synthesis of oxide nanoparticles: the perspective of SN1 reaction mechanism," *Dalt. Trans.*, vol. 42, no. 26, p. 9777, 2013, doi: 10.1039/c3dt50680k.

[12] N. Shi, W. Cheng, H. Zhou, T. Fan, and M. Niederberger, "Facile synthesis of monodisperse Co_3O_4 quantum dots with efficient oxygen evolution activity," *Chem. Commun.*, vol. 51, no. 7, pp. 1338–1340, 2015, doi: 10.1039/C4CC08179J.

[13] M. Wolf, N. Fischer, and M. Claeys, "Surfactant-free synthesis of monodisperse cobalt oxide nanoparticles of tunable size and oxidation state developed by factorial design," *Mater. Chem. Phys.*, vol. 213, pp. 305–312, 2018, doi: 10.1016/j.matchemphys.2018.04.021.

[14] S. K. Tiwari, V. Kumar, A. Huczko, R. Oraon, A. De Adhikari, and G. C. Nayak, "Magical allotropes of carbon: Prospects and applications," *Crit. Rev. Solid State Mater. Sci.*, vol. 41, no. 4, pp. 257–317, 2016, doi: 10.1080/10408436.2015.1127206.

[15] D. A. C. Brownson, D. K. Kampouris, and C. E. Banks, "An overview of graphene in energy production and storage applications," *J. Power Sources*, vol. 196, no. 11, pp. 4873–4885, 2011, doi: 10.1016/j.jpowsour.2011.02.022.

[16] X. Fan, G. Zhang, and F. Zhang, "Multiple roles of graphene in heterogeneous catalysis," *Chem. Soc. Rev.*, vol. 44, no. 10, pp. 3023–3035, 2015, doi: 10.1039/c5cs00094g.

[17] S. Nasir, M. Z. Hussein, Z. Zainal, and N. A. Yusof, "Carbon-based

nanomaterials/allotropes: A glimpse of their synthesis, properties and some applications," *Materials (Basel).*, vol. 11, no. 2, pp. 1–24, 2018, doi: 10.3390/ma11020295.

[18] J. Bartelmess and S. Giordani, "Carbon nano-onions (multi-layer fullerenes): Chemistry and applications," *Beilstein J. Nanotechnol.*, vol. 5, no. 1, pp. 1980–1998, 2014, doi: 10.3762/bjnano.5.207.

[19] L. Dai, D. W. Chang, J. B. Baek, and W. Lu, "Carbon nanomaterials for advanced energy conversion and storage," *Small*, vol. 8, no. 8, pp. 1130–1166, 2012, doi: 10.1002/smll.201101594.

[20] B. Liu, J. Xie, H. Ma, X. Zhang, Y. Pan, J. Lv, H. Ge, N. Ren, H. Su, X. Xie, L. Huang and W. Huang "From graphite to graphene oxide and graphene oxide quantum dots," *Small*, vol. 13, no. 18, pp. 1–7, 2017, doi: 10.1002/smll.201601001.

[21] S. Gu, C. Te Hsieh, Y. M. Chiang, D. Y. Tzou, Y. F. Chen, and Y. A. Gandomi, "Optimization of graphene quantum dots by chemical exfoliation from graphite powders and carbon nanotubes," *Mater. Chem. Phys.*, vol. 215, no. May, pp. 104–111, 2018, doi: 10.1016/j.matchemphys.2018.05.016.

[22] S. Shen, J. Wang, Z. Wu, Z. Du, Z. Tang, and J. Yang, "Graphene quantum dots with high yield and high quality synthesized from low cost precursor of aphanitic graphite," *Nanomaterials*, vol. 10, no. 2, 2020, doi: 10.3390/nano10020375.

[23] T. W. Ebbesen and T. Takada, "Topological and sp^3 defect structures in nanotubes," *Carbon*, vol. 33, no. 7, pp. 973–978, 1995, doi: 10.1016/0008-6223(95)00025-9.

[24] R. Saito, M. Hofmann, G. Dresselhaus, A. Jorio, and M. S. Dresselhaus, "Raman spectroscopy of graphene and carbon nanotubes," *Adv. Phys.*, vol. 60, no. 3, pp. 413–550, 2011, doi: 10.1080/00018732.2011.582251.

[25] H. Xiong, L. L. Jewell, and N. J. Coville, "Shaped carbons as supports for the catalytic conversion of syngas to clean fuels," *ACS Catal.*, vol. 5, no. 4, pp. 2640–2658, 2015, doi: 10.1021/acscatal.5b00090.

[26] M. A. M. Motchelaho, H. Xiong, M. Moyo, L. L. Jewell, and N. J. Coville, "Effect of

acid treatment on the surface of multiwalled carbon nanotubes prepared from Fe-Co supported on $CaCO_3$: Correlation with Fischer-Tropsch catalyst activity," *J. Mol. Catal. A Chem.*, vol. 335, no. 1–2, pp. 189–198, 2011, doi: 10.1016/j.molcata.2010.11.033.

[27] A. Sharma, T. Kyotani, and A. Tomita, "Comparison of structural parameters of PF carbon from XRD and HRTEM techniques," *Carbon N. Y.*, vol. 38, no. 14, pp. 1977–1984, 2000, doi: 10.1016/S0008-6223(00)00045-2.

[28] H. B. A. Sousa, C. S. M. Martins, and J. A. V. Prior, "You don't learn that in school: An updated practical guide to carbon quantum dots," *Nanomaterials*, vol. 11, no. 3, pp. 1–88, 2021, doi: 10.3390/nano11030611.

[29] M. W. Dlamini, T. N. Phaahlamohlaka, D. O. Kumi, R. Forbes, L. L. Jewell, and N. J. Coville, "Post doped nitrogen-decorated hollow carbon spheres as a support for Co Fischer-Tropsch catalysts," *Catal. Today*, vol. 342, npp. 99–110, 2020, doi: 10.1016/j.cattod.2019.01.070.

[30] H. Xiong, M. Moyo, M. A. Motchelaho, Z. N. Tetana, S. M. A. Dube, L. L. Jewell and N. J. Coville, "Fischer-Tropsch synthesis: Iron catalysts supported on N-doped carbon spheres prepared by chemical vapor deposition and hydrothermal approaches," *J. Catal.*, vol. 311, pp. 80–87, 2014, doi: 10.1016/j.jcat.2013.11.007.

[31] H. Xiong, M. Moyo, M. K. Rayner, L. L. Jewell, D. G. Billing, and N. J. Coville, "Autoreduction and catalytic performance of a cobalt Fischer-Tropsch synthesis catalyst supported on nitrogen-doped carbon spheres," *ChemCatChem*, vol. 2, no. 5, pp. 514–518, 2010, doi: 10.1002/cctc.200900309.

[32] J. Van De Loosdrecht, I. M. Ciobîca, P. Gibson, N. S. Govender, D. J. Moodley, A. M. Saib, C. J. Weststrate and J. W. Niemantsverdriet, "Providing fundamental and applied insights into Fischer-Tropsch catalysis: Sasol-eindhoven university of technology collaboration," *ACS Catal.*, vol. 6, no. 6, pp. 3840–3855, 2016, doi: 10.1021/acscatal.6b00595.

[33] P. R. Somani and M. Umeno, "Importance of transmission electron microscopy for carbon nanomaterials research," *Mod. Res. Educ. Top. Microsc.*, vol. 3, pp. 634–642, 2007.

[34] K. Jurkiewicz, M. Pawlyta, and A. Burian, “Structure of carbon materials explored by local transmission electron microscopy and global powder diffraction probes,” *C*, vol. 4, no. 4, p. 68, 2018, doi: 10.3390/c4040068.

[35] C. A. Schneider, W. S. Rasband, and K. W. Eliceiri, “NIH Image to ImageJ: 25 years of image analysis,” *Nat. Methods*, vol. 9, no. 7, pp. 671–675, 2012, doi: 10.1038/nmeth.2089.

[36] V. C. Hoang, K. Dave, and V. G. Gomes, “Carbon quantum dot-based composites for energy storage and electrocatalysis: Mechanism, applications and future prospects,” *Nano Energy*, vol. 66, p. 104093, 2019, doi: 10.1016/j.nanoen.2019.104093.

[37] Z. Q. Li, C. J. Lu, Z. P. Xia, Y. Zhou, and Z. Luo, “X-ray diffraction patterns of graphite and turbostratic carbon,” *Carbon N. Y.*, vol. 45, no. 8, pp. 1686–1695, 2007, doi: 10.1016/j.carbon.2007.03.038.

[38] S. J. L. Billinge, “The rise of the X-ray atomic pair distribution function method: A series of fortunate events,” *Philos. Trans. R. Soc. A Math. Phys. Eng. Sci.*, vol. 377, no. 2147, 2019, doi: 10.1098/rsta.018.0413.

[39] A. C. Forse, C. Merlet, P. K. Allan, E. K. Humphreys, J. M. Griffin, M. Aslan, M. Zeiger, V. Presser, Y. Gogotsi and C. P. Grey, “New insights into the structure of nanoporous carbons from NMR, Raman, and pair Distribution Function analysis,” *Chem. Mater.*, vol. 27, no. 19, pp. 6848–6857, 2015, doi: 10.1021/acs.chemmater.5b03216.

[40] B. H. Toby and R. B. Von Dreele, “GSAS-II : the genesis of a modern open-source all purpose crystallography software package,” *J. Appl. Crystallogr.*, vol. 46, no. 2, pp. 544–549, 2013, doi: 10.1107/S0021889813003531.

[41] C. L. Farrow, P. Juhas, J. W. Liu, D. Bryndin, E. S. Bozin, J. Bloch, T. Proffen, and S. J. L. Billinge, “PDFfit2 and PDFgui: Computer programs for studying nanostructure in crystals,” *J. Phys. Condens. Matter*, vol. 19, no. 33, 2007, doi: 10.1088/0953-8984/19/33/335219.

[42] G. G. Hoffmann, G. De With, and J. Loos, “Micro-Raman and tip-enhanced Raman spectroscopy of carbon allotropes,” *Macromol. Symp.*, vol. 265, no. 1, pp. 1–11, 2008, doi: 10.1002/masy.200850501.

[43] M. M. Lucchese, F. Stavale, E. M. Ferreira, C. Vilani, M. Moutinho, R. B. Capaz, C. Achete and A. Jorio,“ Quantifying ion-induced defects and Raman relaxation length in graphene,” *Carbon*, vol. 48, no. 5, pp. 1592–1597, 2010, doi: 10.1016/j.carbon.2009.12.057.

[44] A. C. Ferrari, “Raman spectroscopy of graphene and graphite: Disorder, electron-phonon coupling, doping and nonadiabatic effects,” *Solid State Commun.*, vol. 143, no. 1–2, pp. 47–57, 2007, doi: 10.1016/j.ssc.2007.03.052.

[45] E. F. Antunes, A. O. Lobo, E. J. Corat, V. J. Trava-Airoldi, A. A. Martin, and C. Veríssimo, “Comparative study of first- and second-order Raman spectra of MWCNT at visible and infrared laser excitation,” *Carbon N. Y.*, vol. 44, no. 11, pp. 2202–2211, 2006, doi: 10.1016/j.carbon.2006.03.003.

[46] R. Jelinek, *Carbon Quantum Dots*, 1st ed., Springer International Publishing: Cham, Switzerland, 2017, pp.1-130.

CHAPTER 4: SYNTHESIS OF POORLY FUNCTIONALIZED CARBON DOTS

The simultaneous synthesis of carbon dots and carbon spheres with tuneable sizes using a vertical chemical vapour deposition method

Lerato L Mokoloko[a], Roy P Forbes[a] and Neil J Coville[a*]

Abstract

Herein we report on the direct simultaneous synthesis of solid hydrophobic carbon dots (CDs) and simultaneously carbon spheres (CSs), using a vertical chemical vapour deposition (CVD) reactor. The HRTEM data indicated that the CDs and CSs originated from different carbon building blocks. The CDs were obtained by reacting acetylene (C_2H_2) and Ar mixtures at high flow rates (≥500 sccm) and high temperatures (800–1000 °C). TEM studies indicated that the CDs produced were graphene-like quantum dots that increased in size from *ca.* 3 nm to 8 nm as the Ar flow rate (constant C_2H_2 flow rate) was decreased, while small solid CSs (*ca.* 100 nm) were also synthesised in the process. The CSs had a typical spherical layered structure with no graphitic core. A mechanism to rationalise the observation that the CDs and CSs grew simultaneously by different pathways with no formation of intermediate-sized particles is given.

KEYWORDS: carbon dots, chemical vapour deposition, nanostructure, spectroscopy.

* author for correspondence: neil.coville@wits.ac.za

4.1 Introduction

Carbon dots (CDs) are described as carbonaceous nanoparticles composed of discrete, quasi-spherical structures with particle sizes below 10 nm. They have been a subject of interest particularly due to their extraordinary fluorescence properties - a characteristic that is not very common for carbon-based nanomaterials [1]–[3]. In addition, their size- and luminescence-dependent behaviour is similar to the properties known for conventional metal-based quantum dots. However, unlike the metal-based quantum dots, CDs have a high stability, low production cost, low toxicity, show good biocompatibility and can also be produced in high abundance [3]. It is because of these properties that CDs have been used for application in bioimaging [4], [5], biosensing [5], [6], water purification [7], photocatalysis [8], [9], solar cells [10], and various other systems.

Many synthesis methods have been developed and optimized to produce CDs with *hydrophilic* surface functionalities [11], but only a new methods have been developed for the synthesis of *hydrophobic* CDs. The two most commonly used routes to synthesize CDs that contain *hydrophobic* groups usually involve reacting a carbon source with a hydrophobic capping agent [12]–[15], or post modification of functionalized CDs with an amino dopant [16]. Another method to produce *hydrophobic* CDs is by carbonizing a non-functionalized carbon source that contains only C and H atoms such as C_2H_2 [17], [18], toluene [19], [20], natural gas [21], among others. The *hydrophobic* properties can also be conferred by the post reaction removal of all functional groups from the CD surface.

The carbonization of C_2H_2 in a CVD reactor has been extensively studied for the synthesis of carbon nanomaterials such as graphite, graphene, fullerene, carbon nanotubes (CNTs) and carbon spheres (CSs) [22]–[26]. These carbon materials show interesting surface chemistry, electronic properties, degree of graphitization and thermal stabilities that can be varied and made

suitable for tailored applications [22]–[26]. Surprisingly, to date only a few reports have highlighted the synthesis of CDs using the CVD reaction. Yan et al. [17] reported for the first time the synthesis of CDs using a horizontal CVD method. CDs with an average particle size of *ca.* 3.5 nm were produced using C_2H_2 as a carbon source and argon (Ar) as a carrier gas [17], [18].

To expand on the CVD approach, we have investigated the use of a *vertical* CVD method, using C_2H_2 as carbon source and different Ar flow rates, to synthesize CDs with controlled particle sizes. Reports have shown that carbon spheres (CSs) with tuneable sizes can be synthesized using this *vertical* CVD method [24]. This method limits the growth of the carbon, and consequently should make it possible to obtain CDs with controlled sizes. To the best of our knowledge, the synthesis of CDs with particle size control using the vertical CVD method is a novel approach to making CDs. To gain more insight into the properties of these new CDs, they were characterized using microscopy, spectroscopy and thermal analysis. The properties of these CDs were compared with those obtained using the horizontal CVD method. Additionally, using this methodology, CSs with a narrow size were also produced and analysed.

4.2 Methods

4.2.1 Materials

Acetylene gas (C_2H_2, 99.99 %) and argon gas (Ar, 99.9 %) were supplied by Afrox, South Africa. Reagent grade toluene ($C_6H_5CH_3$, 99.5 %), was purchased from Sigma-Aldrich, South Africa.

4.2.2 Synthesis procedure

The synthesis procedure followed here is a modification of a procedure reported by Mutuma et al. [24] for the synthesis of solid CSs using a vertical CVD reactor under atmospheric pressure. In a typical reaction set up, a vertical CVD reactor fitted with a quartz tube (2.4 cm i.d. × 1.15

m length), and a 3 L round bottom flask (RBF) was used as a sample collection chamber (SCC#1) as shown in **Figure 4.1**. For the collection of CDs, a bubbler containing toluene was used as a second sample collection chamber (SCC#2). Ar gas was passed through the quartz tube as the reactor was heated at 10 °C/min. When the desired temperature of reaction was reached, C_2H_2 gas from a second delivery line (see **Figure 4.1**) was introduced to the reactor, and the reaction allowed to proceed for 2 h. The C_2H_2 gas flow was kept constant at 25 sccm in all experiments and the temperature was held at 1000 °C in the initial experiments. After 2 h, SCC#2 contained a mixture of carbon products including CDs, while SCC#1 contained mostly CSs. The mixture from SCC#2 (see **Figure S4.1** for the product before any purification) was sonicated for 1 h, thereafter, centrifuged at 15 000 rpm and subsequently syringe filtered through a 0.45 µm polytetrafluoroethylene (PTFE) filter to further remove larger agglomerates. The toluene was then removed by rotary evaporator at 80 °C. The product from SCC#1 was collected and then purified using Soxhlet extraction in 200 mL toluene at 120 °C for 24 h. The products were then dried in an oven at 80 °C.

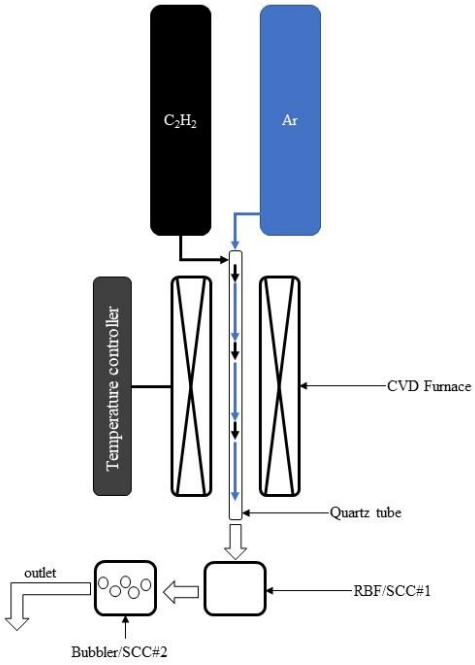

Figure 4. 1: Illustration of the reactor used to make and collect the CDs (and CSs) from C_2H_2 using the vertical CVD method.

Other syntheses were also conducted at different temperatures and flow rates. **Table 4.1** details the temperature, Ar flow rate used and synthesis % yield obtained for each synthesis of the CDs and CSs. The samples obtained were denoted according to their type (CDs or CSs), and with subscripts that represent the Ar flow rate (in sccm), the temperature (*100, in °C) and the collector (SCC#) in which the sample was collected, respectively. For example, the CDs were named $CDs_{520/10/2}$, when an Ar flow rate of 520 sccm, T = 1000 °C and collector #2 were used.

Table 4.1: Parameters used for the syntheses of CDs and CSs at 25 sccm C_2H_2 and the resulting particle sizes derived from TEM images.

Sample Notation[a]	Temperature (°C)	Ar flow rate (sccm)	Particle sizes (nm)	Yield (%)
$CSs_{600/10/1}$	1000	600	105 ±17	42.1
$CSs_{600/10/2}$			110±15	6.0
$CDs_{600/10/2}$			3±1	2.4
$CSs_{550/10/1}$	1000	550	105 ±17	42.4
$CSs_{550/10/2}$			109 ±19	9.7
$CDs_{550/10/2}$			6 ±2	4.3
$CSs_{520/10/1}$	1000	520	107 ±18	43.5
$CSs_{520/10/2}$			109 ±14	9.2
$CDs_{520/10/2}$			8 ±2	5.1
$CSs_{400/10/1}$	1000	400	108 ±17	44.0
$CSs_{400/10/2}$			95 ±14	14.0
$CDs_{400/10/2}$			-	-
$CSs_{350/10/1}$	1000	350	109 ±16	44.7
$CSs_{350/10/2}$			109 ±17	17.7
$CDs_{350/10/2}$			-	-
$CSs_{600/9/1}$	900	600	110 ±15	41.0
$CSs_{600/9/2}$			111 ±27	8.0
$CDs_{600/9/2}$			3 ±2	2.0
$CSs_{600/8/1}$	800	600	109 ±18	34.5
$CSs_{600/8/2}$			110 ±34	3.2
$CDs_{600/8/2}$			3 ±2	0.9
$CSs_{400/8/1}$	800	400	322 ±60	31.7
$CSs_{400/8/2}$			220 ±23	15.2
$CDs_{400/8/2}$			-	-
No CSs	700	600	-	-
No CDs			-	-
No CSs	700	400	-	-
No CDs			-	-

[a] The notation used in the table describes the types of products obtained. The subscripts represents the Ar flow rate (in sccm), the temperature (*100, in °C) and the sample collection chamber (SCC# in **Figure 4.1**), respectively.

4.2.3 Characterization

The particle size distribution and morphology of the as prepared CDs and CSs were determined by transmission electron microscopy (TEM) using a FEI G2 TECNAI Spirit T12 instrument

operated at 120 kV. For high resolution imaging, a JEOL JEM 2100 high resolution transmission electron microscopy (HRTEM) fitted with a LaB6 gun was used. Powder X-ray diffraction (PXRD) patterns were collected using a Bruker D2 phaser X-ray diffractometer equipped with a $Cu_{K\alpha 1/2}$ X-ray radiation source (λ = 1.54060 Å). Raman and photoluminescence (PL) spectroscopy measurements were conducted using a Horiba LabRAM HR micro-Raman spectrometer coupled with a PL excitation laser of 245 nm (Lexel Model 95 SHG argon ion laser). Ultraviolet-visible (UV-vis) spectroscopy analyses were carried out on an Agilent Technologies Cary (100) Series UV-vis spectrophotometer, using a tungsten halogen light source. The samples were excited at 365 nm. Infrared (IR) spectra were collected using a Brucker TENSOR 27 Fourier transform infrared (FT-IR) spectrometer. The thermal stability of the CDs and CSs were determined using a Perkin Elmer Pyris STA6000 thermal gravimetric analyser (TGA), and the samples were subjected to temperatures ranging from 35 to 900 °C, at a ramp rate of 10 °C/min. N_2 gas (20 sccm flow rate) was used as a purge gas, and air (10 sccm) as an analysis gas.

4.3 Results and discussion

CDs with different particle sizes were synthesized using a simple "bottom-up" approach using a vertical CVD reactor under atmospheric pressure. The reaction involved carbonization of C_2H_2, a non-functionalized carbon precursor, at high temperature that directly produced hydrophobic CDs. In preliminary studies, many experiments were performed to evaluate the collection of the CDs. Eventually, through trial and error, a high Ar flow rate (500-600 sccm), a low C_2H_2 flow rate (25 sccm) and high temperatures ($\geq$ 800 ^{o}C) were chosen for the study. However, even using these conditions, CSs were still produced with the CDs. For the syntheses conducted > 800 °C (> 500 sccm Ar), the CSs products were mainly collected in the first collector (SCC#1) at the bottom of the CVD reactor, while the less dense (fluffy) and smaller

products such as CDs and other carbon agglomerates were collected in SCC#2. Other conditions produced only CSs in SCC#1 and in SCC#2 and no CDs in SCC#2 (**Table 4.1**). Similar reactions performed at 700 °C yielded no CDs or CSs products.

The TEM images of the CDs products obtained in SCC#2 at different flow rates (together with their corresponding particle size distributions) are shown in **Figure 4.2**. The results show that the CDs are quasi-spherical in shape, well dispersed and have a narrow particle size distribution. The average particle sizes recorded for $CDs_{600/10/2}$, $CDs_{550/10/2}$ and $CDs_{520/10/2}$ were 3 ± 1 nm, 6 ± 2 nm and 8 ± 2 nm, respectively. This shows that as the flow rate of Ar gas was decreased, the resulting particle size increased. As more C_2H_2 is introduced into the reactor, the C species produced increased (as C_2H_2 decomposed) to form aggregates that grew, nucleated and crystallized into larger C nanoparticles [17]. Therefore, the increased carrier gas flow rate reduced the growth stage of the C aggregates and the formed particles were quickly transported into the collection chambers, resulting in the collection of smaller particles.

Only CSs were collected in SCC#1 at an Ar flow rate of 600, 550, 520, 400 and 350 sccm and all the CSs were similar in particle size as shown in **Table 4.1**. Thus, at 1000 °C (C_2H_2= 25 sccm; Ar = 350-600 sccm) the CSs collected in SCC#1 show that the CS growth is little affected by the varying flow rates, and their average particle sizes are ~100-110 nm. At higher C_2H_2 flow rates much larger CSs are formed [24]. The TEM image of the CSs product (named $CSs_{520/10/1}$, $CSs_{550/10/1}$ and $CSs_{600/10/1}$) obtained at Ar = 600 sccm are shown in **Figure S4.2-4)**.

The HRTEM images of $CDs_{600/10/2}$ (**Figure S4.5a)**) show well-resolved lattice fringes with a lattice *d*-spacing of *ca.* 0.21 nm, which is associated with the (100) facets of a graphitic carbon [27]. The HRTEM images of the $CSs_{600/10/1}$ (**Figure S4.5b)**) showed a highly amorphous; with no lattice fringes observed. This indicates that the nature of these CSs is different to that found

for the CDs. Particle growth of carbon black (CB) is similar to that of CSs growth and yields an amorphous core surrounded by concentric layers of short-length graphene-like sheets.

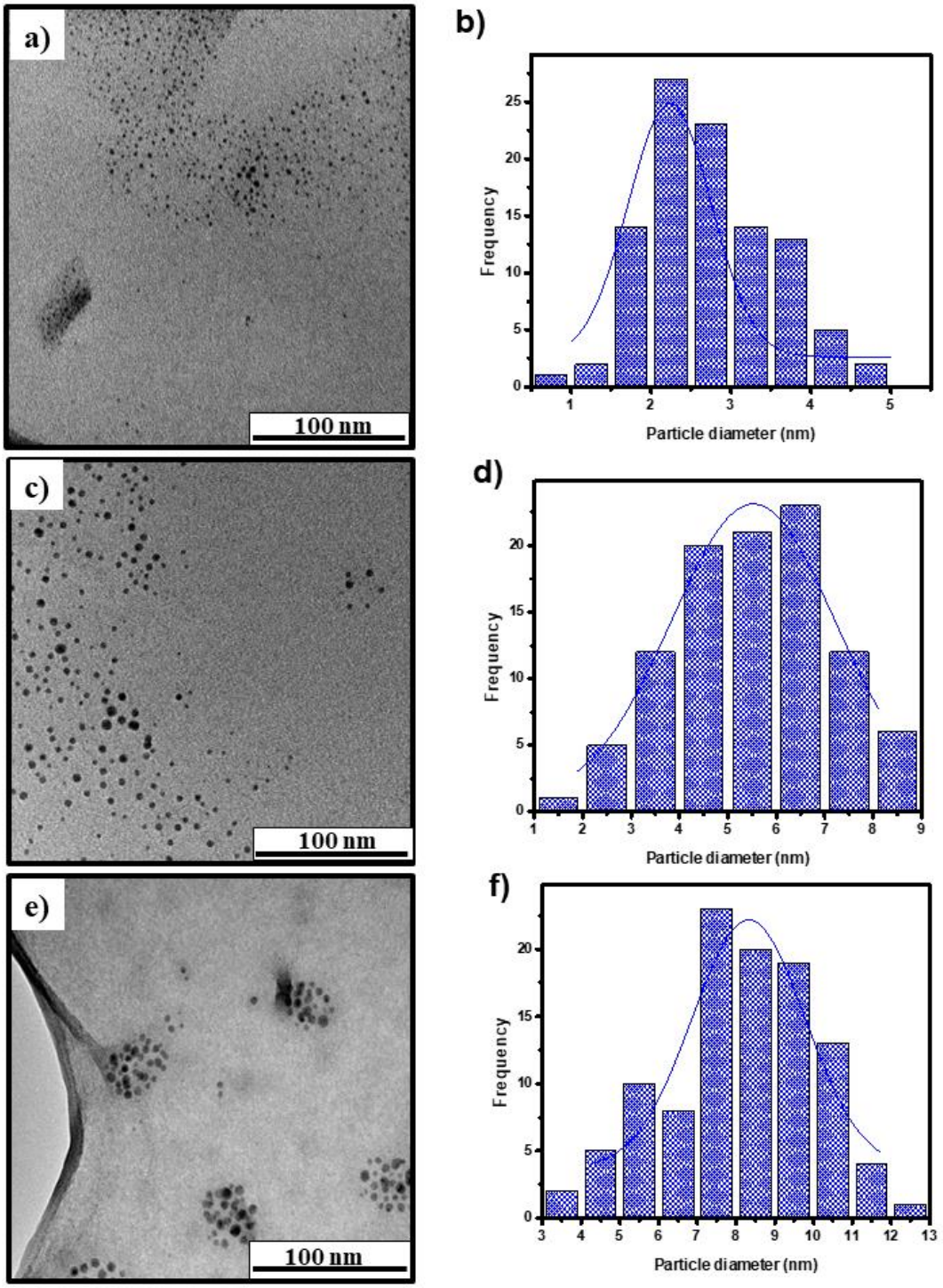

Figure 4. 2: TEM images and particle size distribution histograms of CDs produced at 1000 ^{o}C and different argon flow rates **a-b)** $CDs_{600/10/2}$, **c-d)** $CDs_{550/10/2}$, **e-f)** $CDs_{520/10/2}$.

The effect of temperature on the particle sizes was also investigated. When the temperature was reduced from 1000 to 900 °C and 800 °C (C_2H_2 = 25 sccm; Ar = 600 sccm) the CDs formed had $d = 3 \pm 2$ nm (**Figure S4.6**). At these conditions, the CSs size was also unaffected by the temperatures used. However, the effect of temperature was only detected at a low Ar flow rate (400 sccm) and a low temperature (800 °C) where only CSs were collected; with particle sizes of 322 ± 60 nm (SCC#1) and 220 ± 23 nm (SCC#2) (**Figure S4.7 and S4.8**). When the temperature was further decreased to ≤ 700 °C, no CDs or CSs were formed.

The % yields of the products are recorded in **Table 4.1**. The CDs were produced in low amounts (< 5 %) with the highest yields observed at 1000 °C. In contrast, good yields of CSs were formed (*ca.* 40 %). The CDs formed are light weight. To enhance the CD yield, a second bubbler was placed next to SCC #2 to collect any product that may have been lost by the rapid gas flow rates. However, for Ar flow rates between 520 - 600 sccm, the CDs yield only increased by ~ 0.5 %.

The PXRD patterns of the CD and CS products (**Figure 4.3a)**) show broad feature at *ca.* 25 ° and *ca.* 44 ° 2θ, which are attributed to the (002) plane of a graphitic carbon, respectively [28]. The Raman spectra of the CDs (**Figure S4.9a**) show the Raman D-band (~1330 cm^{-1}), indicating the presence of sp^3 amorphous type carbon, and the G-band (~1595 cm^{-1}), which arises due to the presence of sp^2 graphitic type carbon [29]. The resulting I_D/I_G ratios of the material were ~ 0.5, confirming the presence of both amorphous and graphitic components [29]. The PL spectra (**Figure 4.3b)**) showed that the CDs and not the CSs have optical properties. The $CDs_{600/10/2}$, $CDs_{550/10/2}$ and $CDs_{520/10/2}$ all show a broad peak with blue to green emission in the visible light region [30], [31], with peak maximum at *ca.* 450 nm and a shoulder at *ca.* 500 nm. Previous reports have indicated that the PL peak shifts to higher wavelengths when the particle sizes of functionalized CDs increase [32]. However, this was not the case with the CDs studied here. The TEM particle size distribution histograms of the CDs also showed that the nanoparticle ranges overlapped, suggesting an inhomogeneous composition of nanoparticles, leading

to the broad peaks observed in the PL spectra. The CSs did not show any excitation activity at this excitation wavelength. The UV-vis spectra for $CDs_{600/10/2}$, $CDs_{550/10/2}$ and $CDs_{520/10/2}$ (**Figure 4.3b)** show strong absorptions in the UV region, similar to that observed for CDs synthesized using a horizontal CVD [17]. As with the PL spectroscopy analysis, the CSs did not show any UV optical activity.

FT-IR spectra (**Figure S4.9b**) of the $CDs_{600/10/2}$, $CDs_{550/10/2}$, $CDs_{520/10/2}$, $CSs_{400/10/2}$ and $CSs_{350/10/2}$ all had a similar pattern which showed the presence of weak C-H bonds (3000-2850 cm^{-1},1456-1377 cm^{-1}), C=C bonds (1668-1271 cm^{-1}), and C=O bonds (~1724 cm^{-1}). The C=O absorption peak indicates that there are some functional groups present on the surface. When compared to the FT-IR spectra of CDs produced by other routes [33]–[35], it is clear that the CDs prepared here have fewer functional groups. To further confirm this, the dispersibility of $CDs_{600/10/2}$ in distilled water was investigated and compared with the CDs obtained from carbonizing vitamin C in a microwave-assisted hydrothermal reaction following the reaction procedure reported by Mokoloko [36]. It was found that the $CDs_{600/10/2}$ were not dispersible in distilled water even after sonicating for 1 h, while the functionalized CDs (from vitamin C) dispersed readily in water even without sonication (**Figure S4.10**). The CDs are known to inherit some of the chemical make-up of their precursors, this is also the case with the CDs obtained from vitamin C. Vitamin C contains a significant number of O-functional groups, which makes it water dispersible. Likewise, the CDs were found to contain O-functional groups on their surface, and these were responsible for their water dispersibility [36].

The thermograms in **Figure 4.3d)** show that the materials decompose completely in air. The derivative weight loss of these thermographs is shown in **Figure S4.11.** and indicates the insignificant amount of surface functional group on these CDs. CDs that contain large amounts of functional groups also show major thermal decomposition peaks between *ca.* 200-500 °C

[33], [34], [37]. The graphs show a small weight loss peak at *ca.* 100 °C, which can be attributed to the loss of absorbed moisture. The decomposition of the CDs occurred between 701 °C and 711 °C. Typically, the decomposition temperatures of the CDs reported here are comparable to those reported for amorphous and graphitized carbon nanomaterials such as CSs [24], CNTs [25], and CNOs [38].

Although the synthesized CDs have different particle size distributions, there was no significant difference in their thermal, spectral and structural properties. The results are to be compared to CDs made by alternative procedures where large shifts in spectral properties were observed as a function of CD size and surface coverage [39]. This implies that the key factor in the spectral variability of functionalised CDs must reside more with the surface functional groups rather than with their size.

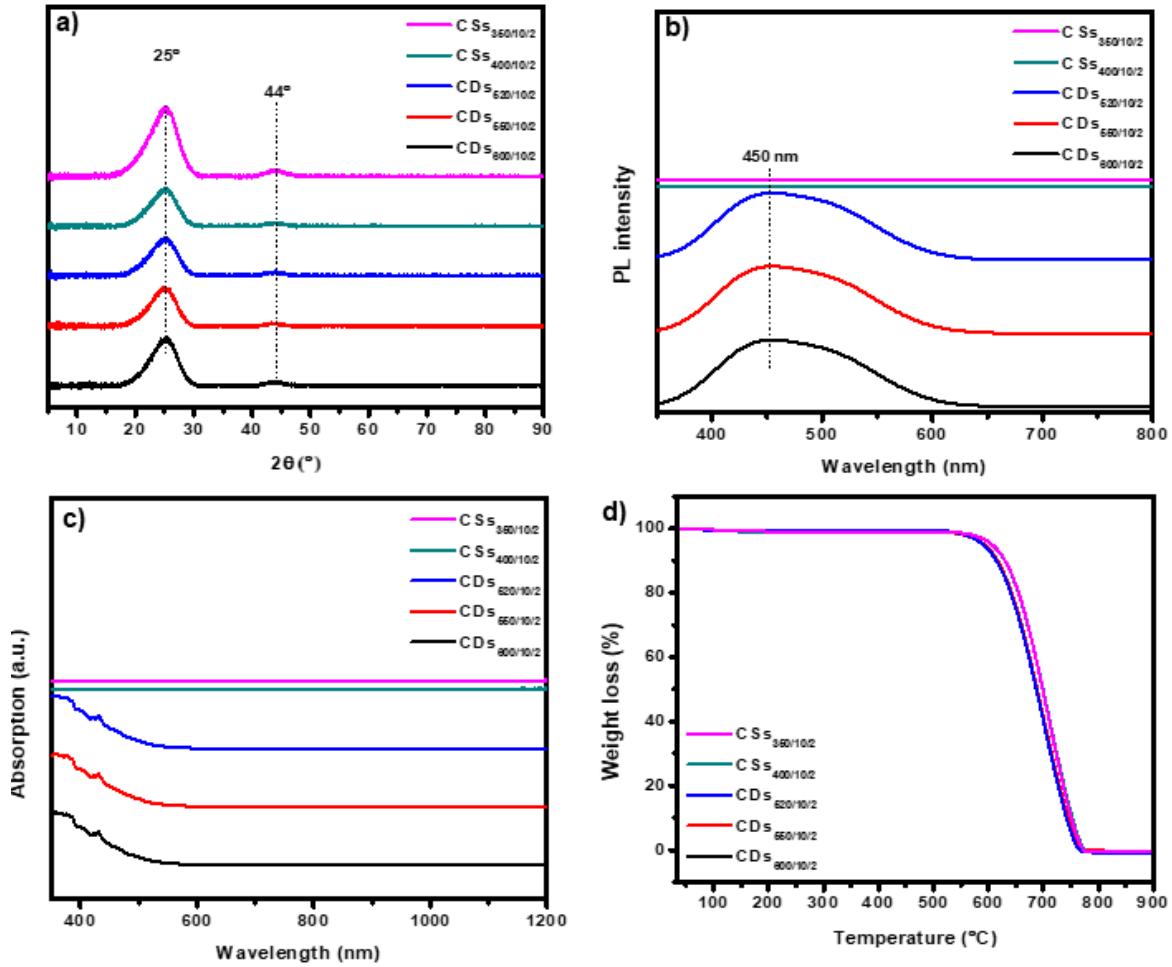

Figure 4. 3: a) PXRD, **b)** PL, **c)** UV-Vis spectra, and **d)** TGA, data for $CDs_{600/10/2}$, $CDs_{550/10/2}$ and $CDs_{520/10/2}$, $CSs_{400/10/2}$ and $CSs_{350/10/2}$.

The CDs produced in this study were compared those produced by means of the horizontal CVD method [17], [18]. It appears that the CDs all produce similar TEM, UV-vis and FT-IR data. The PXRD patterns together with the HRTEM lattice fringes and the Raman spectra suggested that our CVD method produced graphitic-like quantum dots, similar to those reported from the horizontal CVD method [17]. The advantage in using a vertical reactor relates to the control of the time that the CDs remain in the reactor. Thus, the method appears to be effective for the synthesis of (i) small and narrow sized CSs (≤ 100-320 nm), (ii) producing a good % yield of the CSs and (iii) provide a method to produce CDs with controlled size. This

use of a vertical reactor makes it is possible to produce CDs < 5 nm using controlled temperature and flow rate conditions (from 70/700 sccm C_2H_2/Ar at 1000 °C [17], [18] to 25/600 C_2H_2/Ar at 800-1000 °C).

4.4 CDs and CSs growth mechanism

One would expect that the CDs and CSs originate from common building blocks generated from the C_2H_2. Indeed, the Raman spectra, TGA data and PXRD patterns of both CDs and CSs appear to be similar. However, TEM data suggest otherwise.

i) The HRTEM images indicate graphite-like CDs [40] while the CSs show no core that is made of graphene layers in a graphite arrangement (**Figure S4.5**).

ii) The CDs made in a horizontal reactor also generate a graphene like structure [17], [18]. Thus, the important issue in making the CDs relates to the rapid removal of the CDs from the reactor. The use of a vertical CVD reactor allows this to be done in a controlled manner.

iii) The general outline of the mechanism to grow CDs from fragments generated form C_2H_2 [17], would apply to the CDs made in the vertical reactor.

iv) The sizes of the CDs and CSs as a function of Ar gas flow show no overlap (**Figure 4.4**). Indeed, the sizes show only a small change in size within each type, as the Ar flow rate varies. The observation of only two sizes of products implies two different growth mechanisms for the CDs and CSs from different building blocks.

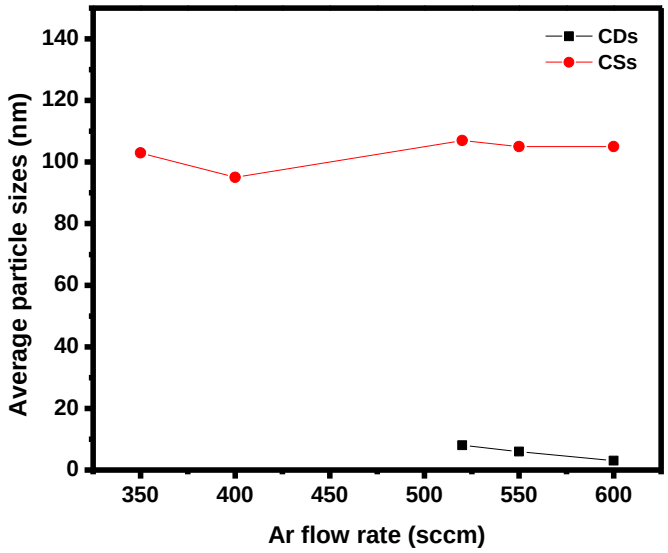

Figure 4. 4: CDs and CSs particle sizes as a function of Ar flow rate at 1000 °C.

v) At high temperature, it is well known that acetylene is transformed into polycyclic aromatic hydrocarbons (PAHs) which consists of fused hexagonal, pentagonal, heptagonal carbon fragments, among others [41]–[43]. In the case of CSs, the presence of pentagonal and hexagonal carbon fragments pair to form a spiral core, and a spherical structure, which is terminated by graphitic flakes [44], [45]. A cartoon showing the synthesis of the CSs (and CDs) from PAHs is given in **Figure 4.5**.

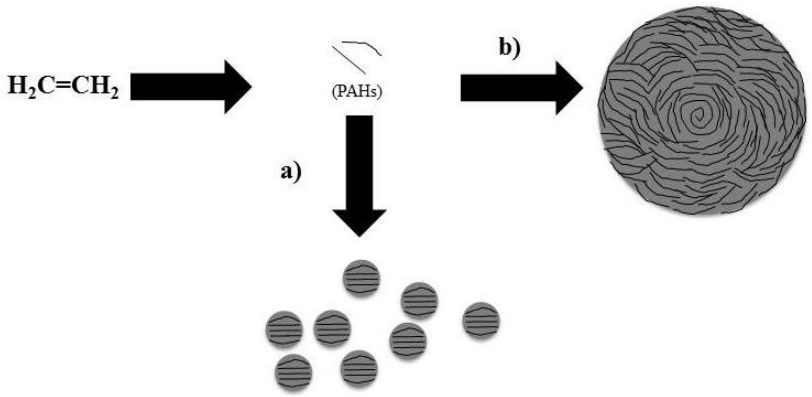

Figure 4. 5: Possible mechanism to show growth of a) CDs and b) CSs from curved and planar PAHs.

vi) The CDs do not show this effect; they consist of stacked graphene layers. This implies that the ratio of C_6 planar rings to C_5/C_7 rings leads to the different structures seen. This is associated with the different flow rates used which could lead to different carbon growth patterns in the CVD reactor (**Figure 4.5**).

vii) It is possible that a catalytic effect of the quartz tube could also play a role in generating the two different carbons formed [41].

4.5 Conclusions

This study reports, for the first time, the synthesis of CDs with different particle sizes (below 10 nm) made in a vertical CVD reactor. This method produced hydrophobic CDs, using an *in-situ* method. The structural and electronic properties of the CDs were studied and it was confirmed that the CDs are similar in their physical and optical properties to those produced by a horizontal CVD method. This includes their quasi-spherical shape that is made of graphitic layers, UV-vis absorption properties resulting from $\pi \rightarrow \pi^*$ transitions and the presence of a limited number of functional groups as suggested by their FTIR spectra. The TGA results showed that these CDs have a thermal stability similar to those reported for well-known carbon allotropes such as CSs, CNTs and CNOs. The data suggests that these CDs could be used in high temperature applications. This method also produced small CSs (*ca.* 100 nm) with a narrow particle size distribution and high thermal stability. Most importantly it is clear that the CDs produces in this study are made by a different mechanism to that used to make CSs.

Acknowledgements

We wish to thank the NRF, the University of the Witwatersrand and the DSI-NRF Centre of Excellence in Catalysis for financial support. We would also like to express our gratitude to Dr Rudolph Erasmus (School of Physics, University of the Witwatersrand, South Africa) for PL

and Raman spectroscopy data and Rhandzu Rikhotso (Council for Scientific and Industrial Research, South Africa) for HRTEM data.

Competing interests

The authors have no competing interests

Author contributions

Conceptualization (NJC, LM); Formal analysis (NJC, LM, RF) Funding acquisition (NJC, LM), Writing (NJC, LM, PF)

4.6 References

[1] R. Jelinek, *Carbon Quantum Dots*, 1st ed., Springer International Publishing: Cham, Switzerland, 2017, 1-130.

[2] A. Sciortino, A. Cannizzo, and F. Messina, "Carbon nanodots: A review—From the current understanding of the fundamental photophysics to the full control of the optical response," *J. Carbon Res.*, vol. 4, no. 4, p. 67, 2018, doi: 10.3390/c4040067.

[3] F. Yuan, T. Yuan, L. Sui, Z. Wang, Z. Xi, Y. Li, X. Li, L. Fan, A. Chen and M. Jin, "Engineering triangular carbon quantum dots with unprecedented narrow bandwidth emission for multicolored LEDs," *Nat. Commun.*, vol. 9, no. 1, pp. 1–11, 2018, doi: 10.1038/s41467-018-04635-5.

[4] R. V, V. Gujar, H. Pathan, S. Islam, M. Tawre, K. Pardesi, M.K. Santra and D. Ottoor, "Bioimaging applications of carbon dots (C. dots) and its cystamine functionalization for the sensitive detection of Cr(vi) in aqueous samples," *J. Fluoresc.*, vol. 29, no. 6, pp. 1381–1392, 2019, doi: 10.1007/s10895-019-02448-3.

[5] Z. Fan, S. Li, F. Yuan, and L. Fan, "Fluorescent graphene quantum dots for biosensing and bioimaging," *RSC Adv.*, vol. 5, no. 25, pp. 19773–19789, 2015, doi: 10.1039/c4ra17131d.

[6] M. L. Liu, B. Bin Chen, C. M. Li, and C. Z. Huang, "Carbon dots: Synthesis, formation mechanism, fluorescence origin and sensing applications," *Green Chem.*, vol. 21, no. 3, pp. 449–471, 2019, doi: 10.1039/c8gc02736f.

[7] U. A. Rani, L. Y. Ng, C. Y. Ng, and E. Mahmoudi, "A review of carbon quantum dots and their applications in wastewater treatment," *Adv. Colloid Interface Sci.*, vol. 278, p. 102124, 2020, doi: 10.1016/j.cis.2020.102124.

[8] M. Han, S. Zhu, S. Lu, Y. Song, T. Feng, S. Tao, J. Liu and B. Yang, "Recent progress on the photocatalysis of carbon dots: Classification, mechanism and applications," *Nano Today*, vol. 19, pp. 201–218, 2018, doi: 10.1016/j.nantod.2018.02.008.

[9] K. W. Chu, S. L. Lee, C. J. Chang, and L. Liu, "Recent progress of carbon dot precursors and photocatalysis applications," *Polymers (Basel).*, vol. 11, no. 4, 2019, doi: 10.3390/polym11040689.

[10] J. B. Essner and G. A. Baker, "The emerging roles of carbon dots in solar photovoltaics: A critical review," *Environ. Sci. Nano*, vol. 4, no. 6, pp. 1216–1263, 2017, doi: 10.1039/c7en00179g.

[11] M. Z. Fahmi, D. L. N. Wibowo, S. C. W. Sakti, H. V. Lee, and Isnaeni, "Human serum albumin capsulated hydrophobic carbon nanodots as staining agent on HeLa tumor cell," *Mater. Chem. Phys.*, vol. 239, p. 122266, 2020, doi: 10.1016/j.matchemphys.2019.122266.

[12] V. Gude, "Synthesis of hydrophobic photoluminescent carbon nanodots by using L-tyrosine and citric acid through a thermal oxidation route," *Beilstein J. Nanotechnol.*, vol. 5, no. 1, pp. 1513–1522, 2014, doi: 10.3762/bjnano.5.164.

[13] L. Lu, C. Feng, J. Xu, F. Wang, H. Yu, Z. Xu and W. Zhang, "Hydrophobic-carbon-dot-based dual-emission micelle for ratiometric fluorescence biosensing and imaging of Cu^{2+} in liver cells," *Biosens. Bioelectron.*, vol. 92, pp. 101–108, 2017, doi: 10.1016/j.bios.2017.01.066.

[14] M. Bodik, P. Siffalovic, P. Nadazdy, M. Benkovicova, Z. Markovic, J. Chlpik, J. Cirak, M. Kotlar, M. Micusik, M. Jergel and E. Majkova, "On the formation of hydrophobic carbon quantum dots Langmuir films and their transfer onto solid substrates," *Diam. Relat. Mater.*, vol. 83, pp. 170–176, 2018, doi: 10.1016/j.diamond.2018.02.011.

[15] A. Talib, S. Pandey, M. Thakur, and H. F. Wu, "Synthesis of highly fluorescent hydrophobic carbon dots by hot injection method using Paraplast as precursor," *Mater. Sci. Eng. C*, vol. 48, pp. 700–703, 2015, doi: 10.1016/j.msec.2014.11.058.

[16] W. Shang, M. Ye, T. Cai, L. Zhao, Y. Zhang, D. Liu and S. Liu," Tuning of the hydrophilicity and hydrophobicity of nitrogen doped carbon dots: A facile approach towards high efficient lubricant nanoadditives," *J. Mol. Liq.*, vol. 266, pp. 65–74, 2018, doi: 10.1016/j.molliq.2018.06.042.

[17] L. Yan, Y. Yang, C. Q. Ma, X. Liu, H. Wang, and B. Xu, "Synthesis of carbon quantum dots by chemical vapor deposition approach for use in polymer solar cell as the electrode buffer layer," *Carbon N. Y.*, vol. 109, pp. 598–607, 2016, doi: 10.1016/j.carbon.2016.08.058.

[18] B. Cui, L. Yan, H. Gu, Y. Yang, X. Liu, C.-Q. Ma, Y. Chen and H. Jia, "Fluorescent

carbon quantum dots synthesized by chemical vapor deposition: An alternative candidate for electron acceptor in polymer solar cells," *Opt. Mater. (Amst).*, vol. 75, pp. 166–173, 2018, doi: 10.1016/j.optmat.2017.10.010.

[19] H. Yu, X. Li, X. Zeng, and Y. Lu, "Preparation of carbon dots by non-focusing pulsed laser irradiation in toluene," *Chem. Commun.*, vol. 52, no. 4, pp. 819–822, 2016, doi: 10.1039/c5cc08384b.

[20] Z. Zhu, S. Wang, Y. Chang, D. Yu, and Y. Jiang, "Direct photodissociation of toluene molecules to photoluminescent carbon dots under pulsed laser irradiation," *Carbon N. Y.*, vol. 105, pp. 416–423, 2016, doi: 10.1016/j.carbon.2016.04.047.

[21] A. P. Vijaya Kumar Saroja, M. S. Garapati, R. ShyiamalaDevi, M. Kamaraj, and S. Ramaprabhu, "Facile synthesis of heteroatom doped and undoped graphene quantum dots as active materials for reversible lithium and sodium ions storage," *Appl. Surf. Sci.*, vol. 504, p. 144430, 2020, doi: 10.1016/j.apsusc.2019.144430.

[22] N. J. Coville, S. D. Mhlanga, E. N. Nxumalo, and A. Shaikjee, "A review of shaped carbon nanomaterials," *S. Afr. J. Sci.*, vol. 107, no. 3/4, pp. 1–15, 2011, doi: 10.4102/sajs.v107i3/4.418.

[23] B. K. Mutuma, "Synthesis and characterization of solid, hollow, core-shell and worm-like carbon nanostructures for applications in organic photovoltaic devices and chemical sensors," PhD thesis, University of the Witwatersrand, Johannesburg, South Africa, 2016.

[24] B. K. Mutuma, B. J. Matsoso, K. Ranganathan, J. M. Keartland, D. Wamwangi, and N. J. Coville, "Generation of radical species in CVD grown pristine and N-doped solid carbon spheres using H2 and Ar as carrier gases," *RSC Adv.*, vol. 7, no. 34, pp. 21187–21195, 2017, doi: 10.1039/c7ra03142d.

[25] H. Xiong, M. A. Motchelaho, M. Moyo, L. L. Jewell, and N. J. Coville, "Fischer-Tropsch synthesis: Iron-based catalysts supported on nitrogen-doped carbon nanotubes synthesized by post-doping," *Appl. Catal. A Gen.*, vol. 482, pp. 377–386, 2014, doi: 10.1016/j.apcata.2014.06.019.

[26] B. J. Matsoso, K. Ranganathan, B. K. Mutuma, T. Lerotholi, G. Jones, and N. J. Coville, "Time-dependent evolution of the nitrogen configurations in N-doped graphene films,"

RSC Adv., vol. 6, no. 108, pp. 106914–106920, 2016, doi: 10.1039/c6ra24094a.

[27] R. Atchudan, T. N. Jebakumar Immanuel Edison, S. Perumal, R. Vinodh, and Y. R. Lee, "Multicolor-emitting carbon dots from Malus floribunda and their interaction with Caenorhabditis elegans," *Mater. Lett.*, vol. 261, p. 127153, 2020, doi: 10.1016/j.matlet.2019.127153.

[28] A. D. Faisal and A. A. Aljubouri, "Synthesis and production of carbon nanospheres using noncatalytic CVD method," *Int. J. Adv. Mater. Res.*, vol. 2, no. 5, pp. 86–91, 2016.

[29] A. C. Ferrari, "Raman spectroscopy of graphene and graphite: Disorder, electron-phonon coupling, doping and nonadiabatic effects," *Solid State Commun.*, vol. 143, no. 1–2, pp. 47–57, 2007, doi: 10.1016/j.ssc.2007.03.052.

[30] C. Russo, B. Apicella, and A. Ciajolo, "Blue and green luminescent carbon nanodots from controllable fuel-rich flame reactors," *Sci. Rep.*, vol. 9, no. 1, pp. 1–8, 2019, doi: 10.1038/s41598-019-50919-1.

[31] Z. H. Wen and X. B. Yin, "Excitation-independent carbon dots, from photoluminescence mechanism to single-color application," *RSC Adv.*, vol. 6, no. 33, pp. 27829–27835, 2016, doi: 10.1039/c5ra27172j.

[32] P. Roy, P. Chen, A. P. Periasamy, Y. Chen, and H. Chang, "Photoluminescent carbon nanodots : synthesis , physicochemical properties and analytical applications," vol. 18, no. 8, pp. 447–458, 2015, doi.org/10.1016/j.mattod.2015.04.005 .

[33] D. Wang, Z. Wang, Q. Zhan, Y. Pu, J.-X. Wang, N.R. Foster and L. Dai, "Facile and scalable preparation of fluorescent carbon dots for multifunctional applications," *Engineering*, vol. 3, no. 3, pp. 402–408, 2017, doi: 10.1016/J.ENG.2017.03.014.

[34] R. Bandi, B. R. Gangapuram, R. Dadigala, R. Eslavath, S. S. Singh, and V. Guttena, "Facile and green synthesis of fluorescent carbon dots from onion waste and their potential applications as sensor and multicolour imaging agents," *RSC Adv.*, vol. 6, pp. 28633–28639, 2016, doi: 10.1039/C6RA01669C.

[35] S. Pandey, A. Mewada, M. Thakur, A. Tank, and M. Sharon, "Cysteamine hydrochloride protected carbon dots as a vehicle for the efficient release of the anti-schizophrenic drug haloperidol," *RSC Adv.*, vol. 3, no. 48, pp. 26290–26296, 2013, doi:

10.1039/c3ra42139b.

[36] J. Gong, X. Lu, and X. An, "Carbon dots as fluorescent off-on nanosensors for ascorbic acid detection," *RSC Adv.*, vol. 5, no. 11, pp. 8533–8536, 2015, doi: 10.1039/c4ra13576h.

[37] A. Mewada, S. Pandey, S. Shinde, N. Mishra, G. Oza, M. Thakur, M. Sharon and M. Sharon, "Green synthesis of biocompatible carbon dots using aqueous extract of Trapa bispinosa peel," vol. 33, pp. 2914–2917, 2013, doi.org/10.1016/j.msec.2013.03.018.

[38] T. H. Mongwe, B. J. Matsoso, B. K. Mutuma, N. J. Coville, and M. S. Maubane, "Synthesis of chain-like carbon nano-onions by a flame assisted pyrolysis technique using different collecting plates," *Diam. Relat. Mater.*, vol. 90, pp. 135–143, 2018, doi: 10.1016/j.diamond.2018.10.002.

[39] S. Sarkar, D. Banerjee, U. K. Ghorai, N. S. Das, and K. K. Chattopadhyay, "Size dependent photoluminescence property of hydrothermally synthesized crystalline carbon quantum dots," *J. Lumin.*, vol. 178, pp. 314–323, 2016, doi: 10.1016/j.jlumin.2016.05.033.

[40] C. Xia, S. Zhu, T. Feng, M. Yang, and B. Yang, "Evolution and synthesis of carbon dots: From carbon dots to carbonized polymer dots," *Adv. Sci.*, vol. 6, no. 23, 2019, doi: 10.1002/advs.201901316.

[41] M. Tian, B. S. Liu, M. Hammonds, N. Wang, P. J. Sarre, and A. S. C. Cheung, "Formation of polycyclic aromatic hydrocarbons from acetylene over nanosized olivine-type silicates," *Phys. Chem. Chem. Phys.*, vol. 14, no. 18, pp. 6603–6610, 2012, doi: 10.1039/c2cp23309f.

[42] T. Bensabath, M. D. Le, H. Monnier, and P. A. Glaude, "Polycyclic aromatic hydrocarbon (PAH) formation during acetylene pyrolysis in tubular reactor under low pressure carburizing conditions," *Chem. Eng. Sci.*, vol. 202, pp. 84–94, 2019, doi: 10.1016/j.ces.2019.03.030.

[43] K. Ono, M. Yanaka, Y. Saito, H. Aoki, O. Fukuda, T. Aoki and T. Yamaguch, "Effect of benzene-acetylene compositions on carbon black configurations produced by benzene pyrolysis," *Chem. Eng. J.*, vol. 215–216, pp. 128–135, 2013, doi: 10.1016/j.cej.2012.10.085.

[44] R. Panickar, C. B. Sobhan, and S. Chakravorti, “Chemical vapor deposition synthesis of carbon spheres: Effects of temperature and hydrogen,” *Vacuum*, vol. 172, p. 109108, 2020, doi: 10.1016/j.vacuum.2019.109108.

[45] A. A. Deshmukh, S. D. Mhlanga, and N. J. Coville, “Carbon spheres,” *Mater. Sci. Eng. R Reports*, vol. 70, no. 1–2, pp. 1–28, 2010, doi: 10.1016/j.mser.2010.06.017.

CHAPTER 5: REMOVAL OF CARBON DOTS SURFACE FUNCTIONAL GROUPS BY ANNEALING

Evolution of large-area reduced graphene oxide nanosheets from carbon dots via thermal treatment

Lerato L Mokoloko[a], Boitumelo J Matsoso [b, c], Roy P. Forbes[a], Dean H. Barrett [a, d], Beatriz D. Moreno[e], and Neil J Coville[a]*

Abstract

Herein, we reveal a novel and facile pathway for the synthesis of reduced graphene oxide (rGO) from annealed carbon dots (CDs). The CDs (~ 2.5 nm) were synthesized from *L*- ascorbic acid via microwave synthesis at 180 °C, after which formation of rGO nanosheets (≥ 40% yield) was achieved through 10 min annealing of CDs under N_2 from 250-700 °C. The TEM images showed that the CDs are initially transformed into an accreted sphere-like turbostratic carbon (d = 0.3390 nm) after annealing at 250 °C, and finally to a layered 'graphene-like' nanomaterial (length ≈ 0.2-2.6 μm) at thermal treatment temperatures ≥500 °C. The transformation into rGO was evidenced by the decrease in the oxygenated functional group content and removal of the oxygen functional groups facilitated the growth of rGO nanosheets through the interconnection of the C-C bonds at the defected CD edges. The FTIR, PL, PDF, and ^{13} C NMR spectra confirmed the loss of functional groups after annealing at 700 °C. Raman, and in particular PDF data, confirmed and rationalised the growth and evolution of the structured carbon domains with increasing annealing temperature. A mechanism to rationalize the data is proposed.

Keywords: carbon dots; microwave reaction; thermal treatment; reduced graphene oxide; chemical vapour deposition

*Corresponding author. Tel: 27 11 717 6738 863-2685. E-mail: neil.coville@wits.ac.za (Neil Coville)

5.1 Introduction

Carbon dots (CDs), which includes graphene quantum dots (GQDs), carbon nanodots (CNDs), and polymer dots (PDs), are an interesting new group of fluorescent nanomaterials that can be derived from many carbon-based precursors [1]–[4]. CDs are described as zero-dimensional (0-D) carbon nanostructures of < 10 nm in size. Their structural morphology is defined by the small number of layers of ordered and/or disordered graphene sheets with sp^2/sp^3 carbon terminal sites [4]–[6]. The differently hybridized carbon terminal sites enable modulation of the properties of CDs through the attachment of a variety of surface functional groups [4]–[8]. Generally, CDs have been found to have interesting properties such as tuneable fluorescence, good dispersibility, low toxicity, biocompatibility and extensive surface chemistry [4]–[7]. Owing to their diverse properties, CDs are of technological importance in a variety of fields and have recently become a widely studied carbon allotrope [4], [9]. As such, CDs have been exploited in a range of applications including biosensing and bioimaging [10]–[12], photocatalysis [13]–[15], electrocatalysis [15]–[17] and in optoelectronic devices [18], [19].

Due to the ever-growing demand for the use of CDs for next generation electronics, two generic synthesis approaches have been developed for the preparation of these carbon nanostructures [20], [21]. They are the "top-down" and the "bottom-up" approaches. The "top-down" approach involves breaking down large carbon structures such as carbon nanotubes (CNTs), graphene, carbon fibres and fullerenes to make CDs. The "bottom-up" approach involves building up small CDs from molecular sources such as ascorbic acid, carbohydrates and citric acid to large structures [20], [21]. The "bottom-up" methods are preferred since they are environmentally friendly, simple, cost effective and useful for large scale synthesis [3], [22]. Interestingly, reports have shown that CDs can be used to produce other carbon nanostructures such as graphene-based nanosheets (GNSs) via the modified "bottom up" process, however, these associated synthetic routes have rarely been described [23]–[26].

Graphene nanosheets (GNSs) that include pristine graphene, graphene oxide (GO) and reduced graphene oxide (rGO) [27], are well-known for their extraordinary structural, mechanical, thermal, and optical characteristics and have been studied in the electronics [28], [29], biomedicine [30]–[34] and construction fields [35]. Furthermore, rGO plays a significant role as an intermediate product in the transformation of GO to pristine graphene. It also has properties similar to those of pristine graphene when compared to other GNSs [36], [37]. As such, rGO has been

used as an alternative for pristine graphene formation due to the high cost associated with pristine graphene synthesis [36], [37]. Although GNSs have been known for many years, their synthesis can be challenging. The synthesis of GNSs includes the "top-down" approaches such as mechanical, chemical, thermal, electronical and solvent-/surfactant-based exfoliation of graphite, and the "bottom-up" growth from molecular substrates using the CVD method and graphitization of silicon carbide (SiC) [38]–[44]. Many of these syntheses approaches still suffer from drawbacks such as the use of expensive substrates and equipment as well as the use of high volumes of toxic solvents and surfactant molecules. There is therefore a need for other alternative methods for the production of GNSs using simple, cost effective and environmentally friendly methods [40].

In this study, CDs were synthesized by a simple single-step "bottom-up" microwave-assisted hydrothermal method using *L*-ascorbic acid as a carbon source. The CDs obtained were highly hygroscopic, due to the absorption of moisture by the surface functional group [45], [46]. During thermal deoxygenation of CDs, the CDs self-assembled to form rGO. The reaction products were monitored by a variety of characterization techniques (including microscopy and spectroscopy), and the data compared with literature reports detailing the synthesis of rGO from the chemical reduction of graphene oxide. The CDs to rGO conversion observed in this study was also compared with the work by Hu et al. who reported the transformation of CDs to 3-D porous carbon framework (PCF) material after heat treatment of the CDs at elevated temperatures (> 400°C) [26]. Furthermore, a mechanism for the conversion was also proposed for the rGO produced in this study.

5.2 Experimental section

5.2.1 Reagents

L-ascorbic acid (analytical grade) was purchased from Sigma-Aldrich, South Africa, and used as received. Distilled water was used as a solvent in the experiments. Ultra-high purity nitrogen gas (N_2, 99.99 %) was supplied by Afrox, South Africa.

5.2.2 Sample synthesis

CDs were prepared using a microwave-assisted hydrothermal reaction method reported by Gong et al. [47], but with modification. An Anton-Paar Multiwave 3000 SOLV microwave system with maximum power output of 1400 W and a controlled pressure of 60 bar was used.

In a typical experimental reaction set- up, *L*-ascorbic acid (2.4 g) and 240 mL distilled water were mixed in a 500 mL beaker. Thereafter, 4 ×60 mL of this homogeneous reaction mixture was transferred into 4 ×100 mL microwave reaction vessels. The mixture was irradiated for 10 min at 600 W to attain an infrared temperature of 180 °C. During synthesis, the colour of the solution changed from colourless to dark brown, indicating carbonization. The resulting solution was treated in a centrifuge at 15000 rpm for 15 min to separate the precipitates (large carbon agglomerates) from the supernatants. This precipitated material, made of aggregates of spheroidal carbons, was not further investigated. A TEM image of this product is given in **Figure S5.1**. Thereafter, the supernatants were filtered through a 0.22 μm polytetrafluoroethylene (PTFE) filter. The purified CDs solution was placed in a rotary evaporator to remove water, and subsequently dried in an oven (60 °C) for 3 days to obtain the CDs (28 % yield). The reaction was repeated multiple times until a desired amount of product was obtained.

For the thermal reaction studies, 0.5 g of the CDs were loaded into a quartz boat and annealed at different temperatures (200, 250, 300, 400, 500, 600 and 700 °C) in a CVD furnace for 10 min under N_2 (100 sccm). After the annealing was completed, the furnace was cooled to room temperature in N_2. In each case, the solid products obtained were crushed using a pestle and mortar to give a powdered layered carbon material. For simplicity, the samples will be referred to as T200, T250, T300, T400, T500, T600 and T700 for samples annealed at 200, 250, 300, 400, 500, 600 and 700 °C, respectively. The un-annealed CDs will be referred to as pristine CDs (pCDs). The yields obtained for T200, T250, T300, T400, T500, T600 and T700 are shown in **Table 5.1** below. After annealing, the samples were characterized.

Table 5.1: The sheet sizes and % yields of T200-T700 samples.

Sample name	Approx. sheet size (μm)	% yield[a]
T200	-	78
T250	-	62
T300	0.352 ± 0.104 × 0.24 ± 053	55
T400	1.44 ± 0.199 × 0.82 ± 0.13	42

T500	$0.953 \pm 0.070 \times 0.525 \pm 0.017$	41
T600	$2.597 \pm 0.143 \times 1.65 \pm 0.131$	40
T700	$1.71 \pm 0.104 \times 0.909 \pm 0.0577$	40

[a]*Yield after annealing at different temperatures.*

5.2.3 Sample characterization

Morphology studies were conducted using an FEI G2 TECNAI Spirit T12 transmission electron microscope (TEM), with electrons accelerated at 120 kV, and a JEOL JEM 2100 high resolution trans- mission electron microscope (HRTEM) fitted with a LaB6 gun for high resolution imaging. A lacy carbon grid was used in the TEM studies. A Veeco Di-3100 atomic force microscopy (AFM) was used in tapping mode. Scanning electron microscopy (SEM) analysis was performed using a ZEISS SIGMA 03–39 FESEM at 20 kV. The Fourier transform-infrared (FTIR) spectra of the samples were collected (128 scans) using a Brucker TENSOR 27 FT-IR spectrometer, scanning between 4000 and 600 cm^{-1}. ^{13}C solid-state nuclear magnetic resonance (NMR) spectra were measured using a Bruker-500 MHz NMR spectrometer at a spinning frequency of 62.5 kHz (4.0 μs, 115 W). X-ray photoelectron spectroscopy (XPS) analysis was conducted using a Physical Electronics Quantum 2000 equipped with a monochromatic Al Kα excitation source operating at 1486.7 eV. Powder X-ray diffraction (PXRD) patterns were collected on a Bruker D2 Phaser X-ray diffractometer equipped with a $CuK_{\alpha 1/2}$ radiation ($\lambda_{K\alpha}$= 0.15406 nm) source and a Lynxeye detector. Samples were scanned over the 2θ range from 10 - 90 ° 2θ using a 0.026 ° step size. Raman spectra and solid-state photoluminescence spectroscopy (PL) data were collected using a Horiba LabRAM HR micro-Raman spectrometer (frequency double Lexel SHG argon ion laser). Silica was used as a substrate. Raman measurements were done with a 514.5 nm (green) laser and the PL measurements were done with a 244 nm excitation wavelength. Total scattering data were collected on the Brockhouse high-energy wiggler beamline at the Canadian Light Source using a wavelength of λ= 0.2081 Å and a PerkinElmer XRD1621 area detector placed 160 mm after the sample. The data were processed using GSAS-II [48]. The Q_{max} used to produce the PDF of the measured samples was 23.4 $Å^{-1}$. The instrumental resolution parameters Qdamp and Qbroad, as defined in PDFgui software, were determined by fitting a Ni powder standard measurement.

Further data analysis was done using the xPDFsuite [49]. A PerkinElmer STA6000 analyser was used to monitor the thermal stability of the samples from 35 to 900 °C at a heating rate of 10 °C/min, in air at 10 sscm with N_2 as the purge gas.

5.3 Results and discussion

5.3.1 Morphology evaluation.

Carbonization of *L*-ascorbic acid to CDs using microwave-irradiation is amongst the most common synthetic methods used to make CDs in the "bottom-up" synthetic approach [22]. This method possesses environmentally friendly attributes such as direct heating and a relatively short synthesis time [50]–[52]. Pristine CDs (pCDs) tend to be hygroscopic, due to their hydrophilic functional groups [45], [46]. Despite the 3-day period used to dry this sample, it was still obtained as a gel-like solid. The pCDs were then subjected to annealing for 10 mins at temperatures between 200- 700 °C to obtain the products, T200-T700. The aim of this treatment was to remove the moisture and/or surface functional groups and obtain solid CDs. The pCDs before annealing were analysed using TEM and HRTEM. From **Figure 5.1a** the TEM images revealed quasi-spherical CDs with average particle sizes of 2.5 ± 0.2 nm, and a very narrow particle size distribution range between 1 and 4 nm (see **Figure 1a** and **Figure S5.2a**) , comparable to those previously reported [47]. The HRTEM images in **Figure S5.2b** also indicated also indicated that the CDs exhibited lattice fringes with a *d*-spacing of 0.204 nm, similar to that of the (101) plane lattice of graphite [53], [54]. The CDs synthesized in this study were classified under the crystalline quasi-type CDs as defined by Verma et al. [55] due to their size, *d*-spacing and low thermal stability.

In order to study the effect of temperature on the CDs, the pCDs were then heated to 200 °C (T200, **Figure S5.3**). However, little change was noted in their morphology and the size of the nanoparticles as the TEM micrographs showed that the T200 samples were similar to the pCDs. When the pCDs were heated to 250 °C, a drastic change in the morphology of the CDs (T250) was observed. At this temperature, the pCDs accrete and formed quasi-spherical nanoparticles, as seen in **Figure 5.1b)** and **S5.4a)**. The particle sizes of T250 could not be determined because the material was accreted. The material revealed lattice fringes, with a *d*-spacing of 0.3390 nm, corresponding to the lattice spacing of a turbostratic graphite [56]. On further heat treatment of the CDs from 300 °C to 700 °C, the TEM images of the T300-T700 showed that the pCDs were transformed into large area layered carbonaceous nanostructures (see **Figure 5.1c)**, **5.1d)**,

Figures S5.4b, **c** and **S5.5a-c**). In particular, the T300-T400 materials appeared to be multi-layered carbon nanomaterials stacked on top of each other, with some of the accreted quasi-spherical nanoparticles embedded in between the layers and/or within the layered material (**Figure 5.1c)** and **Figure S5.5a**). Most importantly, the T500-T700 samples revealed that the quasi-spherical nanoparticles had fully developed into a layered material (**Figure 5.1d)** and **S5.5b, c**). For example, the HRTEM micrographs of the T700 sample showed no separation of layers and no visible lattice fringes (**Figure S5.4c**). To determine the possibility that the layer formation was due to the presence of residual starting *L*-ascorbic acid precursor, a reaction at 700 °C was performed, either with *L*-ascorbic acid or with *L*-ascorbic acid mixed with pCDs (50/50) under the same reaction condition used to synthesize T700. The TEM images (**Figures S5.5d, e**) of the resulting product showed that the morphology was different from the large area layered carbonaceous nanostructures observed in T700. The results indicated that the *L*-ascorbic acid actually hindered the formation of the layered nanostructures from pCDs. The results showed that evolution of the layered nanostructured from pCDs was facilitated by the heat treatment of the pCDs through the removal of functional groups (see below). The sheet sizes of samples are reported in **Table 5.1**. The data showed that the nanosheets produced in these experiments were fairly large, typically with length 0.2-2.6 μm, and did not vary significantly in size for temperatures > 400 °C.

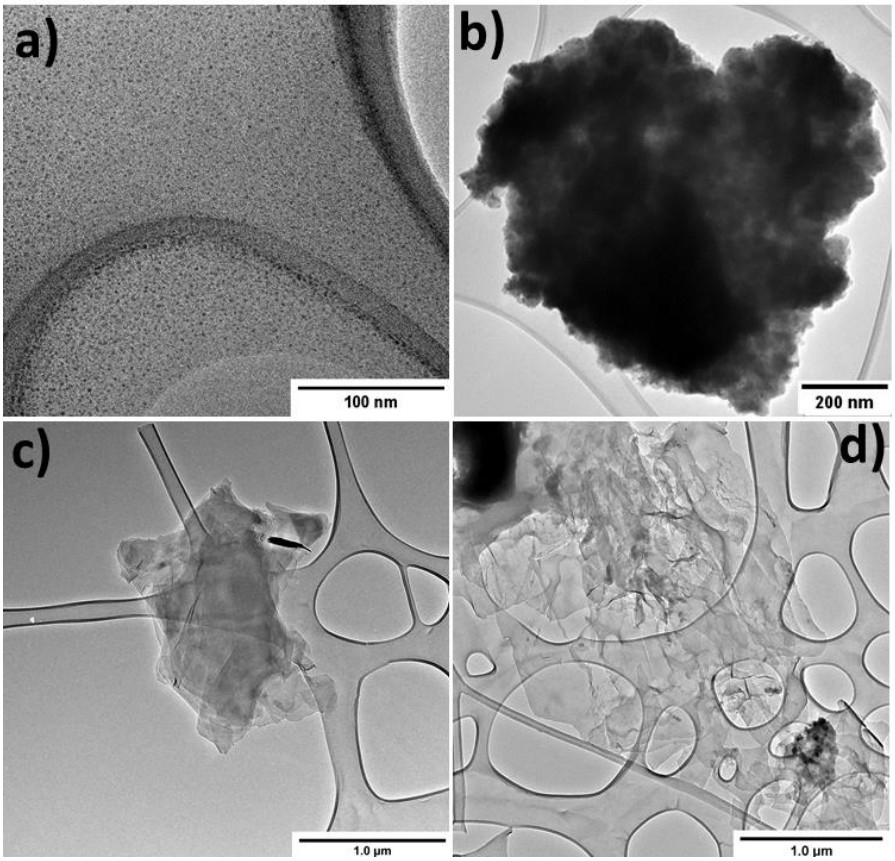

Figure 5. 1: The TEM images of the a) pCDs, **b)** T250, **c)** T400 and **d)** T700 samples.

It is interesting to compare these products with a related study by Hou et al. [26] in which CDs were produced from acetone/NaOH solutions. The authors also observed a conversion of CDs to sheet like carbons, but that the carbons did not form layered sheets but 3-D porous carbon frameworks (PCFs).

The SEM images of T250, T400 and T700 are shown in **Figure S5.6**. The SEM images showed that the materials contained layered nanosheets. The T250 image (**Figure S5.6a**) showed a layered material with a rougher surface texture as compared to samples T400 and T700. This may be attributed to the accreted quasi-spherical structure that formed before the material was fully transformed into layers as observed in the TEM image (**Figure 5.1b**). AFM surface topography profiles in **Figure S5.7** confirmed the quasi-spherical nanoparticles embedded surfaces of the sheets, with loss of CDs at the higher temperatures.

5.3.2 Changes in the functional group content.

FTIR analysis (**Figure 5.2a**) was performed to gain insight into the type/number of surface functional groups that were removed from the pCDs during the formation of the layered materials. The data showed a broad band at 3287 cm^{-1} that indicated the presence of an O-H stretch, due to residual water in the sample, and also likely the presence of the hydroxyl-functional groups on the carbon surface [47], [57]. The low intensity bands at ~3000 cm^{-1} and between 2986 and 2872 cm^{-1} were attributed to the aromatic and aliphatic C-H stretches, respectively. The band at 1739 cm^{-1}, was ascribed to the C=C bending mode in aromatic rings. The band at 1610 cm^{-1} suggested the presence of the carboxylic acid, C=O group. The peaks between 1215 and 970 cm^{-1} corresponded to the asymmetric (alcohol C-O-H) and symmetric (ether C-O-C) stretching bands, respectively. After heat treatment, the O-H band for the T200-T700 samples disappeared, and this was evident from the formation of 'dry' solid samples. Moreover, the O-H, C=O, C-O-C bands decreased dramatically for T300-T500, signifying the removal of oxygen functional groups, while sample T600 and T700, showed little to no bands associated with any functional group.

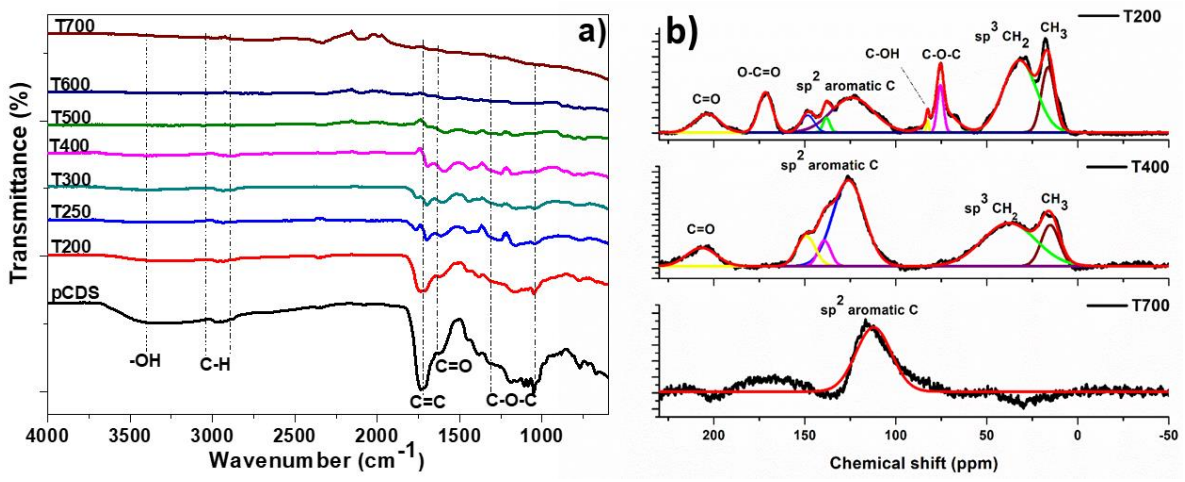

Figure 5. 2: a) FTIR spectra of samples pCDs, T200-T700 and **b)** ^{13}C NMR spectra (deconvoluted) of the T200, T400 and T700.

To further understand the role of temperature on the surface functional groups present in these samples, ^{13}C solid-state NMR spectra were recorded on the T200, T400 and T700 samples (see **Figure 5.2b**); these are the 3 samples that showed large changes in morphology with temperature. The spectra were deconvoluted and the contribution of each deconvolution peak to the

overall spectrum is summarized in **Table 5.2**. Note that the aromatic region (sp^2 carbons) is observed as a broad peak indicating C atoms in a range of different chemical environments.

Significant changes in functional groups with temperature were observed. For example, the T200 sample showed peaks at *ca.* δ170, 75, and 67 ppm, corresponding to the O-C=O, C-OH and C-O-C, respectively [58]. These peaks were not observed in the T400 spectrum. This indicated that annealing removed the O-C = O, C-OH and C-O-C functional groups from the pCDs surface at the lower temperatures. Since the aliphatic CH_2 and the CH_3 content remained similar (*ca.* 48 % to 40 %), while the aromatic content increased (*ca.* 27 % to 52 %), this suggests that the major source of the increased aromatic content were from the carbons containing the functional groups. Interestingly, when the pCDs were further annealed to 700 °C, the only prominent broad peak was found at *ca.* δ117 ppm, corresponding to sp^2 aromatic C. The trend observed in these spectra showed some similarities to those observed when GO is converted to rGO [59].

Table 5.2: Chemical shift assignment and main peak estimated percentage abundance.

Sample	Chemical shift (ppm)	Functional group	Estimated amount (%)
T200	203	C=O	6
	170	O-C=O	8
	149-123	Aromatic C	27
	75	C-OH	10
	67	C-O-C	1
	36	CH_2	35
	17	CH_3	13
T400	205	C=O	8
	160-103	Aromatic C	52
	36	CH_2	30
	17	CH_3	10
T700	107	Aromatic C	100

XPS data confirmed the presence of the T200, T250, T400 and T700 samples surface functional groups. The expanded XPS plots for C1s and O1s are presented in **Figure S5.8**, while **Table S5.1** shows the peak positions and their relative percentage atomic concentrations. For T200, C1s was deconvoluted into C=C, sp^3 C −C, C-O (from C-O-C/C-OH) and O-C = O with binding energies at 284.79 eV, 285.52 eV, 286.83 eV and 288.82 eV, respectively [57]. Similar peak positions were obtained for T250, T400 and T700, but the peak intensities varied with temperature. In particular, there was an increase in the C=C and a decrease in C-O content as the annealing temperature was increased. The atomic ratio of carbon to oxygen (C/O) quantified by XPS was calculated to be 3.00, 3.36, 4.94, and 5.55 for T200, T250, T400 and T700, respectively. This is consistent with the increase in the estimated percentage abundance obtained from the ^{13} C NMR spectrum (**Table 5.2**).

In summary, the TEM, FT-IR, ^{13}C NMR and XPS results show that there is a correlation between the reduction in oxygen functional groups on the surface of the pCDs that is related to the changes in morphology leading to the formation of the layered structures.

5.3.3 Structural changes.

Powder XRD studies by Yadav et al. have shown that a reduction in oxygen functional groups can be accompanied by a shift of the GO peak from ca. 10 ° 2θ, to a graphitic (002) peak at *ca.* 26° 2θ for rGO [60]. This implies that when graphitization takes place, oxygen moieties are thermally removed from the carbon surface and this suggests that similar data should be seen as the CDs convert to rGO.

The transformation of the pCDs as a function of temperature were evaluated by recording PXRD patterns of the products, and the results are presented in **Figure 5.3**. The pCDs PXRD pattern showed a broad feature *ca.* 18 ° 2θ that has previously been shown to be typical of amorphous carbon nanomaterials and is associated with the (002) peak of disordered graphite [61]. The same feature was found to have broadened in the T200 sample when compared to pCDs. The PXRD of the T300 sample showed further broadening of the feature. This was also observed in the T400 sample, and there was a shift in position of the feature from *ca.* 18 ° to *ca.* 21 ° 2θ. The shift in peak position coincided with the removal of oxygen functional groups, as seen in the FTIR, ^{13}C NMR and XPS spectra [62] and also the change in morphology of the samples. In the case of the T500, T600 and T700 samples, the major peak shifted from

ca. 21 ° to *ca.* 24 ° 2θ, while the appearance of an additional smaller broad feature at *ca.* 14 ° 2θ was noted. The small peak at *ca.* 43 ° 2θ was also observed in these three samples. Prior literature examples have shown that the occurrence of these features and the shifts that are observed in the relative 2 θ positions are due to the conversion of GO to rGO [62]–[66]. The small sharp peak at *ca.* 30 ° in T500-T700 samples has also been reported previously when GO is converted to rGO [64], [66], but its identity is not known. Moreover, the feature at *ca.* 14 ° 2θ is usually seen in rGO when it is synthesized by the reduction of GO and broadly corresponds to the graphite oxide (001) plane [64].

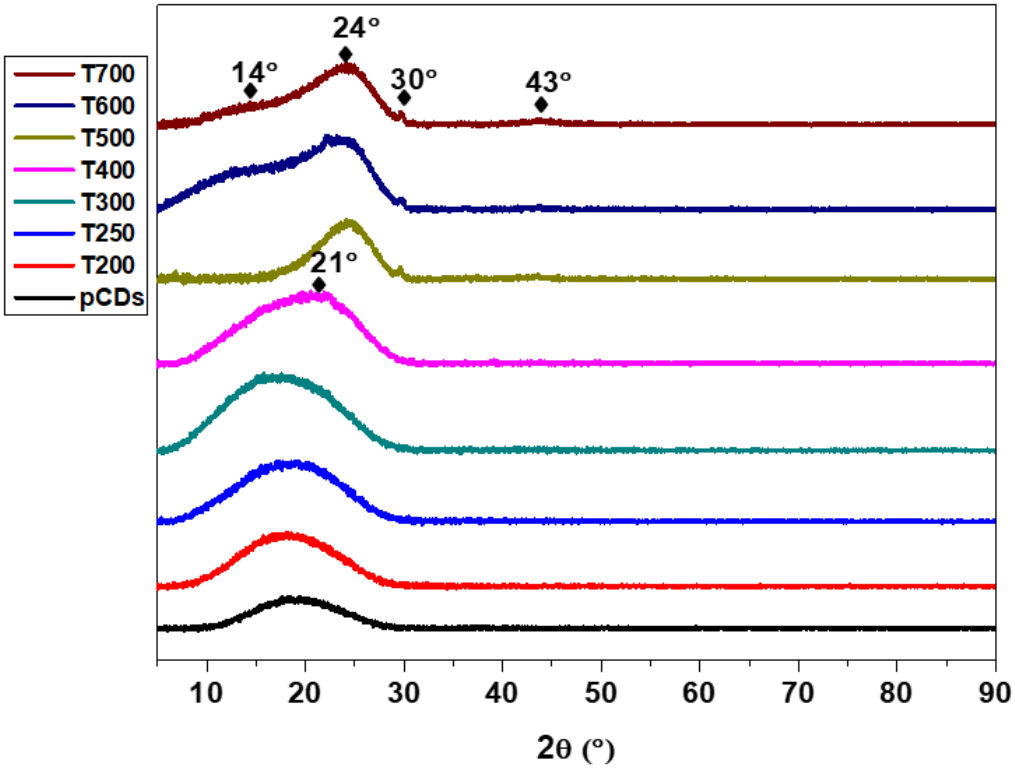

Figure 5. 3: Powder XRD patterns for samples pCDs and T200-700.

Raman spectra were measured to obtain further information about the structural properties of the pCDs and annealed samples. Carbon nanomaterials are mainly characterized by two distinct peaks, namely the G (~1600 cm^{-1}) and D peak (1300 cm^{-1}), as well as some minor peaks; the 2D (~2700 cm^{-1}) and the D + G (~2900 cm^{-1}) overtones [67]–[69]. The Raman spectra shown in **Figure 5.4** and **Table S2** summarizes the peak positions as well as the I_D/I_G ratios of the material. In the case of pCDs and T200 samples, the Raman modes could not be characterized. This is associated with photoluminescence excitation of the carbon (see PL data in **Figure S5.12**) by the Raman radiation source. However, on heating the samples to 300 °C and 400 °C,

the spectra for the T300 and T400 samples revealed the presence of a small G peak at *ca.* 1600 cm^{-1}. The inclined baseline indicated that these materials still contained some fluorescence properties that are associated with the pCDs, from which the non-florescent carbons were formed, thus making quantification of the Raman spectra very difficult. However, the spectra of the T400 to T700 samples showed the D band (~1350-1380 cm^{-1}), the G band (1590-1598 cm^{-1}) and a 2D peak over- lapping with the D + G overtones. Additionally, a band associated with diamond-like dangling bonds (∗, ~1150 cm^{-1}) was evident, an indication of growth of in-plane two dimensional structures. The first order Raman spectra were peak fitted to reveal the presence of more defect-sensitive bands such as the dangling diamond-like bonds (TPA, ~1204-1230 cm^{-1}) as well as the vibrational modes corresponding to the presence of amorphous carbon domains (A band, ~1460-1501 cm^{-1}), either around the graphitic carbon grain boundaries, or in between the layered carbon nanostructures [70], [71]. The values of the defect density ratios (I_D/I_G) were > 1 (**Table S5.2** and **Table S5.3**), an indication of the low degree of graphitization with increasing annealing temperature. This can be ascribed to the structural changes associated with the realignment of the carbon lattice upon formation of larger graphitic domains. However, the reduction in the ratio corresponding to the amount of the amorphous domains (I_A/I_G) with increased annealing temperature was suggestive of the improvement of the structure of the layered carbonaceous structures. This implied that the higher annealing temperature removed the amorphous carbons and facilitated the linking of the CDs to the defective sites on the layered carbonaceous structures. The linking and growth of bigger layered carbon domains was further shown by the increasing ratio of the dangling diamond-like carbons (I_{TPA}/I_G) to ~0.55. Moreover, inter-linking of pCDs was observed to generate defective sites as seen by the relatively large values for the defect density per square centimetre (N_D , **Table S5.3**) as well as the decrease in the sizes of the sp^2 crystallites (L_a, **Table S5.3**) [68]. Additionally, a blue shift was observed in the graphitic G-band with increasing annealing temperature (**Figure S5.9**). These phenomena were attributed to the compressive strain on the C-C bonds with the carbon lattice due to the formation of more defects and/or the lateral growth of the carbon domains [44], [72].

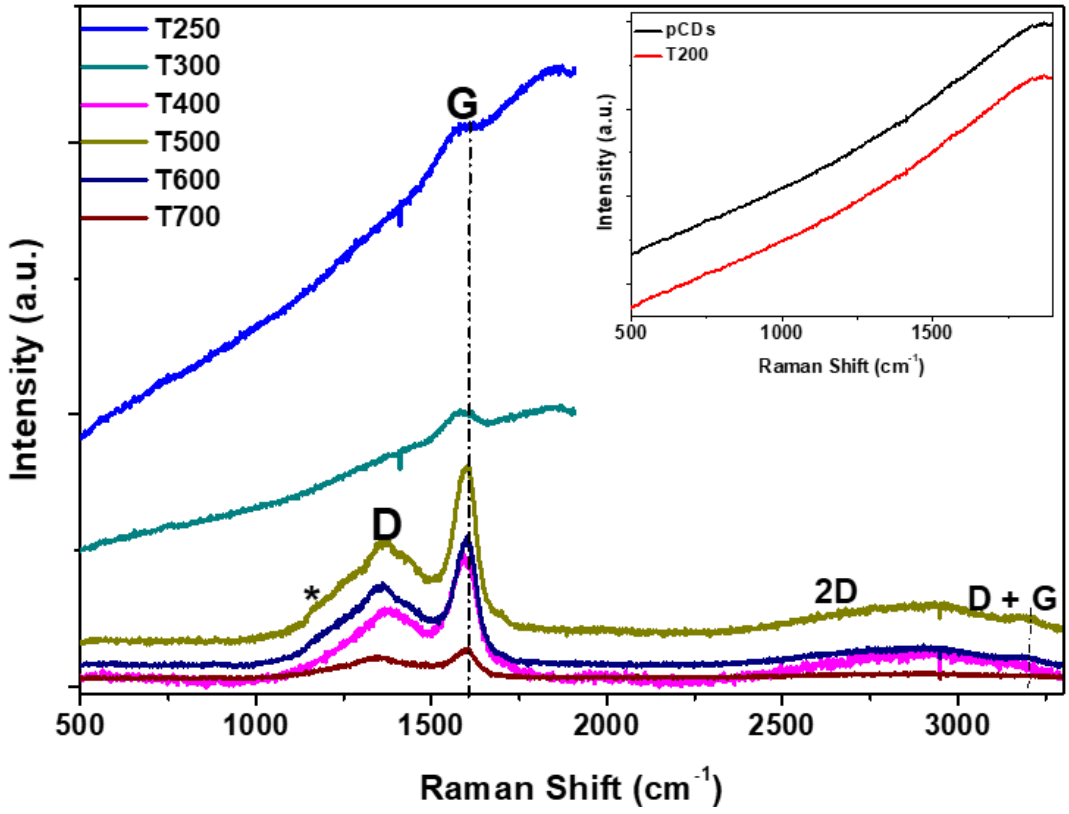

Figure 5. 4: Raman spectra of samples T250-T700 samples. Inset: Spectra of pCDs and T200 samples.

Pair distribution function (PDF) experiments were conducted to examine the local structure of the pristine and annealed CDs. The resulting PDFs are shown in **Figures 5.5** and **S5.10**, and the fitting parameters in **Figure S5.11** and **Table S5.4**. **Figure S5.10** shows the PDFs of pristine CDs (CDs), and samples annealed at 250, 400 and 700 °C (i.e., T250, T400 and T700) to 40 Å. All of the PDFs, except the T400 sample, show no significant structural order past 10 Å corresponding to both intra and interlayer interactions. In the case of the pCDs and T250, the small domain sizes seen in the HRTEM would account for this lack of medium to longer range order. Sample T400 however, showed a marked increase in the structural coherence extending over the entire PDF range up to 70 Å. For T400, TEM images showed the material contained multi-layered carbons stacked on top of each other, with some of the accreted quasi- spherical nanoparticles embedded in between the layers and/or within the layered material resulting in greater 3-D coherence with respect to the pCDs and T250 samples.

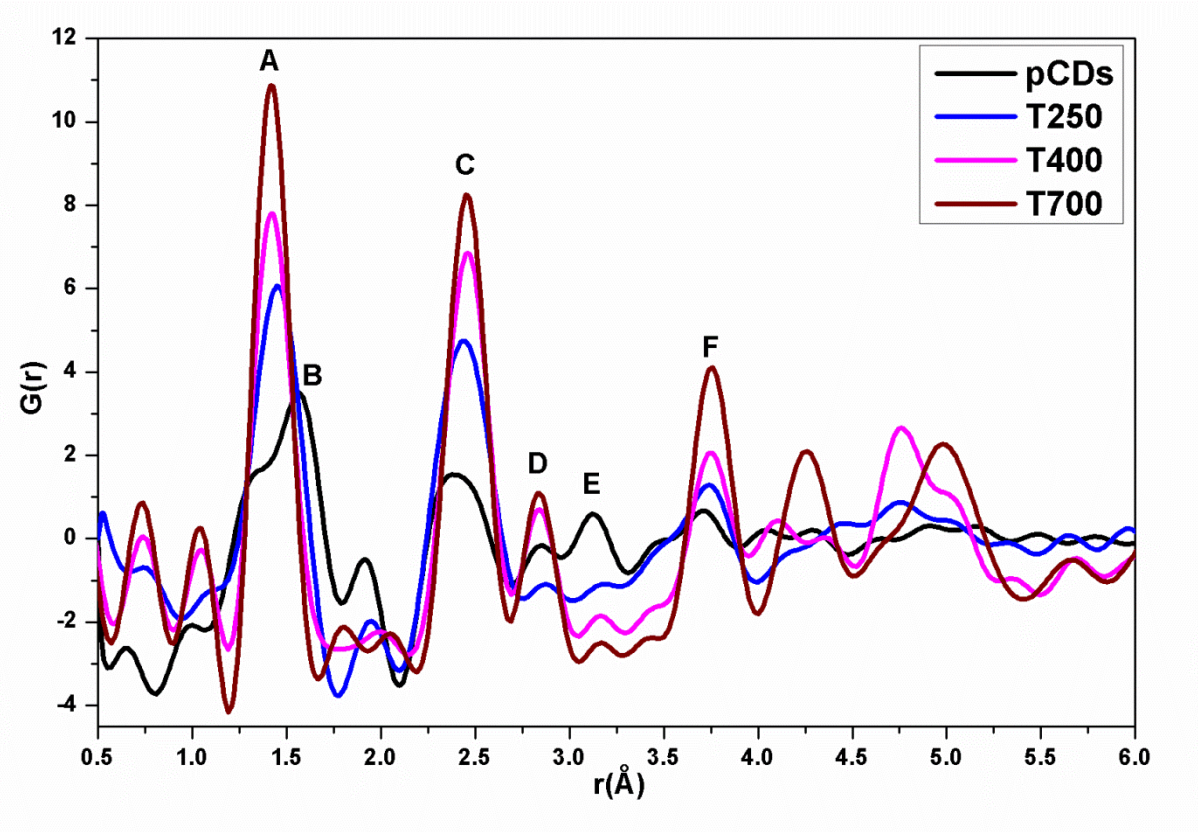

Figure 5. 5: Zoomed region of PDFs of pCDs, T250, T400 and T700.

Figure 5.5 shows a zoomed in region of the PDFs to 6 Å. This region of the PDF relates to the in plane carbon structure [73]. The increasing peak intensity (peaks A, B, and F) and reduction in the FWHM, with increase in annealing temperature, indicates an increase in the uniformity of the C-C bond distances. This is expected once the 1-D sheets are formed and functional groups have been removed from the structure and with them, electron withdrawing oxygen groups. Further, as the graphene sheets are formed a reduction in strain occurs from a reduction in the curvature of the surface from the elimination of the spherical domains.

The PDF of pCDs, peaks B and E give information about the structure of the starting pCDs material. Peak B corresponds to sp^3 carbon functional groups in a diamond type structure with a nearest neighbours bond length of 1.54 Å [74]. The broad shoulder occurring from peak A, extends to lower r and shows that some of the C-C bond lengths are reduced due to electron withdrawal from electronegative oxygen-containing functional groups. As these functional groups are removed as the annealing temperature increases, from 250 to 400 °C, the shoulder narrows and intensifies into peak A as the C-C distances become uniform as seen in peak A (sp^2 C). Peak A corresponds to the C-C nearest neighbour distance in graphite for the C=C

bonds with d = 1.42 Å [73]. As the annealing temperature is increased (≥ 250 °C), the tetragonally bonded sp^3 C groups are converted to sp^2 graphitic structures as shown by the conversion of peak B to A. Finally, peak E at 3.2 Å, noted in the pCDs, corresponds to the inter-layer atomic correlations, i.e. the lattice spacing of turbostratic graphite [56]. This peak reduces as the temperature is increased and as layered carbonaceous nanostructures are formed.

The peaks positioned at the real space distances of 1.41 (A), 2.48 (C) and 2.84 Å (D), respectively, exactly match the in-plane carbon-carbon bond distances in the aromatic-type ring of graphite [75]. The intensities of these three peaks increase as the annealing temperature increased from 250 to 700 °C, indicating an increase of the graphene phase order and coherence with increasing annealing temperature as well as a normalization of the bond distances once functional end groups were removed.

The third peak at 2.84 Å (D), is double the first C-C distance, and corresponds to the second, long diagonal in the carbon hexagon. If the carbon plane was buckled, this third peak would not be exactly twice the bond distance of the first one. However, this peak is broadened in the pristine sample showing that bond length distortions that occur may arise from the presence of oxygen containing electron withdrawing end groups that have not yet been eliminated. The G(r) peaks for A, C, D, and F are narrower (reduced FWHM) for T700 compared to T400 and are found at the expected graphite bond distances [76]. These peaks correspond to the in plane carbon structure, with reduced FWHM indicating less disorder and therefore less defects, for T700. This is expected as the structure grows and rearranges itself once functional groups are removed under annealing conditions.

A distinct feature of all three experimental PDFs for the annealed samples is that they have no peak at a real space distance of 3.4 - 3.5 Å where the interlayer atomic correlations in graphite are expected. Instead, the fourth peak (F) in the experimental PDFs appears at 3.75 Å, which is the subsequent in-plane C-C bond distance in graphite [75]. This is expected as the quasi nano-spherical domains are converted into 1D sheet like structures where no interlayer atomic correlation are expected.

These results further illustrate how the surface oxygen functional groups affect the structure of the produced nanosheets. The data suggests that the nanosheets are formed by the interlinking and growth of the carbon domains accompanied by the removal of surface oxygen functional groups. This process can be referred to as the "bottom-up" synthesis of rGO from pCDs. One

might expect the interlinking of carbons to form C-C bonds would remove defects in the carbon planes; however, these defects were not totally removed. A similar effect was observed in the rGO produced via the conventional "top-down" synthesis, i.e. from graphite to GO to rGO. The thermal reduction of GO also produced rGO with a defected surface [60].

5.3.4 Optical properties.

Changes in the optical properties of the samples as a function of thermal annealing were studied using photoluminescence (PL) spectroscopy, as shown in **Figure S5.12**. The pCDs and T200 samples showed a peak in the near IR region with a peak maximum at 631 nm [77]. The peak intensity was significantly reduced as the temperature was increased from 200 °C to 250 and 300 °C. For temperatures > 300 °C (sample T400-T700), the photoluminescence excitation was completely lost. This was be ascribed to the removal of the surface functional groups that played a significant role in the PL excitations of the materials.

5.3.5 Thermal properties.

Numerous research reports have indicated that graphitic carbon decomposes in air to give CO and CO_2 at temperatures above 700 °C, while carbonaceous materials with amorphous properties and/or containing large amounts of defects start to decompose at temperatures as low as 500 °C [78], [79]. Additionally, the removal of the strongly anchored surface functional groups are shown by the decomposition peak at ~200 °C in thermograms [80]–[82]. The thermogravimetric profiles of the samples were recorded. **Figure 5.6** displays the first order derivative thermograms, whilst the thermal stability profiles are shown in **Figure S5.13**. The thermogram of the pCDs showed that the material started to decompose between *ca.* 200 - 300 °C, due to the loss of the oxygen functional groups [83]. The ~10 % weight loss at *ca.* 337 °C was associated with the loss of strongly bound functional groups on the carbon skeleton [83]. Finally, the ~37 % weight loss at *ca.* 509 °C was attributed to the loss of the carbon skeleton, indicating that the pCDs were only stable up to this temperature. For the T200 sample, the profile showed ~28 % and ~16 % loss at *ca.* 161 °C and 365 °C, respectively, associated with the loss of the surface functional groups. The sample lost its core (~ 56 % loss) at *ca.* 479 °C.

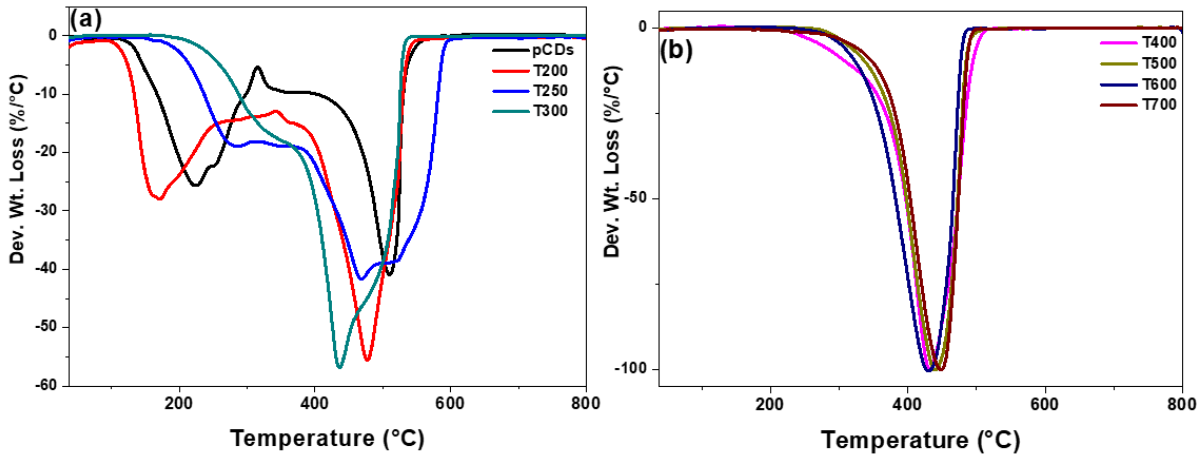

Figure 5. 6: DTG thermograms of pCDs and samples annealed at **a)** low and **b)** high temperatures.

In the T250 sample, the functional groups start decomposing at *ca.* 281 °C (~19 % weight loss). At *ca.* 466 °C and 530 °C, there was an ~81 % weight loss which may be associated with the loss of strongly bound functional groups and the carbon core. Similarly, the profile of the T300 sample showed an initial weight loss of ~17 % at *ca.* 329 °C associated with loss of the surface functional groups, and the major weight loss between *ca.* 436 and 504 °C could be attributed to the remaining functional groups and the carbon core. Additionally, the DTG profile for the T400 sample showed a major decomposition peak at *ca.* 432 °C, with ~99 % weight loss, and a small peak at *ca.* 542 °C which signified the complete decomposition of the carbon core. This data agrees with what was observed from the FTIR, ^{13}C NMR and XPS data which showed that the sample still contained functional groups; however, the improved thermal stability further suggested that most of the surface functional groups had been removed. Interestingly, for the T500, T600 and T700 samples only one major decomposition peak at *ca.* 422, 430 and 450 °C, respectively, was observed. The results obtained for the annealed samples (T400-T700) are comparable with the TGA results of rGO found in the literature, in which the TGA profile of the defective rGO exhibited a thermal stability up to 480 °C in air [84].

5.4 Mechanism of CD conversion

The data presented here provides a facile route to the synthesis of a layered carbon material like rGO. Furthermore, the characterization data has provided evidence for a method that can be used to study the assembly of carbon atoms in small CDs into generate large sheets of a graphitic like material.

We can speculate as to the mechanism by which this occurs (see **Figure 5.7** in page 124). The CDs are comprised of graphitic layers (d_{max} = 2.5 nm, see **Figure S5.3b**) capped with functional groups. In the first step, removal of the functional groups occurred and at 400 °C and the carbon atoms were mainly sp^2/sp^3 type (^{13}C NMR and XPS data). PDF data also confirms the formation of C=C bonds with increasing annealing temperature. However, as shown by PXRD data, this is not the final structure of the material even though the carbon has aromatic character (Raman and TGA data). The TEM data (**Figure 5.1c**) indicated that CDs that form these sheets were initially embedded in the sheets themselves. Further heating completed the process to form large graphitic sheets.

The carbon growth process can only occur via two processes: i) an Ostwald ripening in which the carbons agglomerated via the gas phase or ii) a solid phase reaction involving reaction of CD edges. **Figure 5.4b)** suggest that the CDs merge to form a flake. In this remarkable reaction the carbons edges react together to form the large flakes. C=C bonds are thus being formed at T = 400 °C. This temperature is similar to that used to produce carbon-carbon bond formation/cleavage. The mechanism is different from a study by Hou et al. [26] in which carbon sheets were also prepared from CDs. In their study the role of Na^+ ions were shown to be important; the C-C bond separation distances were much larger and the carbons did not form a layered structure.

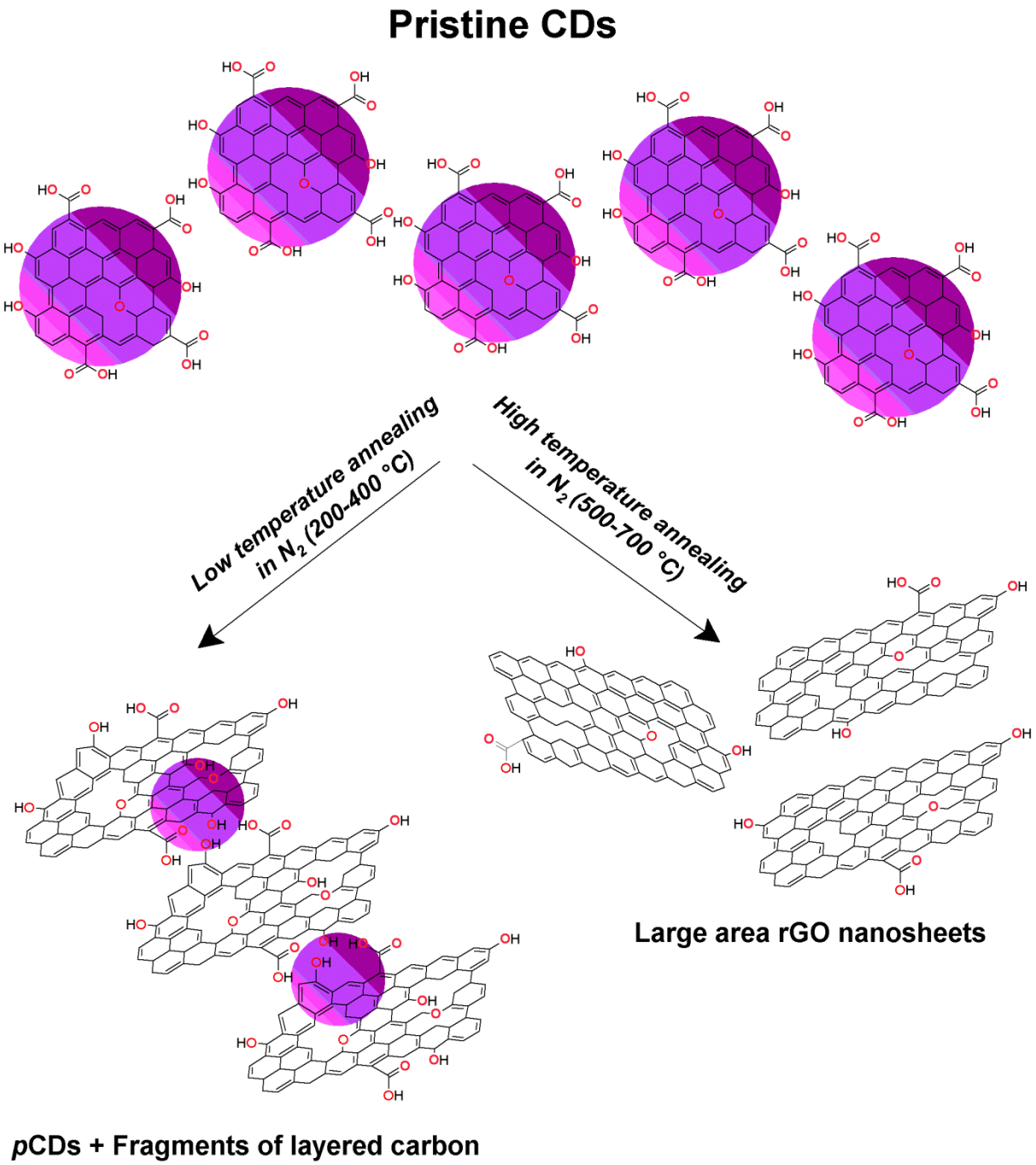

Figure 5. 7: A schematic illustration showing a possible mechanism for the formation of rGO nanosheets from pCDs.

5.5 Conclusion

Reduced graphene oxide (rGO) has been synthesized from a novel "bottom-up" method using carbon dots (CDs) as precursors. The results showed that the conversion of CDs to rGO involved a loss of the hydroxyl-, ether-, carboxylic- and carbonyl- surface functional groups of the CDs at T > 400 °C. This conversion suggested that the residual carbon atoms in the CDs assemble to form layers that are comprised of an rGO like material. The PDF data allowed for a comprehensive study of the changes of C-C bonds with annealing, data shown to be consistent with the TEM images. Raman and PDF data suggested that the rGO was most likely highly defective. This synthetic method presented a facile pathway for generating rGO using a relatively inexpensive method. Furthermore, it is clear that this method opens up a simple pathway to doping rGO and that catalysts could be used to further reduce the temperature of the C-C bond knitting process.

Acknowledgements

This work is supported by the NRF, the University of the Witwatersrand (post graduate merit award to LMM) and the DSI-NRF Centre of Excellence in Catalysis (*c*∗change). We would like to thank Dr Rudolph Erasmus from the School of Physics at University of the Witwatersrand for his assistance with Raman and photoluminescence collection and analysis. We would like to also thank Ms Rhandzu Rhikhotso for the high resolution TEM data, and Dr Werner Jordaan for XPS analysis (CSIR, Pretoria, South Africa). We are also thankful to Dr Memory Zimuwandeyi and Mr Mudzuli Maphupha (School of Chemistry at University of the Witwatersrand) for NMR data collection and data processing, respectively. We would also like to acknowledge Dr Cebisa Linganiso from the Microscopy and Microanalysis Unit (MMU) at the University of the Witwatersrand for AFM analysis. We thank Dr Graham King for the PDF measurements performed at the Canadian Light Source, a national research facility of the University of Saskatchewan, which is supported by the Canada Foundation for Innovation (CFI), the Natural Sciences and Engineering Research Council (NSERC), the National Research Council (NRC), the Canadian Institutes of Health Research (CIHR), the Government of Saskatchewan, and the University of Saskatchewan. Finally, sincere gratitude goes to Ms Petra Dinham from the School of Chemical and Metallurgical Engineering (CHMT), University of the Witwatersrand for the SEM analysis.

Competing interests

The authors declare that they have no known competing financial interests or personal relationships that could have appeared to influence the work reported in this paper.

5.6 References

[1] Y. Song, S. Zhu, and B. Yang, "Bioimaging based on fluorescent carbon dots," *RSC Adv.*, vol. 4, no. 52, pp. 27184–27200, 2014, doi: 10.1039/c3ra47994c.

[2] M. L. Liu, L. Yang, R. S. Li, B. Bin Chen, H. Liu, and C. Z. Huang, "Large-scale simultaneous synthesis of highly photoluminescent green amorphous carbon nanodots and yellow crystalline graphene quantum dots at room temperature," *Green Chem.*, vol. 19, no. 15, pp. 3611–3617, 2017, doi: 10.1039/c7gc01236e.

[3] S. Zhu, X. Zhao, Y. Song, S. Lu, and B. Yang, "Beyond bottom-up carbon nanodots: Citric-acid derived organic molecules," *Nano Today*, vol. 11, no. 2, pp. 128–132, 2016, doi: 10.1016/j.nantod.2015.09.002.

[4] S. Zhu, Y. Song, X. Zhao, J. Shao, J. Zhang, and B. Yang, "The photoluminescence mechanism in carbon dots (graphene quantum dots, carbon nanodots, and polymer dots): current state and future perspective," *Nano Res.*, vol. 8, no. 2, pp. 355–381, 2015, doi: 10.1007/s12274-014-0644-3.

[5] X. Wang, Y. Feng, P. Dong, and J. Huang, "A Mini review on carbon quantum dots: Preparation, properties, and electrocatalytic application," *Front. Chem.*, vol. 7, p. 671, 2019, doi: 10.3389/fchem.2019.00671.

[6] C. Xia, S. Zhu, T. Feng, M. Yang, and B. Yang, "Evolution and synthesis of carbon dots: From carbon dots to carbonized polymer dots," *Adv. Sci.*, vol. 6, no. 23,p. 1901316, 2019, doi: 10.1002/advs.201901316.

[7] T. V. De Medeiros, J. Manioudakis, F. Noun, J. R. Macairan, F. Victoria, and R. Naccache, "Microwave-assisted synthesis of carbon dots and their applications," *J. Mater. Chem. C*, vol. 7, no. 24, pp. 7175–7195, 2019, doi: 10.1039/c9tc01640f.

[8] L. Li and T. Dong, "Photoluminescence tuning in carbon dots: Surface passivation or/and functionalization, heteroatom doping," *J. Mater. Chem. C*, vol. 6, no. 30, pp. 7944–7970, 2018, doi: 10.1039/c7tc05878k.

[9] R. Atchudan, T. N. J. I Edison, S. Perumal, R. Vinodh, and Y. R. Lee, "Multicolor-emitting carbon dots from Malus floribunda and their interaction with Caenorhabditis elegans," *Mater. Lett.*, vol. 261, no. 15, p. 127153, 2020, doi:

10.1016/j.matlet.2019.127153.

[10] Z. Fan, S. Li, F. Yuan, and L. Fan, “Fluorescent graphene quantum dots for biosensing and bioimaging,” *RSC Adv.*, vol. 5, no. 25, pp. 19773–19789, 2015, doi: 10.1039/c4ra17131d.

[11] X. Hai, J. Feng, X. Chen, and J. Wang, “Tuning the optical properties of graphene quantum dots for biosensing and bioimaging,” *J. Mater. Chem. B*, vol. 6, no. 20, pp. 3219–3234, 2018, doi: 10.1039/c8tb00428e.

[12] C. Ji, Y. Zhou, R. M. Leblanc, and Z. Peng, “Recent developments of carbon dots in biosensing: A review,” *ACS Sensors*, vol. 5, no. 9, pp. 2724–2741, 2020, doi: 10.1021/acssensors.0c01556.

[13] Z. Zhang, T. Zheng, X. Li, J. Xu, and H. Zeng, “Progress of carbon quantum dots in photocatalysis applications,” *Part. Part. Syst. Charact.*, vol. 33, no. 8, pp. 457–472, 2016, doi: 10.1002/ppsc.201500243.

[14] M. Han, S. J. Zhu, S. Y. Lu, Y. B. Song, T. L. Feng, S. Y. Tao, J. J. Liu, and B. Yang, “Recent progress on the photocatalysis of carbon dots: Classification, mechanism and applications,” *Nano Today*, vol. 19, pp. 201–218, 2018, doi: 10.1016/j.nantod.2018.02.008.

[15] Z. Zhang, G. Yi, P. Li, X. Zhang, H. Fan, Y. Zhang, X. Wang, and C. Zhang, “A minireview on doped carbon dots for photocatalytic and electrocatalytic applications,” *Nanoscale*, vol. 12, no. 26, pp. 13899–13906, 2020, doi: 10.1039/d0nr03163a.

[16] Z. Zhuang, H. Lin, X. Zhang, F. Qiu, and H. Yang, “A glassy carbon electrode modified with carbon dots and gold nanoparticles for enhanced electrocatalytic oxidation and detection of nitrite,” *Microchim. Acta*, vol. 183, no. 10, pp. 2807–2814, 2016, doi: 10.1007/s00604-016-1931-3.

[17] T. Feng, Q. Zeng, S. Lu, M. Yang, S. Tao, Y. Chen, Y. Zhao, and B. Yang, “Morphological and interfacial engineering of cobalt-based electrocatalysts by carbon dots for enhanced water splitting,” *ACS Sustainable Chem. Eng.*, vol. 7, no. 7, pp. 7047–7057, 2019, doi: 10.1021/acssuschemeng.8b06832.

[18] X. Li, M. Rui, J. Song, Z. Shen, and H. Zeng, “Carbon and graphene quantum dots for

optoelectronic and energy devices: A review," *Adv. Funct. Mater.*, vol. 25, no. 31, pp. 4929–4947, 2015, doi: 10.1002/adfm.201501250.

[19] T. Yuan, T. Meng, P. He, Y. Shi, Y. Li, X. Li, L. Fan, and S. Yang, "Carbon quantum dots: An emerging material for optoelectronic applications," *J. Mater. Chem. C*, vol. 7, no. 23, pp. 6820–6835, 2019, doi: 10.1039/c9tc01730e.

[20] S. N. Baker and G. A. Baker, "Luminescent carbon nanodots : Emergent nanolights," *Angew. Chem. Int. Ed.*, vol. 49, pp. 6726–6744, 2010, doi: 10.1002/anie.200906623.

[21] Z. L. Wu, Z. X. Liu, and Y. H. Yuan, "Carbon dots: Materials, synthesis, properties and approaches to long-wavelength and multicolor emission," *J. Mater. Chem. B*, vol. 5, no. 21, pp. 3794–3809, 2017, doi: 10.1039/c7tb00363c.

[22] D. M. A. Crista, J. C. G. E. da Silva, and L. P. da Silva, "Evaluation of different bottom-up routes for the fabrication of carbon dots," *Nanomaterials*, vol. 10, no. 7, p. 1316, 2020, doi: 10.3390/nano10071316.

[23] G. Chen, S. Wu, L. Hui, Y. Zhao, J. Ye, Z. Tan, W. Zeng, Z. Tao, L. Yang, and Y. Zhu, "Assembling carbon quantum dots to a layered carbon for high-density supercapacitor electrodes," *Sci. Rep.*, vol. 6, p. 19028, 2016, doi: 10.1038/srep19028.

[24] G. Bharathi, D. Nataraj, S. Premkumar, M. Sowmiya, K. Senthilkumar, T. D. Thangadurai, O. Y. Khyzhun, M. Gupta, D. Phase, N. Patra, S. N. Jha, and D. Bhattacharyya, "Graphene quantum dot solid sheets: Strong blue-light-emitting & photocurrent-producing band-gap-opened nanostructures," *Sci. Rep.*, vol. 7, p. 10850, 2017, doi: 10.1038/s41598-017-10534-4.

[25] S. Zhang, J. Zhu, Y. Qing, C. Fan, L. Wang, Y. Huang, R. Sheng, Y. Guo, T. Wang, Y. Pan, Y. Lv, H. Song, and D. Jia, "Construction of hierarchical porous carbon nanosheets from template-assisted assembly of coal-based graphene quantum dots for high performance supercapacitor electrodes," *Mater. Today Energy*, vol. 6, pp. 36–45, 2017, doi: 10.1016/j.mtener.2017.08.003.

[26] H. Hou, C. E. Banks, M. Jing, Y. Zhang, and X. Ji, "Carbon quantum dots and their derivative 3D porous carbon frameworks for sodium-ion batteries with ultralong cycle life," *Adv. Mater.*, vol. 27, no. 47, pp. 7861–7866, 2015, doi: 10.1002/adma.201503816.

[27] G. Shim, M. G. Kim, J. Y. Park, and Y. K. Oh, "Graphene-based nanosheets for delivery of chemotherapeutics and biological drugs," *Adv. Drug Deliv. Rev.*, vol. 105, pp. 205–227, 2016, doi: 10.1016/j.addr.2016.04.004.

[28] J. An, T. D. Le, Y. Huang, Z. Zhan, Y. Li, L. Zheng, W. Huang, G. Sun, and Y. J. Kim, "All-graphene-based highly flexible noncontact electronic skin," *ACS Appl. Mater. Interfaces*, vol. 9, no. 51, pp. 44593–44601, 2017, doi: 10.1021/acsami.7b13701.

[29] R. You, Y. Q. Liu, Y. L. Hao, D. D. Han, Y. L. Zhang, and Z. You, "Laser fabrication of graphene-based flexible electronics," *Adv. Mater.*, vol. 32, no. 15, p. 1901981, 2020, doi: 10.1002/adma.201901981.

[30] S. Pattnaik, K. Swain, and Z. Lin, "Graphene and graphene-based nanocomposites: biomedical applications and biosafety," *J. Mater. Chem. B*, vol. 4, no. 48, pp. 7813–7831, 2016, doi: 10.1039/C6TB02086K.

[31] T. P. Dasari Shareena, D. McShan, A. K. Dasmahapatra, and P. B. Tchounwou, "A review on graphene-based nanomaterials in biomedical applications and risks in environment and health," *Nano-Micro Lett.*, vol. 10, no. 3, p. 53, 2018, doi: 10.1007/s40820-018-0206-4.

[32] Y. Chen, C. Tan, H. Zhang, and L. Wang, "Two-dimensional graphene analogues for biomedical applications," *Chem. Soc. Rev.*, vol. 44, no. 9, pp. 2681–2701, 2015, doi: 10.1039/c4cs00300d.

[33] S. Han, J. Sun, S. He, M. Tang, and R. Chai, "The application of graphene-based biomaterials in biomedicine," *Am. J. Transl. Res.*, vol. 11, no. 6, pp. 3246–3260, 2019.

[34] J. Byun, "Emerging frontiers of graphene in biomedicine," *J. Microbiol. Biotechnol.*, vol. 25, no. 2, pp. 145–151, 2015, doi: 10.4014/jmb.1412.12045.

[35] E. Shamsaei, F. B. de Souza, X. Yao, E. Benhelal, A. Akbari, and W. Duan, "Graphene-based nanosheets for stronger and more durable concrete: A review," *Constr. Build. Mater.*, vol. 183, pp. 642–660, 2018, doi: 10.1016/j.conbuildmat.2018.06.201.

[36] J. Wang, E. C. Salihi, and L. Šiller, "Green reduction of graphene oxide using alanine," *Mater. Sci. Eng. C*, vol. 72, pp. 1–6, 2017, doi: 10.1016/j.msec.2016.11.017.

[37] S. J. Rowley-Neale, E. P. Randviir, A. S. Abo Dena, and C. E. Banks, "An overview of

recent applications of reduced graphene oxide as a basis of electroanalytical sensing platforms," *Appl. Mater. Today*, vol. 10, pp. 218–226, 2018, doi: 10.1016/j.apmt.2017.11.010.

[38] F. Liu, C. Wang, X. Sui, M. A. Riaz, M. Xu, L. Wei, Y. Chen, "Synthesis of graphene materials by electrochemical exfoliation: Recent progress and future potential," *Carbon Energy*, vol. 1, no. 2, pp. 173–199, 2019, doi: 10.1002/cey2.14.

[39] U. Khan, A. O'Neill, M. Lotya, S. De, and J. N. Coleman, "High-concentration solvent exfoliation of graphene," *Small*, vol. 6, no. 7, pp. 864–871, 2010, doi: 10.1002/smll.200902066.

[40] V. B. Mohan, K. tak Lau, D. Hui, and D. Bhattacharyya, "Graphene-based materials and their composites: A review on production, applications and product limitations," *Compos. Part B Eng.*, vol. 142, pp. 200–220, 2018, doi: 10.1016/j.compositesb.2018.01.013.

[41] T. F. Emiru and D. W. Ayele, "Controlled synthesis, characterization and reduction of graphene oxide: A convenient method for large scale production," *Egypt. J. Basic Appl. Sci.*, vol. 4, no. 1, pp. 74–79, 2017, doi: 10.1016/j.ejbas.2016.11.002.

[42] M. D. P. Lavin-Lopez, A. Romero, J. Garrido, L. Sanchez-Silva, and J. L. Valverde, "Influence of different improved hummers method modifications on the characteristics of graphite oxide in order to make a more easily scalable method," *Ind. Eng. Chem. Res.*, vol. 55, no. 50, pp. 12836–12847, 2016, doi: 10.1021/acs.iecr.6b03533.

[43] R. Dagher, S. Matta, R. Parret, M. Paillet, B. Jouault, L. Nguyen, M. Portail, M. Zielinski, T. Chassagne, S. Tanaka, J. Brault, Y. Cordier, A. Michon, "High temperature annealing and CVD growth of few-layer graphene on bulk AlN and AlN templates," *Phys. Status Solidi A.*, vol. 214, no. 4, p. 1600436, 2017, doi: 10.1002/pssa.201600436.

[44] B. J. Matsoso, K. Ranganathan, B. K. Mutuma, T. Lerotholi, G. Jones, and N. J. Coville, "Time-dependent evolution of the nitrogen configurations in N-doped graphene films," *RSC Adv.*, vol. 6, no. 108, pp. 106914–106920, 2016, doi: 10.1039/c6ra24094a.

[45] V. Raveendran, A. R. Suresh Babu, and N. K. Renuka, "Mint leaf derived carbon dots for dual analyte detection of Fe(iii) and ascorbic acid," *RSC Adv.*, vol. 9, no. 21, pp. 12070–12077, 2019, doi: 10.1039/c9ra02120e.

[46] G. A. M. Hutton, B. Reuillard, B. C. M. Martindale, C. A. Caputo, C. W. J. Lockwood, J. N. Butt, and E. Reisner, "Carbon dots as versatile photosensitizers for solar-driven catalysis with redox enzymes," *J. Am. Chem. Soc.*, vol. 138, no. 51, pp. 16722–16730, 2016, doi: 10.1021/jacs.6b10146.

[47] J. Gong, X. Lu, and X. An, "Carbon dots as fluorescent off–on nanosensors for ascorbic acid detection," *RSC Adv.*, vol. 5, no. 11, pp. 8533–8536, 2015, doi: 10.1039/C4RA13576H.

[48] B. H. Toby and R. B. Von Dreele, "GSAS-II : the genesis of a modern open-source all purpose crystallography software package," *J. Appl. Crystallogr.*, vol. 46, no. 2, pp. 544–549, Apr. 2013, doi: 10.1107/S0021889813003531.

[49] C. L. Farrow, P. Juhas, J. W. Liu, D. Bryndin, E. S. Bozin, J. Bloch, T. Proffen, and S. J. L. Billinge, "PDFfit2 and PDFgui: Computer programs for studying nanostructure in crystals," *J. Phys. Condens. Matter*, vol. 19, no. 33,p. 335219, 2007, doi: 10.1088/0953-8984/19/33/335219.

[50] Y. Liu, N. Xiao, N. Gong, H. Wang, X. Shi, W. Gu, and L. Ye, "One-step microwave-assisted polyol synthesis of green luminescent carbon dots as optical nanoprobes," *Carbon*, vol. 68, pp. 258–264, 2014, doi: 10.1016/j.carbon.2013.10.086.

[51] N. Arsalani, P. Nezhad-Mokhtari, and E. Jabbari, "Microwave-assisted and one-step synthesis of PEG passivated fluorescent carbon dots from gelatin as an efficient nanocarrier for methotrexate delivery," *Artif. Cells, Nanomedicine Biotechnol.*, vol. 47, no. 1, pp. 540–547, 2019, doi: 10.1080/21691401.2018.1562460.

[52] X. Liu, T. Li, Y. Hou, Q. Wu, J. Yi, and G. Zhang, "Microwave synthesis of carbon dots with multi-response using denatured proteins as carbon source," *RSC Adv.*, vol. 6, no. 14, pp. 11711–11718, 2016, doi: 10.1039/c5ra23081k.

[53] C. C. Wang and S. Y. Lu, "Carbon black-derived graphene quantum dots composited with carbon aerogel as a highly efficient and stable reduction catalyst for the iodide/tri-iodide couple," *Nanoscale*, vol. 7, no. 3, pp. 1209–1215, 2015, doi: 10.1039/c4nr06118g.

[54] T. Wang, A. Wang, R. Wang, Z. Liu, Y. Sun, G. Shan, Y. Chen, and Y. Liu, "Carbon dots with molecular fluorescence and their application as a 'turn-off' fluorescent probe

for ferricyanide detection," *Sci. Rep.*, vol. 9, no. 1, pp. 1–9, 2019, doi: 10.1038/s41598-019-47168-7.

[55] N. C. Verma, A. Yadav, and C. K. Nandi, "Paving the path to the future of carbogenic nanodots," *Nat. Commun.*, vol. 10, no. 1, pp. 8–11, 2019, doi: 10.1038/s41467-019-10394-8.

[56] M. Li, H. Zhao, L. Qi, and H. Li, "Analysis techniques of lattice fringe images for quantified evaluation of pyrocarbon by chemical vapor infiltration," *Microsc. Microanal.*, vol. 20, no. 5, pp. 1591–1600, 2014, doi: 10.1017/S143192761400169X.

[57] A. Prasannan and T. Imae, "One-pot synthesis of fluorescent carbon dots from orange waste peels," *Ind. Eng. Chem. Res.*, vol. 52, no. 44, pp. 15673–15678, 2013, doi.org/10.1021/ie402421s.

[58] M. Khandelwal and A. Kumar, "One-step chemically controlled wet synthesis of graphene nanoribbons from graphene oxide for high performance supercapacitor applications," *J. Mater. Chem. A*, vol. 3, no. 45, pp. 22975–22988, 2015, doi: 10.1039/c5ta07603j.

[59] T. K. Das, S. Banerjee, M. Pandey, B. Vishwanadh, R. J. Kshirsagar, and V. Sudarsan, "Effect of surface functional groups on hydrogen adsorption properties of Pd dispersed reduced graphene oxide," *Int. J. Hydrogen Energy*, vol. 42, no. 12, pp. 8032–8041, 2017, doi: 10.1016/j.ijhydene.2016.12.024.

[60] A. Yadav, R. Kumar, U. P. Pandey, and B. Sahoo, "Role of oxygen functionalities of GO in corrosion protection of metallic Fe," *Carbon*, vol. 173, pp. 350–363, 2021, doi: 10.1016/j.carbon.2020.11.029.

[61] S. Sahu, B. Behera, T. K. Maiti, and S. Mohapatra, "Simple one-step synthesis of highly luminescent carbon dots from orange juice: Application as excellent bio-imaging agents," *Chem. Commun.*, vol. 48, no. 70, pp. 8835–8837, 2012, doi: 10.1039/c2cc33796g.

[62] H. H. Huang, K. K. H. De Silva, G. R. A. Kumara, and M. Yoshimura, "Structural evolution of hydrothermally derived reduced graphene oxide," *Sci. Rep.*, vol. 8, no. 1, pp. 2–10, 2018, doi: 10.1038/s41598-018-25194-1.

[63] S. K. Mishra, S. N. Tripathi, V. Choudhary, and B. D. Gupta, "SPR based fibre optic ammonia gas sensor utilizing nanocomposite film of PMMA/reduced graphene oxide prepared by in situ polymerization," *Sensors Actuators, B Chem.*, vol. 199, pp. 190–200, 2014, doi: 10.1016/j.snb.2014.03.109.

[64] C. Fu, G. Zhao, H. Zhang, and S. Li, "Evaluation and characterization of reduced graphene oxide nanosheets as anode materials for lithium-ion batteries," *Int. J. Electrochem. Sci.*, vol. 8, no. 5, pp. 6269–6280, 2013.

[65] G. Liu, L. Wang, B. Wang, T. Gao, and D. Wang, "A reduced graphene oxide modified metallic cobalt composite with superior electrochemical performance for supercapacitors," *RSC Adv.*, vol. 5, no. 78, pp. 63553–63560, 2015, doi: 10.1039/c5ra09748g.

[66] B. Gupta, N. Kumar, K. Panda, V. Kanan, S. Joshi, and I. Visoly-Fisher, "Role of oxygen functional groups in reduced graphene oxide for lubrication," *Sci. Rep.*, vol. 7, p. 45030, 2017, doi: 10.1038/srep45030.

[67] M. M. Lucchese, F. Stavale, E. H. Ferreira, C. Vilani, M. V. O. Moutinho, R. B. Capaz, C. A. Achete, and A. Jorio, "Quantifying ion-induced defects and Raman relaxation length in graphene," *Carbon*, vol. 48, no. 5, pp. 1592–1597, 2010, doi: 10.1016/j.carbon.2009.12.057.

[68] A. C. Ferrari, "Raman spectroscopy of graphene and graphite: Disorder, electron-phonon coupling, doping and nonadiabatic effects," *Solid State Commun.*, vol. 143, no. 1–2, pp. 47–57, 2007, doi: 10.1016/j.ssc.2007.03.052.

[69] E. F. Antunes, A. O. Lobo, E. J. Corat, V. J. Trava-Airoldi, A. A. Martin, and C. Veríssimo, "Comparative study of first- and second-order Raman spectra of MWCNT at visible and infrared laser excitation," *Carbon*, vol. 44, no. 11, pp. 2202–2211, 2006, doi: 10.1016/j.carbon.2006.03.003.

[70] B. K. Mutuma, B. J. Matsoso, K. Ranganathan, J. M. Keartland, D. Wamwangi, and N. J. Coville, "Generation of radical species in CVD grown pristine and N-doped solid carbon spheres using H_2 and Ar as carrier gases," *RSC Adv.*, vol. 7, no. 34, pp. 21187–21195, 2017, doi: 10.1039/c7ra03142d.

[71] A. Makhongoana, B. J. Matsoso, T. H. Mongwe, N. J. Coville, D. Wamwangi, and M.

S. Maubane-Nkadimeng, “The role of oxygen in a carbon source (castor oil versus paraffin oil) in the synthesis of carbon nano-onions,” *Nanotechnology*, vol. 32, no. 13, p. 135603, 2021, doi: 10.1088/1361-6528/abd0b1.

[72] A. C. Ferrari and J. Robertson, “Interpretation of Raman spectra of disordered and amorphous carbon,” *Phys. Rev. B*, vol. 61, no. 20, pp. 14 095– 14 106, 2000, doi:10.1103/PhysRevB.61.14095

[73] W. Dmowski, C. I. Contescu, A. Llobet, N. C. Gallego, and T. Egami, “Local atomic density of microporous carbons,” *J. Phys. Chem. C*, vol. 116, no. 4, pp. 2946–2951, 2012, doi: 10.1021/jp209824f.

[74] D. F. R. Mildner and J. M. Carpenter, “On the short range atomic structure of non-crystalline carbon,” *J. Non-Cryst. Solids*, vol. 47, no. 3, pp. 391–402, 1982, doi.org/10.1016/0022-3093(82)90215-0.

[75] V. Petkov, R. G. Difrancesco, S. J. L., “Local structure of nanoporous carbons,” *Philos. Mag. B*, vol. 79, no. 10, pp. 1519–1530, 1999, doi: 10.1080/014186399256376.

[76] M. A. Smith, H. C. Foley, and R. F. Lobo, “A simple model describes the PDF of a non-graphitizing carbon,” *Carbon*, vol. 42, no. 10, pp. 2041–2048, 2004, doi: 10.1016/j.carbon.2004.04.009.

[77] K. Jiang, X. Feng, X. Gao, Y. Wang, C. Cai, Z. Li, H. Lin, “Preparation of multicolor photoluminescent carbon dots by tuning surface states,” *Nanomaterials*, vol. 9, no. 4, pp. 529–531, 2019, doi: 10.3390/nano9040529.

[78] H. Xiong, M. A. M. Motchelaho, M. Moyo, L. L. Jewell, and N. J. Coville, “Correlating the preparation and performance of cobalt catalysts supported on carbon nanotubes and carbon spheres in the Fischer-Tropsch synthesis,” *J. Catal.*, vol. 278, no. 1, pp. 26–40, 2011, doi: 10.1016/j.jcat.2010.11.010.

[79] K. S. Kumar, S. Pittala, S. Sanyadanam, and P. Paik, “A new single/few-layered graphene oxide with a high dielectric constant of 106: Contribution of defects and functional groups,” *RSC Adv.*, vol. 5, no. 19, pp. 14768–14779, 2015, doi: 10.1039/c4ra10800k.

[80] R. Bandi, B. R. Gangapuram, R. Dadigala, R. Eslavath, S. S. Singh, and V. Guttena,

"Facile and green synthesis of fluorescent carbon dots from onion waste and their potential applications as sensor and multicolour imaging agents," *RSC Adv.*, vol. 6, no. 34, pp. 28633–28639, 2016, doi: 10.1039/c6ra01669c.

[81] A. Mewada, S. Pandey, S. Shinde, N. Mishra, G. Oza, M. Thakur, M. Sharon and M. Sharon, "Green synthesis of biocompatible carbon dots using aqueous extract of Trapa bispinosa peel," *Mater. Sci. Eng. C*, vol. 33, no. 5, pp. 2914–2917, 2013, doi: 10.1016/j.msec.2013.03.018.

[82] R. Gao, N. Hu, Z. Yang, Q. Zhu, J. Chai, Y. Su, L. Zhang, and Y. Zhang, "Paper-like graphene-Ag composite films with enhanced mechanical and electrical properties," *Nanoscale Res. Lett.*, vol. 8, no. 32, pp. 1–8, 2013, doi.org/10.1186/1556-276X-8-32.

[83] D. Wang, Z. Wang, Q. Zhan, Y. Pu, J.-X. Wang, N.R. Foster, L. Dai, "Facile and scalable preparation of fluorescent carbon dots for multifunctional applications," *Engineering*, vol. 3, no. 3, pp. 402–408, 2017, doi: 10.1016/J.ENG.2017.03.014.

[84] O. K. Park, Y. M. Choi, J. Y. Hwang, C. M. Yang, T. W. Kim, N. H. You, H. Y.

Koo, J. H. Lee, B. C. Ku, and M. Goh, "Defect healing of reduced graphene oxide via intramolecular cross-dehydrogenative coupling," *Nanotechnology*, vol. 24, no. 18, p. 185604, 2013, doi: 10.1088/0957-4484/24/18/185604.

CHAPTER 6: APPLICATION OF THE CARBON DOTS-DERIVED GRAPHENE-LIKE SHEETS IN THE FISCHER-TROPSCH SYNTHESIS

Use of carbon dots-derived graphene-like sheets for the autoreduction of cobalt nanoparticles for Fischer–Tropsch synthesis: A limitation on the use of carbon supports

Abstract

Many studies have shown that various carbon allotropes can act as support materials and also as reducing agents for metals in catalysis reactions. The latter is due to a phenomenon known as *autoreduction*, when a metal oxide that is supported on a carbon-based support material is reduced by the carbon support to its metallic form at elevated temperatures and under inert atmospheric conditions. In this study, cobalt oxide (Co_3O_4) was autoreduced on different graphene-like carbon sheets (d≈ 0.2 - 2.6 μm). These sheets were synthesized by annealing quasi-spherical carbon dots (CDs, d < 3 nm size) at temperatures ranging from 250-700 °C under N_2, for 10 min. *In situ* powder X-ray diffraction (PXRD) was used to study the phase evolution of the supported Co under hydrogen (H_2) and under autoreduction using nitrogen gas (N_2) to create an inert atmosphere. It was observed that the Co_3O_4 was reduced to Co(fcc) under both gas atmosphere, but with H_2 being superior to carbon as a reducing agent. Thus, at 400 °C, the samples contained > 70 % Co(fcc) under H_2 but > 70 % CoO under N_2. The catalysts were tested for *syngas* conversion under Fischer-Tropsch synthesis (FTS) at 220 °C (10 bar P; H_2:CO ratio = 2:1). All catalysts showed low activity and high selectivity towards CH_4, compared to the desired C_{5+} hydrocarbons. The catalyst performance for the autoreduced catalysts showed the worst results, due to the poorer reduction of the Co. Analysis of the spent catalyst revealed excessive Co metal sintering under the reaction conditions. The results obtained in this study have shown a limitation to the use of these type of carbons as support in FT catalytic reactions.

6.1 Introduction

The Fischer-Tropsch synthesis (FTS) process is a well-established catalytic conversion technology for gas to liquid (GTL), coal to liquid (CTL) and biomass to liquid (BTL) fuel production [1], [2]. This technology has become increasingly important for fuel (and chemical) production due to the increasing demand for clean and sustainable energy (and chemicals) [2], [3]. The FTS makes use of different metal catalysts to produce fuel, however, cobalt (Co), iron (Fe), ruthenium (Ru) and nickel (Ni) are considered to be the most efficient catalysts for the FTS conversion process [1], [4], [5]. Co in particular, has shown good selectivity towards fuel production (C_{5+}), a high stability in the reaction, and a low selectivity towards the water gas shift reaction [1], [6].

As with many other heterogeneous catalysis processes, metal catalysts are dispersed on a support material to improve dispersion, durability and reduce the cost of the catalysts [7], [8]. For the FTS, many studies have shown that inorganic oxides and carbon allotropes are good supports for metal catalysts. Silica (SiO_2), alumina (Al_2O_3) and titania (TiO_2) are the preferred supports for commercial FTS processes. These supports give a strong metal-support interaction (MSI) with the catalytically active metal, and this decreases the amount of active metal catalyst facilitating hydrogenation of CO to hydrocarbons [1]. Carbon allotropes do not suffer this drawback to the same extent since they tend to form weaker MSIs with the catalyst. Consequently, more catalytically active metal is available for reaction. The weak MSI can however lead to a high susceptibility to metal catalyst sintering. To circumvent this, the carbon allotropes are often functionalized (i.e., the inert carbon surface is activated) with oxygen and/or nitrogen functional groups, and these heteroatoms act as metal anchoring sites to improve the MSIs and also increases the metal dispersion [8]. Thus, numerous carbon allotropes such as carbon black, activated carbon (AC), carbon nanotubes (CNTs), carbon nanofibers (CNFs), carbon spheres (CSs), and ordered mesoporous carbon (OMCs) have been evaluated in the FTS process [8].

In the past 7-10 years, graphene and graphene based nanosheets (GNSs, 2-D sheets/sheet-like materials containing predominantly sp^2 type C) have been evaluated for use as support materials in the FTS process due to their high surface area, high thermal stability and favourable electronic properties. Studies on graphene supported Co-based FTS catalysts have shown pronounced Co sintering due to a weak MSI effect. This arises since the graphene sheets lack

defects that helps anchor the metal catalyst [9]. Hajjar et al. studied the effect of support porosity and surface area of nanoporous graphene (NPG) and graphene oxide (GO) sheets and compared them to Al_2O_3 [10]. Their results showed that NPG gave better activity and product selectivity when compared to GO and Al_2O_3. The NPG and GO supported Co showed an increase in C_{5+} selectivity and a decrease in C_2-C_4 formation compared to the Al_2O_3 supported Co. Torshizi et al. studied the effect of Co catalyst loading (i.e., 5, 15 and 30 wt%) on a reduced graphene oxide (rGO) surface in FTS [11]. The results showed that a high metal loading (i.e., 30 wt%) led to increased % CO conversion. However, a low metal loading (5 wt%) led to the formation of larger Co particle sizes (d ~ 28 nm) and also higher selectivity to C_{5+} products.

Carbon allotropes not only can act as metal supports but they also have the ability to reduce metal oxides to their metallic state under an inert atmosphere and at elevated temperature [12]–[16]. The literature shows that the reducing ability of carbon for active metal catalysts found in heterogeneous catalysis has not been explored to a great extent. It has been proposed that the reducing effect is enhanced in allotropes with surface curvature (such as CNTs and CSs), where the aromatic carbon atom(s) on the edge of a carbon undergoes partial rehybridization. These partially rehybridized carbon edges then interact with oxygen in a metal oxide in a redox reaction, where the carbon is oxidised, and the metal is reduced [16].

Xiong et al. studied the autoreduction behaviour of Co_3O_4 into metallic Co (i.e. Co^0) on solid CSs and the catalytic performance of the Co in the FTS. The authors showed with *in situ* PXRD that the Co_3O_4 supported on CSs can autoreduce to form Co^0 at temperatures > 480 °C under an inert argon (Ar) gas, while under H_2 reduction conditions the Co^0 formed at T = 400 °C. The overall FT catalytic performance of the Co^0 produced under the two different conditions was evaluated. The Co^0 produced under Ar atmosphere gave better CO conversion compared to the Co^0 produced under H_2 atmosphere (Co specific activity of 0.27×10^{-4} $mol_{CO}g^{-1}_{Co}s^{-1}$ and 0.14×10^{-4} $mol_{CO}g^{-1}_{Co}s^{-1}$, respectively) but similar product selectivity results (C_{4+} selectivity was ~47 % for both catalysts) [13]. In another study, Xiong et al. showed that Co_3O_4 supported on either CNTs or CSs produced a better FTS performance when the catalysts were autoreduced compared to the H_2 reduced catalysts [12].

Yang et al. evaluated the effect of nitrogen doping of ordered mesoporous carbon (OMC) on the autoreduction behaviour of Co_3O_4. They found that N-doping improved the dispersion of the Co catalysts. The *in-situ* PXRD studies were performed under Ar gas. The studies revealed

that the N-doped OMC showed complete reduction of Co_3O_4 to Co^0 at 500 °C, while at these temperatures pristine (i.e., undoped) OMC samples still showed a mixture of Co^0 and CoO. This was attributed to an increase in defects in the nitrogen doped OMC which improved the ability of the carbon to reduce Co_3O_4 to Co^0. Furthermore, the Co specific activity was higher for the Co supported on N-doped OMC compared to pristine OMC (2.67×10^{-4} $mol_{CO}g^{-1}_{Co}s^{-1}$ and 1.97×10^{-4} $mol_{CO}g^{-1}_{Co}s^{-1}$, respectively), but both these catalysts showed comparable selectivity towards hydrocarbons (C_{5+} selectivity of 60-65 %) [17].

Another study has shown that graphitic carbon can also induce autoreduction. The autoreduction behaviour of Co_3O_4 on graphitic carbon nitride (g-C_3N_4)-coated alumina (CN-Al) was investigated by Park et al. [15]. In their studies, the authors combined helium temperature programmed reduction (He-TPR) with *ex situ* PXRD to evaluate the reduction temperatures as well as the phase evolution during Co_3O_4 reduction, respectively. It was found that Co_3O_4 supported on CN-Al was autoreduced to Co^0 at 550 °C. It was also found that during this reduction, g-C_3N_4 decomposed to form CO which was monitored using mass spectrometry. The CO gas that was released was believed to be the reducing agent in the Co_3O_4 reduction to Co^0, before being oxidized to CO_2. Their FTS results showed that the catalytic performance of Co supported on CN-Al was similar for the H_2 reduced catalysts and the autoreduced catalyst, with Co specific activity of 21.84 and 21.52 $\mu mols^{-1}g_{co}^{-1}$, respectively, and a C_{5+} selectivity of ~76 %.

All the mentioned studies indicate that the autoreduction behaviour of metal oxides on carbon allotropes is a viable procedure to reduce Co and that the Co/C catalyst can show better FTS performance when compared to metal oxides reduced using conventional means. The economic implications of the autoreduction process for industrial scale heterogeneous catalysis is that it could potentially be used to reduce FTS operating costs by eliminating the need for a separate reducing agent [15].

In a previous study (**Chapter 5**) we have shown that graphene-like materials can be made from carbon dots (CDs) in a facile thermal process at temperatures ranging from 250 to 700 °C [18]. The carbons formed contained mixtures of CDs and reduced graphene oxides (see **Figure 5.1**, **S5.5-5.7**). To expand on the autoreduction studies on carbon allotropes, a study of the reducibility of Co_3O_4 supported on these graphene-like materials was undertaken. The catalysts prepared by the autoreduction process, after addition of Co_3O_4, were evaluated for activity in the FTS reaction.

CDs on their own are unstable at *ca.* > 200 °C [18]. Above this temperature, the CD nanoparticles are knitted together to form sheets to give porous carbon frameworks(PCFs) [19]–[21], graphene [22] and rGO [18]. In this study, we have observed that the reduction of the Co_3O_4 by the carbons at high temperatures (> 200 °C) altered the physical structure of the carbons and suggests that this phenomenon might also be present in other carbon supports.

6.2 Experimental

$Co(OAc)_2.4H_2O$ (ACS reagent, ≥98.0 %) and benzyl alcohol (BA) anhydrous (99.8 %) were purchased from Sigma-Aldrich, South Africa. Ammonia solution (25 %) was purchased from Associated Chemical Enterprises (ACE), South Africa. Ethanol (EtOH, 98%) and acetone (98 %) we purchased from MK Labs, South Africa. Ultra-high purity hydrogen (H_2, 99.999 %) and nitrogen gas (N_2, 99.99 %), as well as *syngas*: $H_2/CO/N_2$ mixture (~60/30/10vol., purity: 99.99%) and air (21% oxygen/ balance N_2) was supplied by Afrox, South Africa. All chemicals were used as received.

6.2.1 Preparation

6.2.1.1 Synthesis of Co_3O_4

Co_3O_4 nanoparticles were synthesized using the benzyl-alcohol route as reported by Wolf et al. with modification [23]. Typically, 3.2 g of $Co(OAc)_2.4H_2O$ in a 600 mL beaker was dissolved in 140 mL BA and continuously stirred for 2 h. Thereafter, 140 mL NH_4OH (25 %) was added dropwise (through a separating funnel) to form a brown emulsion. Distilled water (70 mL) was then added to the mixture. Adding water to the precursor mixture increases the resulting particle sizes of the metal oxide [23]. The mixture was then transferred into a 1 L flat bottom flask equipped with a magnetic stirrer bar (8×30 mm) and placed inside an oil bath (165 °C) on a magnetic stirrer with a hotplate and a thermocouple to measure the temperature of the oil bath. The mixture was allowed to react for 3 h. Air was flushed through the system to help accelerate the Co oxidation reaction. Upon completion of the reaction, the reaction mixture was cooled to room temperature. After cooling, 120 mL diethyl ether was added to the mixture and nanoparticles were obtained after centrifugation at 15000 rpm for 15 min. These nanoparticles were washed several times with ethanol (EtOH), thereafter re-dispersed in a mixture of EtOH and acetone (3:1 ratio) and finally allowed to dry in a fume hood for three days. It is important to mention that the nanoparticles were shown to be spinel Co_3O_4 (35 % yield) without calcination.

6.2.1.2 Synthesis of the supported catalysts

Information regarding the preparation and annealing of CDs has previously been described (and published; see **Chapter 5**) [18]. In this study, the CDs were annealed under a N_2 atmosphere at temperatures ranging from 250 - 700 °C [18] to yield carbon structures for the Co-based FTS studies. The samples studied were made at three temperatures, 250, 400 and 700 °C and were labelled T250, T400 and T700.

The graphene-like sheets (2.7 g - T250, T400 or T700) were dispersed in 600 mL of distilled ethanol (EtOH) in a 1 L beaker placed on a magnetic stirrer and the solution was stirred (with a 8×30 mm magnetic stirrer bar) for 6 h at room temperature under constant stirring. Thereafter, 0.3 g of the Co_3O_4 nanoparticles (*ca.* 15.7 ± 2.7 nm) were dispersed on the carbon by an impregnation method [12] from an aqueous suspension of the graphene-like sheets, and the mixture was allowed to react for 24 h at room temperature. To obtain the solid samples of Co_3O_4/Tx (were x= 250, 400 or 700 °C), the alcohol media was removed by rotary evaporation at 60 °C.

6.2.1.3 Material characterization

The morphology of the prepared samples was studied using TEM images obtained on a FEI G2 TECNAI Spirit T12 transmission electron microscope at an accelerating voltage of 120 kV and for high resolution imaging, a JEOL JEM 2100 equipped with a LaB6 gun. Textual properties based on the nitrogen adsorption−desorption isotherms and the Brunauer−Emmett−Teller (BET) surface areas were determined from a Micromeritics Flow Prep 060 unit in the relative pressure range P/P_0 = 0.05–0.30, and the total pore volumes of the samples were calculated at a relative pressure of P/P_0 = 0.995. The Barrett-Joyner-Halenda (BJH) pore size distributions were calculated by analysing the desorption data of the N_2 isotherms. Thermogravimetric analysis (TGA) was determined out using a PerkinElmer STA6000 analyser. The experiments were carried out in air (flow of 10 sccm) where N_2 was used as a purge gas and the samples were heated from 35 to 900 °C at a heating rate of 10 °C/min.

The reducibility of Co_3O_4 nanoparticles to metallic Co catalysts supported on T250, T400 or T700 was monitored both by hydrogen temperature-programmed reduction (H_2-TPR) and *in-situ* powder X-ray diffraction (PXRD) techniques. The reduction experiments were conducted under both H_2 and N_2 in order to gain insights into the autoreduction effect. A Micromeritics AutoChem II unit fitted with a thermal conductivity detector (TCD) was used for H_2-TPR studies, and the reduction measurements were taken from room temperature to 900 °C at the rate of 10 °C/min. 5 %H_2/ 95%Ar gas was used as a reducing gas, and the flow rate was kept at 45

sccm. The gas flow was monitored using Brooks mass-flow controllers. *In situ* PXRD studies were performed on a Bruker D8 Advance diffractometer equipped with an Anton Paar XRK 900 reaction furnace. A CuK$\alpha_{1/2}$ radiation source and VÅNTEC PSD detector was used. Data was collected in the scan ranging from 10 ° to 80 ° 2θ with a step size of 0.028 ° with a total scan time of 1 h. 99.9 % H_2 gas was blended in N_2 gas using a mass flow controller system. The H_2 was used as a reducing gas, and for autoreduction studies; the N_2 gas (99.9 %) was used to create an inert atmosphere. Under both H_2 and N_2 atmospheres, the gas flow rate was kept at *ca.* 50 sccm. Phase identification was done using a Bruker AXS Diffrac.EVA V.4.0 and a local copy of the Crystallography Open Database (COD). Further information such as the relative phase abundance, the degree of crystallinity, and the estimated microstructures, were obtained via Rietveld refinement of the PXRD data using TOPAS V4.2 [24].

To determine the quality of the *in situ* PXRD data, a graph of the Rietveld refinement of the diffraction pattern of Co_3O_4/T700 obtained at 550 °C (under H_2 conditions) was measured (**Figure S6.1)**. By visual inspection of the data, one can note that the observed data and the calculated (i.e. model) data show reasonably good agreement based on the difference curve (blue glaph) produced being very flat with only a few features (at *ca.* 43 ° and 51 ° 2θ) that were not accounted for. These features may be attributed to the lattice strain, the crystallite size effect and/or deficiency in the model that describes the optics of the diffractometer (error during instrument alignment). The goodness of fit (i.e. the measure of the statistical significance of fit) was 1.06, suggesting that the model did not over characterize the data set. The value of the residual weight profile (RWP, i.e. how well the structure model fitted the data) for this data was 1.6 %, which is significantly lower compared to the typical values (around 5 to 15 %) which suggest that the data has low information content (i.e. not enough PXRD peaks to describe the data) relative to what is expected from the technique. The weighted Durbin Watson was 1.79, and the ideal value of this calculation is 2. Therefore, this implies that the data has very minor serial correlation.

6.2.1.4 Catalytic activity

The FTS reactions were performed in a tubular fixed-bed stainless-steel reactor (i.d. = 16 mm). The Co_3O_4/Tx catalysts (x= 250, 400 or 700 °C) with *ca.* 0.5 g mass was first reduced under H_2 (45 sccm) at 350 °C (450 °C for autoreduction studies) for 18 h with the pressure set at 2 bar. The reactor was allowed to cool to room temperature before being heated again to 220 °C and the gas was then switched to a *syngas* mixture (30 % CO, 60 % H_2 and 10 % Ar) with a

flow rate of a 20 sccm and a pressure of 10 bar at (STP) for 50 h. The activity (according to % CO conversion) and hydrocarbon selectivity were monitored using online gas chromatographs coupled to a thermal conductivity detector (GC-TCD) and a flame ionization detector (GC-FID) connected to the gas line. Two hot and cold traps connected after the fixed-bed reactor were kept at 150 °C and room temperature, respectively, and were used to collect wax and oil products (if any) after reaction. The CO conversion, selectivity of C_{5+} hydrocarbons and chain growth probability (α value) were used to evaluate the FTS performance. The CO conversions and the selectivities of the hydrocarbons and CO_2 were calculated using the following formulae:

$$X_{CO} = \frac{F_{CO,in-F_{CO,out}}}{F_{CO,in}} \times 100\ \%$$

$$S_{CH_4} = \frac{F_{CO_2,out}}{F_{CO,in}-F_{CO,out} - F_{CO_2,out}} \times 100\ \%$$

$$S_{CO_2} = \frac{F_{CO_2,out}}{F_{CO,in}-F_{CO,out}} \times 100\ \%$$

$$S_{C_x} = \frac{F_{C_x,out}}{F_{CO,in}-F_{CO,out} - F_{CO2,out}} \times 100\ \%\ (x = 2-4)$$

$$S_{C_{5+}} = 100\ \% - S\ (CH_4) - S(C_x)$$

where *F* is the molar flow rate of each component, and *S* is the % selectivity.

6.3 Results and discussion

6.3.1 Synthesis and characterization of Co_3O_4

The TEM images as well as the size distribution images of the Co_3O_4 particles that were prepared for this study, are shown in **Figures 6.1a)-b)**. Their structure resembles that of a nanocube, as noted previously [23]. The particle sizes (measured as the length of the cube) ranged between 11 and 20 nm, with an average size of 15.7±2.7 nm. **Figure S6.2a)** shows a PXRD pattern of the nanoparticles, and phase identification of this data indicated the presence of the spinel Co_3O_4 crystalline phase. Reduction under hydrogen gave a classical H_2-TPR profile of the Co_3O_4 as shown in **Figure S6.2b)**. The results are similar to the classical two reduction steps of Co_3O_4 at *ca.* 240 °C and 340 °C, which are typically associated with the reduction of Co_3O_4 to CoO and CoO to Co^0, respectively [25].

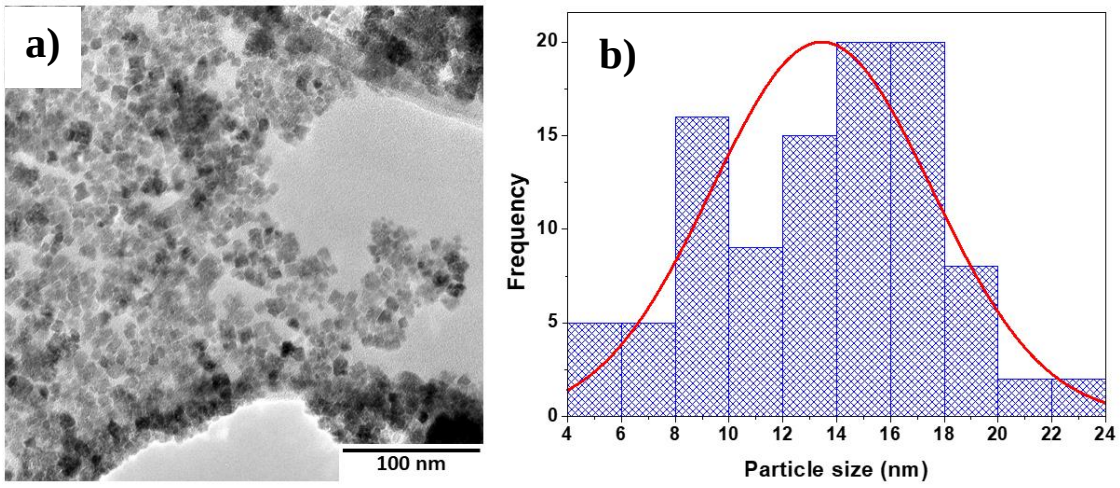

Figure 6. 1: a) TEM image and **b)** particle size distribution measured from TEM images of the Co_3O_4 nanoparticles.

6.3.2 Synthesis and characterization of Co/CD derived graphene

The synthesized CDs had particle sizes that ranged between 1 and 4 nm, and an average diameter of 2.5 ± 0.2 nm, as reported previously (see **Figure S5.2** in **Chapter 5**) [30]. The estimated sheet sizes of the resulting graphene-like sheets (T400 and T700) are recorded in **Table S6.1**. T250 did not form sheet materials but gave a type of accreted turbostratic carbon structure. TEM images of T250-T700 before Co_3O_4 nanoparticle addition are shown in **Figure 6.2a-c**.

Co_3O_4 was added to the carbons and TEM images (see **Figure 6.2d-f**) showed that the Co_3O_4 nanoparticles were well dispersed on the graphene-like carbon supports. For Co_3O_4/T250, the Co_3O_4 nanoparticles were clearly observed in the HRTEM images (**Figure S6.3**). The images indicated the presence of a 0.2829 nm lattice *d*-spacing, corresponding to the (220) lattice spacing of the cubic spinel Co_3O_4 phase [26]. There was no significant change observed in the support materials before and after the addition of the metal nanoparticles.

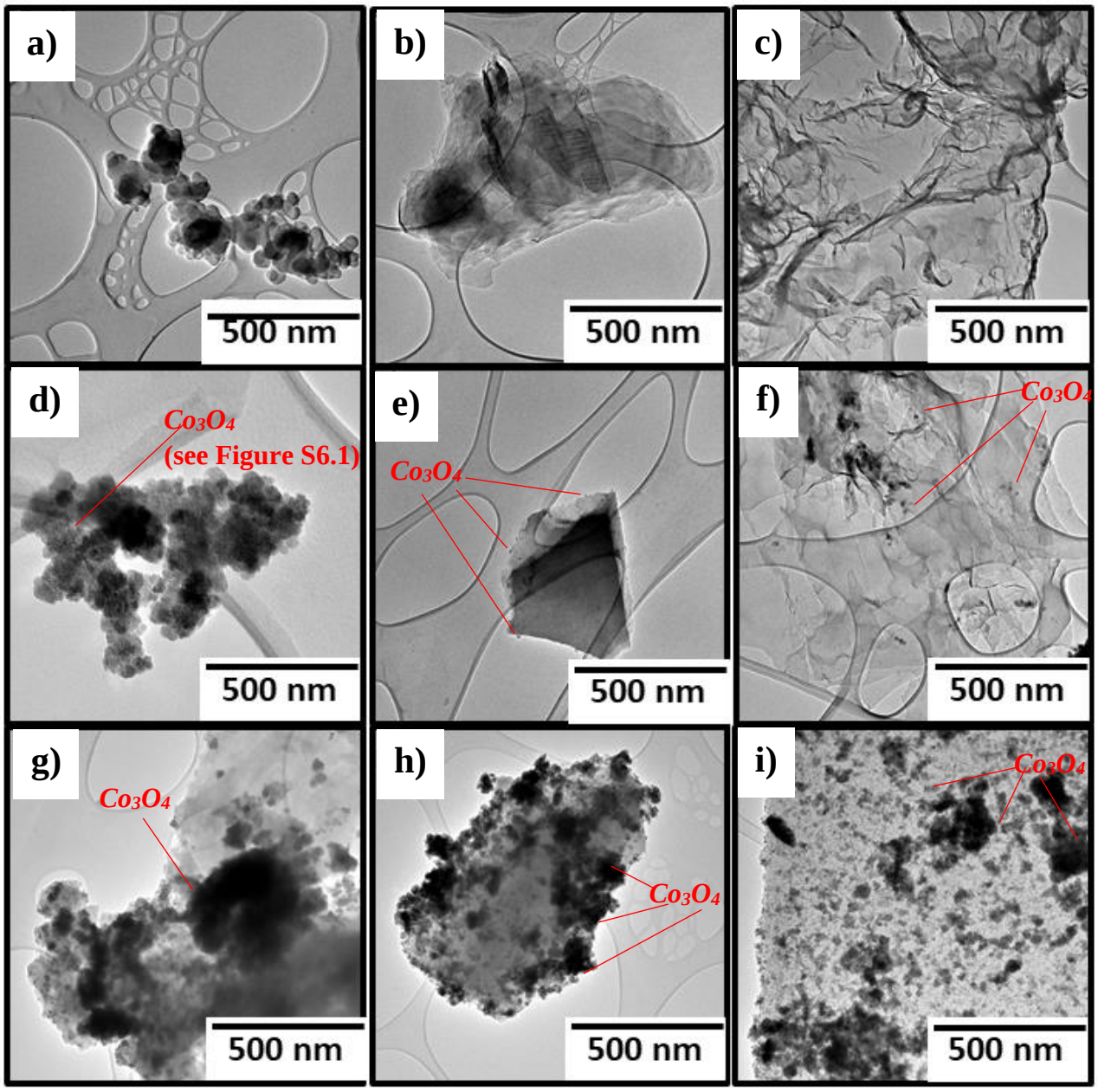

Figure 6. 2: TEM images of samples after autoreduction. Before FTS **a)** T250, **b)** T400 and **c)** T700, **d)** Co_3O_4/T250, **e)** Co_3O_4/T400, **f)** Co_3O_4/T700 and after FTS. **g)** Co_3O_4/T250, **h)** Co_3O_4/T400, and **i)** Co_3O_4/T700.

The obtained BET analysis results (before and after Co_3O_4 nanoparticle addition) are summarized in **Table S6.1**, and the BET isotherms are shown in **Figure S6.4**. It is clear that both the surface area and pore volume before and after Co_3O_4 addition are very low compared to the typical surface areas reported for GNSs (> 100 m^2/g [9], [10]). This is typical of non-porous

samples. The specific surface area increased slightly when the catalyst was added to the support [27].

TGA was conducted on the samples to determine the thermal stability and the approximate metal catalyst loading on the T250-T700 catalysts. The TGA data showed that the T250-T700 catalyst samples decomposed in air at *ca.* 600 °C. The % Co_3O_4 loading was calculated from the residue left after the complete thermal decomposition of carbon [27], [28] and found to be *ca.* 11.4 %, 10.5 % and 9.6 % for Co_3O_4/T250, Co_3O_4/T400 and Co_3O_4/T700, respectively, close to the theoretical value of 10 % (see **Figure S6.5**). The derivative weight loss thermograms of the samples are shown in **Figure 6.3**. Comparing the thermograms before and after loading of the Co_3O_4 nanoparticles, it can be observed that the onset decomposition starts at slightly lower temperatures when in the presence of the Co_3O_4 nanoparticles. However, the final decomposition temperature of the carbon samples increased significantly. Typically, decomposition temperatures of carbon decrease in the presence of a metal catalysts. This is because the metal catalyst catalyses the decomposition of carbon [13], [29]. Therefore, the increase in the decomposition temperature of carbons in this study may result from the slightly strong metal to support interactions (MSIs) which may increase the activation energy needed for carbon decomposition. Additionally, the increase in thermal decomposition temperature could mean that the Co_3O_4 nanoparticles are embedded within the carbon structure in such a way that it remains inactive, and unable to facilitate catalytic thermal decomposition. Then, at higher TGA temperature, as the carbon is decomposed, the catalysts get exposed, and then potentially help facilitate thermal decomposition of the carbon support. To confirm this speculation, further studies such as HRTEM to find out whether the catalyst nanoparticles are covered by the carbon support or not, as well as the extent of this coverage will be needed.

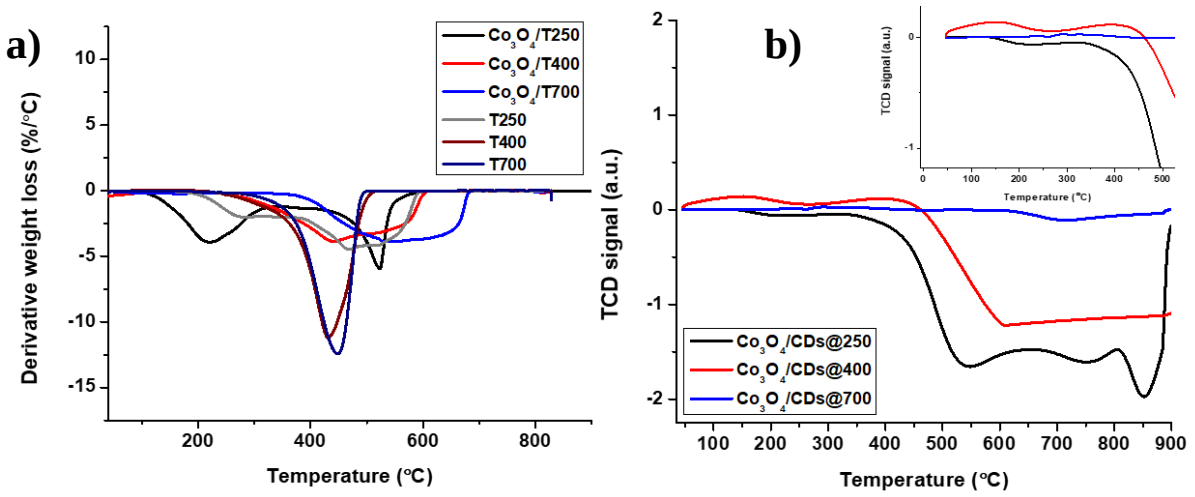

Figure 6. 3: a) DTG curves of T250, T400 and T700 with and without Co_3O_4, and **b)** H_2-TPR profiles of Co_3O_4/250, Co_3O_4/T400 and Co_3O_4/T700 (inset: expanded regions below 500 °C).

The reduction of Co_3O_4 to metallic Co on the supported catalysts was studied using H_2-TPR. The H_2-TPR profiles in **Figure 6.3b)** did not clearly show the two-step reduction peaks associated with Co_3O_4 (as shown in **Figure 6.3b)** insert), only small 'humps' (relative to baseline) with TCD signal values around zero were observed. The large peaks above *ca.* 500 °C are associated with the metal-assisted catalytic methanation of the carbon support [29]. It is clear that the reduction of the carbon (to CH_4) dominates the profiles.

6.3.2.1 Autoreduction investigations of the supported Co_3O_4

In situ PXRD experiments (from 30 to 550 °C) were conducted to evaluate the phase transformation of the Co viz. $Co_3O_4 \rightarrow CoO \rightarrow Co^0$ (both Co(fcc) and Co(hcp)) for the supported catalysts under two different gas atmospheres, H_2 and N_2. It has been reported that unsupported Co_3O_4 is reduced to metallic Co without going through the intermediate phase, CoO. This typically takes place at temperatures < 200 °C under pure H_2 [30]. This reduction temperature is affected by the Co morphology and size, as well as the presence of a support material and the type of reducing agent used [30], [31]. For the samples prepared in this study, the reduction of Co_3O_4 to Co^0 under both H_2 and N_2 is seen to occur via the intermediate, CoO.

Full details of the quantitative and qualitative data from *in situ* PXRD results of all samples under H_2 and N_2 are given in **Figure S6.6**, **Table 6.1** and **Table S6.2**. **Figure 6.4** shows data chosen to highlight features of the reduction reaction for Co_3O_4/T250 and Co_3O_4/T700. The Co_3O_4/T250 and the Co_3O_4/T700 samples show significantly different results.

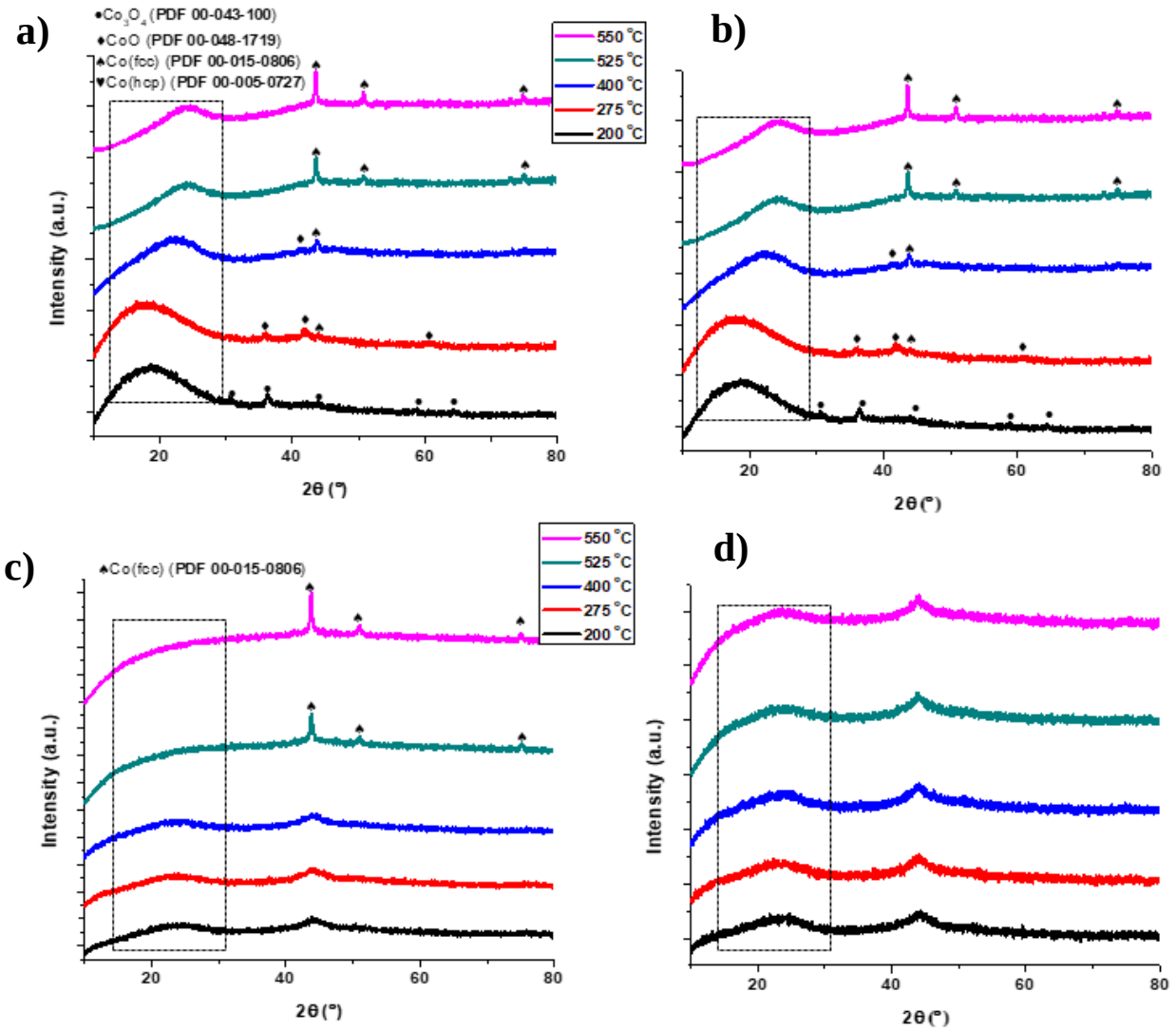

Figure 6. 4: *In situ* PXRD plot of **a)-b)** Co_3O_4/T250, and **c)-d)** Co_3O_4/T700 samples under H_2 (left) and N_2 (right) analysed at discrete temperatures of 200 to 550 °C. The region in the dotted box shows the contribution of the carbon support to the PXRD pattern and the changes that occur as a result of an increase in temperature.

Table 6.1: Phase quantification and structural details of the Co_3O_4/T250, Co_3O_4/T400 and Co_3O_4/T700 catalysts obtained via Rietveld Refinement of the data collected *in situ* PXRD experiments.

Sample name	Temperature (°C)	Phase ID	% of each phase	Microstructure (approx. sizes)	Degree of crystallinity (%) of metal
Co_3O_4/T250_H_2	200	Co_3O_4	100	15.0 ±1.9	97.18
	275	CoO , Co(fcc)	94.40 5.60	11.4 ±0 x	98. 22 99.9
	400	CoO , Co(fcc)	20.43 79.57	21. 8 ±0 29.6±0	99.66 98.68
	525	Co(fcc)	100	50±0	96.89
	550	Co(fcc)	100	62.3±6.8	96.89
Co_3O_4/T250_N_2	200	Co_3O_4	100	13.7 ±0	97.37
	275	CoO	98.90	10.9±0	97.98
	400	CoO , Co(fcc)	73.87 26.13	11.6 ±0 10.0±0	97.3 99.18
	525	Co(fcc)	100	49.4±0	97.35
	550	Co(fcc)	100	62.3±6.8	97.16
Co_3O_4/T400_H_2	200	Co_3O_4	100	17.3 ±0	95.65
	275	Co(fcc)	100	x	99.04
	400	Co(fcc) Co(hcp)	84.12 15.88	31.4 ± 8.1	98.72
	525	Co(fcc)	100	58.8 ± 4.8	99.28
	550	Co(fcc)	100	60.9 ± 4.6	97.15
Co_3O_4/T400_N_2	200	Co_3O_4	100	18.3 ±0	94.65
	275	CoO	100	14±0.9	95.91
	400	CoO ,	100	13.0	96.26
	525	Co(fcc)	100	46.1 ± 2.9	96.41
	550	Co(fcc)	100	63.3 ± 3.6	96.82
Co_3O_4/T700_H_2	200	Co_3O_4	100	16.1 ± 1.8	4.51
	275	Co_3O_4	100	10.1 ± 1.4	2.12
	400	CoO, Co(fcc)	9 91	13.2 ± 11.3 26.0 ± 4.4	1.32
	525	Co(fcc)	100	64.3 ± 6.2	2.13
	550	Co(fcc)	100	69.7 ± 6.5	2.59
Co_3O_4/T700 _N_2	200	-	-	-	-
	275	-	-	-	-
	400	-	-	-	-
	525	-	-	-	-
	550	-	-	-	-

-: No crystallographic phases were detected x: microstructure sizes could not be determined

**: Estimated % of each crystalline component in the analysis that contributes to the overall diffraction pattern*

Reduction under H_2: Under an H_2 atmosphere (275 °C) the Co in the Co_3O_4/T250 catalyst was completely reduced, and *ca.* 94 % of CoO (and *ca.* 5 % Co) was formed. The full transformation of CoO to Co(fcc) was observed at temperatures above 400 °C. For the Co_3O_4/T400 catalyst, the data shows that the reduction of the Co_3O_4 to CoO has started at 225 °C (**Figure 6.5a)**) and that the CoO phase was fully reduced to the Co(fcc) phase at 275 °C.

For the Co_3O_4/T700 catalyst, the Co was only observed at 400 °C, where CoO (*ca.* 9 %) and Co(fcc) (*ca.* 91 %) were formed. Above this temperature, only the Co(fcc) phase was observed.

Reduction under N_2: Under a N_2 (inert) atmosphere, the support materials induce the autoreduction of Co_3O_4 via the same reduction route (spinel $Co_3O_4 \rightarrow CoO \rightarrow Co^0$) as observed under an H_2 atmosphere (**Figure 6.5b))**. However, reduction takes place at elevated temperatures compared to the reduction under H_2 [12], [13]. For the Co_3O_4/T250 catalyst, the Co_3O_4 to CoO transition was observed from 275 °C (*ca.* 98.90 %) and the completion of this transition was only observed at 400 °C. Under a H_2 atmosphere, complete reduction was also observed at 400 °C. Under N_2 atmosphere, Co(fcc) phase started to appear at 300 °C (**Figure 6.5b)**), but at 400 °C, CoO was still the most abundant Co-containing phase at this temperature (*ca.* 73.87 %). At 500 °C the CoO was fully reduced to Co(fcc). Under a H_2 atmosphere, at 400 °C, only *ca.* 20.42 % CoO was observed, and the full conversion of CoO to Co(fcc) was first observed at 425 °C (**Figure 6.5a)**). Similar results were noted for the Co_3O_4/T400 catalyst. Here the Co_3O_4 to CoO reduction started at 225 °C and full reduction was observed at 500 °C under N_2. In contrast, the full reduction was observed at 275 °C when using a H_2 atmosphere. For the Co_3O_4/T700 catalyst, however, the CoO and Co phases were not clearly observed in the *in situ* PXRD data even at high reduction temperatures. This could mean that i) the support could not reduce the Co_3O_4, ii) the Co_3O_4 was spontaneously reduced prior to the *in situ* PXRD measurements or iii) that the reduced Co crystallites were too small to be detected by laboratory based PXRD.

It is also noted that the final Co^0 phase formed in all the experiments was Co(fcc). However, the Co_3O_4/T400 catalyst showed that at 400 °C, some Co(hcp) was also observed (**Figure S6.6e)**), but as the reduction temperature was increased further, this Co(hcp) phase was converted to the thermodynamically more stable Co(fcc).

In contrast to reactions performed in the H_2 atmosphere, reduction of Co_3O_4 under N_2 is much more rapid with the increase in oxygen content on the support, i.e., T400→T250. Two more

reactions were performed using a sample made of CDs annealed at 300 °C and 10 % Co_3O_4 (Co_3O_4/T300), shown in **Figure S6.6c)-d)** and **Table S6.1**. This sample also showed that the reduction of Co_3O_4 takes place at higher temperatures under a N_2 atmosphere. Furthermore, the CoO to Co^0 reduction reaction took place at temperatures above 400 °C, similar to the Co_3O_4/T400 catalyst. This further suggests that the reduction properties of the carbon decreases with a decrease in concentration of the oxygen moieties on the carbon surface. A mechanism to explain the data is given later.

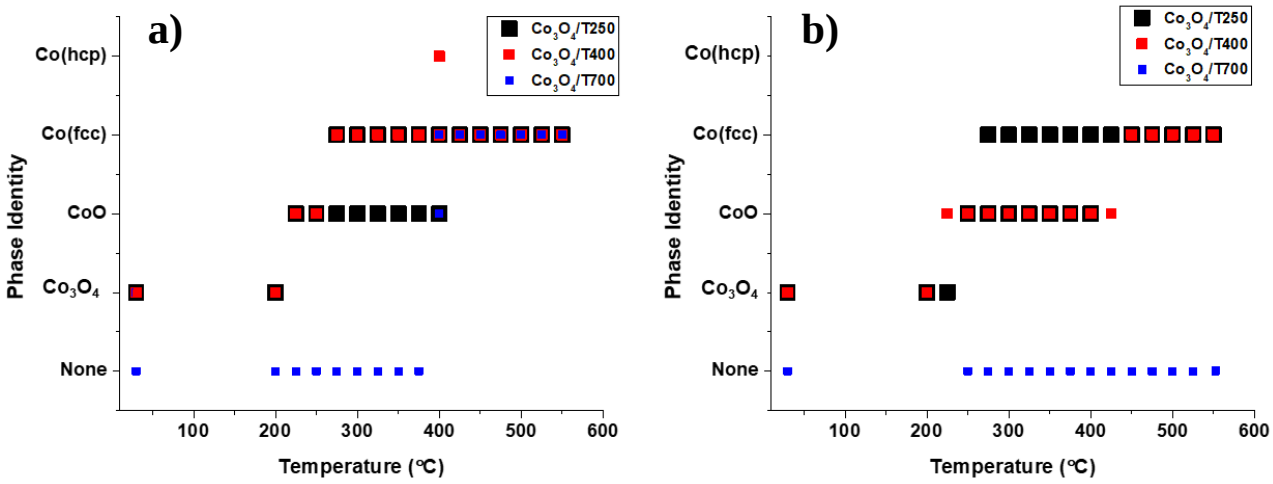

Figure 6. 5: The support effect on cobalt phase transformation at different temperatures under **a)** H_2 and **b)** N_2 atmosphere.

Crystallite sizes: Not unexpectedly, a significant increase in the calculated crystallite sizes of the observed Co phases with increase in temperature occurred for all the samples and the data are shown in **Table 6.1** and **Table S6.2** The crystallite sizes of the Co increased from ~10-18 nm for Co_3O_4 to > 60 nm for the resulting Co(fcc) phase at 550 °C. It is typical for Co metal supported on carbon allotropes to sinter since the MSI effects are weaker than for metal oxide supported catalysts [8], [12]. However, it is often believed that functionalizing the carbon support, especially with oxygen functional groups can improve the MSI effect and consequently decrease the degree of sintering [8], [12]. The carbon allotropes used in this study each have an estimated XPS oxygen content of *ca.* 23 %, 17 % and 15 % for T250, T400 and T700, respectively. This oxygen content results from the presence of hydroxyl, carbonyl and carboxyl functional groups [18]. Stronger MSIs and reduced Co metal sintering were expected to correlate with the O content. But as seen in the data discussed above, this was not observed.

Summary: The effect of the support, temperature, reducing atmosphere and phase identity of the Co (and C containing phases) are summarised in **Figure 6.5a)-b).**

1. The reduction of Co in the Co_3O_4/T250 catalyst occurs under both N_2 and H_2 and they produce similar results. H_2 is the better reducing agent (see **Figure 6.4**) but the reduction under N_2 is readily achieved.
2. The reduction of Co in the Co_3O_4/T700 catalyst is very different. Here, there is no evidence that Co reduction has occurred under N_2. The TGA residue showed the presence of ~ 10 % Co after T700 decomposition, confirming that the Co was successfully incorporated into the carbon support. It is possible that in this sample that Co_3O_4 autoreduction occurred before the sample was exposed to the high temperature treatment. The *in situ* PXRD feature at *ca.* 45 ° 2θ may be associated with the Co(fcc) phase, as it corresponds to the major peak observed for the Co(fcc) phase. However, further studies such as X-ray photoelectron spectroscopy (XPS) analysis of the Co_3O_4/T700 before and after *in situ* PXRD analysis will be required to determine the elemental composition of the sample. Additionally, magnetic measurements using an *in situ* magnetometer (based on the Weiss extraction method) will help identify the cobalt phase present. This type of magnetometer is only sensitive to magnetic Co and in this case, the Co metallic phase [32]. Therefore, this technique could be able to confirm whether the Co in the Co_3O_4/T700 sample was reduced *in situ* before temperature treatment or not.
3. The carbon feature at *ca.* 20-25 ° 2θ shifts with temperature for the Co_3O_4/T250 catalyst under both N_2 and H_2 atmospheres. The same shift in the PXRD feature was observed when the carbon support was heated in the absence of Co [18].
4. Little to no shift in the aforementioned carbon peak is observed for the Co_3O_4/T700 catalyst under either N_2 or H_2 atmosphere. This was not unexpected as the carbon had been reheated to 700 ℃ prior to the *in-situ* PXRD reaction.

6.3.2.2 Auto reduction mechanism

Studies have reported that the autoreduction of metals by carbon can occur by two routes. In the first route, and in the case of a curved carbon allotrope, a sp^3 type C is rehybrized to a sp^2 type C at the edge of a carbon structure, consequently making the carbon susceptible to electron donation to a metal oxide [13], [16]. In a second route, Park *et al.* reported that the reduction

of Co_3O_4 to metallic Co is facilitated by the CO that is released during the decomposition of the carbon support [15]. In this study, the surface of the carbon contains oxygen functional groups, and the allotropes are more closely related to graphene than CNTs and CSs, that are curved. During heat treatment, the functional groups decompose, and CO is released. The CO that is released interacts with the Co_3O_4 and is oxidised to CO_2, while reducing the metal oxide to its metallic phase (**Figure 6.6)**.

In this study, the Co reduction took place at a lower temperature in the Co_3O_4/T400 catalyst when compared to the Co_3O_4/T250 catalyst. This may be attributed to the strong MSIs in the Co_3O_4/T250 catalyst, induced by the surface functionalities in T250 interacting with the metal catalyst. The XPS, PDF, FT-IR and NMR studies in our previous publication (**Chapter 5**) [18] showed that the amount of oxygen functional groups on the surface of this support material-decreased in the following manner, i.e., T250 <T400 <T700. Hence it is expected that the strength of MSIs will decrease from Co_3O_4/T250 > Co_3O_4/T400 >Co_3O_4/T700.

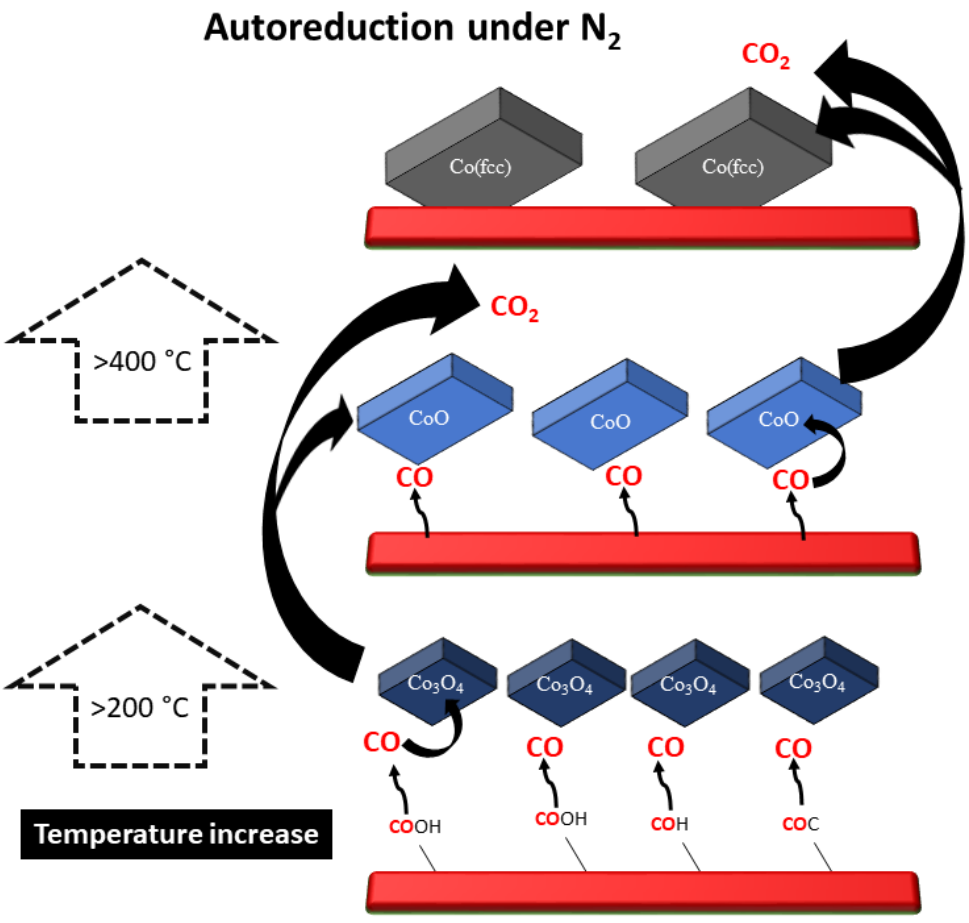

Figure 6. 6: A graphical illustration of possible Co oxide autoreduction mechanism when the released CO act as reducing agents.

6.3.3 Fischer-Tropsch synthesis evaluation

The FTS performance of the various catalysts was studied under similar reaction conditions (10 bar and 220 °C) and the data are shown in **Table 6.2**. The FTS performances of the H_2 reduced supported catalysts was compared with the performance of equivalent unsupported catalysts under the same reaction conditions. The unsupported Co catalyst gave a very high % CO conversion with selectivity towards C_{5+} (81.9 %) hydrocarbons, a low methane (CH_4) conversion (0.9 %), and high cobalt specific activity (39.7 $\mu mol_{CO}/sec.g_{Co}$) compared to the other catalysts. Sintering of the metal catalysts was observed, as shown by a TEM image of the spent catalyst in **Figure S6.7**. The supported catalysts showed a lower % CO conversion. The % CO conversion followed the order Co_3O_4/T400 (14.2 %) > Co_3O_4/T700 (13.0 %) > Co_3O_4/T250 (9.9 %). This order was in agreement with the *in situ* PXRD results discussed earlier, which showed that Co_3O_4 in the Co_3O_4/T400 catalyst was rapidly reduced. However, product distributions showed that these supported catalysts were selective towards CH_4 (> 30 %) with small amounts of C_{5+} (< 30 %) produced, and the C_{5+} selectivity increase followed the order: Co_3O_4/T700 >Co_3O_4/T400> Co_3O_4/T250. The low % CO conversion results from sintering and subsequent deactivation of the metal catalyst. Some of the CH_4 content may be due to catalysed methanation of the support materials at elevated temperatures. The support methanation was higher for carbon supports with a higher oxygen content (T250> T400> T700). It is possible that as the carbonyl and carboxyl groups of the support are removed, the H_2 gas also hydrogenates these CO-x groups to form methane while some CO_2 (> 5 %) gets released as well. The Co_3O_4/T700 reduced under H_2 conditions showed better overall selectivity towards C_{5+} compared to the other supported catalysts. This may be due to the better structural stability of this support compared to the other support materials.

In the autoreduction studies, Co_3O_4/T250, Co_3O_4/T00 and Co_3O_4/T700 were reduced at 450 °C for 18 h. At this temperature, all the Co_3O_4 was converted to metallic Co, as confirmed by *in situ* PXRD data. The autoreduced catalysts, however, showed lower % CO conversion compared to the H_2 reduced catalysts, as well as a lower selectivity towards C_{5+} hydrocarbons and high selectivity towards CH_4. The activities and selectivities of these catalysts were similar. The large amount of CO_2 formed may be due to the CO_2 produced after the autoreduction, (see **Figure 6.6)**. The TEM images of the spent catalysts showed sintered particles (**Figure 6.2g)-i)**). The final products showed large aggregates of the metal catalyst. The crystallite sizes obtained in the *in situ* PXRD experiments were different to the TEM data as the reactions were performed under very different conditions.

Table 6.2: The FTS performances of the prepared catalysts under different conditions

Catalyst name	CO % conversion	Activity ($\mu mol/sec.g_{Co}$)	CO_2 selectivity	Hydrocarbon selectivity (%)					α
				CH_4	C_2	C_3	C_4	C_{5+}	
Co_3O_4	78.9	39.7	0.1	0.9	3.9	4.2	9.0	81.9	0.87
Co_3O_4/T250-H_2	9.9	8.2	6.6	38.2	11.3	12.1	14.6	17.2	0.45
Co_3O_4/T250-AR	8.5	6.8	8.4	42.3	12.8	12.5	9.5	14.5	0.39
Co_3O_4/T400-H_2	14.2	9.0	8.0	34.1	14.5	12.0	10.3	21.1	0.48
Co_3O_4/T400-AR	7.9	6.3	7.9	41.3	12.0	13.7	10.5	14.6	0.43
Co_3O_4/T700-H_2	13.0	7.4	6.1	33.4	20.1	10.1	4.4	27.0	0.52
Co_3O_4/T700-AR	9.1	5.3	8.1	39.3	13.0	14.6	10.0	15.0	0.49

Reaction conditions: H_2/CO = 2, Temperature=220 °C, Pressure =10 bar, time of stream = 50 hrs. *AR = auto reduced at 450 °C*

6.4 Conclusion

The results obtained from this study shows that graphene-based sheets (GNSs), like other carbons can autoreduce Co_3O_4 to Co(fcc). This reduction requires higher temperatures (> 400 °C) when compared to the Co reduction under H_2. The autoreduced Co did not show improved % CO conversion as well as enhanced C_{5+} selectivity when compared to the reduction under H_2, different from literature reports using Co that had been formed by carbon autoreduction. This related to the structural integrity of the carbon support used in this study, which may have affected the catalysts reducibility and overall performances. The results from this study suggests that there is a limit to the amount of surface functional groups necessary for anchoring the metal particles, as too high an oxygen content on the carbon support contributes to the loss of structural integrity of the support under high temperatures. It shows that there is a need to balance the amount of carbon surface functionalization that will allow metal dispersion and stability without compromising the stability of the support materials.

6.5 References

[1] Z. Gholami, Z. Tišler, and V. Rubáš, "Recent advances in Fischer-Tropsch synthesis using cobalt-based catalysts: a review on supports, promoters, and reactors," *Catal. Rev. - Sci. Eng.*, vol. 63, pp. , 512–595, 2020, doi: 10.1080/01614940.2020.1762367.

[2] A. H. Sahir, Y. Zhang, E. C. D. Tan, and L. Tao, "Understanding the role of Fischer–Tropsch reaction kinetics in techno-economic analysis for co-conversion of natural gas and biomass to liquid transportation fuels," *Biofuels, Bioprod. Biorefining*, vol. 13, no. 5, pp. 1306–1320, 2019, doi: 10.1002/bbb.2035.

[3] P. K. Gupta, V. Kumar, and S. Maity, "Renewable fuels from different carbonaceous feedstocks: a sustainable route through Fischer–Tropsch synthesis," *J. Chem. Technol. Biotechnol.*, vol. 96, no. 4, pp. 853–868, 2021, doi: 10.1002/jctb.6644.

[4] A. Y. Khodakov, W. Chu, and P. Fongarland, "Advances in the development of novel cobalt Fischer − Tropsch catalysts for synthesis of long-chain hydrocarbons and clean fuels," *Chem. Rev.*, vol. 107, no. 5, 1692–1744 pp. 1692–1744, 2007, doi.org/10.1021/cr050972v.

[5] H. Tian, X. Li, L. Zeng, and J. Gong, "Recent advances on the design of group VIII base-metal catalysts with encapsulated structures," *ACS Catal.*, vol. 5, no. 8, pp. 4959–4977, 2015, doi: 10.1021/acscatal.5b01221.

[6] M. Rahmati, B. Huang, M. K. Mortensen Jr., K. Keyvanloo, T. H. Fletcher, B. F. Woodfield, W. C. Hecker and M. D. Argyle, "Effect of different alumina supports on performance of cobalt Fischer-Tropsch catalysts," *J. Catal.*, vol. 359, pp. 92–100, 2018, doi: 10.1016/j.jcat.2017.12.022.

[7] S. J. Tauster, S. C. Fung, R. T. K. Baker, and J. A. Horsley, "Strong interactions in supported-metal catalysts," vol. 211, no. 4487, pp. 1121–1125, 1981.

[8] H. Xiong, L. L. Jewell, and N. J. Coville, "Shaped carbons as supports for the catalytic conversion of syngas to clean fuels," *ACS Catal.*, vol. 5, no. 4, pp. 2640–2658 2015, doi: 10.1021/acscatal.5b00090.

[9] S. Karimi, A. Tavasoli, Y. Mortazavi, and A. Karimi, "Cobalt supported on graphene - A promising novel Fischer-Tropsch synthesis catalyst," *Appl. Catal. A Gen.*, vol. 499, pp. 188–196, 2015, doi: 10.1016/j.apcata.2015.04.024.

[10] Z. Hajjar, M. Doroudian Rad, and S. Soltanali, “Novel Co/graphene oxide and Co/nanoporous graphene catalysts for Fischer–Tropsch reaction,” *Res. Chem. Intermed.*, vol. 43, no. 3, pp. 1341–1353, 2017, doi: 10.1007/s11164-016-2701-x.

[11] H. O. Torshizi, A. Nakhaei Pour, A. Mohammadi, Y. Zamani, and S. M. Kamali Shahri, “Fischer-Tropsch synthesis by reduced graphene oxide nanosheets supported cobalt catalysts: Role of support and metal nanoparticle size on catalyst activity and products selectivity,” *Front. Chem. Sci. Eng.*, vol. 15, no. 2, pp. 299–309, 2021, doi: 10.1007/s11705-020-1925-x.

[12] H. Xiong, M. A. M. Motchelaho, M. Moyo, L. L. Jewell, and N. J. Coville, “Correlating the preparation and performance of cobalt catalysts supported on carbon nanotubes and carbon spheres in the Fischer-Tropsch synthesis,” *J. Catal.*, vol. 278, no. 1, pp. 26–40, 2011, doi: 10.1016/j.jcat.2010.11.010.

[13] H. Xiong, M. Moyo, M. K. Rayner, L. L. Jewell, D. G. Billing, and N. J. Coville, “Autoreduction and catalytic performance of a cobalt Fischer-Tropsch synthesis catalyst Supported on nitrogen-doped carbon spheres,” *ChemCatChem*, vol. 2, no. 5, pp. 514–518, 2010, doi: 10.1002/cctc.200900309.

[14] Y. Yang, L. Jia, B. Hou, D. Li, J. Wang, and Y. Sun, “The oxidizing pretreatment-mediated autoreduction behaviour of cobalt nanoparticles supported on ordered mesoporous carbon for Fischer-Tropsch synthesis,” *Catal. Sci. Technol.*, vol. 4, no. 3, pp. 717–728, 2014, doi: 10.1039/c3cy00729d.

[15] H. Park, K. Y. Kim, D. H. Youn, Y. H. Choi, W. Y. Kim, and J. S. Lee, “Auto-reduction behavior of cobalt on graphitic carbon nitride coated alumina supports for Fischer–Tropsch synthesis,” *ChemCatChem*, vol. 9, no. 21, pp. 4098–4104, 2017, doi: 10.1002/cctc.201700613.

[16] W. Chen, X. Pan, M. G. Willinger, D. S. Su, and X. Bao, “Facile autoreduction of iron oxide/carbon nanotube encapsulates,” *J. Am. Chem. Soc.*, vol. 128, no. 10, pp. 3136–3137, 2006, doi: 10.1021/ja056721l.

[17] Y. Yang, L. Jia, B. Hou, D. Li, J. Wang, and Y. Sun, “The effect of nitrogen on the autoreduction of cobalt nanoparticles supported on nitrogen-doped ordered mesoporous carbon for the fischer-tropsch synthesis,” *ChemCatChem*, vol. 6, no. 1, pp. 319–327, 2014, doi: 10.1002/cctc.201300897.

[18] L. L. Mokoloko, B. J. Matsoso, R. P. Forbes, D. H. Barrett, B. D. Moreno, and N. J. Coville, "Evolution of large-area reduced graphene oxide nanosheets from carbon dots via thermal treatment," *Carbon Trends*, vol. 4, p. 100074, 2021, doi: 10.1016/j.cartre.2021.100074.

[19] H. Hou, C. E. Banks, M. Jing, Y. Zhang, and X. Ji, "Carbon quantum dots and their derivative 3D porous carbon frameworks for sodium-ion batteries with ultralong cycle life," *Adv. Mater.*, vol. 27, no. 47, pp. 7861–7866, 2015, doi: 10.1002/adma.201503816.

[20] S. Zhang, J. Zhu, Y. Qing, C. Fan, L. Wang, Y. Huang, R. Sheng, Y. Guo, T. Wang, Y. Pan, Y. Lv, H. Song, and D. Jia, "Construction of hierarchical porous carbon nanosheets from template-assisted assembly of coal-based graphene quantum dots for high performance supercapacitor electrodes," *Mater. Today Energy*, vol. 6, pp. 36–45, 2017, doi: 10.1016/j.mtener.2017.08.003.

[21] L. Borchardt, Q.-L. Zhu, M. E. Casco, R. Berger, X. Zhuang, S. Kaskel, X. Feng and Q. Xu, "Toward a molecular design of porous carbon materials," *Mater. Today*, vol. 20, no. 10, pp. 592–610, 2017, doi: 10.1016/j.mattod.2017.06.002.

[22] Y. Zhang, C. W. Foster, C. E. Banks, L. Shao, H. Hou, G. Zou, J. Chen, Z. Huang and X. Ji, "Graphene-rich wrapped petal-like rutile TiO_2 tuned by carbon dots for high-performance sodium storage," *Adv. Mater.*, vol. 28, no. 42, pp. 9391–9399, 2016, doi: 10.1002/adma.201601621.

[23] M. Wolf, N. Fischer, and M. Claeys, "Surfactant-free synthesis of monodisperse cobalt oxide nanoparticles of tunable size and oxidation state developed by factorial design," *Mater. Chem. Phys.*, vol. 213, pp. 305–312, 2018, doi: 10.1016/j.matchemphys.2018.04.021.

[24] A. Scheer, H. Kruppke, and R. Heib, *Springer-Verlag Berlin Heidelberg GmbH*. 2001.

[25] L. Macheli, A. Roy, E. Carleschi, B. P. Doyle, and E. van Steen, "Surface modification of Co_3O_4 nanocubes with TEOS for an improved performance in the Fischer-Tropsch synthesis," *Catal. Today*, vol. 343, no. October 2018, pp. 176–182, 2020, doi: 10.1016/j.cattod.2018.10.018.

[26] X. -Y. Yu, Q.-Q. Meng, T. Luo, Y. Jia, B. Sun, Q.-X. Li, J.-H. Liu and X.-J. Huang, "Facet-dependent electrochemical properties of Co_3O_4 nanocrystals toward heavy metal

ions," *Sci. Rep.*, vol. 3, 2013, doi: 10.1038/srep02886.

[27] M. Moyo, "Cobalt and iron supported on carbon spheres catalysts for Fischer,"PhD thesis, University of the Witwatersrand, 2012.

[28] M. W. Dlamini, "Spherical carbons as model supports for Fe , Co and Fe-Co Fischer-Tropsch catalysts," PhD thesis, University of the Witwatersrand, 2016.

[29] M. Moyo, M. A. M. Motchelaho, H. Xiong, L. L. Jewell, and N. J. Coville, "Promotion of Co/carbon sphere Fischer-Tropsch catalysts by residual K and Mn from carbon oxidation by $KMnO_4$," *Appl. Catal. A Gen.*, vol. 413–414, pp. 223–229, 2012, doi: 10.1016/j.apcata.2011.11.012.

[30] O. A. Bulavchenko, S. V. Cherepanova, V. V. Malakhov, L. S. Dovlitova, A. V. Ishchenko, and S. V. Tsybulya, "In situ XRD study of nanocrystalline cobalt oxide reduction," *Kinet. Catal.*, vol. 50, no. 2, pp. 192–198, 2009, doi: 10.1134/S0023158409020086.

[31] O. A. Bulavchenko, E. Y. Gerasimov, and T. N. Afonasenko, "Reduction of double manganese-cobalt oxides:: In situ XRD and TPR study," *Dalt. Trans.*, vol. 47, no. 47, pp. 17153–17159, 2018, doi: 10.1039/c8dt04137g.

[32] M. Wolf, E. K. Gibson, E.J. Olivier, J.H. Neethling, C. R. A. Catlow, N. Fischer, M. Claeys, "Water-induced formation of cobalt-support compounds under simulated high conversion Fischer-Tropsch environment," *ACS Catal.*, vol. 9, no. 6, pp. 4902–4918, 2019, doi: 10.1021/acscatal.9b00160.

CHAPTER 7: APPLICATION OF THE CARBON DOTS-DERIVED GRAPHENE-LIKE SHEETS IN VOLATILE ORGANIC COMPOUNDS SENSING

From 0D to 2D: N-doped carbon nanosheets for detection of alcohol-based chemical vapours

Abstract

The application of N-doped carbon nanosheets, with and without embedded carbon dots, as active materials for the room temperature chemoresistive detection of methanol (MeOH) and/or ethanol (EtOH) is presented. The new carbons were made by converting 0D N-doped carbon dots (NCDs) to 2D nitrogen-doped carbon nanosheets by heat treatment (200–700 °C). The nanosheets exhibited a lateral size of 3 mm and a thickness of 12 nm at the highest annealing temperature. Both Raman and TEM analyses showed morphological transitions of the dots to the sheets, whilst XPS analysis revealed transformation of the N-bonding states with increasing temperature. PDF analysis confirmed the presence of defective carbon sheets. Room temperature screening of the chemical vapours of two alcohols (MeOH and EtOH), revealed that the structure and the type of N-configuration influenced the detection of the chemical vapours. For instance, the lateral size of the nanosheets and the high charge density N-configurations promoted detection of both methanol and ethanol vapours at good sensitivity (-16.8×10^{-5} ppm^{-1}_{EtOH} and 1.2×10^{-5} ppm^{-1}_{MeOH}) and low limit of detection (LoD, ~44 ppm_{EtOH} and ~30.3 ppm_{MeOH}) values. The study showed that the composite nature as well as the large basal area of the carbon nanosheets enabled generation of adequate defective sites that facilitated easy adsorption of the volatile organic compounds (VOC) analyte molecules, thereby eliminating the need to use conducting polymers or the formation of porous molecular frameworks for the alcohol detection.

*Corresponding authors: zdenek.sofer@vscht.cz; neil.coville@wits.ac.za

7.1 Introduction

Volatile organic compounds (VOCs) are known to significantly reduce the quality of air and therefore cause harmful effects to humans and the environment [1], [2]. Unfortunately, a number of simple everyday activities such as painting, application of adhesives, use of cleaning products, production of cosmetics, and cooking, all lead to the emission of many VOCs [3], [4]. Additionally, alcohol-based VOCs such as ethanol are mostly found in alcoholic beverages, disinfectants and food products, and because of their volatility, they produce an impact our daily living [3]. Therefore, the ability to detect and identify alcohol-based VOCs is required for the health and safety of humans, and the environment at large. Additionally, alcohol detection to ensure road safety protocols are obeyed, has also provided a large market for the detection of ethanol vapours [5]. As such, the search for portable, low-cost, low power usage, high response and easily operated sensing devices for VOC detection still continues, in particular for those devices that can operate satisfactorily under room temperature conditions [6]. Owing to this growing demand, several sensing techniques have been explored for the detection of VOCs. These include gas chromatography, infrared detection and chemoresistive detection [7]. Among these various detection methods, chemoresistive devices are particularly useful, especially in terms of low power, easy operation, high selectivity and robust nature [8].

Usually, the performance of the chemoresistive sensing devices is affected by the type of active material used. Given this challenge, an arsenal of active materials, such as conducting polymers, semiconductors, metal oxides, chalcogenides and carbon allotropes, have been extensively studied [8]. Amongst the various candidates, carbon allotropes, particularly graphene and its derivatives, are known to be promising active materials for the fabrication of room temperature chemoresistive sensing devices [9], [10]. Apart from using the graphene derivatives individually as active materials, various studies have shown that formation of composites of carbon allotropes with graphene derivatives can also significantly enhance their electrochemical properties [11], [12]. The synergy between the components of the composites has led to their enhanced sensing properties due to changes in the structural and electronic characteristics of the composites [6], [13]. For instance, Hu et al. reported that a composite of reduced graphene oxide and carbon dots (rGO–CDs) led to a highly selective and stable gas sensor

under room temperature conditions [14]. The enhanced sensitivity was attributed to the increased density of electron-deficient sites as well as adsorption sites. Similarly, a composite of graphene, conductive polymer and carbon nanotubes on a glassy carbon electrode (GCE) was found to produce a methanol sensing device exhibiting fast response, high sensitivity, long-term stability and low-sample volume [15].

Apart from the formation of carbon-based composites, tuning of the electronic properties of graphene derivatives without compromising the structural properties through intentional incorporation or doping with electron-rich nitrogen atoms provides an excellent route for increasing the material's binding sites. This is achieved by the creation of defective sites, while also inducing the formation of n- and/or p-type semiconducting properties, depending on the type of N-bonding configuration formed [16]–[18]. A few reports have shown that these nitrogen-rich nanosheets, with targeted configuration, can be fabricated from facile synthesis procedures such as carbonizing metal–organic frameworks (MOFs) like indium-based coordinated polymers [19]. Despite numerous reports on the synthesis of N-doped graphene derivatives, few studies have investigated the impact of the carbon and/or nitrogen-dopant domains on the sensing ability of N-doped carbon-based nanostructures [20]. To explore this issue, and the effect of dopants, we have used CDs as carbon sources for the synthesis of large domain pristine or doped graphene derivatives.

The transformation of these 0D CDs to 2D graphene-like sheets occurs during the coalescence of CDs in the presence of a metal catalyst and/or upon exposure to temperature treatment [21]–[23]. The transformation route takes advantage of the highly functionalized surface of CDs which subsequently enables easy incorporation of heteroatoms during the doping process [24], [25]. However, little is known on how N-doping impacts on this conversion process and the use of these doped materials as chemical vapour sensing materials. Therefore, to increase the scope of the CDs-derived graphene derivatives, the current study aims to explore N-doped graphene-like nanosheets derived from CDs as active materials for the detection of VOCs. The significant role played by the different nitrogen bonding states and the morphological changes associated with heat treatment on the room temperature sensing performance of these CDs-derived N-doped graphene-like nanosheets is thus described.

7.2 Experimental

7.2.1 Material synthesis and sensor preparation

The nitrogen-doped carbon dots (NCDs) were synthesized using a modified microwave-assisted hydrothermal technique [22], [26]. Typically, 1.2 g of L-ascorbic acid (95 %, Sigma Aldrich) and 1.2 g urea ($CO(NH_2)_2$, 99 %, Sigma Aldrich) were stirred into 240 mL of deionised water, after which 60 mL of the homogeneous solution was transferred into four Teflon lined 100 mL microwave reaction tubes. The reaction tubes were then placed inside an Anton-Paar Multiwave 3000 SOLV microwave digester, equipped with the maximum power output of 1400 W and a controlled pressure of 60 bar. The reaction chamber was then subjected to microwave irradiation for 6 min at a power of 600 W, resulting in a temperature of 180 ℃. After cooling the reaction chamber to room temperature, the product was obtained through centrifugation at 15 000 rpm for 15 min. The supernatants were filtered through a 0.22 µm poly(vinylidene fluoride) (PVDF) membrane (Membrane Solutions), followed by removal of water using a rotary evaporator, and drying at 60 ℃. As previously described for the conversion of the undoped CDs [22], the effect of temperature on the NCDs was achieved by annealing (200, 400 or 700℃) the NCDs (500 mg) in a horizontal chemical vapour deposition (CVD) furnace for 10 min under 100 sccm of nitrogen (>99.999 % N_2, Afrox SA). After cooling to room temperature under N_2 gas, the powdered samples were collected and labelled as NCDs200, NCDs400, or NCDs700 for the samples annealed at 200, 400 or 700 ℃, respectively.

Finally, for the electrochemical impedance spectroscopy (EIS) chemical vapour sensing measurements (**Scheme S7.1**), the NCDs active materials were dispersed with sodium dodecyl sulfate (SDS, ≥98.5 % Sigma Aldrich), as a surfactant, at a concentration of 0.5 mg mL^{-1}. Thereafter, 10 µL of each solution was drop casted onto the ED-IDE 3-Au integrated electrode (Microflux Fluidic, Spain) and the electrodes were dried at 70 ℃ for 30 min. Determination of sensitivity to methanol (MeOH, ≥99.9 %, Lachner) and ethanol (EtOH, ≥96%, Lachner) was achieved through addition of calculated concentrations (ppm, **equation 7.1** of the analyte into the gas chamber:

$$C_{ppm} = \frac{2.46 V_a \rho}{V_c Mw} 10^7 \quad \text{..... equation 7.1}$$

where V_a represents the volume (in µL) of the analyte added to the chamber, V_c is the volume (in mL, 50 mL) of the analysis chamber, ρ is the density of analyte (in gmL^{-1}) and M_w is the molecular weight of analyte in $g\ M^{-1}$. Responses based on EIS measurements were acquired in the 1–10^6 Hz frequency range using the Metrohm Autolab potentiostat controlled by Nova 2.14 software after 5 min saturation. From an average of 3 fabricated electrodes, the response (Resp), limit of detection (LoD) and sensitivity (*S*) were determined by use of **equations 7.2-7.4**:

$$Resp = \frac{\Delta Z}{Z_0} = \frac{Z_{f-Z_0}}{Z_0} \quad \text{..... equations 7.2}$$

$$LoD = Zb + 3db \quad \text{..... equations 7.3}$$

$$S = \frac{d\text{Resp}}{d\text{C}} \quad \text{..... equations 7.4}$$

where, Z_f is the impedance of the sensor when exposed to analyte and Z_0 the resistance of the sensor in ambient condition, Z_b is the average impedance, d_b is the standard deviation of the device impedance without analyte, and *C* is an analyte concentration.

7.2.2 Characterization

The morphology of the active materials that have been immobilized on Si-O grids was acquired on an EFTEM Jeol 2200 FS microscope (Jeol, Japan), using 200 keV acceleration voltage, and HRTEM images were collected from a JEOL JEM 2100 fitted with a LaB6 gun. Their thicknesses were determined by atomic force microscopy (AFM) through use of a Ntegra Spectra microscope from NT-MDT. AFM measurements were performed in a tapping (semi-contact) mode under ambient condition with a scan rate of 1 Hz and scan line of 512 after drop-casting a sample suspension on a freshly cleaved mica substrate. ^{13}C solid-state nuclear magnetic resonance (NMR) spectra were measured using a Bruker-500 MHz NMR spectrometer at a spinning frequency of 62.5 kHz (4.0 µs, 115 W). Raman spectra and solid-state photoluminescence (PL) spectroscopy data were collected using a Horiba LabRAM HR micro-Raman spectrometer (frequency double Lexel SHG argon ion laser). Raman measurements were done with a 514.5 nm laser and the PL measurements were done using a 244 nm excitation wavelength.

Thermal stabilities of the samples were monitored by thermal gravimetric analysis (TGA) conjugated with weight loss derivative outputs (DTG) using a PerkinElmer 6000 thermogravimetric analyser. Powder X-ray diffraction (PXRD) patterns were recorded on D2 phaser X-ray diffractometer using a Co Kα X-ray source operating at 30 kV and 10 mA. The measurements were taken between 2θ= 10–90 °, with a 0.026 ° step. Total scattering data were collected on the Brockhouse high-energy wiggler beamline using a wavelength of λ = 0.2081 Å and a PerkinElmer XRD1621 area detector placed 160 mm after the sample. The data were processed using GSAS-II. The Q_{max} used to produce the PDF of the measured samples was 21 $Å^{-1}$. The ESCAProbeP spectrometer (Omicron Nanotechnology Ltd, Germany) X-ray photoelectron spectrometer equipped with a monochromatic Al-α radiation source (1486.7 eV) was used for the wide-scan survey and high-resolution spectral measurements. The wide-scan surveys of all elements were measured in the range of 0–900 eV with a pass energy of 100 eV and a step of 1 eV, whilst high-resolution scans of the C1s, O1s, and N1s peaks were measured with a pass energy of 20 eV and a step of 0.1 eV.

7.3 Results and Discussion

7.3.1 Temperature-dependent morphological evolution

The morphological changes shown by the N-doped carbon dots (NCDs) as a function of heat treatment were investigated using both TEM and AFM micrographs. Both microscopic analyses showed changes in the lateral dimensions of the graphene-like nanosheets with heat treatment (**Figures 1, S7.1–S7.3**); from the small pristine NCDs of average particle size of 4.1 ± 0.9 nm (**Figure S7.1a**) to an amorphous mass (**Figure S7.1b**) and multi-layered nanostructures. For instance, TEM analysis showed that heat treatment at 700 ℃ produced large and multi-layered nanosheets with an average size of 3.71 ± 0.31 μm by 2.13 ± 0.91 μm (**Figure 7.1a**). Additionally, the HR-TEM images of pristine NCDs and NCDs700 in **Figure S7.2** shows that the pristine NCDs had lattice fine structure, with the lattice *d*-spacing of *ca.* 0.204 and 0.210 nm, similar to that of the (101) and (100) plane lattice of graphite, respectively [22], [27]. In contrast, the NCDs700 did not show any lattice fringes (**Figure S7.2b**). This implies that graphitization is lost when the NCDs are transformed into 2D nanosheets.

AFM images of NCDs700 also confirmed the formation of large-area stacked nanosheets of up to 2.75 µm in lateral size and 14 nm in thickness (**Figures 7.1b** and **c**). The formation of the nanosheets could be attributed to high temperature transformations of the carbon dots nanostructures, which was subsequently followed by the coalescence of the as-produced carbonaceous fragments into stacked two-dimensional (2D) nanostructures [22], [23]. In comparison to the undoped CDs-derived graphene-like nanosheets which exhibited an average size of *ca.* 1.71 ± 0.909 µm [22], it can be concluded that N-doping affected both the temperature required to transform the CDs as well as the final structure obtained at the highest annealing temperature.

The 400 ℃ heat treatment was observed to not only lead to formation of the multi-layered 2D nanosheets (**Figure S7.1c**), but the stacked nanostructures also contained small accreted quasispherical nanoparticles (**Figure S7.3b**). This indicates that the 400 ℃ annealing temperature was insufficient to facilitate a complete transformation of the NCDs into active carbon fragments and consequently resulted to formation of the mixture of CDs and the 2D nanostructures. Height profile analysis by AFM showed the presence of small and thinner (~0.75 nm) nanosheets exhibiting the lateral diameter of ~0.15 µm (**Figure S7.3c**, red line). Further confirmation of the important effect of annealing temperature on the transformation of the NCDs was shown by annealing at 200 ℃ that resulted in formation of an amorphous-looking mass of carbon embedded with quasi-spherical nanoparticles (**Figure S7.1b** and **S7.3a**).

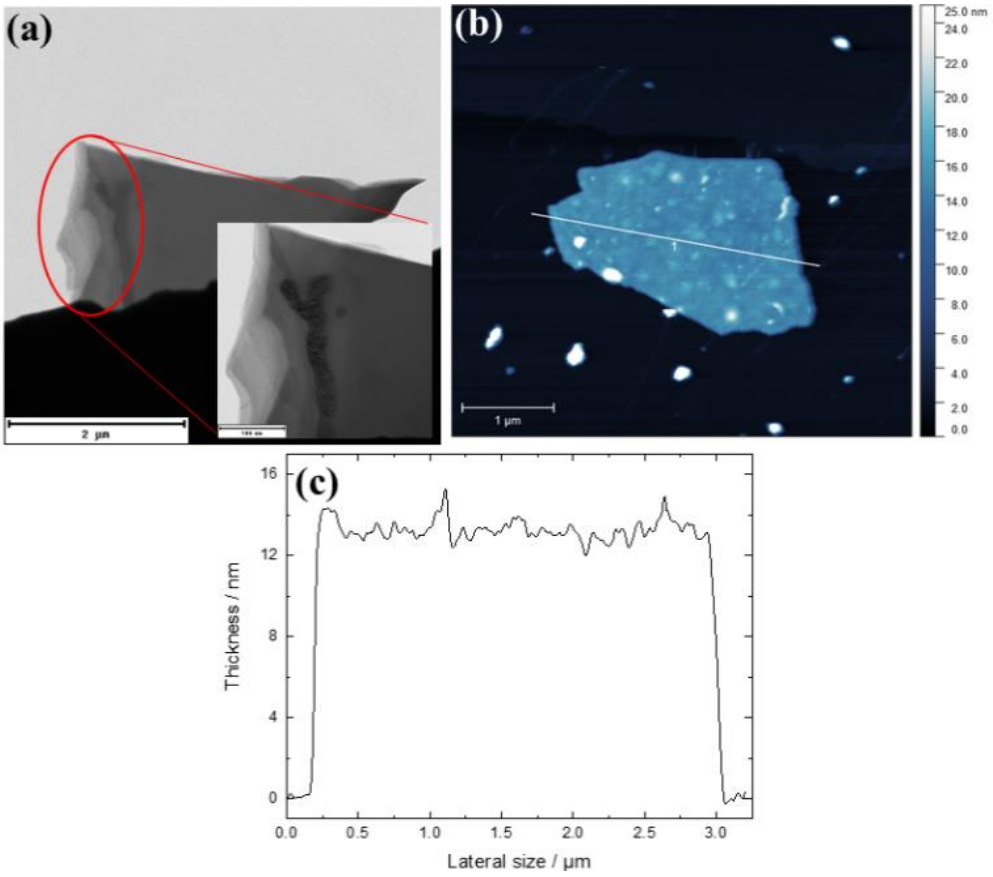

Figure 7.2: (a) Low magnification TEM, **(b)** AFM images and **(c)** height profile of the NCDs700 sample.

7.3.2 Physicochemical properties

Structural disorders associated with the heat treatment and the presence of N-dopants were investigated using Raman spectra. As shown in **Figure 7.2**, the spectra for the NCDs400 and NCDs700 samples exhibited fingerprint Raman peaks characteristic of carbonaceous materials [28], [29]. The first order Raman modes were located between ~1341-1357 cm^{-1} and ~1578–1580 cm^{-1} for the D-band and G-band, respectively, whilst the second-order Raman (2D) band for the NCDs700, overlapped with the overtone of the D + G band at ~2790 cm^{-1} [28], [29]. In the case of the NCDs200 sample (**Figure 7.2** insert), the Raman modes could not be characterized due to the photoluminescent excitation of the carbon dots by the Raman radiation source as well as the fluorescence properties of the CDs [30]. Additionally, the inclined baseline for the NCDs400 sample indicated that these materials still contained some fluorescent carbon

dots. As such, quantification of the structural properties of the NCDs400 sample was difficult. Nonetheless, quantification of the degree of graphitization for the NCDs700 sample was investigated from the estimated ratios of the integrated areas under the D-band and the G-band (viz. I_D/I_G) [28]. The structural defect density ratio (I_D/I_G) was estimated to be *ca.* 3.38 ± 0.12, resulting in a relatively large defect density (n_D, see **equation S7.2** of ~11.6×10^{11} cm^{-2} [31]. Furthermore, the PXRD analysis results in **Figure S7.4a** show that increasing the annealing temperature did not yield highly ordered nanosheets. The low degree of graphitization for the NCDs700 sample was attributed to the realignment of the carbon lattice upon formation of larger graphitic domains as well as the lattice distortion associated with the incorporation of the nitrogen heteroatoms, confirmed by pair distribution function (PDF) analysis (see **section 7.3.4**). Therefore, taking into account, the relation between the excitation wavelength and the defect density ratio, the average sp^2 crystallite sizes (L_a, **equation S7.1** [31]) was found to be ~4.98 ±0.03 nm. The L_a value complimented the TEM and AFM micrograph data (**Figure 7.1a** and **c**), which revealed the formation of bigger lateral size nanosheets upon annealing at 700 ℃, as was also observed from our previous work on undoped nanosheets. Interestingly, bigger sheets were formed for the N-doped samples [22].

Based on the thermal stability results from TGA (**Figure S7.4b**), the first-order derivative profiles of the NCDs400 and NCDs700 samples confirmed the formation of carbonaceous nanosheets as shown by the decomposition peak at ~624 ℃ and 635 ℃, respectively. The single peak indicated a homogenous decomposition of the highly defective 2D structured nanosheets and/ or the carbon core [32]. Furthermore, the peaks at *ca.* 343 ℃ and 380 ℃ for the NCDs200 and NCDs400 samples, respectively, suggested the removal of amorphous carbon phases and organic dangling-bonds from the NCDs upon heat treatment. The lack of the low temperature peak(s) for the NCDs700 sample is indicative of the formation of a CDs-free product [22]. More importantly, the peak at *ca.* 500 ℃ for NCDs400 and the broadness of peaks for the NCDs700 samples can be linked to strongly bound functional groups [33] Taking into account the contribution of the N-configuration on the thermal stability of the NCDs samples, an increased thermal stability of ~200 ℃ was observed for the NCDs samples as compared to their undoped counterparts [22] The observation may be attributed to the presence of the pyrrolic-, pyridinic- and graphitic-N bonds present in the nanosheets as suggested by the

XPS results (see **section 7.3.3**). These groups are thus more stable under air, compared to the O-containing groups [34]. Finally, the small derivative peaks between *ca.* 60 and 80 ℃ in all 3 samples were attributed to moisture found within the samples [35].

^{13}C NMR data were collected and found to be consistent with the TGA results, which showed removal of oxygen functional groups after high-temperature annealing (**Figure 7.2c**). For instance, the ^{13}C NMR spectra of the NCDs200 showed a peak at *ca.* δ 170 corresponding to O–C=O and/or N–C=O [36], which decreased on annealing. More importantly, the sp^2 peak at *ca.* δ 117 ppm increased with increasing annealing temperature which is characteristic of the presence of aromatic carbon atoms, hence signifying the transformation of the carbon into large-area nanostructures. Finally, PL spectra showed that only the NCDs200 was PL active, with an emission peak at *ca.* 609 nm, located in the near-IR region [22]. This emission peak was due to the presence of the NCDs embedded within the formed layered nanostructures. The observed PL quenching that occurred after annealing (**Figure S7.4c**) is further suggestive of the removal of PL active surface functional groups on the CDs [37], thereby leading to structural transformation from CDs to layered materials.

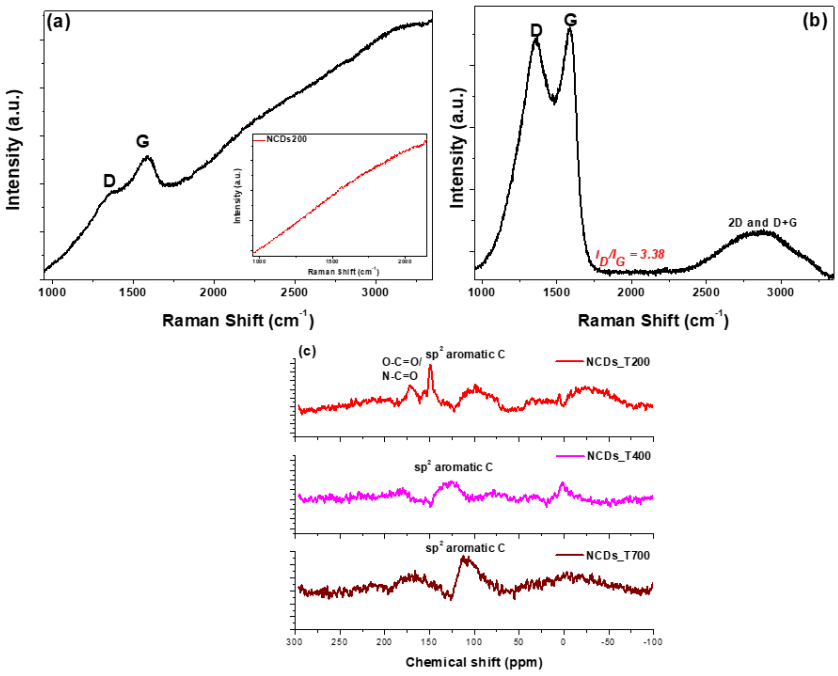

Figure 7. 3: Raman spectra of **(a)** NCDs400 with inset showing that of NCDs200; and **(b)** NCDs700 samples, **(c)** ^{13}C NMR spectra for the variously annealed NCDs samples.

7.3.3 Composition analysis

Through the estimation of the integrated areas under the XPS wide scan spectra, the atomic percentage (at%) compositions of the annealed NCDs were determined (see **Table S7.1**). From **Figure 7.3a**, three distinct characteristic peaks corresponding to C1s (~284 eV), N1s (~398 eV) and O1s (~532 eV) were observed. Detailed analysis of the survey spectra revealed the evolution of the nitrogen content with annealing temperature. For instance, the freshly prepared NCD sample showed the incorporation of *ca.* 15.9 at % of nitrogen heteroatoms, whilst treatment of 700 °C led to a decrease in the N content to *ca.* 7.79 at% within the carbon lattice (**Figure 7.3b**). The decreasing N-content with increasing annealing temperature is consistent with the loss of edge-bonded nitrogen atoms in the form of nitrogen gas, ammonia gas and/or nitrogen radicals [38]. Moreover, the high temperature promoted coalescence of the carbon domains, led to an increased ratio of carbon (%) on annealing, relative to the other elements making up the compositions of the samples (*ca.* 68.8 at% in the NCDs and *ca.* 84.1 at% in the NCDs700).

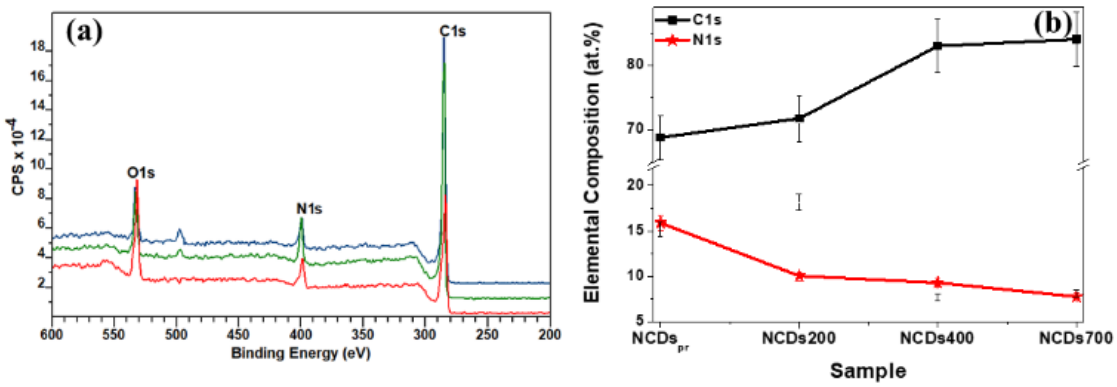

Figure 7.3: (a) XPS survey spectra for NCDs200 (red), NCDs400 (green), and NCDs700 (blue) samples, as well as **(b)** elemental composition of the as-synthesized samples.

The bonding states of carbon (C), nitrogen (N) and oxygen (O) atoms in the annealed samples were determined through the peak fitting of their high resolution XPS spectra. **Figure 7.4** displays the resolved spectra for NCDs700 sample, whilst those of the NCDs200 and NCDs400 samples are shown in Figure **S7.5** and **S7.6**. The broad, tailing C1s spectra (**Figure 7.4a**, **S7.5a** and **S7.6a**) was resolved to at least five components corresponding to graphite-like sp^2 C–C bonds (~283.6–283.8 eV), the sp^2 -N–C bonds (~284.8–285.1 eV), the defect-induced sp^3 -C–

C and/or C–N bonds (~285.6–286.2 eV), and the oxygenated bonding configurations of C=O (~286.6–287.7 eV) as well as the N–C=O and/ or O–C=O bonds (~287.9–288.8 eV) [39], [40]. Similarly, the type of nitrogen dopant in the carbon lattice of the annealed NCDs samples was investigated by the deconvolution of the N1s spectra (**Figure 7.4b**, **S7.5b** and **S7.6b**). Peak fitting revealed four component peaks attributed to contributions from pyridinic-N (~397.7–398.1 eV), pyrrolic-N (~398.9–399.2 eV), substitutional/graphitic-N (400.1–400.3 eV), and the oxidized pyridinic-N bonds (NOx, ~401.2–402.1 eV).39 Finally, the O1s spectra (**Figure 7.4c**, **S7.5c** and **S7.6c**) were deconvoluted into three component peaks which can be assigned to O=C and/or O–N (~528.9–529.9 eV), O–C (~530.1–531.6 eV), and the N–C=O/O– C=O (~532.9–533.5 eV) bonds, respectively [40].

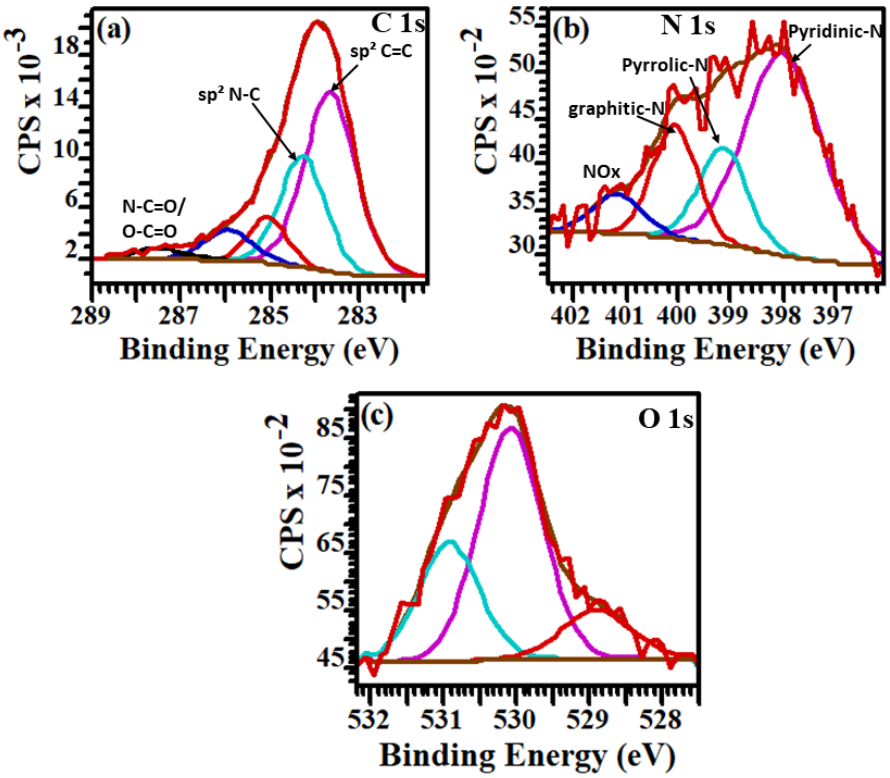

Figure 7.4: Peak fitted XPS curves for **(a)** C1s, **(b)** N1s, and **(c)** O1s of NCDs700 sample.

Noticeably, the different bonding state distributions of the Nitrogen (**Figure S7.7**) showed the formation of different N-configurations through the adjustment of the annealing temperature (**Scheme 7.1**). For instance, annealing at 400 °C led to the formation of predominantly pyrrolic-N bonding states (~45.8 %) and pyridinic-N configurations (39.4%), thereby indicating that

most of the amide groups from urea are bonded to the carbon at the domain edges. Moreover, fewer substitutional N-configurations (~12.3 %) show that the 400 ℃ heat treatment is not sufficient to facilitate the coalescence of the NCDs domains into graphene-like nanostructures. Such coalescence phenomenon could result in the transformation of pyridinic-N bonds into graphitic-N type [38]. On the other hand, a higher annealing temperature (e.g., 700 ℃) was found to enhance the formation of pyridinic-N (~56.9 %) due to the coalescence of the NCDs domains into a bigger graphene-like nanostructures (**Figure 7.1a**). The results are in good agreement with theoretical studies, which have indicated that N atoms are more thermodynamically stable at carbonaceous edges; with the pyridinic-type being the most stable [41], [42].

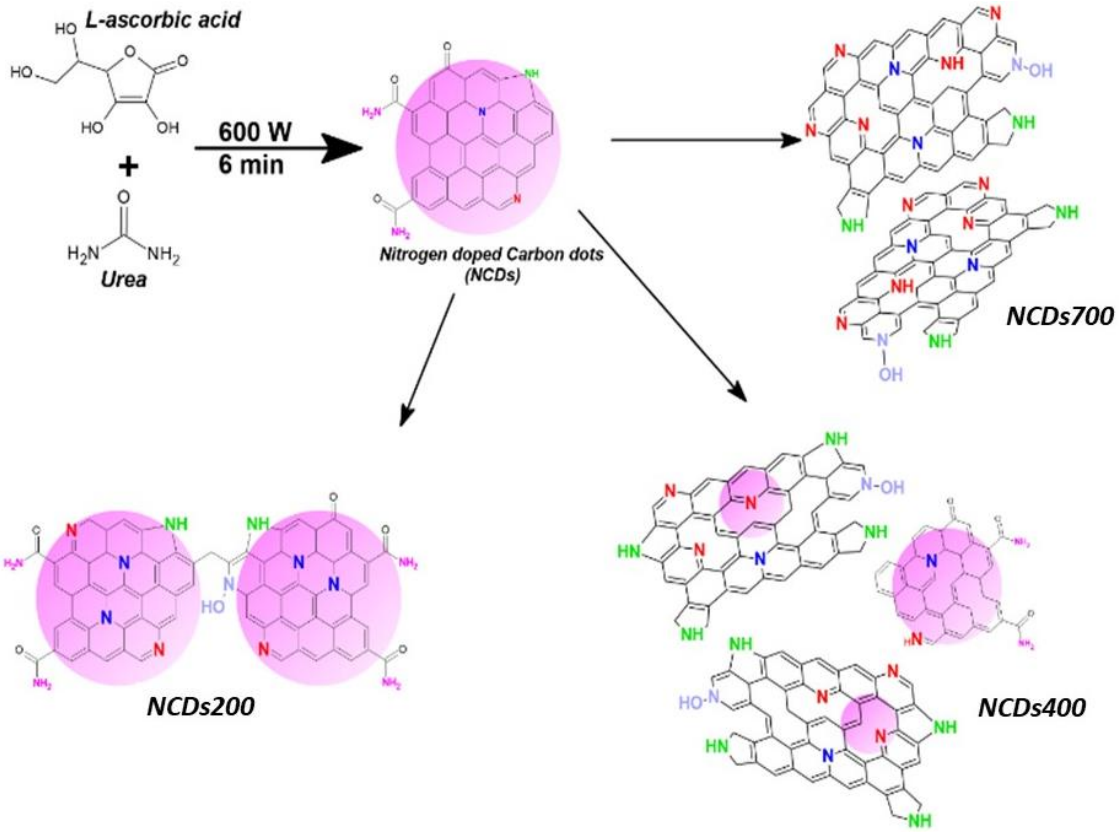

Scheme 7.1: Representation of evolution of N-configurations in NCDs with respect to annealing temperature.

7.3.4 Total scattering measurements (PDF)

Total scattering measurements were conducted at the Canadian Light Source to examine the local structure of the samples synthesized in this study (**Figure 7.5**). The atomic pair distribution function (PDF) technique provides insight into the structure of materials in the short- and medium-range scales [43], Generally, the PDF results showed that the NCDs prior to annealing exhibited the longest range order, as can be seen by the increased dampening in the PDF signal from pristine NCDs to NCDs700 at *r* values as low as 10 Å (**Figure S7.8**). The first prominent peak, around 1.42 Å for the pristine NCDs (**Figure 7.5**), corresponds to the C=C bonds and some C–N bonds with three nearest neighbours to carbons, all with sp^2 bonding [44], bearing in mind that the pristine NCDs contains ~15.9 at% N. In comparison with the C–C bonds at *ca.* 1.42 Å in a pristine graphene structure [45], the C–C peak is observed to shift to lower *r* values (~1.38 Å) with N-doping and annealing, suggesting increasing contribution of the shorter C–N bonds. More importantly, the shifting and broadening of the peak could be ascribed to the varying contributions from both the pyridinic- and pyrrolic-N moieties, as these are characterized by peaks at ca. 1.34 Å and 1.38 Å, respectively.

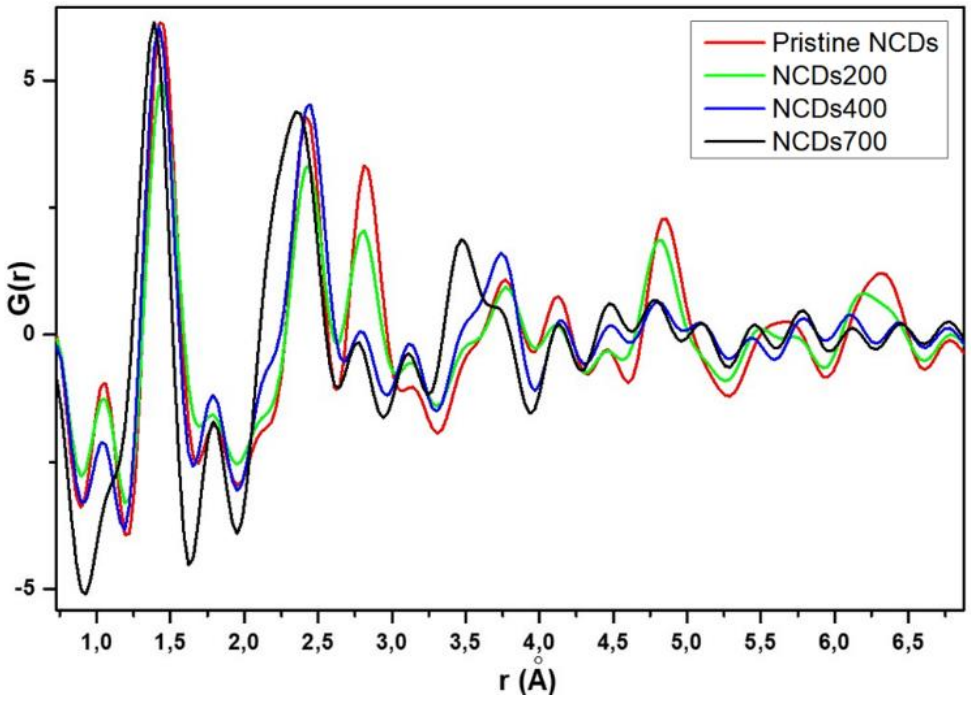

Figure 7. 5: Zoomed region of the PDFs of pristine NCDs and annealed NCDs at 250, 400 and 700 °C.

The peak at 1.1 Å corresponds to C =O bond lengths with slight shortening of the bonds from their regular 1.2 Å length due to electron delocalisation over the graphene resonance structures [45]. It must be noted that these peaks, even though weak, do demonstrate a clear trend showing a reduction in the peak intensity from the pristine NCDs to the NCDs700 sample indicating the removal of these groups as temperature increases. The second prominent peak at *ca.* 2.44 Å corresponds to the shortest diagonal in the carbon hexagon and is close to that of the predicted model (*ca.* 2.46 Å, **Figure 7.6)**. This peak broadened as the annealing temperature increased. Most noticeably, the NCDs700 sample showed significant broadening at this peak position compared to the other samples, indicating the distance between the three atoms coordinating the central carbon in the hexagon, or the shortest diagonal in the hexagon, varies significantly from one ring structure to the next. The third peak at 2.81 Å (close to the *ca.* 2.83 Å, **Figure 7.6**), which is twice the first C–C distance, is the long diagonal in the hexagon [46]. This peak shifts to lower *r* values (~ 2.77 Å) and its intensity decreases with increasing annealing temperatures. The observed trends with higher annealing temperature suggest increasing disorder in the C-ring due to the insertion of N in the rings.

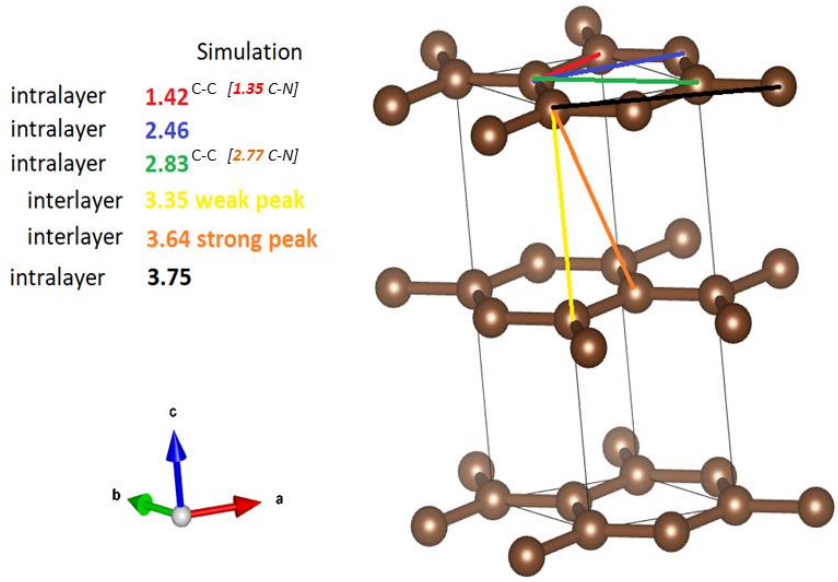

Figure 7. 6: Inter and intralayer bond distances between carbon atoms in graphite. The values in brackets are given for nitrogen-doped graphene. These values correspond to the observed peaks in G(r).

It is clear that the NCDs prior to annealing exhibit the longest range order, as can be seen by the increased dampening in the PDF signal from pristine NCDs to NCDs700. It is noted that the signal attenuation is high, even at *r* values as low as 10 Å, especially for NCDs400 and NCDs700, indicating the existence of short coherence lengths (**Figure S7.8**). Typically, the PDF pattern that originates from interlayer atomic correlations is signified by the weak 3.35 Å and strong 3.64 Å peaks (**Figure 7.6**) and is indicative of well-ordered graphite structure. In all samples, the weak peak at 3.35 Å (**Figure 7.6**) shifts to slightly higher *r* values (3.48 Å, **Figure 7.5**) indicating a small increase in the interlayer spacing. A similar trend is noted when examining the 3.64 Å peak (**Figure 7.6**) which is also shifted to slightly higher r values and is positioned around 3.75 Å (**Figure7.5**), with lower than expected peak intensity. Therefore, the shift of these peaks and the noted reduction in the intensity of the 3.75 Å peak indicates a higher degree of turbostratic and positional disorder from one graphene sheet to the next [47]. Therefore, the aforementioned shifted peak positions to higher *r* values are due to disorder arising from the defective structures within the nitrogen-doped graphitic sheets leading to the slightly larger interlayer spacing coupled with turbostratic disorder [47]. The data shows that by 700 °C, significant insertion of nitrogen into the structure has occurred, as well as the formation of higher-order ring structures and an increase in defective structures.

7.3.5 Sensing properties

7.3.5.1 Chemoresistive behaviour of the sensors

Prior to the determination of the chemoresistive behaviour of the electrode materials, the sensors were screened for the detection of a range of VOCs (methanol, ethanol, acetone, isopropyl alcohol and acetonitrile). From this study, the NCDs400 and NCDs700 samples were found to be responsive to both methanol and ethanol, whilst NCDs200 sample was responsive to only methanol. As a result, a detailed investigation of the chemoresistive behaviour of the active materials was performed by recording the Nyquist plots after exposure to 1200 ppm MeOH and 1100 pm EtOH (**Figure 7.7**). For both analytes, the Nyquist plots exhibited a single semicircle which indicated that, regardless of the analyte, the electrical interaction between the analyte and the electrode followed a parallel circuit connection with the impedance resistance

parallel with the double-layer capacitance [48]. More importantly, the relatively equal solution resistance (RS, **Table 7.1**) values for the detection of either MeOH or EtOH for the devices revealed similar charge transport properties of the accumulated analyte vapour solution-like electrolyte around the nanostructures [49].

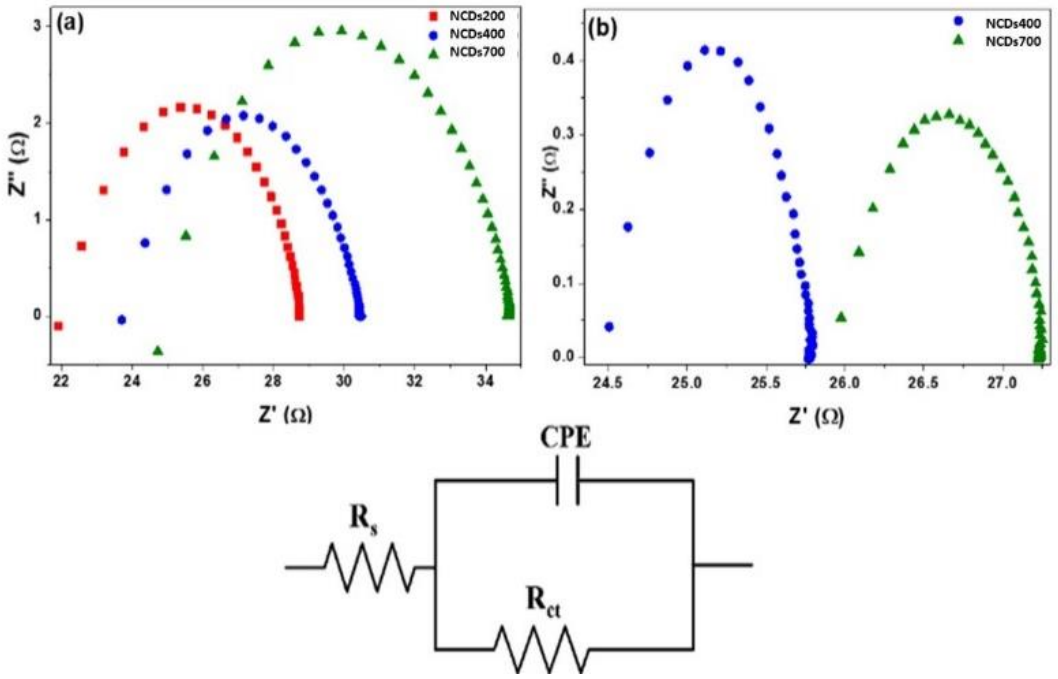

Figure 7. 7: Nyquist plots for the sensor devices after exposure to **(a)** 1200 ppm of MeOH and **(b)** 1100 ppm EtOH vapours, **(c)** representative equivalent Randle circuit.

On the other hand, owing to the different structural properties and the varying composition of the N-dopants within the active materials, it was observed that each electrode responded differently to the two analytes. Specifically, the NCDs700 device exhibited the highest resistance in the presence of MeOH, followed by the NCDs200 and eventually the NCDs400 device, as shown by the values of the charge transfer resistance (R_{CT}, **Table 7.1**). The faster charge transfer for the NCDs400 can be attributed to the abundance of pyrrolic-N (~45.8%) and pyridinic-N-configurations (~39.4%) through an improved π -π interaction with the analyte molecules as well as the availability of extra π-electrons on the N-dopants for the ionization of adsorbed oxygen species [50]. Moreover, the presence of a combination of NCDs fragments and small-sized graphene-like nanosheets could have created an abundance of defective sites which enabled quicker transport of charge-carriers. The slower charge transfers for the NCDs700 devices

for detection of both MeOH (8.95 Ω) and EtOH (1.58 Ω) can be ascribed to the charging-hopping effect over the large lateral flakes [50], despite the material having electron-rich centres due to the presence of the graphitic-N (~18.3%) and pyridinic-N (~56.9%) configurations [50]. Based on the results, it can be seen that not only the morphology of the carbon nanostructure, but also the concentration of the different nitrogen bonding states, plays a major role in the charge-carrier transfer properties of the NCDs.

Table 7.1: Circuit parameters of the NCDs for detection of MeOH and EtOH

Analyte	Active material	Resistance (Ω)		Capacitance (μF)
		R_s	R_{CT}	
Methanol	**NCDs200**	22.5	6.11	0.18
	NCDs400	24.2	6.07	0.15
	NCDs700	25.6	8.95	0.10
Ethanol	**NCDs400**	24.3	1.47	17.9
	NCDs700	25.6	1.58	4.86

7.3.5.2 Performance analysis

Following the establishment of the significant roles played by the N-configurations on the electrochemical properties of the NCDs active materials, the sensing parameters of their corresponding devices for the detection of MeOH and/or EtOH vapours were then evaluated. The parameters were estimated through the calculation of the concentration limit of detection (LoD, **equation 7.3** and sensitivity (*S* **equation 7.4**) from plots of sensor response ($\Delta Z/Z_0$, **equation 7.2**) against concentration (**Figures 7.8**, **7.9** and **S7.9**). Upon exposure to increasing concentrations of MeOH vapour, the sensor devices showed a p-type semiconducting behaviour [51] as shown by the increasing sensor response with increasing analyte concentration (**Figure 7.8a** and **S7.9**). The observed p-type semiconducting nature, regardless of the presence of the n-type nitrogen dopants, is representative of the surface chemistry of the active materials. Normally, during the measurement of the sensor response and in the absence of MeOH (i.e., 0 ppm), ionization of the adsorbed oxygen molecules occurs, resulting in formation of O_2^- or O^{2-} active

species through withdrawal of electrons from the nanostructures [52]. This resulted in the formation of an electron-rich depletion layer around the NCDs (**Figure 7.8b**). Therefore, depending on the N-content as well as the structure of the NCDs samples, it can be anticipated that different thicknesses of the depletion layer will be formed around each active material. Consequently, the sensing parameters will then be influenced by the consumption of the depletion layer upon exposure to the analyte vapour. For instance, the extremely low sensitivity value for the NCDs700- based device (1.2×10^{-5} ppm^{-1}, **Table S7.2**) is indicative of a strong interaction of the MeOH molecules with the large-area electrode surface, thereby leading to compromised adsorption of MeOH and desorption of the by-products. On the contrary, the large-area, basal morphology of the nanosheets ($La \approx 4.98$ nm) and the defective regions from both the N-dopants and carbon edges ($I_D/I_G \approx 3.38$) provided an abundance of adsorption sites for MeOH, as shown by the low LoD value (~30.3 ± 0.7 ppm). Interestingly, an improved sensing performance for the detection of MeOH was observed for the NCDs200- and NCDs400-based devices (**Figure S7.9**), as evidenced by the large sensitivity values of $11.6 \times 10^{-5} \pm 0.6$ ppm^{-1} and $4.36 \times 10^{-5} \pm 0.1$ ppm^{-1}, as well as low LoD values of 37.1 ± 0.3 ppm and 34.9 ± 0.5 ppm, respectively. The enhanced sensitivity could be attributed to the increased charge carrier density from an N-configuration, such as the pyridinic-N (20.7–39.4 at%) and NO_x (2.5–9.9 at%) bonding states. Additionally, the NCDs/ fragmented nanosheets composite nature of both NCDs200 and NCDs400 active materials created an abundant amount of charge capture sites, leading to a faster adsorption–desorption mechanism of MeOH molecules and their reduction products.

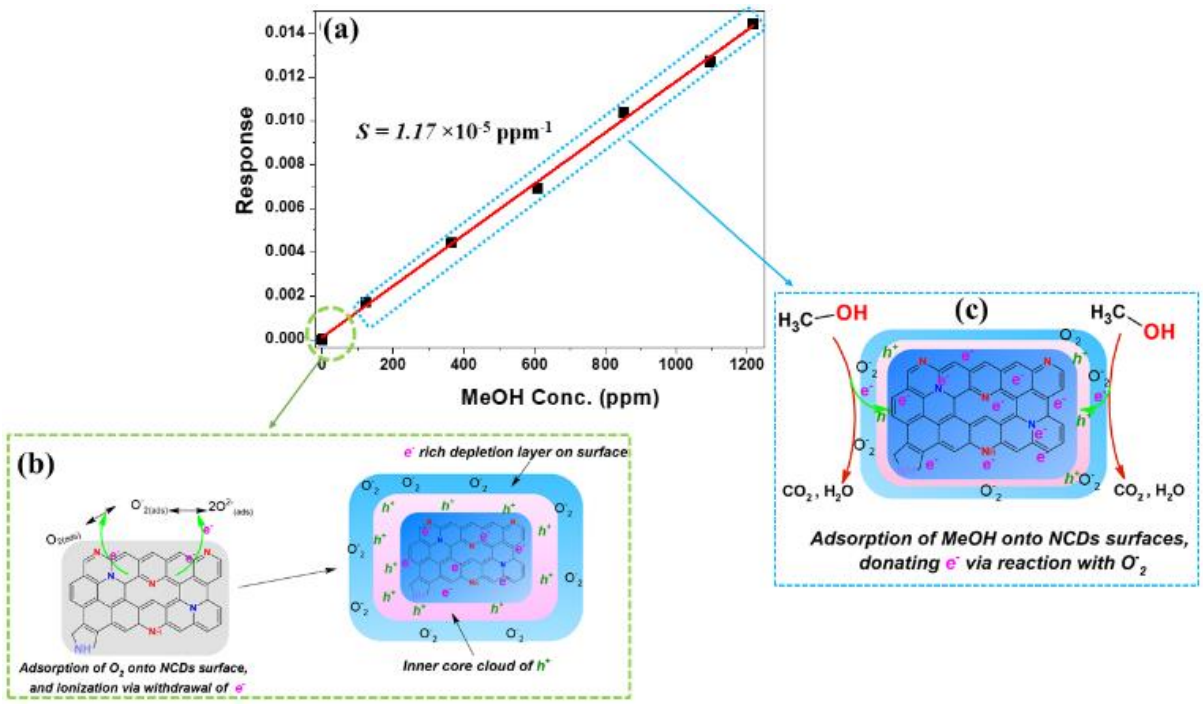

Figure 7. 8: (a) Sensor response as a function of MeOH vapour concentrations for the NCDs700 sensor devices, **(b)** ionization of adsorbed O_2, and **(c)** detection mechanism of MeOH.

In the case of the sensing of EtOH, both the NCDs400 and NCDs700 sensor devices exhibited an n-type semiconducting behaviour [51] as shown by the decreasing sensor response with increasing analyte concentration (**Figure 7.9**). Lack of response to EtOH for the NCDs200 samples indicated that not only the type of N-configurations but also the structural properties of the active material influence the sensing mechanism for ethanol. For instance, the large sensitivity of -16.8 $\times 10^{-5} \pm 0.5$ pm^{-1} and low LoD value (43.5 ± 0.4 ppm) for the NCDs700-based sensor devices in comparison to the sensing performance of the NCDs400-based device (S = -2.09 $\times$ $10^{-5} \pm 0.8$ ppm^{-1} and LoD ≈ 91.4 ± 0.1 ppm) can be attributed to the weak interaction between EtOH molecules and the basal plane of the NCDs700. It is also possible that the slightly increased charge carrier density moieties in the form of graphitic-N (~18.3 at%) and pyridinic-N (~56.9 at%) bonding states play a role in the process. Therefore, the sensing mechanism for EtOH on the active materials can also be explained by the change in the surface depletion layer around the NCDs nanostructures (**Figures 7.9b** and **c**). Similar to the sensing mechanism for MeOH, prior to exposure to the EtOH analyst vapour, an electron-rich depletion

layer is formed on the surface of the NCDs (**Figure 7.8b**) through ionization of adsorbed oxygen molecules. On exposure to the EtOH vapour, which acts as a reducing atmosphere [53], the ionized oxygen species are removed so as to convert EtOH into water and carbon dioxide. The removal of the ionized O_2 species is then followed by the injection of electrons back into the NCDs nanostructures, thereby increasing the conductance channel within the NCDs structures (**Figure 7.9c**) [54].

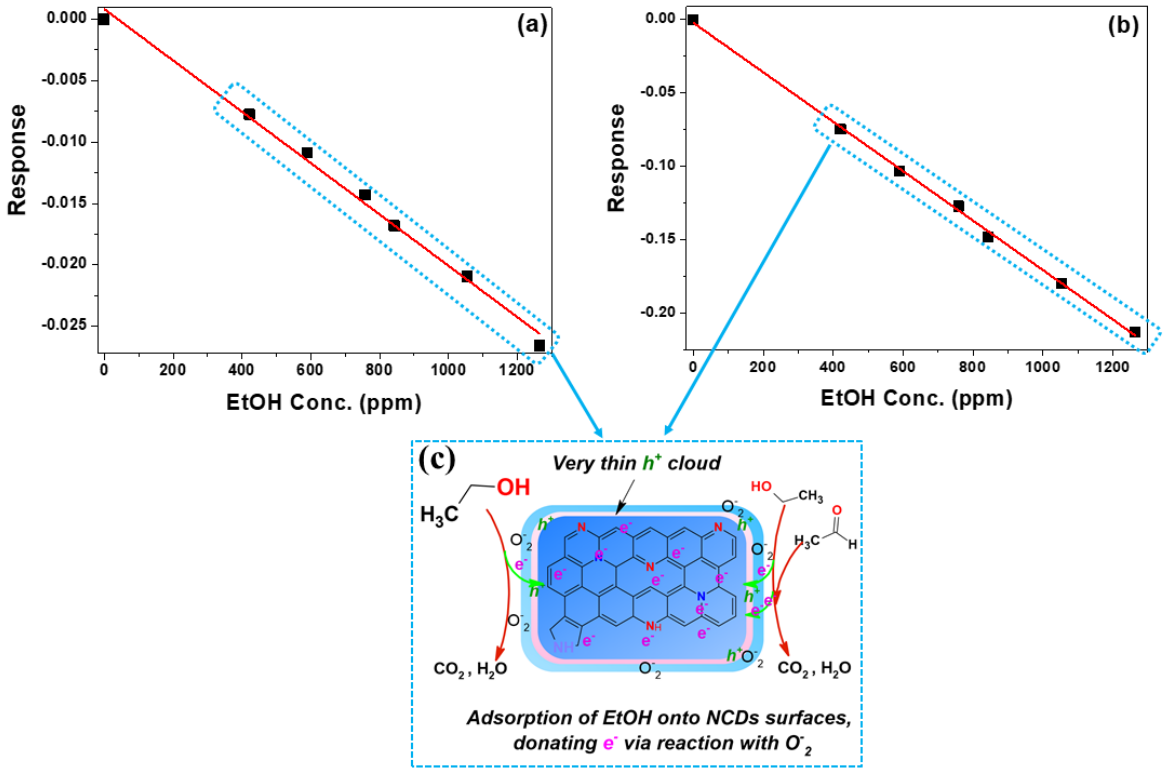

Figure 7.9: Sensor response as a function of EtOH vapour concentrations for the **(a)** NCDs400 and **(b)** NCDs700 sensor devices; **(c)** detection mechanism of EtOH.

From **Table 7.2**, the reported impedimetric sensing performances for the detection of either MeOH or EtOH are seen to be comparable to data measured for graphene oxide, transition metal dichalcogenides (TMDs), metal oxides, and metal frameworks. More importantly, the facile route for transforming 0D CDs into 2D nanostructures [22] also produced a composite of CDs/NCDs carbon fragments that improved the charge carrier retention and formation of the depletion layers. This facilitated a faster charge carrier transportation from the active material to the analyte molecules, and hence enhanced the sensitivity. Moreover, the use of the

'composites' (NCDs200 and NCDs400) as well as the NCDs700 (with large basal area), generated enough defective sites for improved adsorption of the VOCs analyte molecules, therefore eliminating the need to use conducting polymers [8] or porous molecular frameworks [55]. This provides an alternative method to make the alcohol sensor without added synthesis steps.

Table 7.2: Comparative MeOH and EtOH detection for EIS-based devices

Analyte	Active Material	Conc. Range (ppm)	Temp. (°C)	LoD (ppm)	Ref
Methanol	Au/TiO_2-NT	200-600	27	-	[56]
	NCDs200 NCDs400 NCDs700	120-1200	RT	37.1 34.9 30.3	*This work*
	MoS_2	200-400	200	-	[57]
	Cu-BTC MOF	250-1500	25	62	[55]
Ethanol	β-In_2S_3	500-1000	350	6[a]	[58]
	NCDs400 NCDs700	420 - 1200	RT	91.4 43.5	*This work*
	PLA-Gr	25-100	50	-	[59]
	GN-PMMA	1.96 -69[b]	RT	19.7	[8]
	ZnO	1-500	RT	100	[60]

Au/TiO_2-NT/Ti -> gold on titania nanotubes, In_2S_3-> indium selenide, ZnO-> zinc oxide, PMMA -> polymethyl methacrylate, MoS_2 -> molybdenum disulphide, Cu-BTC -> copper-benzene tricarboxylate, PLA->poly (lactic acid), MOF -> metal organic framework.

7.4 Conclusions

The study demonstrated that through a facile thermal treatment, nitrogen-doped and large-area 2D graphene-like nanostructures could be easily attained from 0D CDs by adjustment of the CDs annealing temperature (200–700 °C). Furthermore, the nitrogen content as well as the

nitrogen configurations of the N-doped CDs was found to be dependent on the structural transformation due to the annealing temperature. For instance, as higher temperatures favoured the lateral growth, the arrangement of N-atoms was found to be more dominant at the carbon edges (~57 at% pyridinic-N), whilst the coalescence of the CDs into 2D nanostructures led to the ingrowth of interstitial nitrogen dopants (~17 at% graphitic-N). At 200 ℃, the transformation of CDs into 2D nanostructures was incomplete, resulting in the synthesis of a carbon composite made of CDs fragments embedded in an amorphous mass of N-doped carbon. Screening for VOCs through the impedimetric sensing measurements, demonstrated that the NCDs-based devices were responsive to methanol and ethanol. A good correlation between the structural properties of the NCDs as well as the type of N-configurations and their corresponding sensitivity for the alcohol-based VOCs was observed. In particular, the large-area 2D NCDs700 nanosheets facilitated a high charge density via the incorporation of pyridinic-N (~57 at%) and graphitic-N (~18.3 at%) configurations. This subsequently promoted enhanced sensitivity and selectivity of the NCDs700-based devices for the detection and recognition of both methanol and ethanol. Generally, the transformed nanostructures exhibited excellent room temperature impedimetric sensing performance for the detection of alcohol-based VOCs, thereby opening up a new platform for carbon-based materials for chemical vapour sensing. As the different NCDs gave different abilities for the detection of EtOH and MeOH this suggests that a combination of these 'easy to make' structures could be used to develop an 'electronic nose' for the room temperature detection of many other VOCs.

Author Contributions

L.L.M.; J.B.M: Writing, Data Collection, Analysis, Design

N.A., B.D.M.; D.H.B.: Data Collection, Analysis

R.P.F.; Z. S.; N.J.C.: Conception, Design, Supervision, Funding.

Conflicts of interest

There are no conflicts to declare.

Acknowledgements

The study was financially supported by the NRF, the University of the Witwatersrand (post graduate merit award to LLM), the DSI-NRF Centre of Excellence in Catalysis (*c**change, LLM, NJC and RPF), the European Structural and Investment Funds (JBM) under OP RDE-funded project 'CHEMFELLS IV' (No. CZ.02.2.69/0.0/0.0/20_079/0017899), and by the Czech Science Foundation (GAČR No. 18-03346S). Sincere gratitude goes to Dr Rudolph Erasmus from the School of Physics at the University of the Witwatersrand for his assistance with Raman and photoluminescence collection and analysis. We are also thankful to Dr Memory Zimuwandeyi and Mr Mudzuli Maphupha (School of Chemistry, University of the Witwatersrand) for NMR data collection and data processing, respectively. We would also like to thank Mr Solly Motaung and Ms Sinegugu Nzuza (Council for Scientific and Industrial Research, South Africa) for the HRTEM analysis data. Finally, we thank the Canadian Light Source, a national research facility of the University of Saskatchewan, which is supported by the Canada Foundation for Innovation (CFI), the Natural Sciences and Engineering Research Council (NSERC), the National Research Council (NRC), the Canadian Institutes of Health Research (CIHR), the Government of Saskatchewan, and the University of Saskatchewan for PDF data collection.

7.5 References

[1] C. K. McGinn, Z. A. Lamport, and I. Kymissis, “Review of gravimetric sensing of volatile organic compounds,” *ACS Sensors*, vol. 5, no. 6, pp. 1514–1534, 2020, doi: 10.1021/acssensors.0c00333.

[2] B. Li, Q. Zhou, S. Peng, and Y. Liao, “Recent advances of SnO_2-based sensors for detecting volatile organic compounds,” *Front. Chem.*, vol. 8, no. May, pp. 1–6, 2020, doi: 10.3389/fchem.2020.00321.

[3] A. Mirzaei, S. G. Leonardi and G. Neri, "Detection of hazardous volatile organic compounds (VOCs) by metal oxide nanostructures-based gas sensors: A review," *Ceram. Int.*, vol. 42, pp. 15119–15141, 2016, doi:10.1016/j.ceramint.2016.06.145.

[4] W. T. Tsai, “An overview of health hazards of volatile organic compounds regulated as indoor air pollutants,” *Rev. Environ. Health*, vol. 34, no. 1, pp. 81–89, 2019, doi: 10.1515/reveh-2018-0046.

[5] J. M. Celaya-Padilla, J.S. Romero-González, C.E. Galvan-Tejada, J.I. Galvan-Tejada, H. Luna-García, J.G. Arceo-Olague, N.K. Gamboa-Rosales, C. Sifuentes-Gallardo, A. Martinez-Torteya, J.I. De la Rosa, and H. Gamboa-Rosales, “In-vehicle alcohol detection using low-cost sensors and genetic algorithms to aid in the drinking and driving detection,” *Sensors*, vol. 21, no. 22, 2021, doi: 10.3390/s21227752.

[6] G. J. Thangamani, K. Deshmukh, K. C. M. Basheer, A. Kishor, and K. Sadasivuni, “Influence of CuO nanoparticles and graphene nanoplatelets on the sensing behaviour of poly (vinyl alcohol) nanocomposites for the detection of ethanol and propanol vapors,” *J. Mater. Sci. Mater. Electron.*, vol. 29, no. 6, pp. 5186–5205, 2018, doi: 10.1007/s10854-017-8484-z.

[7] S. Lakkis, R. Younes, Y. Alayli, and M. Sawan, “Review of recent trends in gas sensing technologies and their miniaturization potential,” *Sens. Rev.*, vol. 34, no. 1, pp. 24–35, 2014, doi: 10.1108/SR-11-2012-724.

[8] A. Yavarinasab, S. Janfaza, N. Tasnim, H. Tahmooressi, A. Dalili, and M. Hoorfar, “Graphene/poly (methyl methacrylate) electrochemical impedance-transduced

chemiresistor for detection of volatile organic compounds in aqueous medium," *Anal. Chim. Acta*, vol. 1109, pp. 27–36, 2020, doi: https://doi.org/10.1016/j.aca.2020.02.065.

[9] X. Zhu, J. Zhang, Q. Xie, and Z.-L. Hou, "High-sensitivity and ultrafast-response ethanol sensors based on graphene oxide," *ACS Appl. Mater. Interfaces*, vol. 12, no. 34, pp. 38708–38713, Aug. 2020, doi: 10.1021/acsami.0c12196.

[10] L. T. Duy, Y. G. Noh, and H. Seo, "Improving graphene gas sensors via a synergistic effect of top nanocatalysts and bottom cellulose assembled using a modified filtration technique," *Sensors Actuators B Chem.*, vol. 334, p. 129676, 2021, doi: https://doi.org/10.1016/j.snb.2021.129676.

[11] S. Hu, Q. Huang, Y. Lin, C. Wei, H. Zhang, W. Zhang, Z. Guo, X. Bao, J. Shi and A. Hao, "Reduced graphene oxide-carbon dots composite as an enhanced material for electrochemical determination of dopamine," *Electrochim. Acta*, vol. 130, pp. 805–809, 2014, doi: 10.1016/j.electacta.2014.02.150.

[12] J. Fang, Z. Xie, G. Wallace, and X. Wang, "Co-deposition of carbon dots and reduced graphene oxide nanosheets on carbon-fiber microelectrode surface for selective detection of dopamine," *Appl. Surf. Sci.*, vol. 412, pp. 131–137, 2017, doi: 10.1016/j.apsusc.2017.03.257.

[13] F. Meng, Z. Guo, and X. Huang, "Trends in analytical chemistry graphene-based hybrids for chemiresistive gas sensors," *Trends Anal. Chem.*, vol. 68, pp. 37–47, 2015, doi: 10.1016/j.trac.2015.02.008.

[14] J. Hu, C. Zou, Y. Su, M. Li, N. Hu, H. Ni, Z. Yang and Y. Zhang, "Enhanced NO_2 sensing performance of reduced graphene oxide by: In situ anchoring carbon dots," *J. Mater. Chem. C*, vol. 5, no. 27, pp. 6862–6871, 2017, doi: 10.1039/c7tc01208j.

[15] M. M. Rahman, M. A. Hussein, K. A. Alamry, F. M. Al Shehry, and A. M. Asiri, "Sensitive methanol sensor based on PMMA-G-CNTs nanocomposites deposited onto glassy carbon electrodes," *Talanta*, vol. 150, pp. 71–80, 2016, doi: 10.1016/j.talanta.2015.12.012.

[16] H. Xu, L. Ma and Z. Jin, "Nitrogen-doped graphene: Synthesis, characterizations and

energy applications," *J. Energy Chem.*, vol. 27, pp. 146–160, 2018, doi:10.1016/j.jechem.2017.12.006.

[17] R. Yadav and C. K. Dixit, "Synthesis, characterization and prospective applications of nitrogen-doped graphene: A short review," *J. Sci.: Adv. Mater. Devices*, vol. 2 , pp. 141–149, 2017, doi:10.1016/j.jsamd.2017.05.007.

[18] M. Coros, C. Varodi, F. Pogacean, E. Gal, and S. M. Pruneanu, "Nitrogen-doped graphene: The influence of doping level on the charge-transfer resistance and apparent heterogeneous electron transfer rate," *Sensors* , vol. 20, no. 7, 2020, doi: 10.3390/s20071815.

[19] Q. Huang, Y. Xu, Y. Guo, L. Zhang, Y. Hu, J. Qian and S. Huang, "Highly graphitized N-doped carbon nanosheets from 2-dimensional coordination polymers for efficient metal-air batteries," *Carbon*, vol. 188, 135–145, 2022, doi: 10.1016/j.carbon.2021.11.062.

[20] Y. Tang, H. Zhang, W. Chen, Z. Li, Z. Liu, D. Teng and X. Dai, "Modulating geometric, electronic, gas sensing and catalytic properties of single-atom Pd supported on divacancy and N-doped graphene sheets," *Appl. Surf. Sci.*, vol. 508, p. 145245, 2020, doi:10.1016/j.apsusc.2020.145245.

[21] G. Bharathi, D. Nataraj, S. Premkumar, M. Sowmiya, K. Senthilkumar, T. Thangadurai, O. Khyzhun, M. Gupta, D. Phase, N. Patra, S. Jha and D. Bhattacharyya, "Graphene quantum dot solid sheets: Strong blue-light-emitting & photocurrent-producing band-gap-opened nanostructures," *Sci. Rep.*, vol. 7, no. 1, pp. 1–17, 2017, doi: 10.1038/s41598-017-10534-4.

[22] L. L. Mokoloko, B. J. Matsoso, R. P. Forbes, D. H. Barrett, B. D. Moreno, and N. J. Coville, "Evolution of large-area reduced graphene oxide nanosheets from carbon dots via thermal treatment," *Carbon Trends*, vol. 4, p. 100074, 2021, doi: 10.1016/j.cartre.2021.100074.

[23] H. Hou, L. Shao, Y. Zhang, G. Zou, J. Chen, and X. Ji, "Large-area carbon nanosheets doped with phosphorus: A high-performance anode material for sodium-ion batteries,"

Adv. Sci., vol. 4, no. 1, 2017, doi: 10.1002/advs.201600243.

[24] A. Sharma and J. Das, "Small molecules derived carbon dots: Synthesis and applications in sensing, catalysis, imaging, and biomedicine," *J. Nanobiotechnology*, vol. 17, no. 1, pp. 1–24, 2019, doi: 10.1186/s12951-019-0525-8.

[25] S. Zhu, Y. Song, X. Zhao, J. Shao, J. Zhang, and B. Yang, "The photoluminescence mechanism in carbon dots (graphene quantum dots, carbon nanodots, and polymer dots): current state and future perspective," *Nano Res.*, vol. 8, no. 2, pp. 355–381, 2015, doi: 10.1007/s12274-014-0644-3.

[26] S. Sugiarti and N. Darmawan, "Synthesis of fluorescence carbon nanoparticles from ascorbic acid," vol. 15, no. 2, pp. 141–145, 2015, doi.org/10.22146/ijc.21207.

[27] S. K. Bajpai, A. D'Souza and B. Suhail, "Blue light-emitting carbon dots (CDs) from a milk protein and their interaction with Spinacia oleracea leaf cells," *Int. Nano Lett.*, vol. 9, pp. 203–212, 2019, doi:10.1007/s40089-019-0271-9.

[28] A. C. Ferrari, J. Robertson, A. C. Ferrari, and J. Robertson, "Raman spectroscopy of amorphous, nanostructured, diamond–like carbon, and nanodiamond," *Philos. Trans. R. Soc. London. Ser. A Math. Phys. Eng. Sci.*, vol. 362, no. 1824, pp. 2477–2512, Nov. 2004, doi: 10.1098/rsta.2004.1452.

[29] L. M. Malard, M. A. Pimenta, G. Dresselhaus, and M. S. Dresselhaus, "Raman spectroscopy in graphene," *Phys. Rep.*, vol. 473, no. 5, pp. 51–87, 2009, doi: https://doi.org/10.1016/j.physrep.2009.02.003.

[30] P. Luo, C. Li and G. Shi, "Synthesis of gold@carbon dots composite nanoparticles for surface enhanced Raman scattering," *Phys. Chem. Chem. Phys.*, vol. 14, pp. 7360–7366, 2012,doi: 10.1039/c2cp40767a.

[31] L. G. Cançado, K. Takai, T. Enoki, M. Endo, Y. A. Kim, H. Mizusaki, A. Jorio, L. N. Coelho, R. Magalhães-Paniago and M. A. Pimenta, "General equation for the determination of the crystallite size La of nanographite by Raman spectroscopy," *Appl. Phys. Lett.*, vol. 88, no. 16, p. 163106, 2006, doi: 10.1063/1.2196057.

[32] B. K. Mutuma, B. J. Matsoso, K. Ranganathan, J. Keartland, D. Wamwangi, and N. J. Coville, “Generation of radical species in CVD grown pristine and N-doped solid carbon spheres using H_2 and Ar as carrier gases,” *RSC Adv.*, vol. 7, no. 34, 2017, doi: 10.1039/c7ra03142d.

[33] V. N. Mehta, S. Jha, and K. Singhal, “Preparation of multicolor emitting carbon dots for HeLa cell imaging,” *New J. Chem.*, vol. 38, pp. 6152–6160, 2014, doi: 10.1039/c4nj00840e.

[34] X. Mu, B. Yuan, X. Feng, S. Qiu, L. Song, and Y. Hu, “The effect of doped heteroatoms (nitrogen, boron, phosphorus) on inhibition thermal oxidation of reduced graphene oxide,” *RSC Adv.*, vol. 6, no. 107, pp. 105021–105029, 2016, doi: 10.1039/c6ra21329d.

[35] R. Bandi, B. R. Gangapuram, R. Dadigala, R. Eslavath, S. S. Singh, and V. Guttena, “Facile and green synthesis of fluorescent carbon dots from onion waste and their potential applications as sensor and multicolour imaging agents,” *RSC Adv.*, vol. 6, no. 34, pp. 28633–28639, 2016, doi: 10.1039/c6ra01669c.

[36] H. W. Kim, H. Park, J. S. Roh, J. E. Shin, T. H. Lee, L. Zhang, Y. H. Cho, H. W. Yoon, V. J. Bukas, J. Guo, H. B. Park, T. H. Han and B. D. McCloskey, "Carbon defect characterization of nitrogen-doped reduced graphene oxide electrocatalysts for the two-electron oxygen reduction reaction," *Chem. Mater.*, vol. 31, pp. 3967–3973, 2019, doi:10.1021/acs.chemmater.9b00210.

[37] D. Das and R. K. Dutta, “N-doped carbon dots synthesized from ethylene glycol and β-alanine for detection of Cr(VI) and 4-nitrophenol via photoluminescence Quenching,” *ACS Appl. Nano Mater.*, vol. 4, no. 4, pp. 3444–3454, Apr. 2021, doi: 10.1021/acsanm.0c03329.

[38] B. J. Matsoso, K. Ranganathan, B. K. Mutuma, T. Lerotholi, G. Jones, and N. J. Coville, “Time-dependent evolution of the nitrogen configurations in N-doped graphene films,” *RSC Adv.*, vol. 6, no. 108, pp. 106914–106920, 2016, doi: 10.1039/c6ra24094a.

[39] N. Hellgren, R. T. Haasch, S. Schmidt, L. Hultman, and I. Petrov, “Interpretation of X-ray photoelectron spectra of carbon-nitride thin films: New insights from in situ XPS,”

Carbon N. Y., vol. 108, pp. 242–252, 2016, doi: https://doi.org/10.1016/j.carbon.2016.07.017.

[40] X. Chen, X. Wang, and D. Fang, "A review on C1s XPS-spectra for some kinds of carbon materials," *Fullerenes, Nanotub. Carbon Nanostructures*, vol. 28, no. 12, pp. 1048–1058, 2020, doi: 10.1080/1536383x.2020.1794851.

[41] M. Ayiania, A. J. R. Hensley, K. Groden, M. Garcia-Perez, and J.-S. McEwen, "Thermodynamic stability of nitrogen functionalities and defects in graphene and graphene nanoribbons from first principles," *Carbon N. Y.*, vol. 152, pp. 715–726, 2019, doi: https://doi.org/10.1016/j.carbon.2019.06.019.

[42] S. Kabir, K. Artyushkova, A. Serov, B. Kiefer, and P. Atanassov, "Binding energy shifts for nitrogen-containing graphene-based electrocatalysts – experiments and DFT calculations," *Surf. Interface Anal.*, vol. 48, no. 5, pp. 293–300, May 2016, doi: https://doi.org/10.1002/sia.5935.

[43] S. J. L. Billinge, "The rise of the X-ray atomic pair distribution function method: A series of fortunate events," *Philos. Trans. R. Soc. A Math. Phys. Eng. Sci.*, vol. 377, no. 2147, 2019, doi: 10.1098/rsta.018.0413.

[44] W. Dmowski, C. I. Contescu, A. Llobet, N. C. Gallego, and T. Egami, "Local atomic density of microporous carbons," *J. Phys. Chem. C*, vol. 116, no. 4, pp. 2946–2951, 2012, doi: 10.1021/jp209824f.

[45] F. H. Allen, O. Kennard, D. G. Watson, L. Brammer, A. G. Orpen and R. Taylor, "Tables of bond lengths determined by X-ray and neutron diffraction. part I. bond lengths in organic compounds," *J. Chem. Soc.*, Perkin Trans., 2, 1987, S1–S19.

[46] H. Krzton and M. Niewiara, "Studies on commercial carbon black by radial distribution function and rietveld refinement," *Phys. Scr.*, vol. 1995, no. T57, pp. 98–101, 1995, doi: 10.1088/0031-8949/1995/t57/016.

[47] J. A. Garlow, L. K. Barrett, L. Wu, K. Kisslinger, Y. Zhu and J. F. Pulecio, "Large-area growth of turbostratic graphene on Ni(111) via physical vapor deposition," *Sci. Rep.*, vol. 6, p.19804, 2016, doi:10.1038/srep19804.

[48] A. Lasia, “Electrochemical impedance spectroscopy and its applications BT - Modern aspects of electrochemistry,” B. E. Conway, J. O. Bockris, and R. E. White, Eds. Boston, MA: Springer US, 2002, pp. 143–248.

[49] R. Li, J. Fan, H. Li, X. Yan, and Y. Yu, “Dynamic behaviors and transport properties of ethanol molecules in transmembrane cyclic peptide nanotubes,” *J. Chem. Phys.*, vol. 143, no. 1, p. 15101, Jul. 2015, doi: 10.1063/1.4923010.

[50] B. K. Mutuma, C. I. Garcia-Martinez, R. C. Dias, B. J. Matsoso, N. J. Coville and I. A. Hummelgen, “Nitrogen-doped hollow carbon spheres as chemical vapour sensors,” *New J. Chem.*, vol. 43, pp. 8418–8427, 2019,doi: 10.1039/C9nj00628a.

[51] A. Wisitsoraat, A. Tuantranont, E. Comini, G. Sberveglieri, and W. Wlodarski, “Characterization of n-type and p-type semiconductor gas sensors based on NiOx doped TiO_2 thin films,” *Thin Solid Films*, vol. 517, no. 8, pp. 2775–2780, 2009, doi: https://doi.org/10.1016/j.tsf.2008.10.090.

[52] K. Zhang, Y. Feng, F. Wang, Z. Yang, and J. Wang, “Two dimensional hexagonal boron nitride (2D-hBN): synthesis, properties and applications,” *J. Mater. Chem. C*, vol. 5, no. 46, pp. 11992–12022, 2017, doi: 10.1039/c7tc04300g.

[53] S. Navale, M. Shahbaz, A. Mirzaei, S. S. Kim, and H. W. Kim, “Effect of Ag addition on the gas-sensing properties of nanostructured resistive-based gas sensors: An overview,” *Sensors* , vol. 21, no. 19. 2021, doi: 10.3390/s21196454.

[54] Z. Cai and S. Park, Enhancement mechanisms of ethanol sensing properties based on Cr_2O_3 nanoparticle-anchored SnO_2 nanowires, *J. Mater. Res. Technol*., vol. 9, pp. 271–281,2020, doi:10.1016/j.jmrt.2019.10.055.

[55] S. Homayoonnia and S. Zeinali, “Design and fabrication of capacitive nanosensor based on MOF nanoparticles as sensing layer for VOCs detection,” *Sensors Actuators B Chem.*, vol. 237, pp. 776–786, 2016, doi: https://doi.org/10.1016/j.snb.2016.06.152

[56] P. Bindra and A. Hazra, “Impedance behavior of n-type TiO_2 nanotubes porous layer in reducing vapor ambient,” *Vacuum*, vol. 152, pp. 78–83, 2018, doi: https://doi.org/10.1016/j.vacuum.2018.03.008.

[57] M. Barzegar, M. Berahman, and A. I. Zad, “Sensing behavior of flower-shaped MoS_2 nanoflakes: Case study with methanol and xylene,” *Beilstein J. Nanotechnol.*, vol. 9, no. 1, pp. 608–615, 2018, doi: 10.3762/bjnano.9.57.

[58] R. Souissi, N. Bouguila, and A. Labidi, “Ethanol sensing properties of sprayed β-In_2S_3 thin films,” *Sensors Actuators B Chem.*, vol. 261, pp. 522–530, 2018, doi: https://doi.org/10.1016/j.snb.2018.01.175.

[59] G. Chakraborty, G. Pugazhenthi, and V. Katiyar, “Exfoliated graphene-dispersed poly (lactic acid)-based nanocomposite sensors for ethanol detection,” *Polym. Bull.*, vol. 76, no. 5, pp. 2367–2386, 2019, doi: 10.1007/s00289-018-2494-8.

[60] P. Shankar and J. B. B. Rayappan, “Room temperature ethanol sensing properties of ZnO nanorods prepared using an electrospinning technique,” *J. Mater. Chem. C*, vol. 5, no. 41, pp. 10869–10880, 2017, doi: 10.1039/c7tc03771f.

CHAPTER 8: CONCLUSION AND RECOMMENDATIONS

8.1 Synthesis of carbon dots (CDs)

This work has shown that CDs can be obtained from one-step synthesis procedures using non-functionalized and functionalized carbon sources. In **Chapter 4**, CDs of various particle sizes (*ca.* 3 to 8 nm) were synthesized by simply carbonizing acetylene gas (C_2H_2, 25 sccm) at high temperature (> 800 °C) and a high carrier gas flow rate (> 500 sccm) in a vertical chemical vapor deposition (CVD) apparatus. The CDs produced using this method had a high thermal stability, minimal surface functional groups, and exhibited both graphitic and amorphous character as shown by techniques such as thermogravimetric analysis (TGA), Fourier transform infrared (FT-IR) spectroscopy, powder X-ray diffraction (PXRD), and Raman spectroscopy analysis, respectively. To the best of our knowledge, this was the first time the vertical CVD synthesis route or technique was used to make CDs. Thus, the success highlighted by our current work adds a new platform to the already wide range of synthesis methods for making/producing CDs. Importantly, this new procedure could be particularly useful for the facile production of CD nanoparticles with efficiently controlled particle size, which could prove useful for future nanomaterials research.

In our studies, the synthesis of carbon spheres (CSs) with different sizes (≥100 nm) was also achieved using the vertical CVD synthesis technique. A mechanism to differentiate between CDs and CSs formation was proposed. In hindsight, our results suggested that CDs have previously been produced, by ourselves and others, as by-products during CSs synthesis in earlier studies that used a vertical CVD synthesis procedure. However, due to the limitations in characterization procedures available in many laboratories, in particular, high-resolution transmission electron microscopy (HRTEM), their presence had gone unnoticed. It is also possible that in many instances, the CDs may have been removed in washing and filtration procedures.

Despite the possibility of synthesizing CDs via the vertical CVD method, the major drawback of the method is the low yield of CDs produced (< 5 %). This low yield is a consequence of the high flow rates of the carrier gas required during the synthesis step. To improve this yield will require modifications of the experimental set-up by using procedures that can trap the CDs nanoparticles, but also allow the free flow of gases to avoid pressure build-up within the system.

In another study, the synthesis of CDs from *L*-ascorbic acid using microwave radiation was used as a facile and cost-effective method to make CDs. The method produced up to 28 % yield of CDs, with *ca.* 2.5 nm average size and > 20 % oxygen content as determined by transmission electron microscopy (TEM) and X-ray photoelectron spectroscopy (XPS) analysis, respectively. Nonetheless, TGA results showed that the microwave prepared CDs were only stable < 200 °C because of their functionalized surface. Incorporating urea in the synthesis step led to the formation of nitrogen-doped CDs (NCDs) with *ca.* 4.1 nm average size and *ca.* 35 % yield. XPS studies revealed that the NCDs contained *ca.* 16 % N-content. The thermal stabilities of these NCDs were comparable with those of the pristine CDs. Both the pristine CDs and NCDs were only stable at temperatures below 200 °C.

8.2 Annealing of the CDs

Chapter 5 reported the results obtained from annealing the functionalized CDs prepared from *L*-ascorbic acid. The main objective of the annealing reaction of the functionalized CDs was to reduce the oxygen content, with the intention of making them more thermally stable. However, the removal of the functional groups of the CDs also modified their structure, more specifically, the high-temperature treatment of the CDs transformed them into layered materials, resembling the structure of 2-D graphene-like materials. A critical study on the physicochemical structures of these CDs, after annealing, showed that when CDs were heat-treated at 700 °C under N_2 gas (100 sccm), they produced a layered carbon material with a high content of aromatic carbon compared to the original CDs. This was determined using various characterization techniques such as ^{13}C NMR spectroscopy, XPS studies, Raman spectroscopy analysis. The physicochemical properties of this carbon were compared with those of other carbon allotropes, and showed that the CDs annealed at 700 °C under N_2 gas for 10 min had similar properties to reduced graphene oxide (rGO) obtained from oxidation and reduction of graphite and graphene oxide (GO), respectively. Moreover, critical evaluation of the step-by-step transformation of the CDs from 250 to 700 °C under N_2 mimicked the step-by-step transformation of GO to rGO. For example, the rGO formed either from hydrazine reduced GO or hydrothermal treatment of GO as reported in the literature had similar properties to the carbons produced here. Thus, ^{13}C NMR spectra indicated the presence of C-O, C=O, C-C and C=C peaks for the CDs sample, most of which gradually decreased with increasing temperature until at 700 °C, only the C=C peak remained. The C/O ratio increased, and the Raman I_D/I_G peak ratio of these samples also increased with increasing temperature. The single feature in the PXRD data of the CD samples

at 18 ° 2θ, followed by the shift and development of other features at 14 °, 24 °, 30 °, and 42 ° 2θ as the annealing temperature was increased, was similar to studies carried out on GO and rGO. The TEM images of the rGO measured in this study showed a flat layered carbon, resembling the structure of graphene, with estimated sheet sizes of *ca.* $1.71 \pm 0.104 \times 0.909 \pm 0.0577$ μm. Therefore, this study added another synthesis procedure for a facile "bottom-up" production of rGO.

Similar annealing experiments were also explored for nitrogen-doped CDs (NCDs). For these samples, the CDs were transformed into layered materials at temperatures as low as 200 ℃. When the NCDs are annealed at 700 ℃, a multi-layered carbonaceous material is formed with a lateral diameter of *ca.* 2.75 μm and thickness of *ca.* 14 nm, contrary to the formation of a single-layered rGO when pristine CDs are annealed under the same conditions. Additionally, the TEM and AFM results of these multi-layered carbons did not show any evidence of any residual CDs embedded in the layered structure, contrary to the TEM and AFM data reported for the pristine CDs annealed at 700 ℃. This suggests that N-doping accelerates the knitting of these NCDs to form layered carbon structures. Evaluation of the XPS results of the NCDs annealed samples showed that a decrease in the oxygen content from *ca.* 18 % to 8 % occurred for samples annealed at 200 ℃ and 700 ℃, respectively, similarly to the findings on the pristine CDs samples. Only a slight decrease in the nitrogen content was observed for these two samples (from *ca.* 10 % to 8 % for samples annealed at 200 and 700 ℃, respectively). Furthermore, there was an increase in the pyridinic-N and a decrease in the pyrrolic-N and other edge nitrogen bonds such as amides with temperature, suggesting that during annealing, some of the edge atoms were converted to the sp^2 hybridized nitrogen.

Additionally, this study also explored the properties of the new materials using pair distribution function (PDF) analysis of synchrotron X-ray diffraction data. Only a handful of papers have reported PDF analysis of carbon allotropes. The PDF results together with other analysis results reported above, were used to explain the evolution of the rGO from CDs, and a mechanism for the transformation was proposed. It was suggested that as the oxygen functional groups were removed from the surface of the CDs, the increase in the C atoms on the edge of the carbon skeleton, allowed for these C atoms (and C and N atoms at the edge of the NCDs) to be knitted together either from the gas phase (following an Ostwald ripening route) or by solid-solid interactions to give the layered carbon sheets.

Poor Raman spectra were obtained for the pristine and N-doped CDs, and for samples annealed ≤ 400 °C due to the background fluorescence of the samples, and negative adsorption-desorption isotherms were obtained from BET results for these samples. In future studies, to overcome these issues, Fourier transform Raman spectroscopy will be required, as this will reduce background fluorescence. For the BET analysis, krypton (Kr) gas instead of N_2 gas is recommended for adsorption at liquid N_2 temperature for small pore analysis. Unfortunately, these types of analysis techniques could not be accessed during the course of this study.

CDs are considered useful in energy conversion and storage as well as in biological systems and their application in these fields is progressing rapidly. The ability of CDs to assemble into 1-D, 2-D and/or 3-D carbon allotropes at high temperatures and in the presence of a catalyst has opened up new horizons for CDs applications. Many potential industrial applications require the large-scale and cheap preparation of nanomaterials, and this include those made from CDs. Therefore, the thermal and/or catalytically induced conversion of CDs into 1-D, 2-D and/or 3-D carbon could be a route that satisfies larger scale production requirements. In **Chapter 2**, literature evidence highlighted the synthesis conditions, as well as applications needed for the synthesis of these allotropes. Advanced studies on the novel evolution of 1-D, 2-D and/or 3-D carbon allotropes from 0-D CDs are still required. Specifically, the following question still needs to be answered:

1) Can all types of CDs e.g., graphene quantum dots (GQDs), carbon quantum dots (CQDs), carbon nanodots (CNDs), and carbonized polymer dots (CPDs), be used as precursors for the synthesis of large sized carbon allotropes?
2) Does the CD type control the type of allotrope produced as a final product?
3) Can these allotropes be produced from non-functionalized CDs as well?
4) How do these CD-derived allotropes compare to those produced by conventional methods? And can they be applied as conventional allotropes?

8.3 Applications of CDs in the Fischer-Tropsch Synthesis reactions

The initial question posed for this study was: “Are CDs as well as their derivatives viable for use as support materials for application in the Fischer-Tropsch synthesis (FTS) reaction?”

Typically, a good FTS catalyst support has good thermal stability, high surface area, and the ability to anchor metals in such a way that metal attrition is significantly minimized.

The results obtained from this study show that the as-prepared CDs did not meet the requirements of an FTS support. The CDs produced from the vertical CVD method had the physicochemical properties that are required for the FTS support, especially the high thermal stability, however; the produced yields were extremely low, and thus the product could not be used in the FTS studies.

The CDs produced from the microwave-assisted synthesis were found to be temperature-sensitive. Analysis results showed evidence of loss of structural integrity of the CDs at temperatures > 200 °C, which included the FTS operation temperatures. Co/carbon catalysts were made with the annealed carbons. Even Co/carbons that had been annealed at T = 700 °C were not stable at high temperature as shown by the H_2-TPR and *in situ* PXRD studies. All the catalysts made with Co on the various annealed carbons showed very poor % CO conversion (< 15 %) and selectivity (< 30 %) towards the desired C_{5+} hydrocarbons under FTS conditions.

The CD samples annealed at 250 and 400 °C showed that Co_3O_4 was autoreduced to Co(fcc) at temperatures > 400 °C. This is similar to the autoreduction studies conducted on CNTs, CSs, and graphitic carbon nitride supports reported in the literature. This study further confirmed that it is not always necessary to utilize H_2 for the reduction of metal oxides used in the FTS when carbon allotropes are used as supports. Reduction in these systems, however, requires a high temperature to activate the redox reactions between the metal oxide and the carbon support.

8.4 Applications of CDs as volatile organic compound sensors

Though the CDs and their derivatives show only limited applications in the FTS reaction, the material show potential for application as active material in the fabrication of s room temperature chemoresistive sensing device. In **Chapter 7**, the NCDs annealed at 200, 400 and 700 ℃ were tested for sensitivity and selectivity towards two alcohols (methanol and ethanol). The results showed that both the carbon morphology/structure and the configuration of the nitrogen in the structure played an important role in their sensing properties. The samples annealed at 400 and 700 ℃ showed better sensitivity towards the alcohols due to an increase in the lateral size of the carbon materials as well as the sp^2 type nitrogen bonding. More specifically, the sample annealed at 700 ℃ produced a high charge density due to the presence of the pyridinic-N (*ca.* 56.9 %) and graphitic-N (*ca.* 18.3 at. %) configurations. This then led to good sensitivity (-16.8×10^{-5} ppm^{-1} EtOH and 1.2×10^{-5} ppm^{-1} MeOH) and low LoD (~44 ppm EtOH and ~30.3

ppm MeOH) values for the alcohols. Furthermore, these NCDs-derived sheets showed comparable results with other devices described in the literature. To further confirm the correlation between nitrogen bonding configurations and sensing properties, the pristine CDs-derived sheets will be tested for chemoresistive sensing devices under the same conditions in the future.

8.5 Future work

The major problem with the synthesis of high stability and poorly functionalized CDs via CVD, as highlighted in **Chapter 4**, was the % yields of the products. The CDs yields can be improved by employing a new set-up that can trap as much product as possible during synthesis. It is still unclear how the set up could be modified to help improve the yield. Further investigations on this would be required. Obtaining these thermally stable CDs in high % yields will allow the synthesis and FTS properties studies of inverse Co_3O_4/CDs, and the initial objective of the study could then be accomplished. Furthermore, extensive *in situ* laboratory based PXRD FTS and other studies as well as the same experiments will be repeated at a synchrotron.

These high stability and poorly functionalized CDs will be subjected to annealing at 200- 700 ℃, to see whether they will also be transformed to higher dimensional carbon, similarly to the highly functionalized CDs obtained in **Chapters 5** and **7**.

The nitrogen-doped graphene-like sheets obtained in this study have already shown great potential for sensing applications, as shown in **Chapter 7**. Other functionalized CDs and their derivatives (e.g., those obtained in **Chapter 5**, nitrogen and sulfur doped CDs, boron doped CDs, among others) can also be synthesized and tested for VOCs sensing, and compared with the results obtained in **Chapter 7**.

.

APPENDIX A: CHAPTER 4 SUPPLEMENTARY INFORMATION

The simultaneous synthesis of carbon dots and carbon spheres with tuneable sizes using a vertical chemical vapour deposition method

Lerato Mokoloko[a], Roy Forbes[a] and Neil J Coville[a*]

KEYWORDS: carbon dots, chemical vapour deposition, nanostructure, spectroscopy.

List of Figures

Figure S4.1: TEM image of products obtained in SCC#2 before purification

Figure S4.2: a) TEM image with a **b)** particle size distribution histogram and a normal distribution curve of the $CSs_{600/10/1}$

Figure S4.3: a) TEM image with a **b)** particle size distribution histogram and a normal distribution curve of the $CSs_{550/10/1}$

Figure S4.4: a) TEM image with a **b)** particle size distribution histogram and a normal distribution curve of the $CSs_{520/10/1}$

Figure S4.5: HRTEM of **a)** $CDs_{600/10/2}$ showing their lattice fringes **b)** $CSs_{600/10/1}$

Figure S4.6: a) TEM image and **b)** particle size distribution histogram and a normal distribution curve of the $CDs_{600/9/2}$

Figure S4.7: a) TEM image and **b)** particle size distribution histogram and a normal distribution curve of the $CSs_{400/8/1}$

Figure S4.8: a) TEM image and **b)** particle size distribution histogram and a normal distribution curve of the $CSs_{400/8/2}$

Figure S4.9: **a)** Raman spectra and b) FTIR spectra of $CDs_{520/10/2}$, $CDs_{550/10/2}$ and $CDs_{600/10/2}$, $CSs_{400/10/2}$ and $CSs_{350/10/2}$

Figure S4.10: **a)** CDs_{600} and **b)** CDs from vitamin C in distilled water

Figure S4.11: Derivative weight loss thermograms of the samples synthesized at 1000 °C

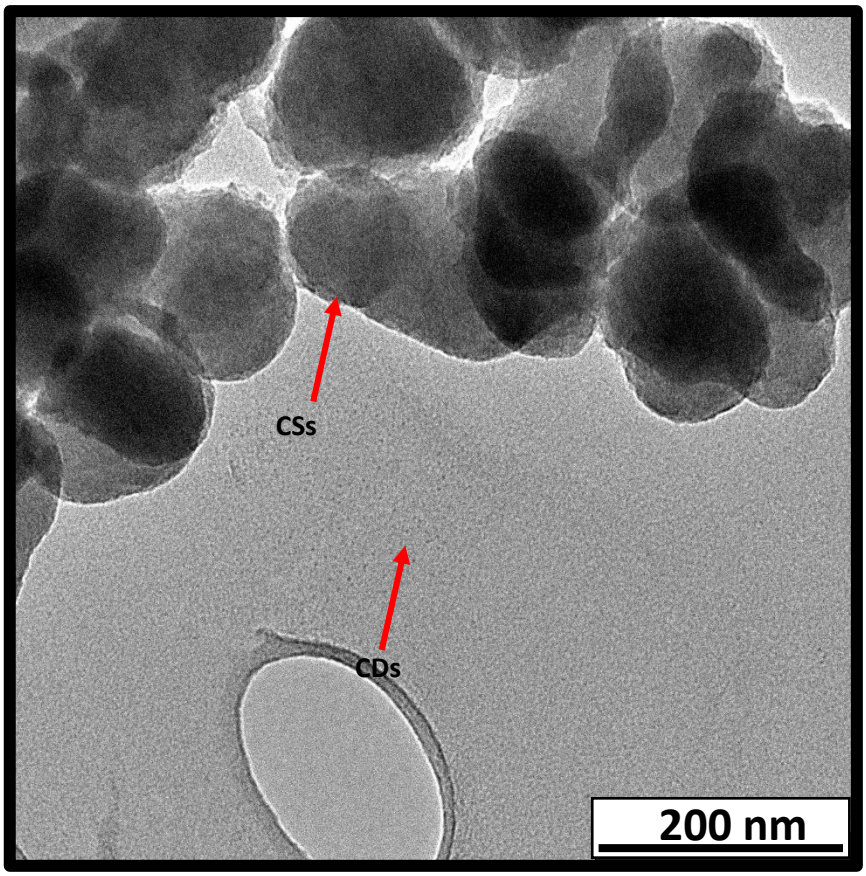

Figure S4. 1: TEM image of products obtained in SCC#2 before purification

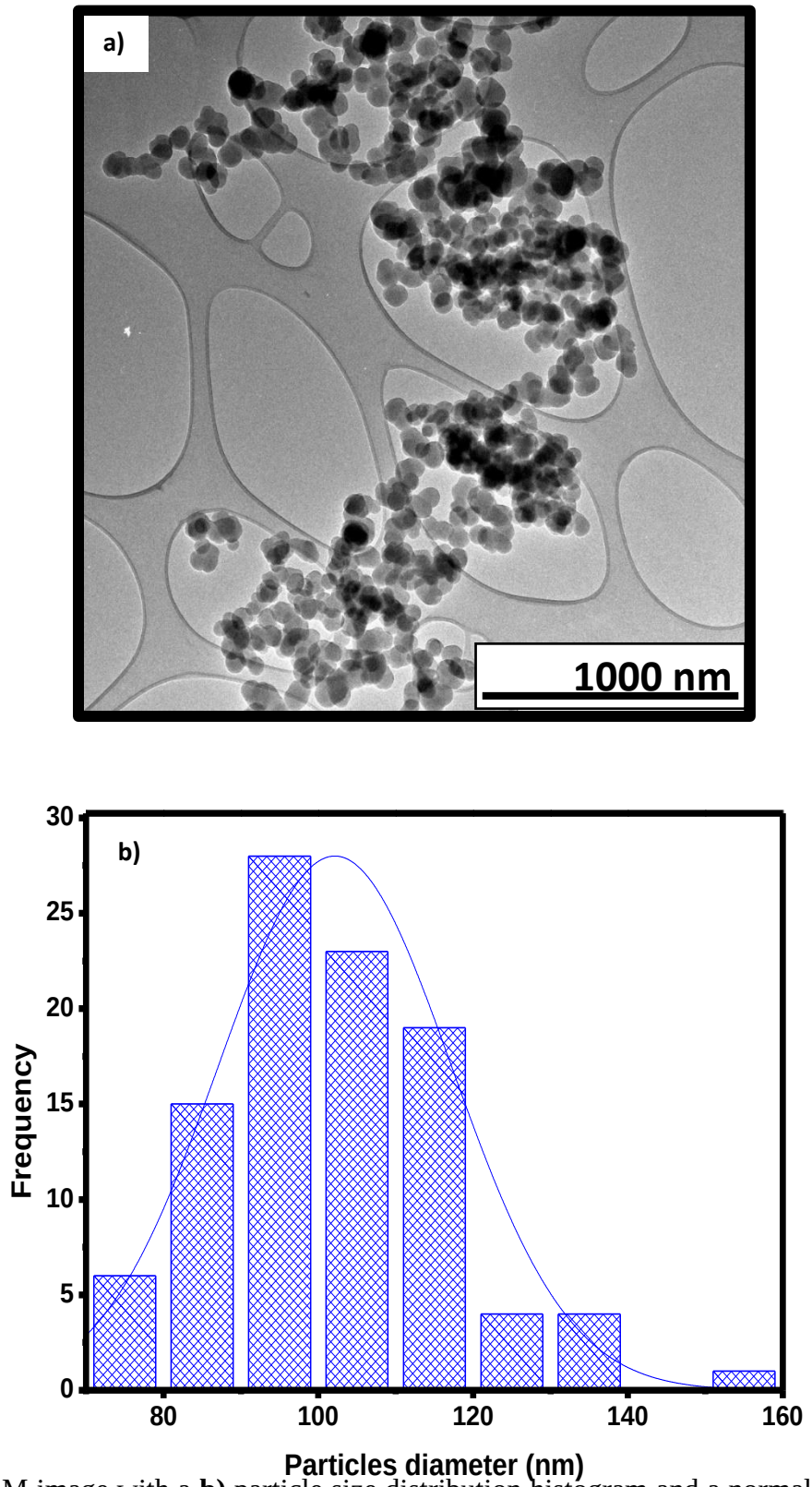

Figure S4. 2:a) TEM image with a **b)** particle size distribution histogram and a normal distribution curve of the $CSs_{600/10/1}$

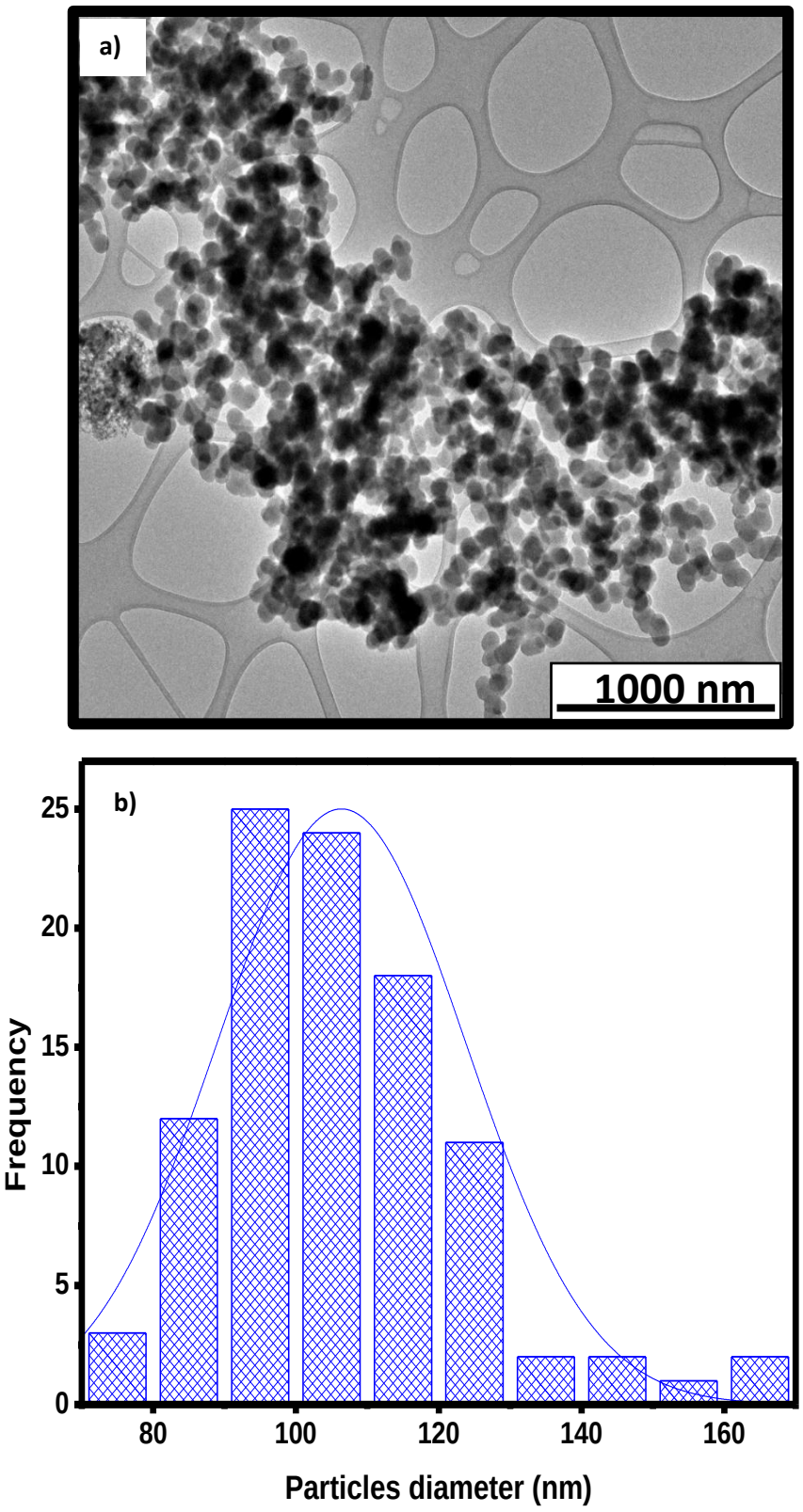

Figure S4. 3: a) TEM image with a **b)** particle size distribution histogram and a normal distribution curve of the $CSs_{550/10/1}$

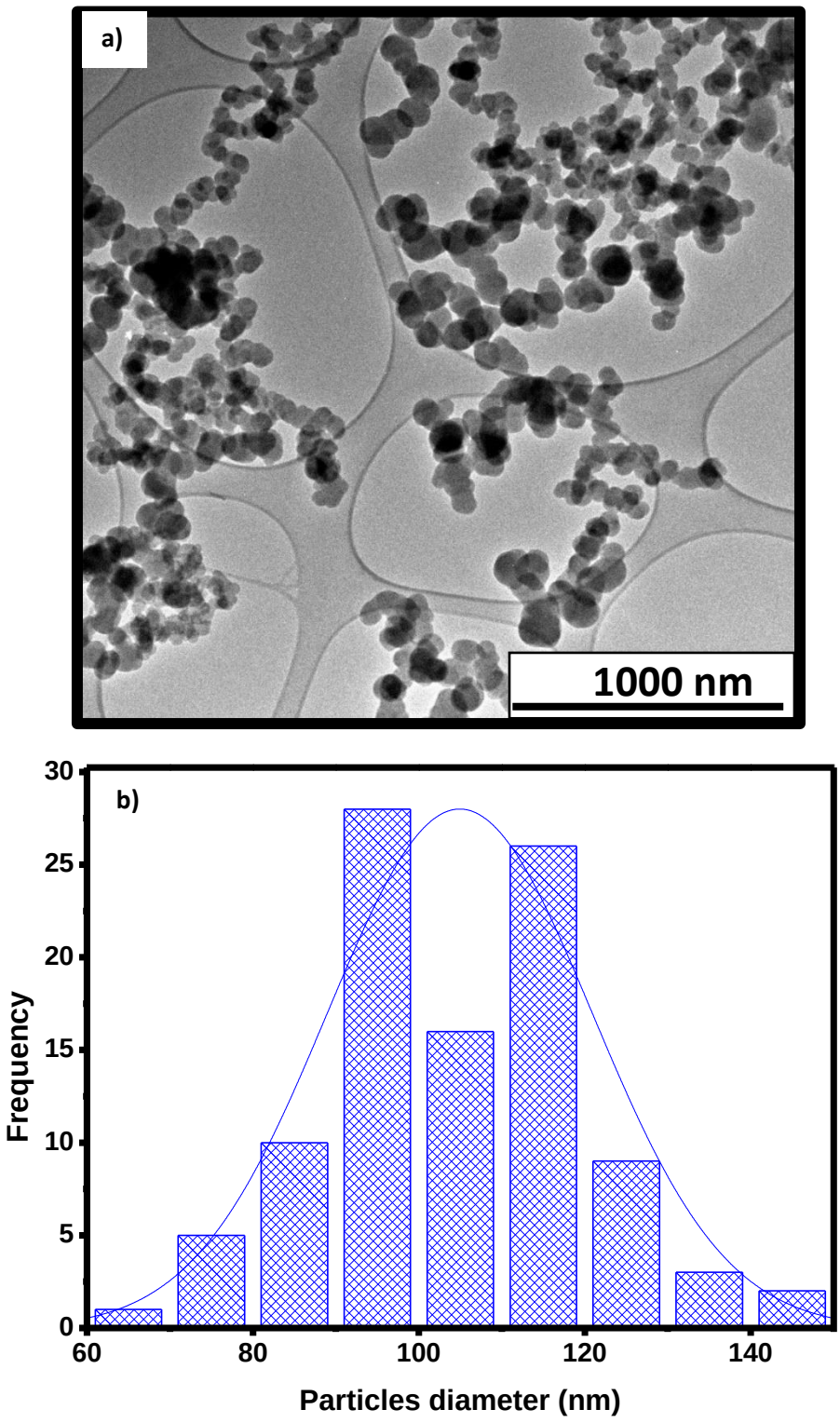

Figure S4. 4: a) TEM image with a **b)** particle size distribution histogram and a normal distribution curve of the $CSs_{520/10/1}$

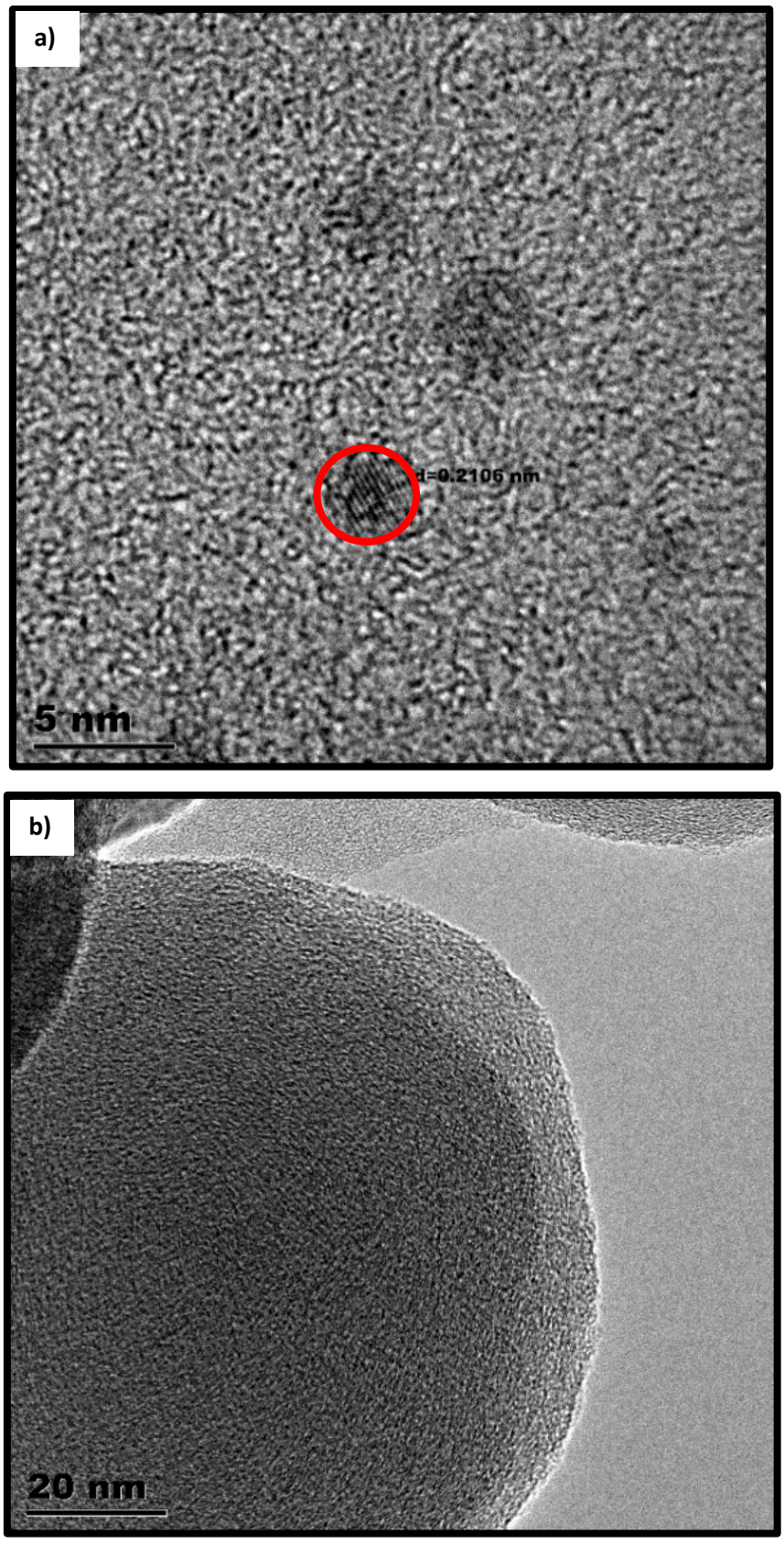

Figure S4. 6: HRTEM of **a)** $CDs_{600/10/2}$ showing their lattice fringes **b)** $CSs_{600/10/1}$

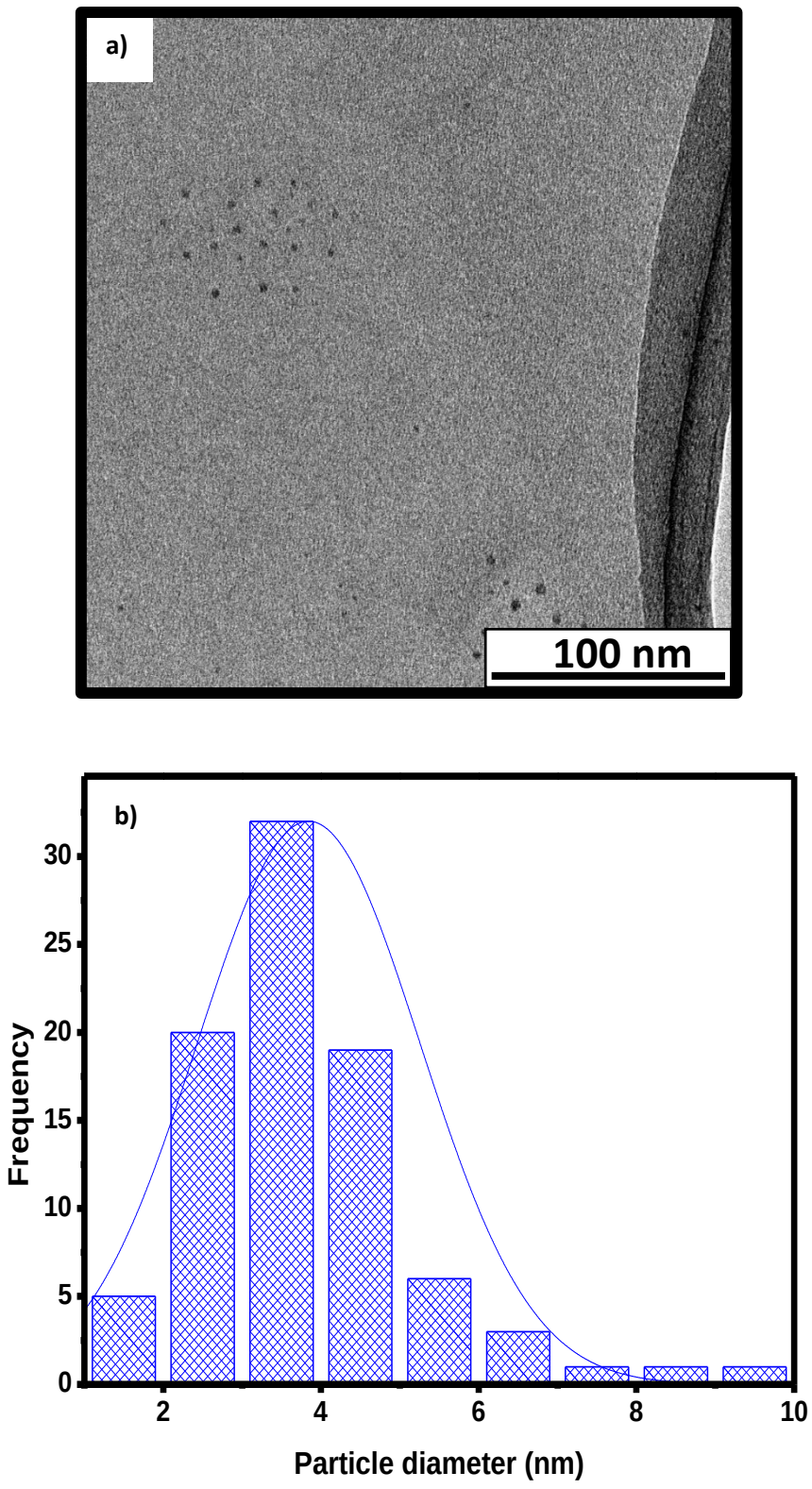

Figure S4. 7: a) TEM image and **b)** particle size distribution histogram and a normal distribution curve of the $CDs_{600/9/2}$

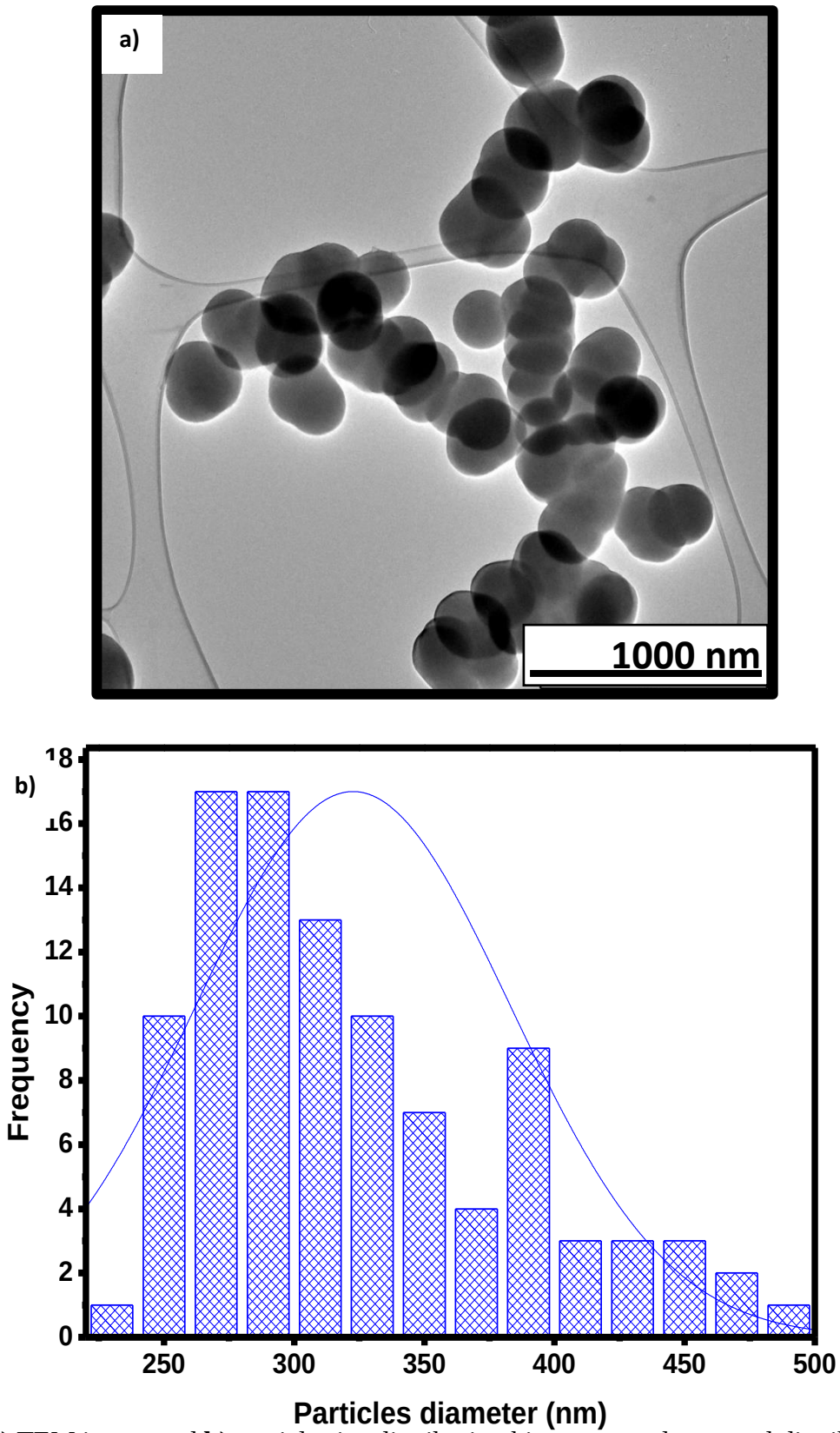

Figure S4. 8: a) TEM image and **b)** particle size distribution histogram and a normal distribution curve of the $CSs_{400/8/1}$

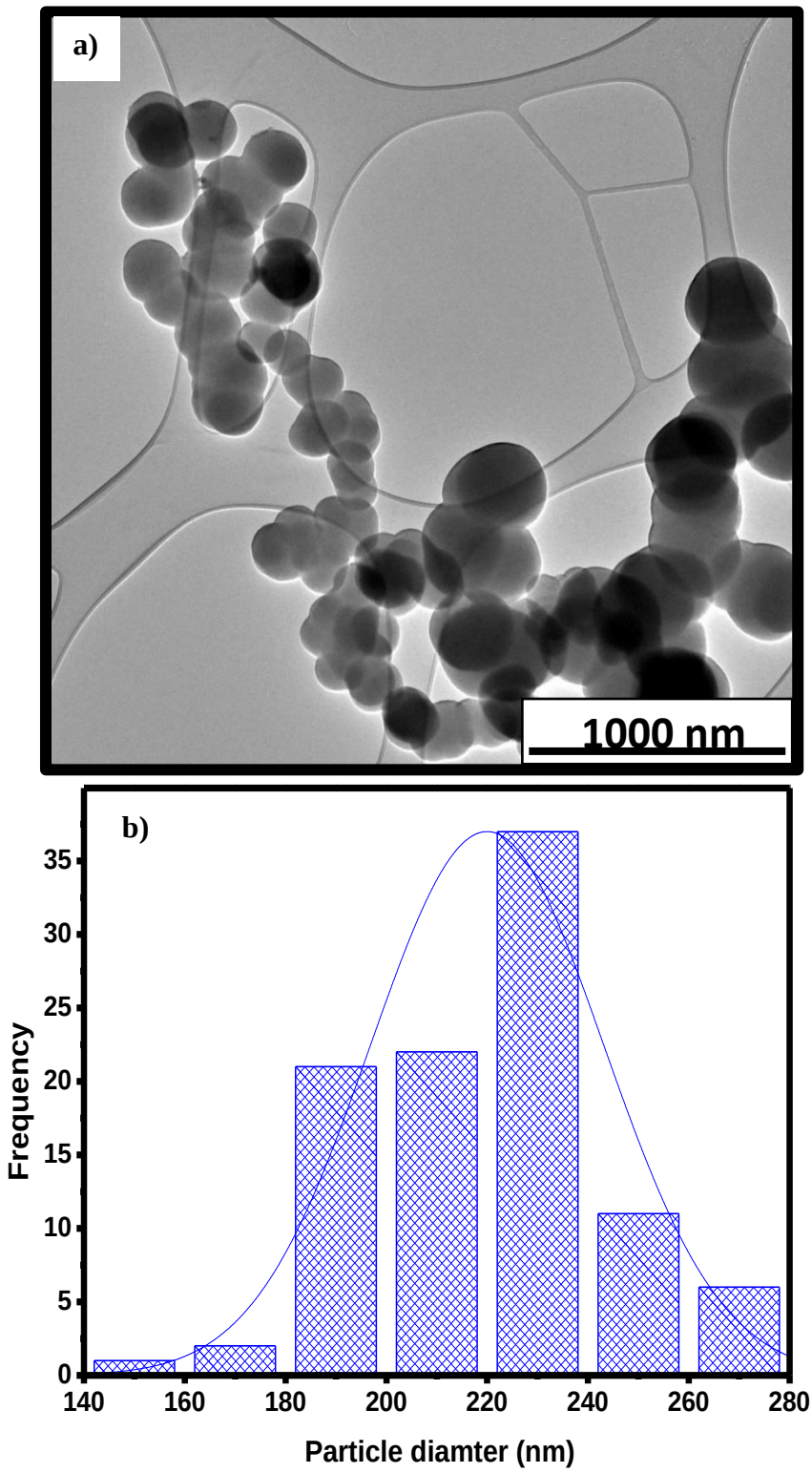

Figure S4. 9: a) TEM image and **b)** particle size distribution histogram and a normal distribution curve of the $CSs_{400/8/2}$

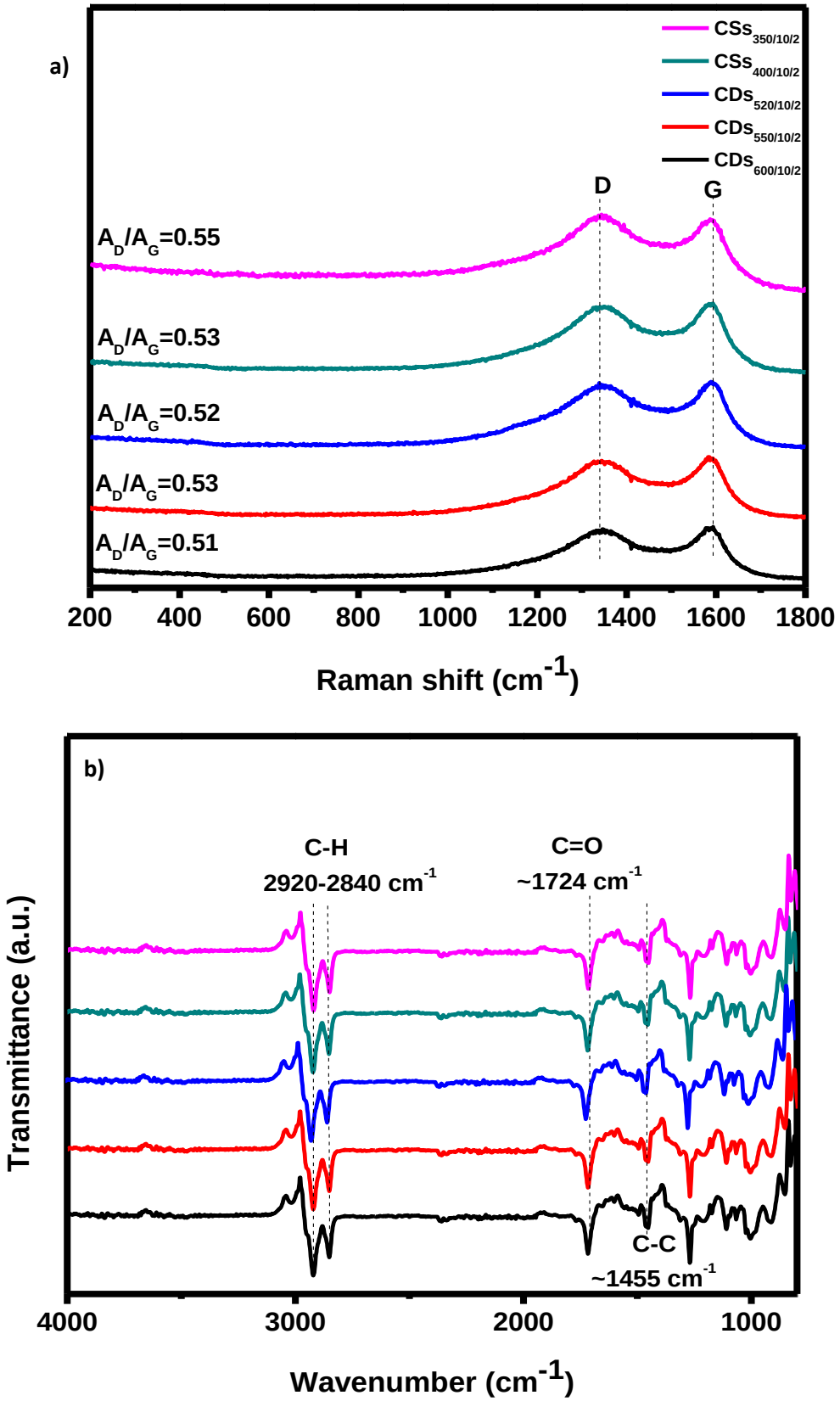

Figure S4. 11: a) Raman spectra and **b)** FT-IR spectra of $CDs_{520/10/2}$, $CDs_{550/10/2}$ and $CDs_{600/10/2}$, $CSs_{400/10/2}$ and $CSs_{350/10/2}$

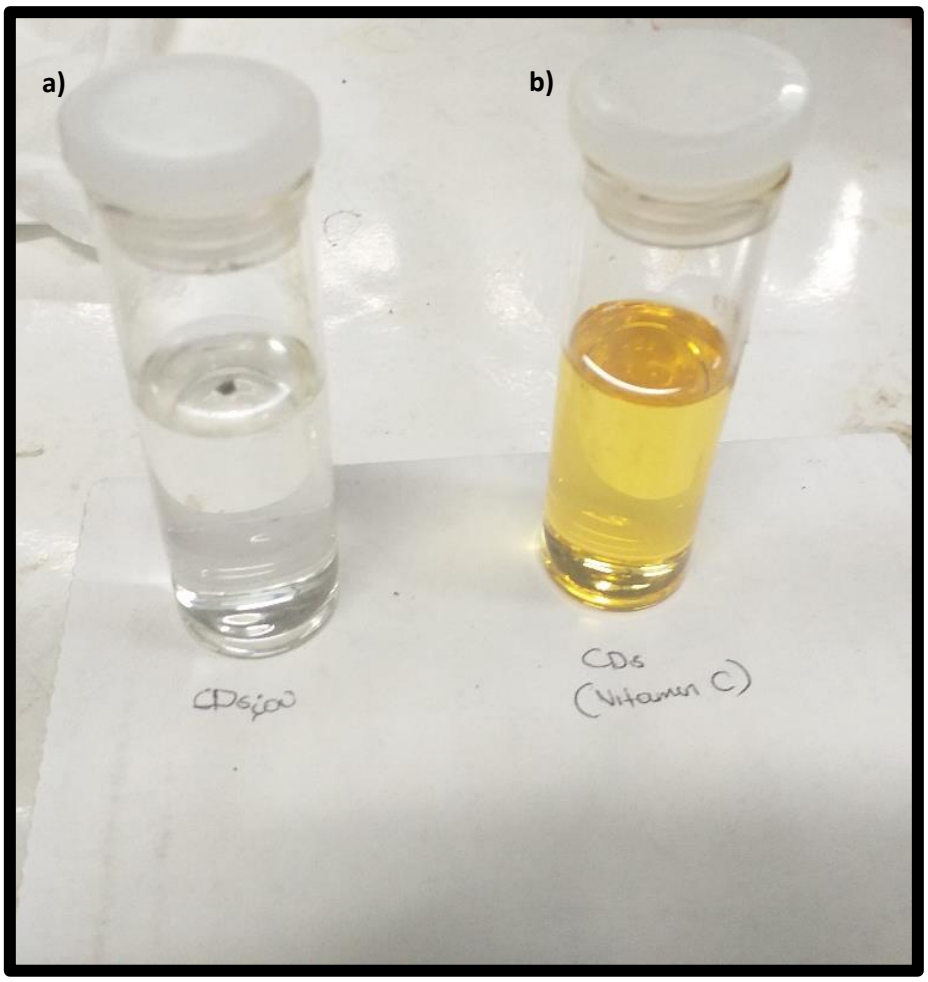

Figure S4. 12: a) CDs_{600} and **b)** CDs from vitamin C in distilled water

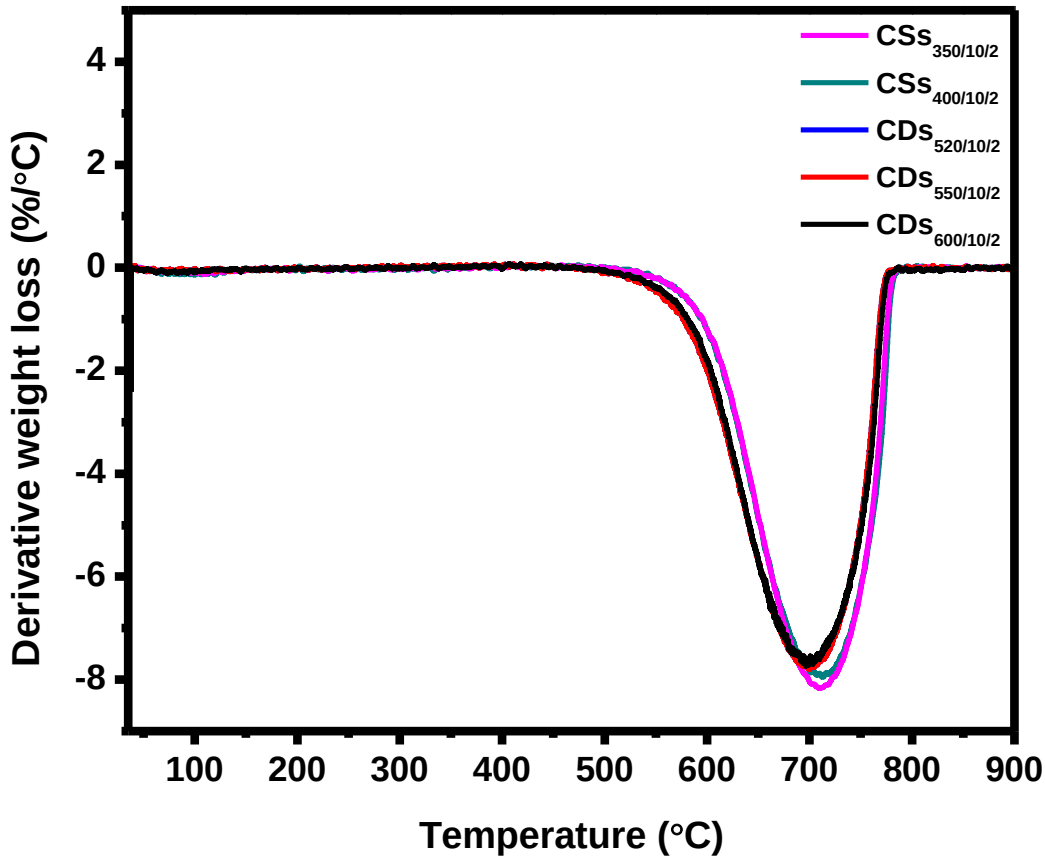

Figure S4. 13: Derivative weight loss thermograms of the samples synthesized at 1000 °C

APPENDIX B: CHAPTER 5 SUPPLEMENTARY INFORMATION

Evolution of large-area reduced graphene oxide nanosheets from carbon dots via thermal treatment

Lerato L Mokoloko[a], Boitumelo J Matsoso [b, c], Roy P. Forbes[a], Dean H. Barrett [a, d], Beatriz D. Moreno[e], and Neil J Coville[a]*

Keywords: carbon dots, microwave reaction, thermal treatment, reduced graphene oxide, chemical vapour deposition

List of Figures

Figure S5.1: TEM image of pCDs by-product.

Figure S5.2: a) HRTEM and **b)** particle size distribution histogram and a normal distribution curve of the pCDs.

Figure S5.3: a) TEM image and **b)** Particle size distribution histogram and a normal distribution curve of T200.

Figure S5.4: HRTEM images of sample **a)** T250 **b)** T400 and **c)** T700.

Figure S5.5: TEM images of sample **a)** T300 **b)** T500, **c)** T600, **d)** *L*-ascorbic acid annealed at 700 °C and **e)** *L*-ascorbic acid and pristine CDs annealed at 700 °C.

Figure S5.6: SEM images of **a)** T250 **b)** T400 and **c)** T700.

Figure S5.7: AFM images of **a)** T250 **b)** T400 and **c)** T700.

Figure S5.8: Expanded **a)** C1s and **b)** O1s survey XPS spectra of T200, T250, T400 and T700

Figure S5.9: a) Defect density ratios and **b)** peak positions for samples T400-T700.

Figure S5.10: PDFs of pCDs, T250, T400 and T700.

Figure S5.11: PDF fitting of the Ni standard to determine fit variables as shown in **Table S4** below.

Figure S5.12: PL spectra of pCDs and samples T200-T700.

Figure S5. 1: TGA profiles of pCDs and samples annealed at **a)** low and **b)** high temperatures.

List of Tables

Table S5.1: **(a-d)** XPS C1s and O1s peak positions and percentage atomic abundance in samples T200, T250, T400 and T700.

Table S5.2: Peak positions of the pristine CDs and samples T200-T700.

Table S5.3: Defect density ratios of the samples T400-T700.

Table S5.4: Fit variables determined from PDF fitting of the Ni standard.

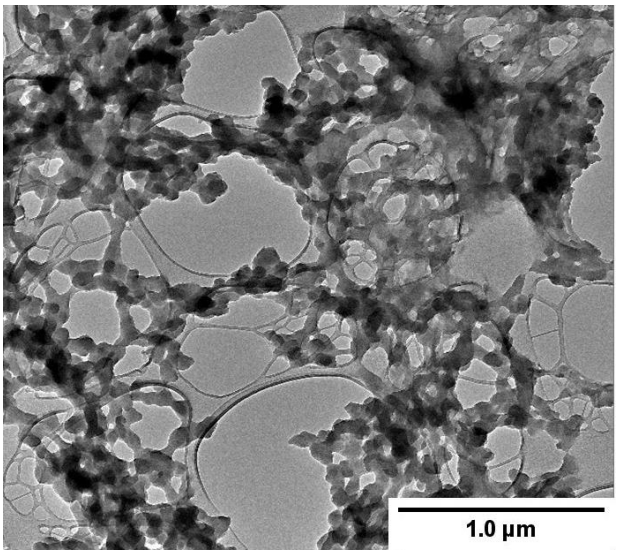

Figure S5. 1: TEM image of pCDs by-product

The by-product (precipitated during CDs purification) contained aggregates of carbon nanoparticles with a spheroidal shape. Similar precipitates were obtained from the synthesis of CDs from orange peels (source of ascorbic acid) [61]. The authors named them "coarse nanoparticles", and these materials had a weak fluorescence compared to the CDs[61].

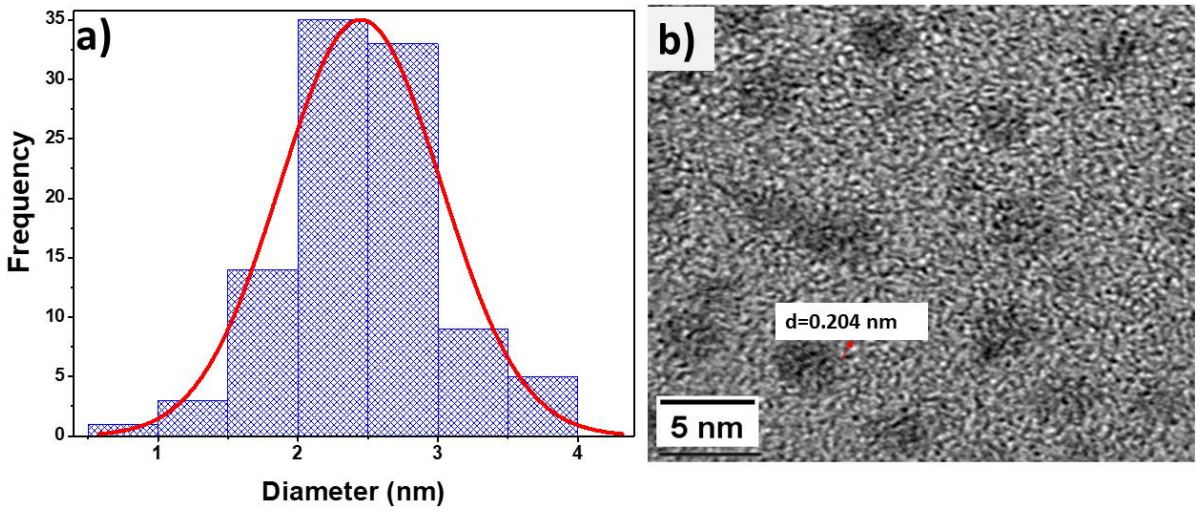

Figure S5. 2: a) HRTEM and **b)** particle size distribution histogram and a normal distribution curve of the pCDs.

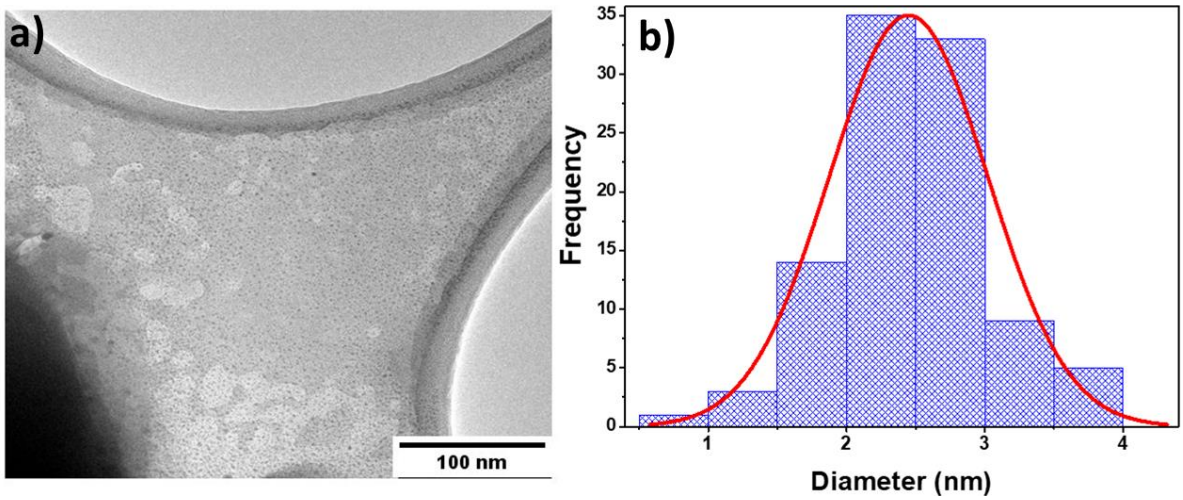

Figure S5. 3: a) TEM image and **b)** Particle size distribution histogram and a normal distribution curve of T200 sample.

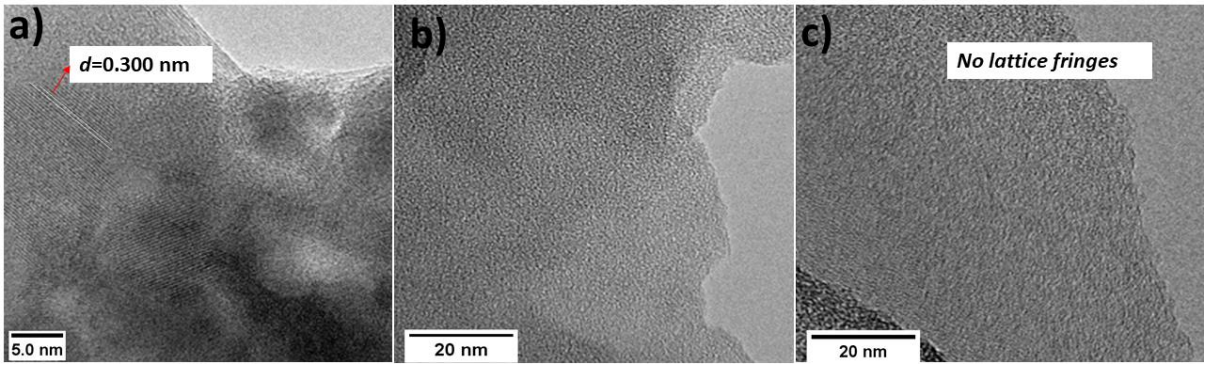

Figure S5. 4: High resolution TEM images of the **a)** T250, **b)** T400 and **c)** T700 samples.

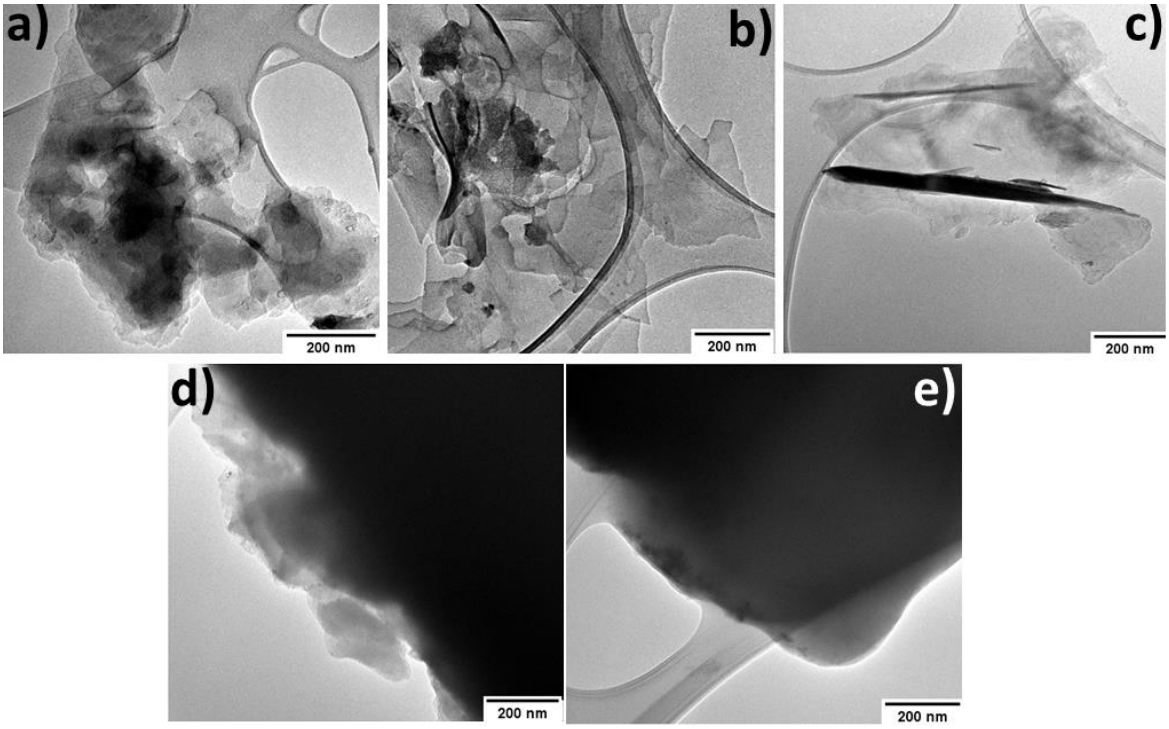

Figure S5. 5: TEM images of sample **a)** T300 **b)** T500, **c)** T600, **d)** *L*-ascorbic acid annealed at 700 °C and **e)** *L*-ascorbic acid and pristine CDs annealed at 700 °C.

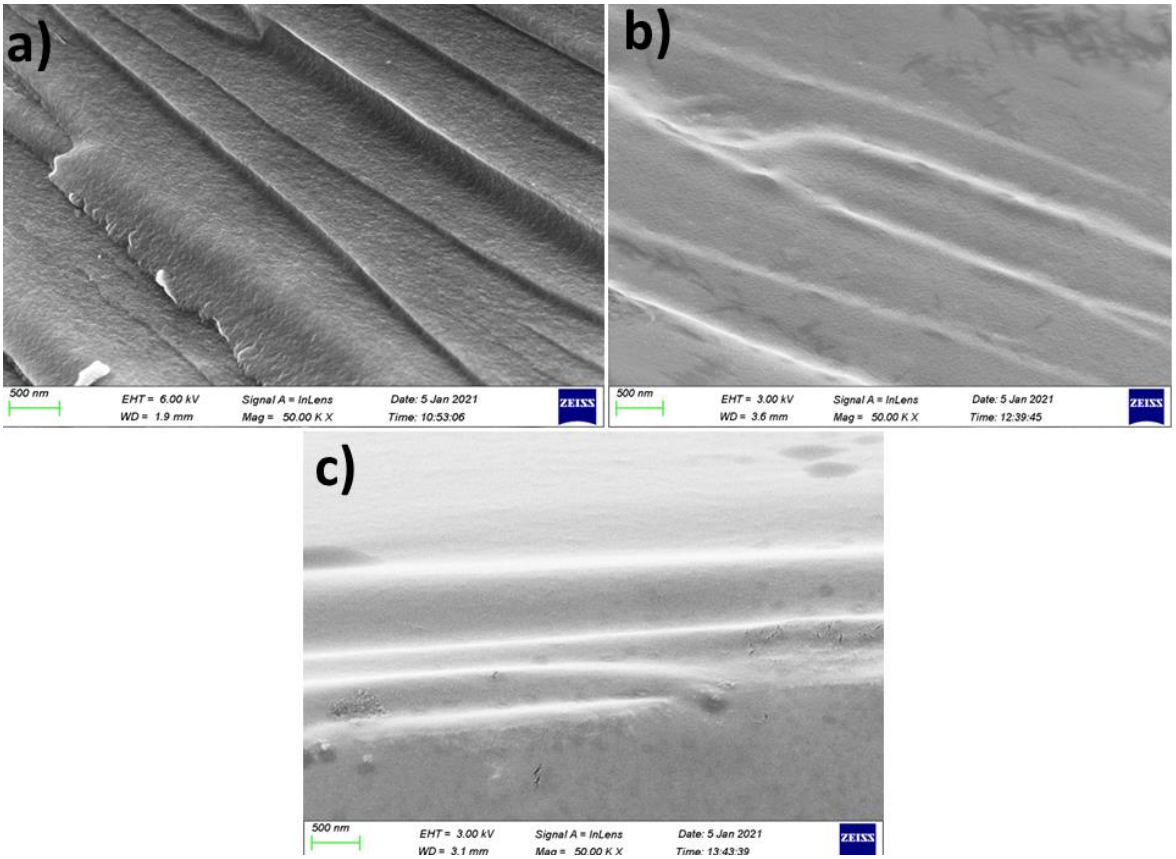

Figure S5. 6: SEM images of **a)** T250 **b)** T400 and **c)** T700 samples.

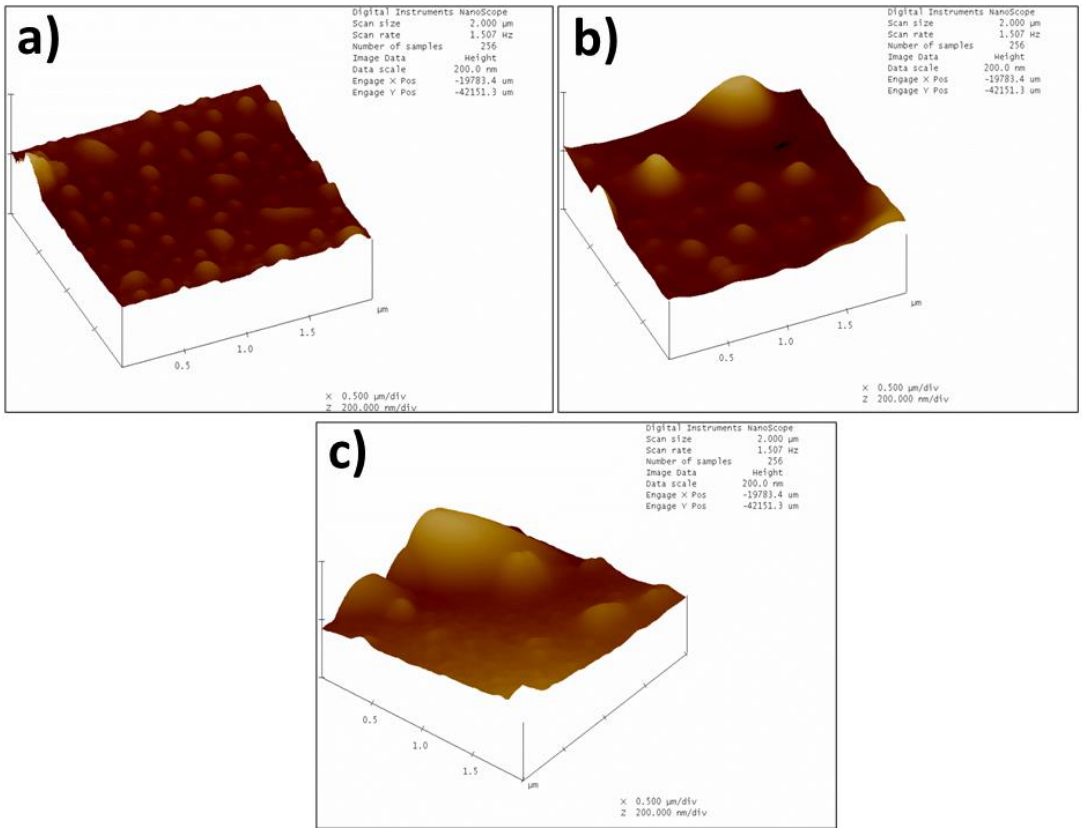

Figure S5. 7: AFM images of **a)** T250 **b)** T400 and **c)** T700 samples.

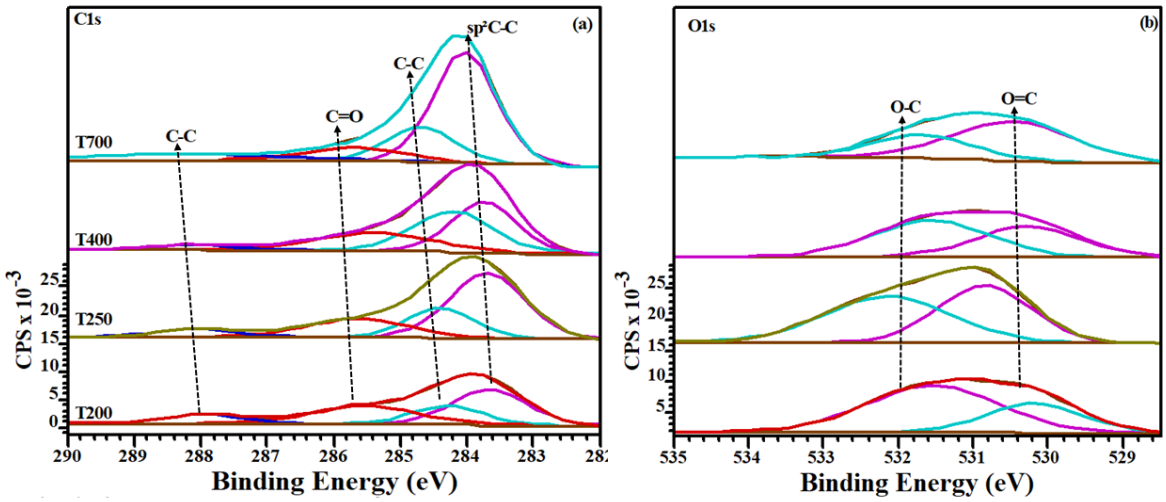

Figure S5. 8: Expanded **a)** C1s and **b)** O1s survey XPS spectra of T200, T250, T400 and T700

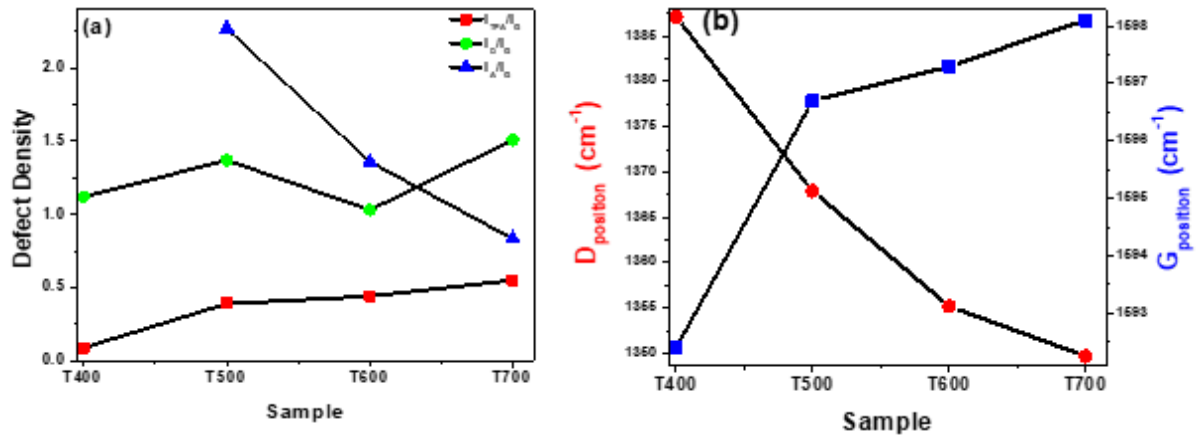

Figure S5. 9: a) Defect density ratios and **b)** peak positions for samples T400-T700.

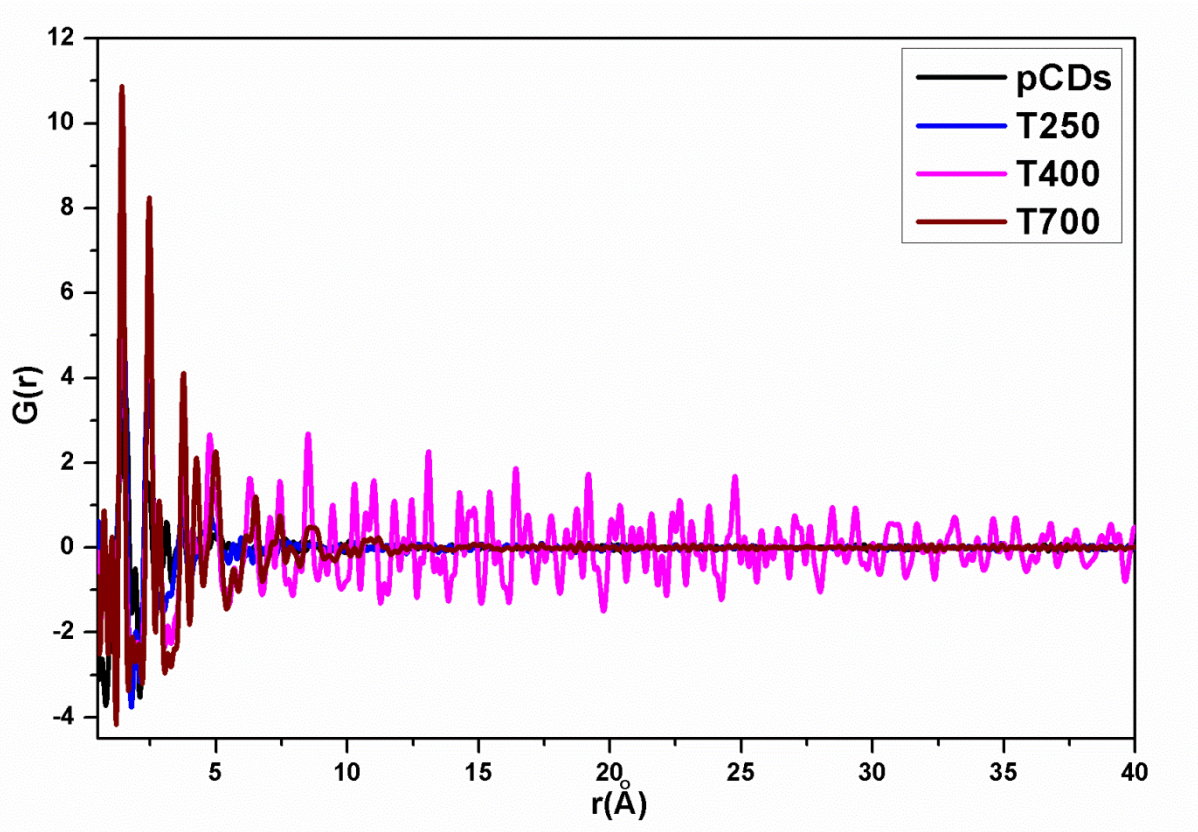

Figure S5. 2: PDFs of pCDs, T250, T400 and T700.

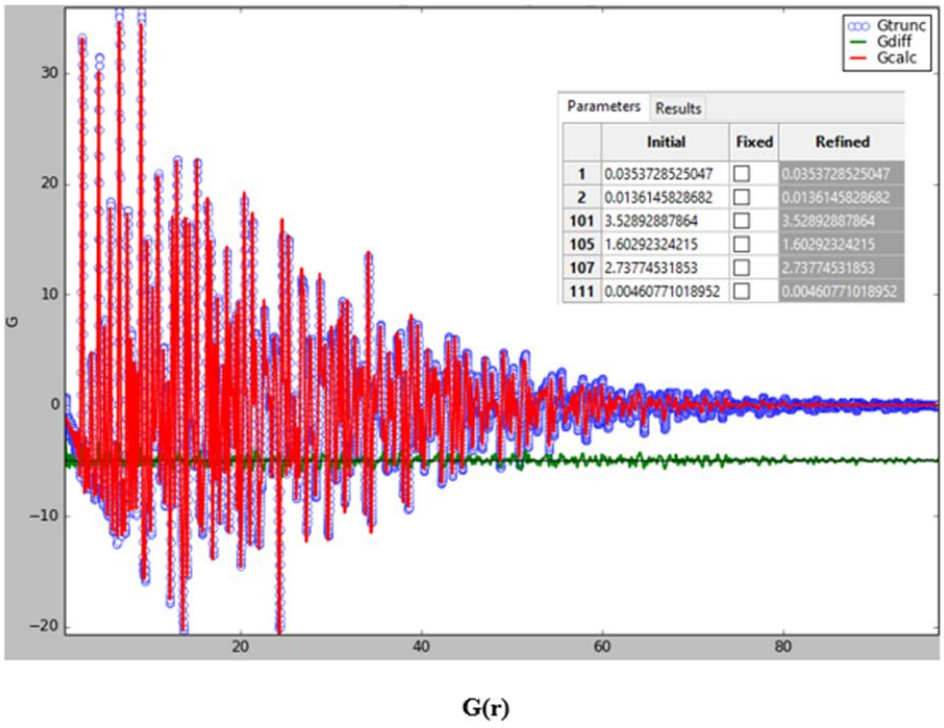

Figure S5. 11: PDF fitting of the Ni standard to determine fit variables as shown in **Table S4** below.

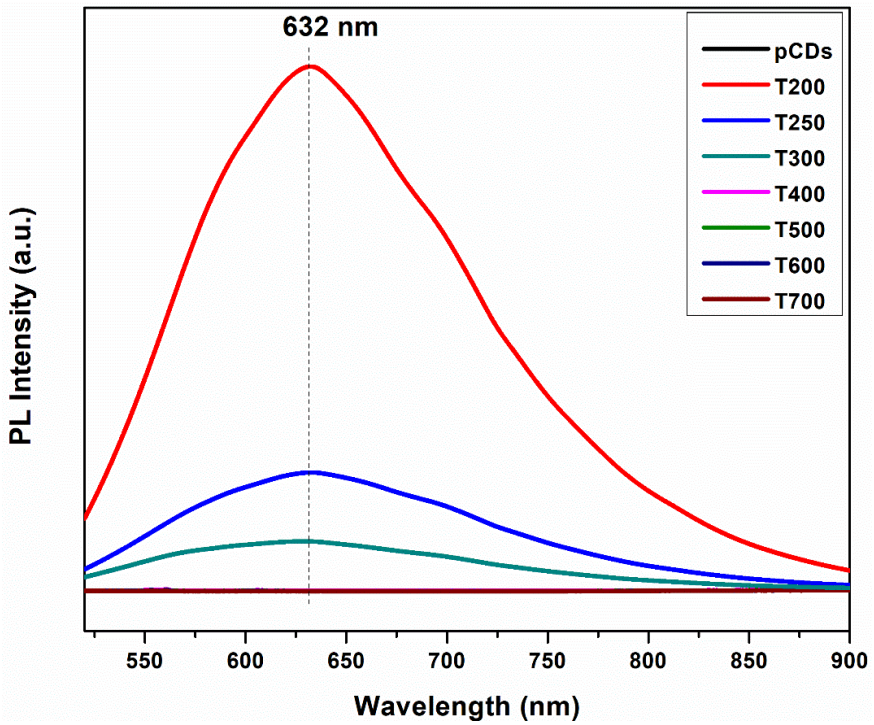

Figure S5. 12: PL spectra of pCDs and samples T200-T700.

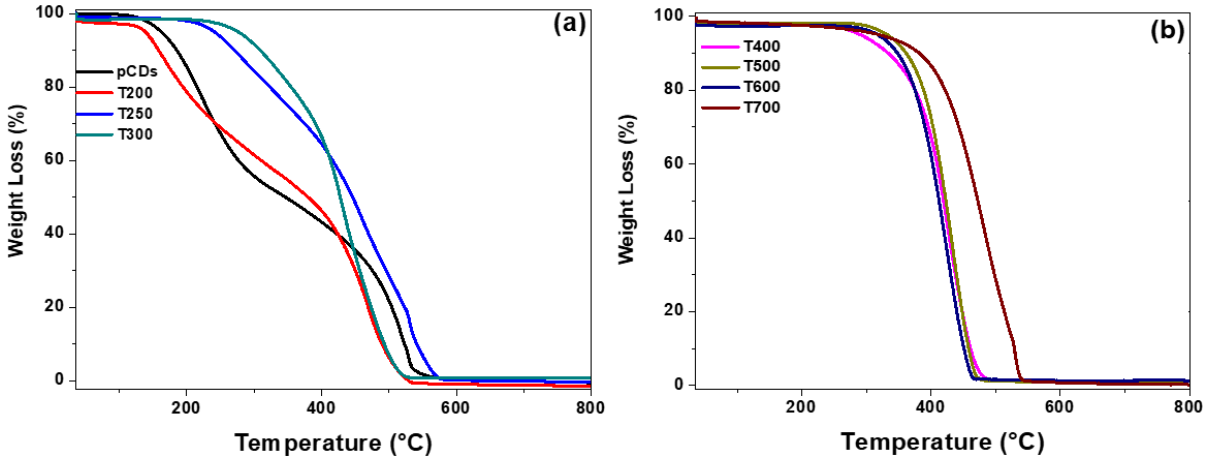

Figure S5. 13: TGA profiles of pCDs and samples annealed at **a)** low and **b)** high temperatures.

Table S5. 1: (a-d) XPS C1s and O1s peak positions and percentage atomic abundance in samples T200, T250, T400 and T700.

a)

Sample	C1s XPS Peak Positions (eV)			
	Sp^2 C-C	Sp^3 C-C	C-O	O-C=O
T200	284.79	285.52	286.83	288.82
T250	284.39	285.07	286.26	288.86
T400	284.43	285.21	286.41	288.83
T700	284.03	284.69	285.66	288.24

b)

Sample	C1s % average concentration			
	Sp^2 C-C	Sp^3 C-C	C-O	O-C=O
T200	43.62	26.71	18.48	11.19
T250	48.22	21.62	23.75	6.42
T400	55.97	23.64	16.02	4.37
T700	58.46	19.96	11.42	10.15

c)

Sample	O1s XPS Peak Positions (eV)	
	C=O	C-O
T200	530.94	532.31
T250	531.94	532.36
T400	530.46	531.77
T700	530.69	532.88

d)

Sample	O1s average % concentration	
	C=O	C-O
T200	32.88	67.12
T250	60.22	39.78
T400	46.97	53.21
T700	75.09	24.91

Table S5. 2: Peak positions of the pristine CDs and samples T200-T700

Sample	Position (cm^{-1})			
	TPA	D	A	G
pCDs	-	-	-	-
T200	-	-	-	-
T250	-	-	-	-
T300	-	-	-	-
T400	1204.5	1387.1	-	1592.4
T500	1230.2	1367.9	1464.6	1596.7
T600	1229.9	1355.2	1491.7	1597.3
T700	1226.4	1349.7	1501.4	1598.1

Table S5. 3: Defect density ratios of the samples T400-T700

Sample	Defect Density Ratios			L_a (nm)[a]	N_D ($\times 10^{11}$ cm^{-2})[b]
	I_{TPA}/I_G	I_D/I_G	I_A/I_G		
T400	0.081	1.12	-	15.02	3.84
T500	0.39	1.37	2.27	12.3	4.69
T600	0.44	1.03	1.36	16.3	3.53
T700	0.55	1.51	0.834	11.1	5.17

[a]*Average in-plane sp^2 crystallite size,* [b]*Defect density per square cm.*

$$L_a(nm) = 2.4 \times 10^{-10} \times \lambda_{laser}^4 \times \frac{I_G}{I_D} \ldots\ldots\ldots\ldots\ldots\ldots\ldots (\lambda = 514.5\ nm)$$

$$n_D(cm^{-2}) = \frac{2.4 \times 10^{22}}{\lambda_{laser}^4} \times \frac{I_D}{I_G}$$

Table S5. 4: Fit variables determined from PDF fitting of the Ni standard

Fit variable	Name	Value
@1	Qdamp	0.0354
@2	Qbroad	0.0136
@101	a,b,c	3.5289
@105	Scale factor	1.6029
@107	Delta2	2.7377
@111	Uij	0.0046

APPENDIX C: CHAPTER 6 SUPPLEMENTARY INFORMATION

Use of carbon dots-derived graphene-like sheets on the autoreduction of cobalt nanoparticles for Fischer–Tropsch synthesis: A limitation on the use of carbon supports

List of Figures

Figure S6.1: The Rietveld refinement results of the diffraction pattern of Co_3O_4/T700 at 550 °C.

Figure S6.2: a) PXRD pattern and **b)** H_2-TPR profile of the Co_3O_4 nanoparticles.

Figure S6.3: HRTEM image of Co_3O_4/T250.

Figure S6.4: BET isotherms of **a)** T250 **b)** T400, **c)** T700, **d)** Co_3O_4/T250 **e)** Co_3O_4/T400 and **f)** Co_3O_4/T700.

Figure S6.5: TG thermograms of T250, T400 and T700 with and without Co_3O_4.

Figure S6.6: In situ XRD plots of a)-b) Co_3O_4/T300, c)-d) Co_3O_4/T300, e)-f) Co_3O_4/T400 and g)-h) Co_3O_4/T700 analyse from 30 to 550 °C under H_2 (left) and N_2 (right).

Figure S6.7: TEM image of the unsupported Co spent catalyst.

Table S6.1: Surface area, porosity and approximate sheet size results of T250-T700 sample set before and after Co addition.

Table S6.2: Phase quantification and structural details of the of Co_3O_4/T300 and Co_3O_4/T400 catalysts obtained via Rietveld Refinement of the data collected in-situ PXRD experiments.

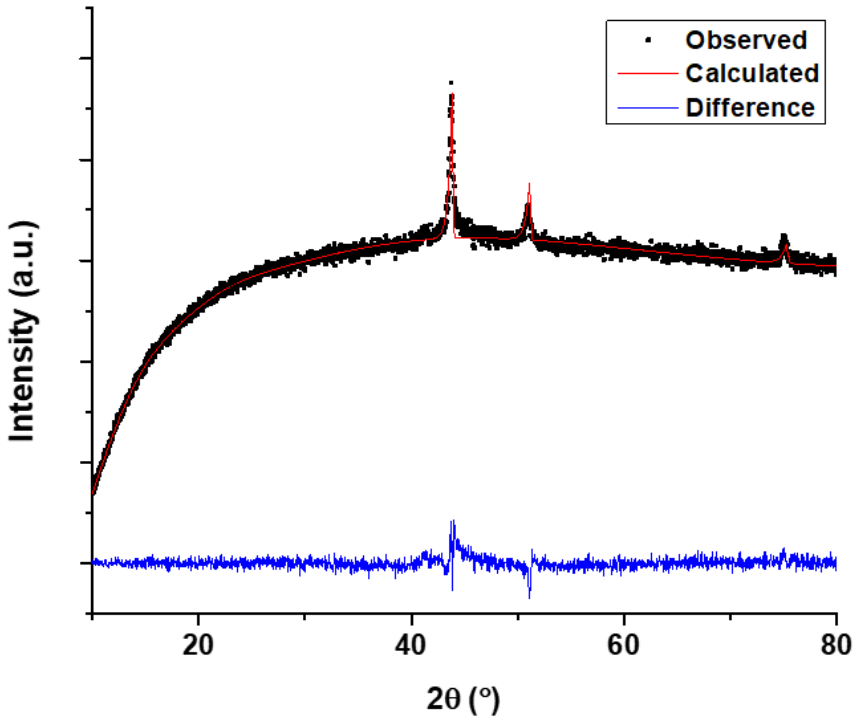

Figure S6. 1: The Rietveld refinement results of the diffraction pattern of Co_3O_4/T700 at 550 ℃

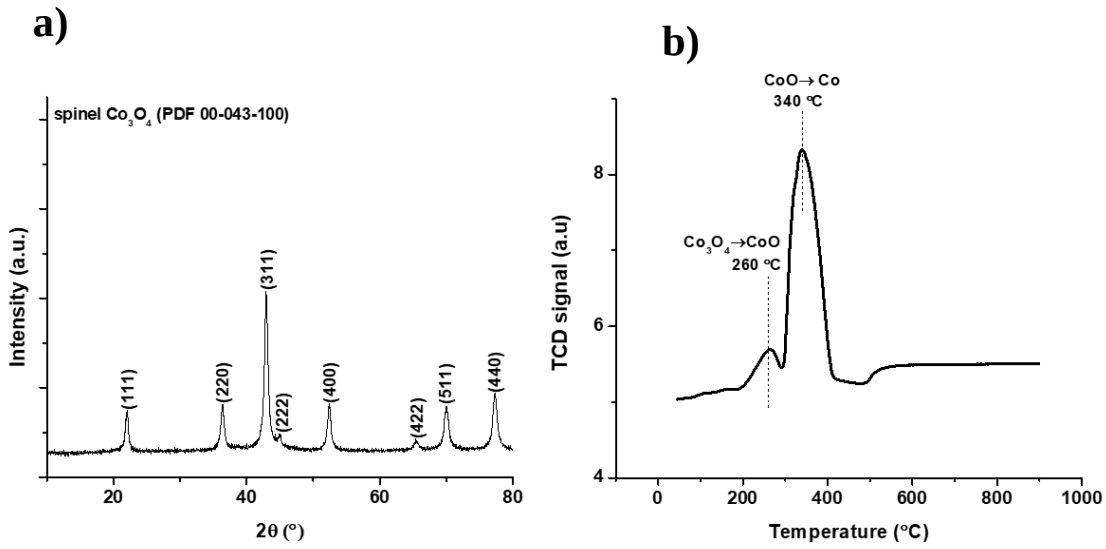

Figure S6. 2: a) PXRD pattern and **b)** H_2-TPR profile of the Co_3O_4 nanoparticles.

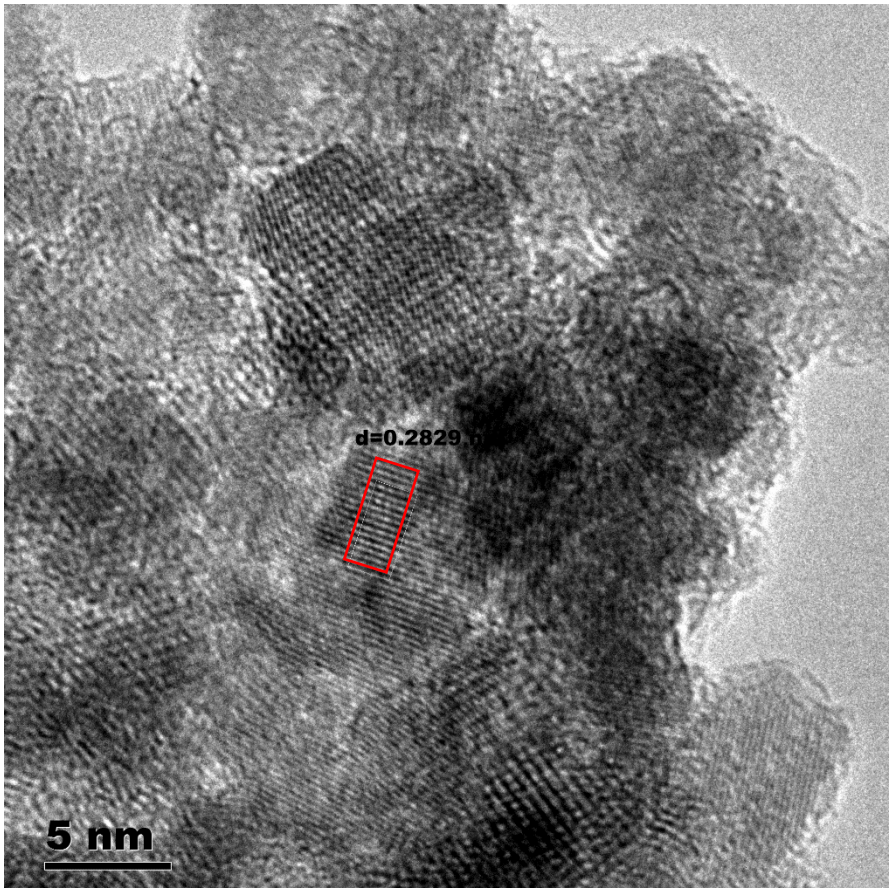

Figure S6. 3: HRTEM image of Co_3O_4/T250.

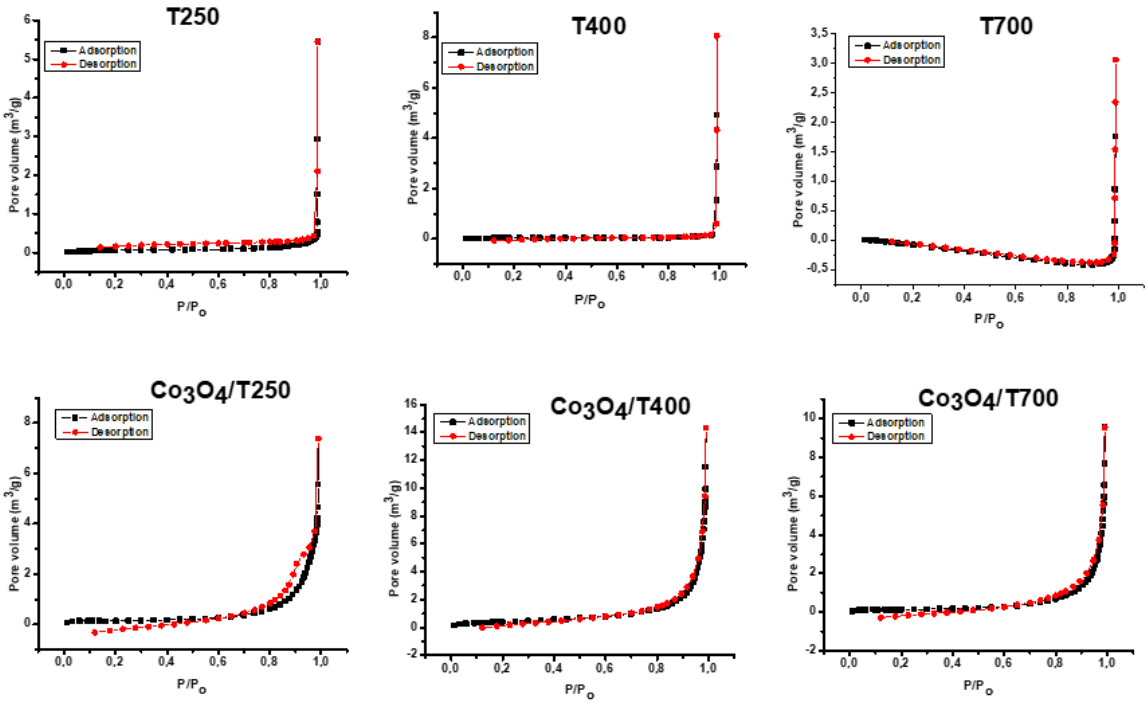

Figure S6. 4: BET isotherms of **a)** T250 **b)** T400, **c)** T700, **d)** Co_3O_4/T250 **e)** Co_3O_4/T400 and **f)** Co_3O_4/T700.

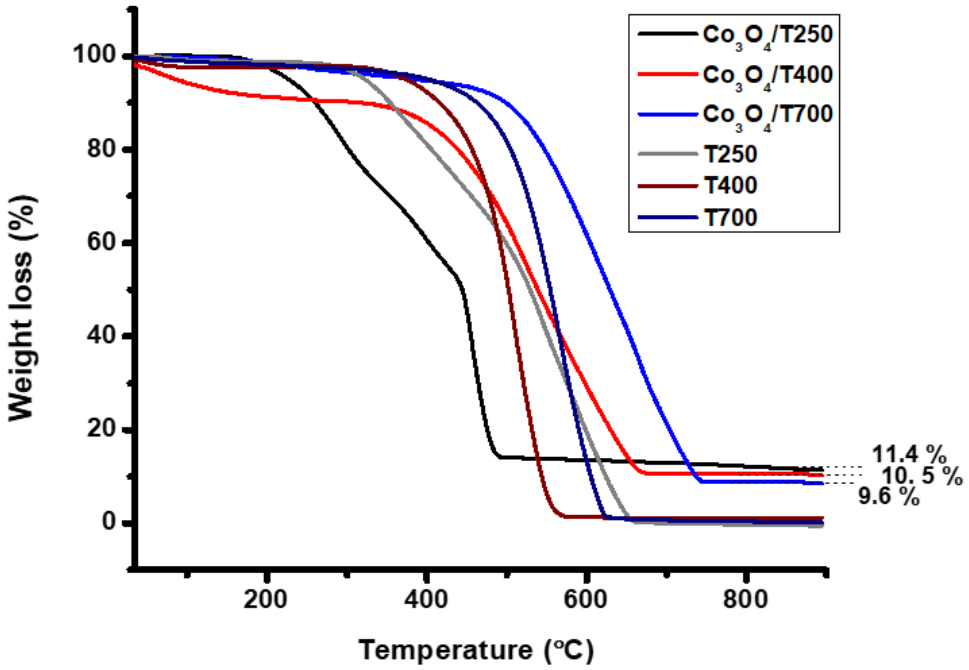

Figure S6. 5: TG thermograms of T250, T400 and T700 with and without Co_3O_4.

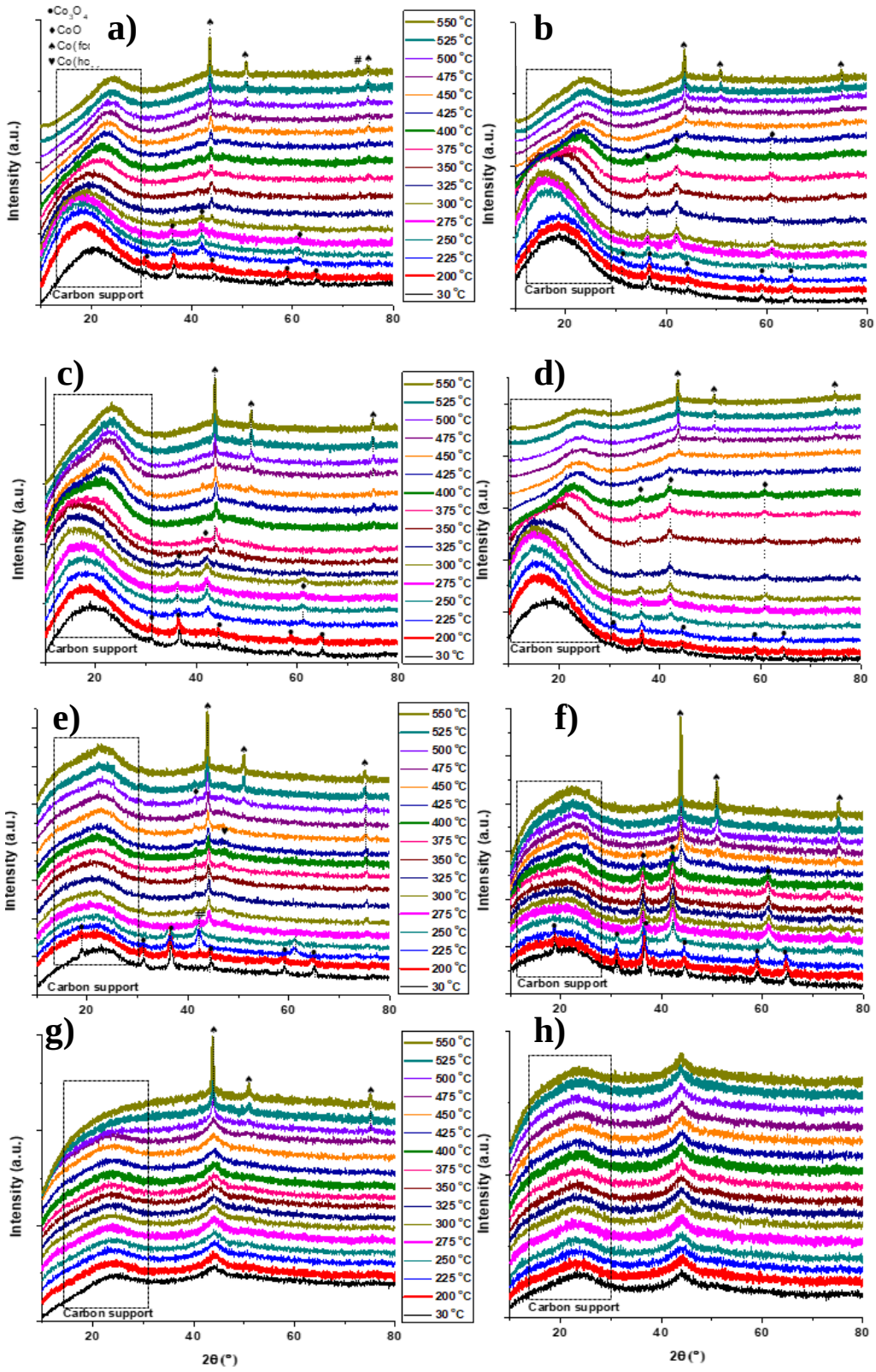

Figure S6. 6: In situ XRD plots of **a)-b)** Co_3O_4/T300, **c)-d)** Co_3O_4/T300, **e)-f)** Co_3O_4/T400 and **g)-h)** Co_3O_4/T700 analyse from 30 to 550 °C under H_2 (left) and N_2 (right).

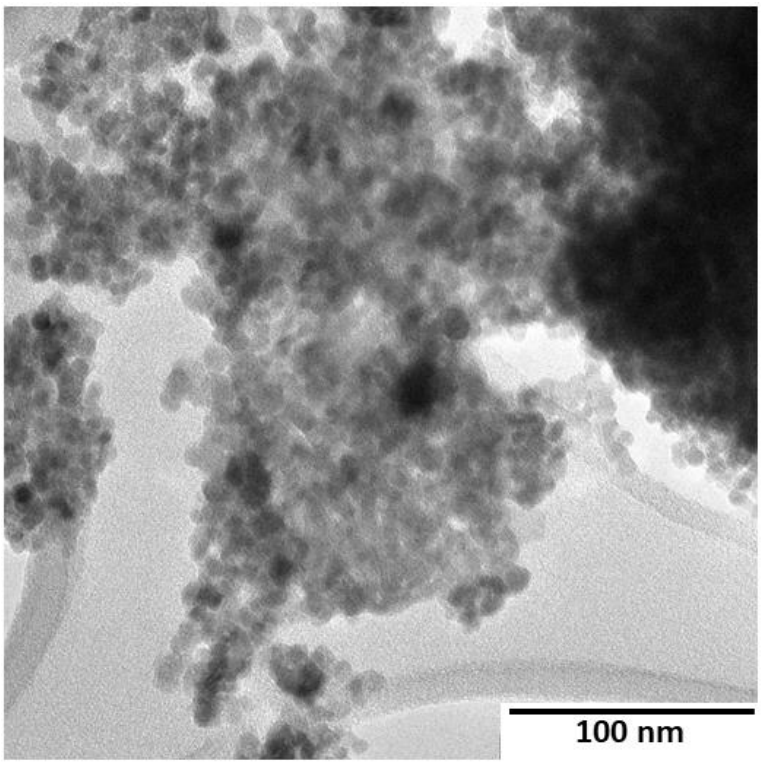

Figure S6. 7: TEM image of the unsupported Co spent catalyst.

Table S6. 1: Surface area, porosity and approximate sheet size results of T250-T700 sample set before and after Co addition.

Sample name	Approx. sheet size (µm)	BET surface area (m^2/g)	Micropore area (m^2/g)	Pore diameter (nm)	Pore volume (m^3/g)
T250	-	0.27	0.45	54	0.01
Co_3O_4/T250	-	0.48	0.38	26	0.02
T400	1.44 ± 0.199 × 0.82 ± 0.13	0.15	0.27	144	0.01
Co_3O_4/T400	1.24 ± 0.199 × 0.82 ± 0.30	1.50	1.62	34	0.02
T700	1.71 ± 0.104 × 0.909 ± 0.0577	0.01	0.13	191	0.04
Co_3O_4/T700	1.71 ± 0.102 × 0.911 ± 0.0497	0.46	0.44	34	0.01

Table S6.2: Phase quantification and structural details of the of Co_3O_4/T300 catalysts obtained via Rietveld Refinement of the data collected in-situ PXRD experiments.

Sample name	Temperature (°C)	Phase ID	% of each phase	Microstructure (approx. sizes)	Degree of crystallinity (%) of metal
Co_3O_4/T300_H_2	200	Co_3O_4	100	16.2 ±0	100
	275	CoO ,	100	10.1±0.9	97.88
	400	Co(fcc)	100	25.7 ±0	98.83
	525	Co(fcc)	100	64.8±0	97.87
	550	Co(fcc)	100	69.2±0	97.41
Co_3O_4/T300_N_2	200	Co_3O_4	100	14.7 ±0	97.92
	275	CoO	99.9	13.4±0.0	97.50
	400	CoO	100	10.9 ±0	96.77
	525	Co(fcc)	100	38.7 ± 5.6	98.45
	550	Co(fcc)	100	39.6 ± 4.6	98.32

APPENDIX D: CHAPTER 7 SUPPLEMENTARY INFORMATION

From 0D to 2D: N-doped carbon sheets for detection of alcohol-based chemical vapours

List of Figures

Figure S7.1: Low magnification TEM micrographs of (a) pristine NCDs, (b) NCDs200, and (c) NCDs400 samples.

Figure S7. 2: High resolution TEM micrographs of (a) pristine NCDs and (b) NCDs700 samples, with an inserted line profile. This does not show lines of similar heights or spacing between the lines indicating that theNCDs700 sample does not have graphitic character.

Figure S7.3: AFM images of (a) NCDs200 and (b) NCDs400 samples as well as (c) their corresponding height profile.

Figure S7.4: (a) PXRD patterns, **(b)** DTG profile and **(c)** PL spectra of the N-doped samples after annealing from 200 °C to 700 °C.

Figure S7.5: Deconvoluted **(a)** C1s, **(b)** N1s, and **(c)** O1s spectra of NCDs200 sample.

Figure S7.6: Deconvoluted **(a)** C1s, **(b)** N1s, and **(c)** O1s spectra of NCDs400 sample.

Figure S7.7: (a) Carbon and **(b)** Nitrogen bonding state distributions for all samples.

Figure S7.8: PDFs of pristine NCDs and annealed NCDs200, NCDs400 and NCDs700..

Figure S7.9: Sensor response as a function of MeOH vapour concentrations for the **(a)** NCDs200 and **(b)** NCDs400 sensor devices.

List of Schemes

Scheme S7. 1: Sensing device preparation and sensing set-up.

List of Tables

Table S7.1: Atomic compositions of the NCDs samples.

Table S7.2: Sensing parameters of the NCDs devices for detection of MeOH and EtOH; sensitivity (*S*, ppm^{-1}) and LoD (ppm).

Results:

Calculation of the average sp² crystallite sizes and defect density were based on equations S1 and S2

$$L_a(nm) = 2.4 \times 10^{-10} \times \lambda_{laser}^4 \times I_G/I_D \quad \text{(S7.1)}$$

$$n_D(nm) = \frac{2.4\times10^{22}}{\lambda_{laser}^4} \times I_D/I_G \quad \text{(S7.2)}$$

Where λ_{laser} is the wavelength of the excitation laser of the instrument, in this case being 514.5 nm and I_G/I_D is the ration of the integrated areas beneath the G and D bands.

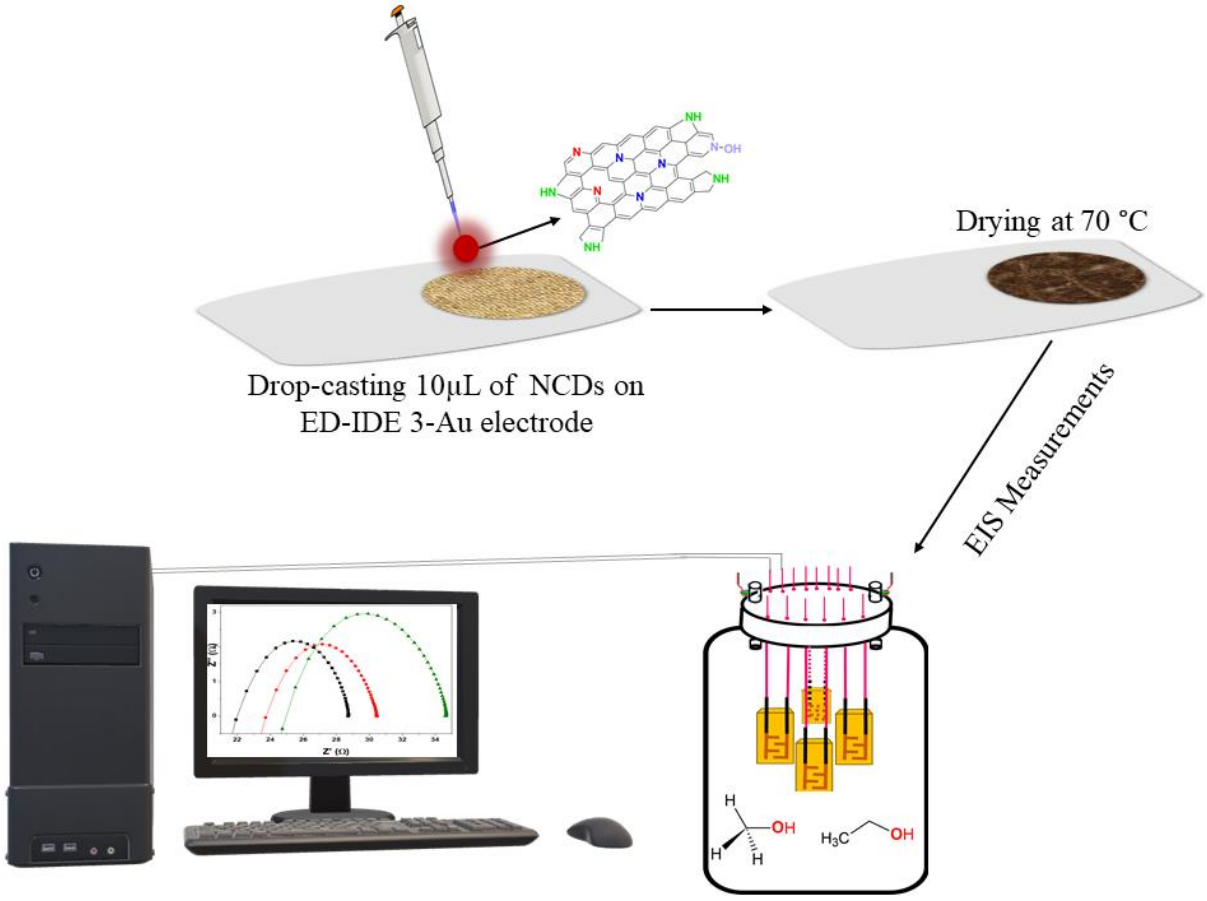

Scheme S7. 2: Sensing device preparation and sensing set-up.

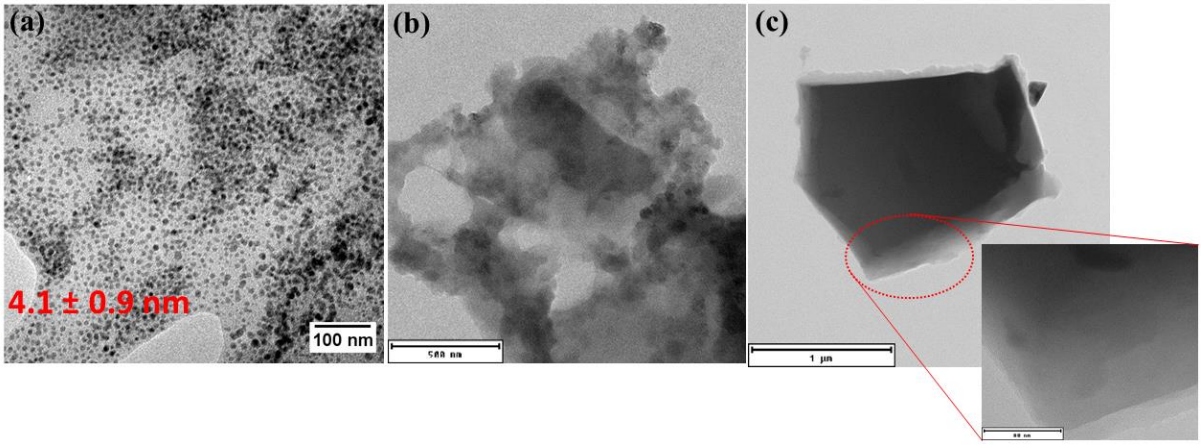

Figure S7. 1: Low magnification TEM micrographs of (a) pristine NCDs, (b) NCDs200, and (c) NCDs400 samples.

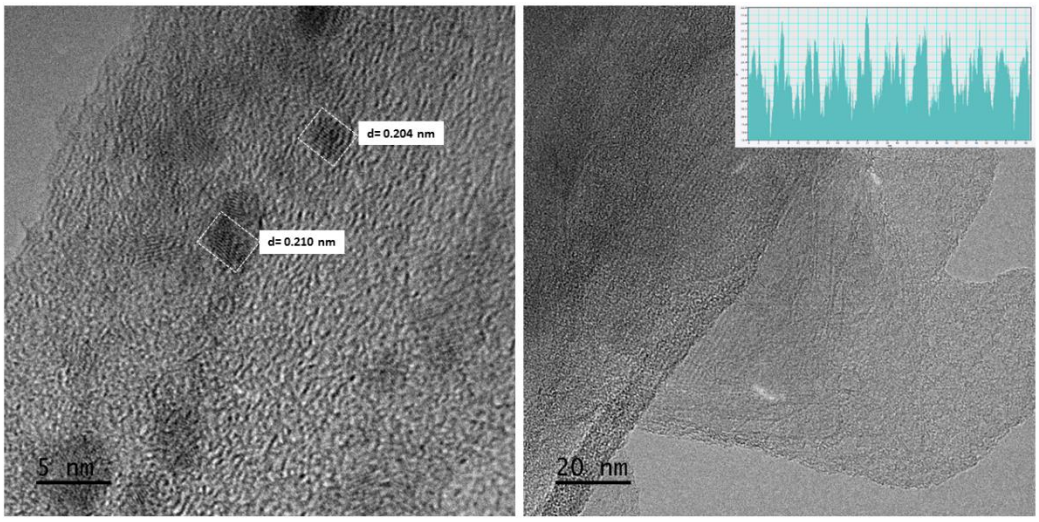

Figure S7. 2: High resolution TEM micrographs of (a) pristine NCDs and (b) NCDs700 samples, with an inserted line profile. This does not show lines of similar heights or spacing between the lines indicating that theNCDs700 sample does not have graphitic character.

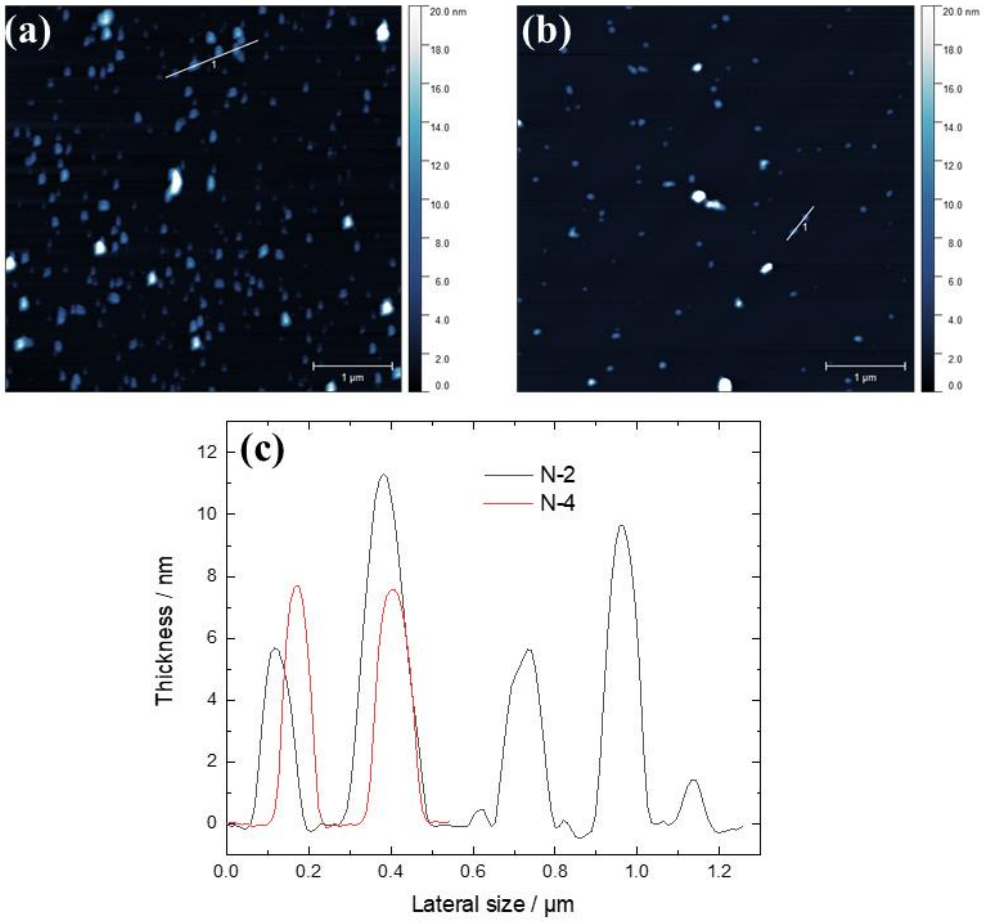

Figure S7. 3: AFM images of (a) NCDs200 and (b) NCDs400 samples as well as (c) their corresponding height profile.

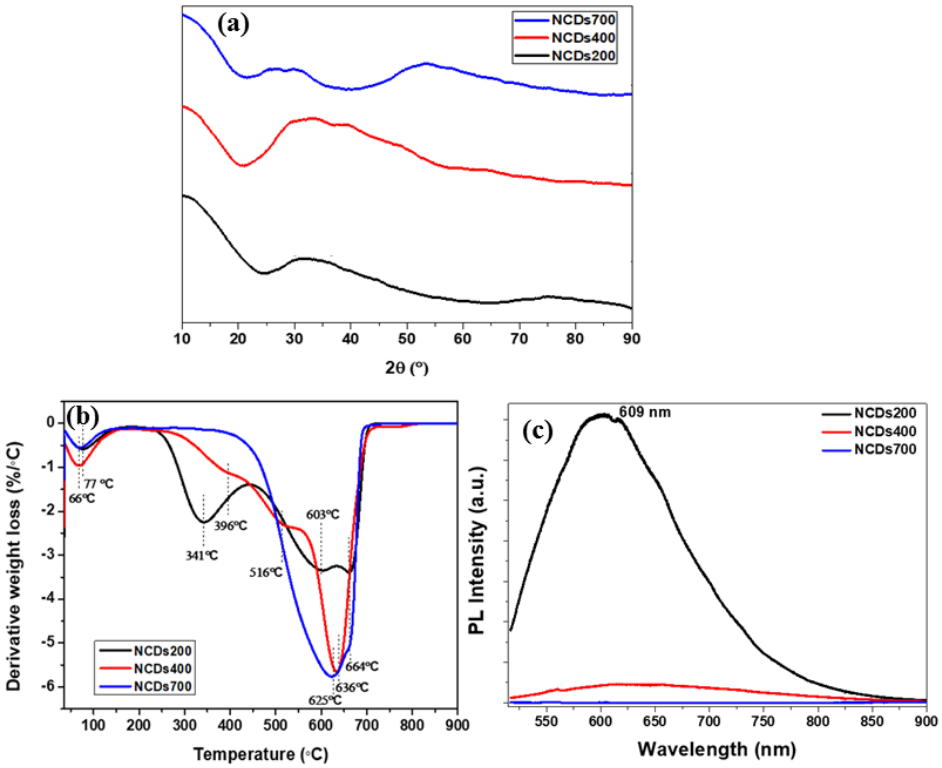

Figure S7. 4: (a) PXRD patterns, (b) DTG profile and (c) PL spectra of the N-doped samples after annealing from 200 °C to 700 °C.

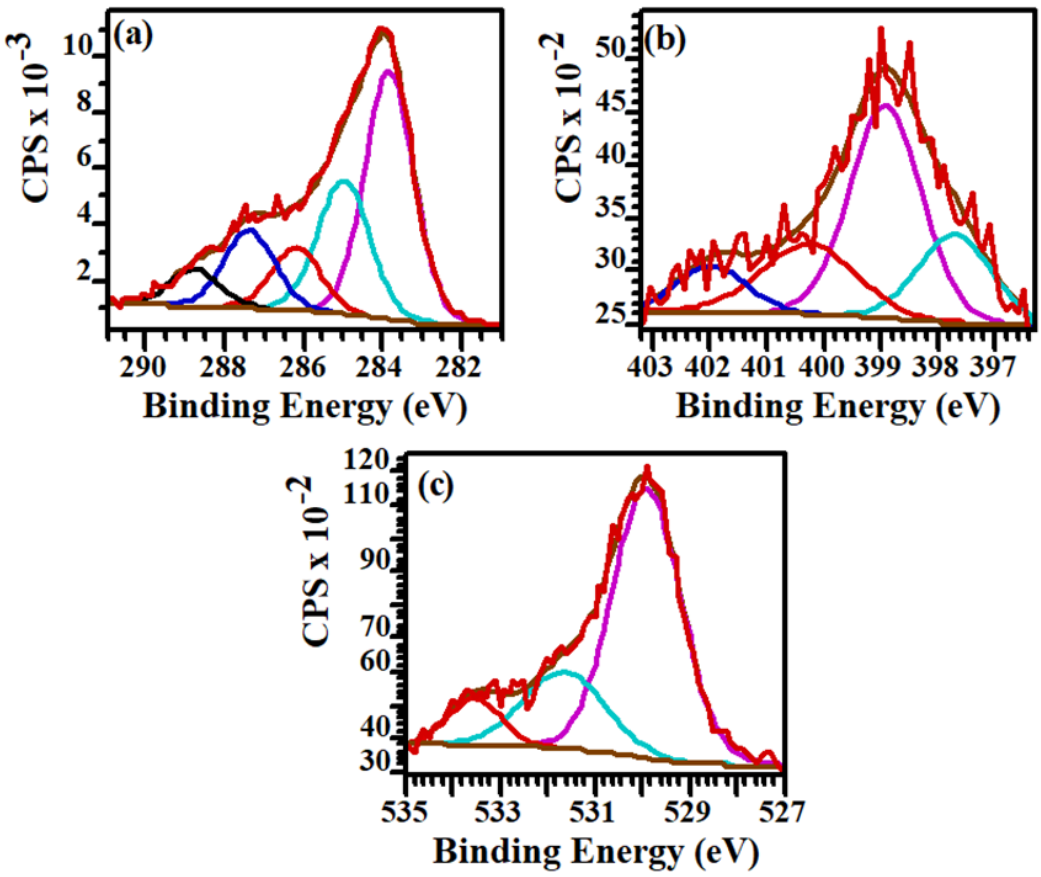

Figure S7. 5: Deconvoluted (a) C1s, (b) N1s, and (c) O1s spectra of NCDs200 sample.

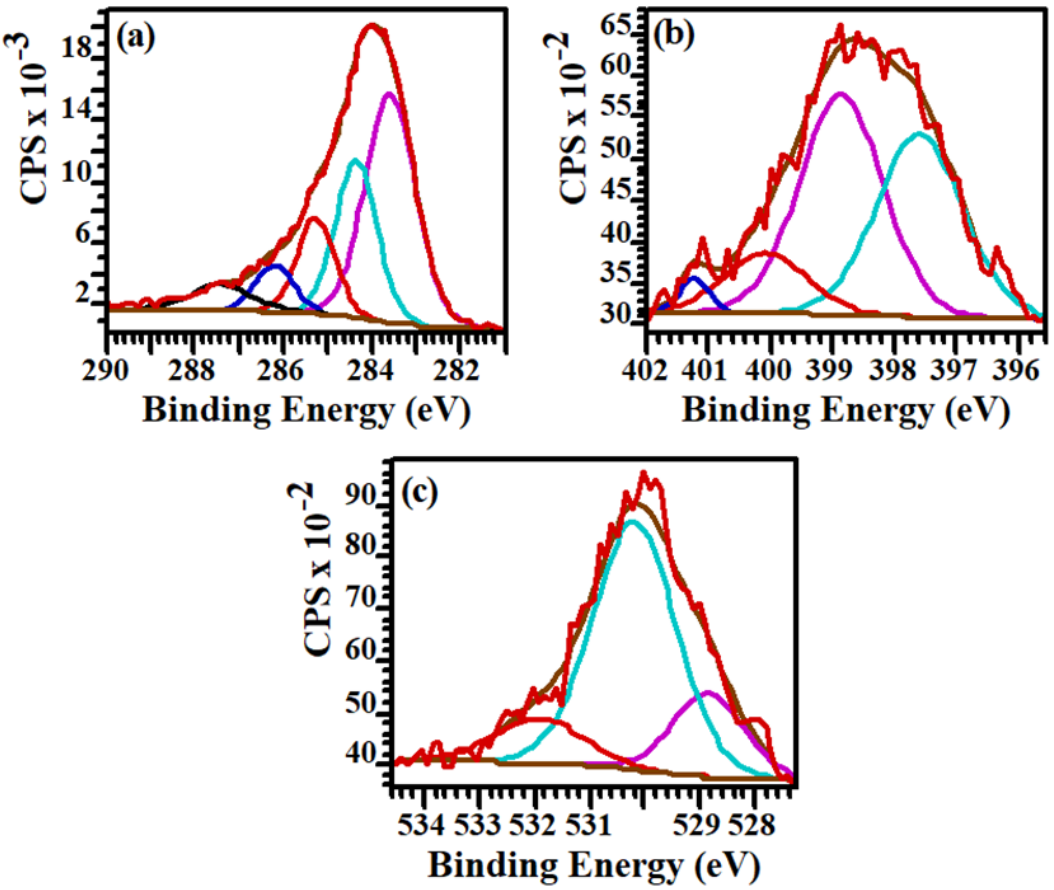

Figure S7. 6: Deconvoluted (a) C1s, (b) N1s, and (c) O1s spectra of NCDs400 sample.

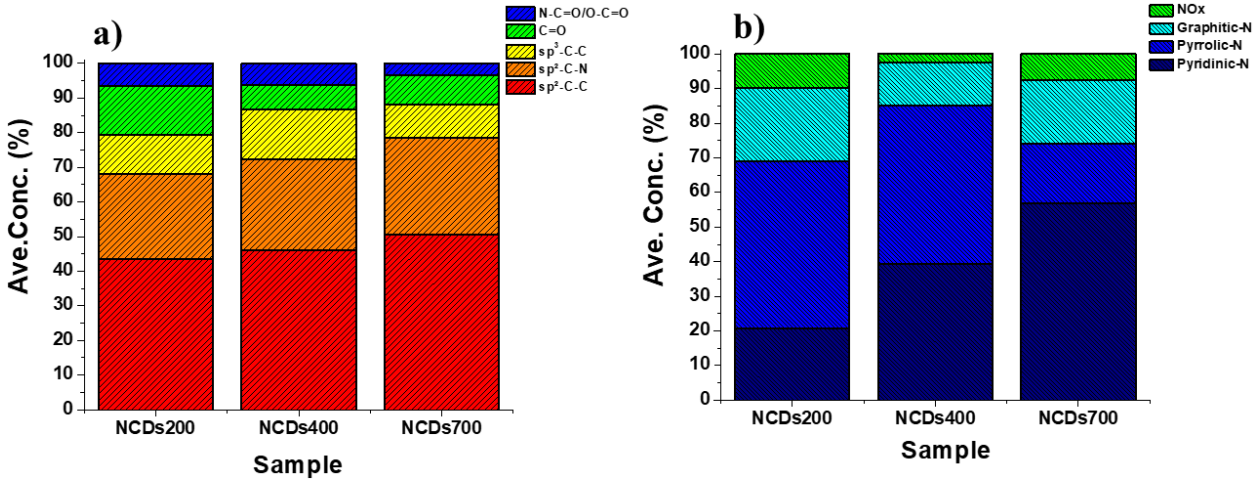

Figure S7. 7: (a) Carbon and (b) Nitrogen bonding state distributions for all samples.

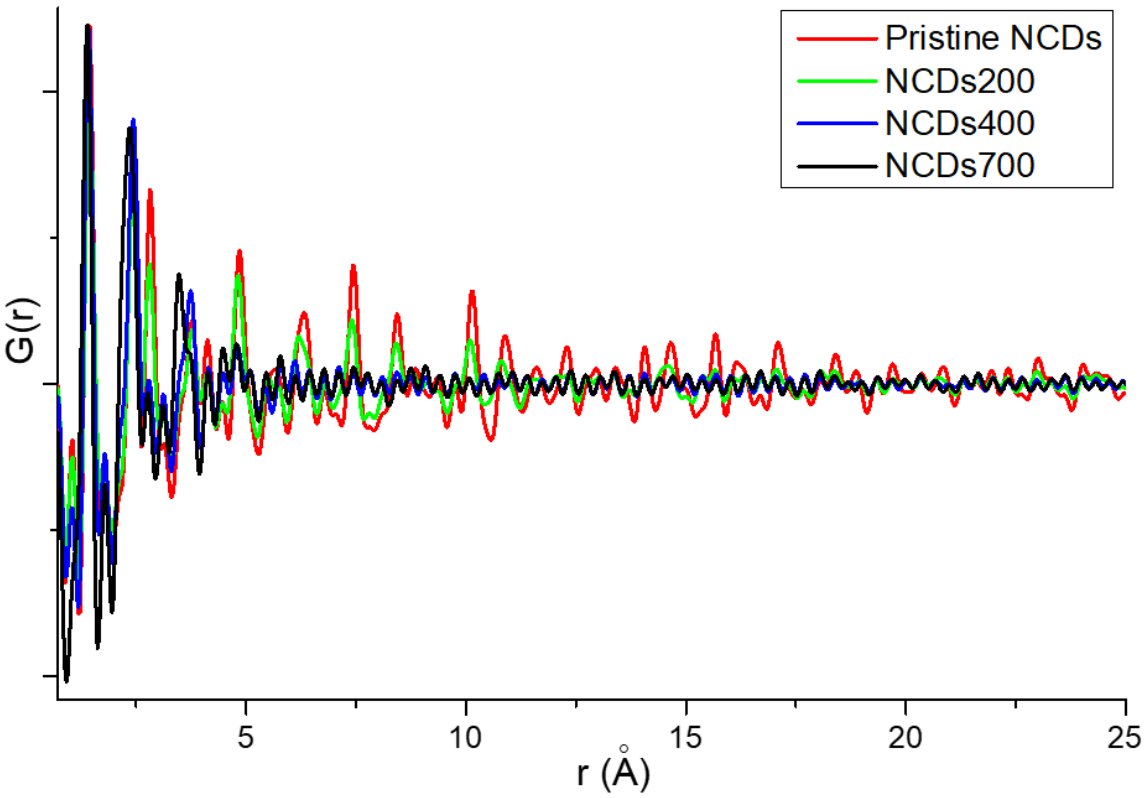

Figure S7. 8: PDFs of pristine NCDs and annealed NCDs200, NCDs400 and NCDs700.

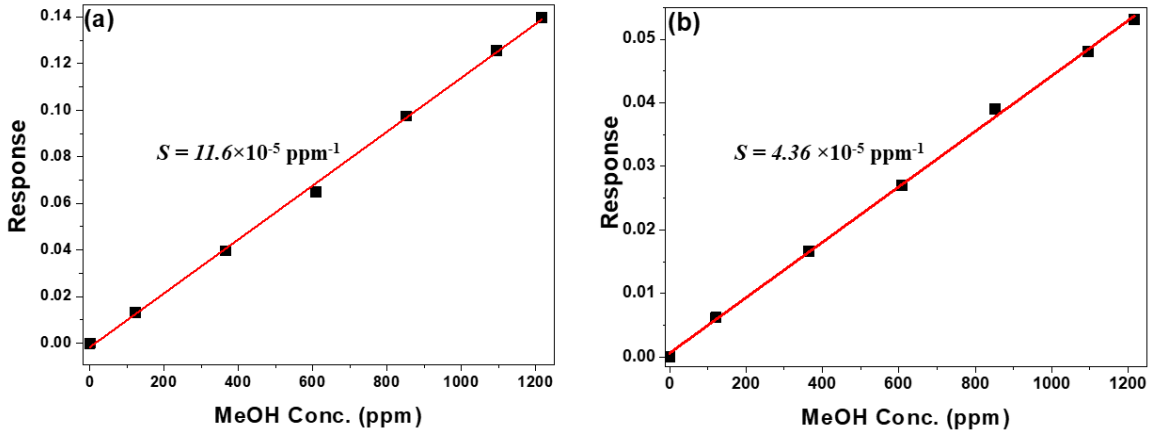

Figure S7. 9: Sensor response as a function of MeOH vapour concentrations for the **(a)** NCDs200 and **(b)** NCDs400 sensor devices.

Table S7. 1: Atomic compositions of the NCDs samples

Samples	Elemental Composition (at.%)		
	C1s	**N1s**	**O1s**
NCDs200	71.76	10.07	18.17
NCDs400	83.00	9.32	7.68
NCDs700	84.05	7.79	8.16

Table S7. 2: Sensing parameters of the NCDs devices for detection of MeOH and EtOH; sensitivity (*S*, ppm^{-1}) and LoD (ppm)

Analyte	Electrode	***S*** **(×10^{-5} ppm^{-1})**	**LoD (ppm)**
Methanol	**NCDs200**	11.6	37.1
	NCDs400	4.36	34.9
	NCDs700	1.17	30.3
Ethanol	**NCDs400**	-2.09	91.4
	NCDs700	-16.4	43.5